

Measurement of neutral current cross sections at high Bjorken- x
with the ZEUS detector at HERA

Yujin Ning

Submitted in partial fulfillment of the
requirements for the degree
of Doctor of Philosophy
in the Graduate School of Arts and Sciences

COLUMBIA UNIVERSITY

2006

Abstract

Measurement of neutral current cross sections at high Bjorken- x with the ZEUS detector at HERA

Yujin Ning

This thesis presents a new method to measure the neutral current cross section up to Bjorken- x values equal to one. This method is employed to the data collected with the ZEUS detector at HERA using an integrated luminosity of 65.1 pb^{-1} for e^+p collisions and of 16.7 pb^{-1} for e^-p collisions at $\sqrt{s} = 318 \text{ GeV}$ and 38.6 pb^{-1} for e^+p at $\sqrt{s} = 300 \text{ GeV}$. Cross sections have been measured for $Q^2 \geq 648 \text{ GeV}^2$ and are compared to predictions using different parton density functions. For the highest x bins, the data has a tendency to lie above the expectations using the recent PDF parametrizations. A preliminary QCD fit shows clear constraints on the form of the parton density functions at the highest values of x .

Contents

1	Deep Inelastic Scattering - Theoretical overview	1
1.1	Introduction	1
1.2	Kinematics	2
1.3	DIS cross section	4
1.4	Parton densities and structure functions	6
1.4.1	Quark-Parton-Model	6
1.4.2	Parton densities	7
1.4.3	Structure function	10
1.5	Summary	13
2	The ZEUS experiment at HERA	16
2.1	HERA ep collider	16
2.2	The ZEUS detector	18
2.2.1	The uranium calorimeter	21
2.2.2	The central tracking detector	23
2.2.3	The presampler	24
2.2.4	The luminosity measurement	24
2.2.5	The trigger and data acquisition system	25
2.3	Monte Carlo simulation	26

2.3.1	DIS event generator	26
2.3.2	Detector simulation	26
2.3.3	Generated event sample	27
2.4	Data sample	29
3	Method and Event Reconstruction	30
3.1	Introduction	30
3.2	New method	33
3.3	The scattered electron	33
3.3.1	Electron finder	34
3.3.2	Energy measurement	35
3.3.3	Angle measurement	35
3.4	The jet	36
3.4.1	Jet finder	36
3.4.2	Energy and angle measurement	37
3.5	Vertex	37
4	Event selection	39
4.1	Characteristics of neutral current events	39
4.2	Background	40
4.2.1	Photoproduction	41
4.2.2	Cosmic and halo muons	42
4.2.3	Proton beam gas interaction	43
4.2.4	QED Compton scattering	44
4.2.5	Calorimeter sparks	45

4.3	Trigger preselection	45
4.4	Offline event-selection	46
4.4.1	Electron selection	47
4.4.2	Jet selection	51
4.4.3	Background suppression	54
4.4.4	Comparison of data and Monte Carlo	58
4.4.5	Comparison of data and Monte Carlo for zero jet events	60
4.4.6	Comparison of data and ARIADNE Monte Carlo in jet	64
5	The cross section measurement	67
5.1	Cross section unfolding method	67
5.2	Binning definition	69
5.3	Cross section measurement	75
5.4	Systematic uncertainties	78
5.4.1	Uncorrelated systematic uncertainties	79
5.4.2	Correlated systematic uncertainties	80
5.5	Other checks	87
5.5.1	Two jets events	87
5.5.2	Cut of y_{JB} on zero jet events	88
5.5.3	Compare with the ZEUS published result	88
5.6	Results	89
5.6.1	Cross section	89
5.6.2	The structure function F_2	91
5.7	Summary	100
A	Control plots for 96-97 e^+p and 98-99 e^-p data	104

B Cross section tables	113
Bibliography	135

List of Figures

1.1	The lowest order Feynman diagram for NC DIS	3
1.2	Scaling behavior as seen by SLAC in 1969.	6
1.3	The four possible parton splitting processes.	9
1.4	DIS phase space covered by different experiments.	10
1.5	The structure function F_2 as a function of Q^2 at different x values.	11
1.6	The ratio of the cross section calculated using different PDFs to CTEQ6D.	12
1.7	PDFs from different fit groups	14
2.1	The HERA accelerator complex at DESY, Hamburg.	17
2.2	Integrated Luminosity delivered by HERA.	19
2.3	The xy view of the ZEUS detector.	20
2.4	The yz view of the ZEUS detector.	21
2.5	The structure of CAL.	22
2.6	The front view of FCAL.	23
2.7	Layout of a CTD octant	24
3.1	Contour lines.	31
3.2	A schematic depiction of the ZEUS detector.	32
4.1	A high Q^2 event display.	41

4.2	A PHP event display.	42
4.3	A cosmic ray event display.	43
4.4	A QED Compton event display.	45
4.5	Electron probability before offline selection.	47
4.6	Electron isolation energy before offline selection.	48
4.7	Track DCA before offline selection.	49
4.8	Track momentum before offline selection.	49
4.9	Electron energy before offline selection.	50
4.10	Electron fiducial cut 1.	50
4.11	Electron fiducial cut 2.	51
4.12	$E_{T,jet}$ before offline selection.	52
4.13	θ_{jet} before offline selection.	52
4.14	Number of jets.	53
4.15	Number of jets in different x_{DA} bins.	53
4.16	Resolution of x for one and two jets events.	54
4.17	Z-vertex before offline selection.	55
4.18	$E - p_Z$ before offline selection.	56
4.19	y_e before offline selection.	56
4.20	$P_T/\sqrt{E_T}$ before offline selection.	57
4.21	The effect of y_{JB} cut.	59
4.22	Control plots for kinematics variables.	60
4.23	Control plots for electron variables.	61
4.24	Control plots for jet variables.	62
4.25	Control plots for kinematics and electron variables for 0 jet events	63

4.26	Control plots for $E - p_Z$ for 0 jet events with +1% electron energy scale	64
4.27	Control plots for θ_{jet} in different E_{jet} bins	65
4.28	Control plots for number of jets jet.	66
5.1	Q^2 resolution	71
5.2	x resolution.	71
5.3	Isoline for different E_p	72
5.4	bin definition	73
5.5	The efficiency and purity in % for each bin for 99 – 00 e^+p are shown.	74
5.6	The dependence of radiative correction on x from jet method.	76
5.7	The high orders of radiative correction.	77
5.8	The uncorrelated systematic uncertainties versus x at low x	80
5.9	The uncorrelated systematic uncertainties versus x at the highest x	81
5.10	Control plots for jet variables with cone algorithm.	82
5.11	Control plots for kinematics and electron variables for 0 jet events with cone algorithm.	83
5.12	Control plots for 2 jet events with cone algorithm.	84
5.13	The correlated systematic uncertainties versus x at low x	84
5.14	The correlated systematic uncertainties versus x at the highest x	85
5.15	The systematic and statistical uncertainty at low x	85
5.16	The systematic and statistical uncertainty at highest x	86
5.17	The definition of the cross section bin number.	86
5.18	Control plots for two jet events.	87
5.19	The relative difference in cross section with one and two jet events.	88
5.20	The systematic check of y_{JB} cut.	89

5.21	The reduced cross section comparison between the value ZEUS published and the value calculated with this new method.	90
5.22	The differential cross section for 96-97 e^+p NC scattering at $\sqrt{s} = 300$ GeV.	92
5.23	The differential cross section for 98-99 e^-p NC scattering at $\sqrt{s} = 318$ GeV.	93
5.24	The differential cross section for 99-00 e^+p NC scattering at $\sqrt{s} = 318$ GeV.	94
5.25	The ratio of cross section to CTEQ6D for 96-97 e^+p NC scattering at $\sqrt{s} = 300$ GeV.	95
5.26	The ratio of cross section to CTEQ6D for 98-99 e^-p NC scattering at $\sqrt{s} = 318$ GeV.	96
5.27	The ratio of cross section to CTEQ6D for 99-00 e^+p NC scattering at $\sqrt{s} = 318$ GeV.	97
5.28	The ratio of the cross section to the PDF including ZEUS-JET and the new measurement in this analysis.	98
5.29	PDFs of the new QCD fit including the result from this analysis.	99
5.30	The structure function F_2 calculated from 98 – 99 e^-p and 99 – 00 e^+p data.	101
5.31	New measured F_2 compared with the measurement by BCDMS.	102
A.1	Control plots for kinematics variables.	105
A.2	Control plots for electron variables.	106
A.3	Control plots for jet variables.	107
A.4	Control plots for kinematics variables.	108
A.5	Control plots for electron variables.	109
A.6	Control plots for jet variables.	110
A.7	Control plots for kinematics and electron variables for 0 jet events	111
A.8	Control plots for kinematics and electron variables for 0 jet events	112

List of Tables

1.1	Quarks and their charges.	8
2.1	1996-2000 HERA running summary.	18
2.2	99-00 MC MEPS.	27
2.3	99-00 MC ARIADNE as the systematic check.	28
2.4	98-99 MC MEPS.	28
2.5	96-97 MC MEPS.	29
B.1	The cross section table for 96-97 e^+p NC scattering.	114
B.2	The integral cross section table for 96-97 e^+p NC scattering.	119
B.3	The cross section table for 98-99 e^-p NC scattering. The first two columns of the table contain the Q^2 and x values at which the cross section is quoted, the third contains the measured cross section $d^2\sigma/dxdQ^2$ corrected to the electroweak Born level, the fourth contains the number of events reconstructed in the bin, the fifth contains the upper limit in case of zero observed events, the sixth contains the statistical uncertainty and the seventh contains the total systematic uncertainty. The right part of the table lists the total uncorrelated systematic uncertainty followed by the bin-to-bin correlated systematic uncertainties δ_1 – δ_6 defined in the text. For the latter, the upper (lower) numbers refer to the variation of the cross section, whereas the signs of the numbers reflect the direction of change in the cross sections. Note that the normalization uncertainty, δ_7 is not listed.	121

B.4 The integral cross section table for 98-99 e^-p NC scattering. The first two columns of the table contain the Q^2 and x_{edge} values for the bin, the third contains the measured cross section $\int_{x_{edge}}^1 d^2\sigma/dxdQ^2$ corrected to the electroweak Born level, the fourth contains the number of events reconstructed in the bin, the fifth contains the upper limit in case of zero observed events, the sixth contains the statistical uncertainty and the seventh contains the total systematic uncertainty. The right part of the table lists the total uncorrelated systematic uncertainty followed by the bin-to-bin correlated systematic uncertainties $\delta_1-\delta_6$ defined in the text. For the latter, the upper (lower) numbers refer to the variation of the cross section, whereas the signs of the numbers reflect the direction of change in the cross sections. Note that the normalization uncertainty, δ_7 is not listed. 126

B.5 The cross section table for 99-00 e^+p NC scattering. 128

B.6 The integral cross section table for 99-00 e^+p NC scattering. 133

Acknowledgments

There are a lot of people helped me and supported me on the thesis work. Here I would like to take this opportunity to thank all of them.

Particularly I would like to thank my advisors: Professor Allen Caldwell and Professor Frank Sciulli. It is impossible to finish this work without their guidance, encouragement and support. I have benefited from their insightful knowledge and great personality. They provided me the nice environment for research in Hamburg and New York. They also spent a lot of time on reading through me thesis and correcting my English.

I really enjoyed doing research in ZEUS collaboration. I would like to thank the coordinators in the ZEUS high Q^2 physics group: Kunihiro Nagano and Alex Tapper. They helped me with a lot of technique and physics questions concerning the analysis. Also I would like to thank other coordinators, Enrico Tassi and Katarzyna Wichmann, for their nice comments. I would like to thank Claire Gwenlan for her kind help on the preliminary QCD fit including the new measurement.

I would like to thank the ZEUS Columbia members, Stathes Paganis, Bill Schmidke, Miroslav Helbich, Xiang Liu and Zhenhai Ren, and the ZUES MPI members, Claudia Buettner, Juraj Sutiak and Iris Abt. It is very nice to work with them. I learned a lot from all of them. Thanks to Stathes for useful discussion on physics and many help on my life in Hamburg. Many thanks to Xiang and Claudia. Xiang helped me start this analysis and gave me many suggestions on this analysis. Claudia did the second analysis on this thesis work.

I would like to thank Lalla Grimes for helping me on all kinds of paper work. I also thank Nicoles Griggs for the arrangement of the defense.

Finally I would like to thank my husband, Zhenhai, who always gives me the support and help on both physics and life.

Chapter 1

Deep Inelastic Scattering - Theoretical overview

1.1 Introduction

The question “what is the structure of matter” is very fundamental. Particle physics tries to address this question. Rutherford’s idea of scattering “point-like” projectiles, such as α particles, off a target, (a gold foil in his case), gave a new technique to investigate the structure of matter. From then on, a series of scattering experiments over the next century led to an ever deeper understanding of the building blocks of matter and the interactions between them.

The proton, a key part of the atom, was initially considered “elementary”. In 1964, Murray Gell-Mann suggested that the proton could be seen as the collection of three smaller fractional electrically charged particles [1] which he called “quarks”. The idea that the proton is not a point-like particle is supported by the value of its gyromagnetic ratio, which is the ratio of the magnetic dipole moment to the spin. For a point-like particle, the gyromagnetic ratio is equal to 2, while the gyromagnetic ratio of the proton is 5.59. In 1969, Feynman [2] suggested that the proton is composed of point-like constituents which he called partons. This model and the Murray Gell-Mann quark model were combined as the quark-parton model. After that, a lot of new models and theories were developed, culminating in the modern theory of strong interactions, quantum chromodynamics (QCD).

In the history of particle physics, scattering point-like particles, like leptons, off nucleons played an important role in testing the new theories and understanding the structure of nucleons. There is no evidence to show that the lepton has size. Compared to scattering between two composite objects, which introduce a more complicated convolution, lepton nucleon scattering has an easier interpretation. In 1956, McAllister and Hofstadter [3] at Stanford measured the charge radius of the proton by scattering the electron with 188 MeV off a hydrogen target. The measured charge radius in this elastic scattering experiment is 0.74 ± 0.24 fm. When the lepton has high enough energy, it can enter the proton deeply and knock out one of the quarks. This process probing the proton with the lepton is called deep inelastic lepton proton scattering (DIS). The first deep-inelastic-scattering experiment was done in 1969 at the Stanford Linear Accelerator Center (SLAC) in California [4]. Electrons of 20 GeV were collided with a hydrogen target. The SLAC experiments showed that there are hard point-like objects inside nucleons.

1.2 Kinematics

In the DIS process ($ep \rightarrow eX$), the electron is scattered on the proton with high momentum transfer. In this process, the electron exchanges a gauge boson with a quark inside the proton. The interaction is “inelastic” when a quark is knocked out of the proton and the proton is broken up. The remaining partons inside the proton tend to fragment into several hadrons, which are called proton remnant. The “deep” means the proton is probed with a gauge boson with small wavelength, resolving small distance scales. The struck quark cannot be seen and radiates more partons. These partons form a hadronic final state particle shower which is called a jet. The jet will follow the direction of the original struck quark. This analysis concentrates on neutral current (NC) DIS, which means a neutral boson, i.e. a photon or Z^0 , is exchanged between the electron and the quark. When a charged W -boson is exchanged resulting in a neutrino in the final state, the process is called charged current (CC) DIS.

A schematic picture of the NC process is shown in Fig. 1.1. The following four Lorentz-

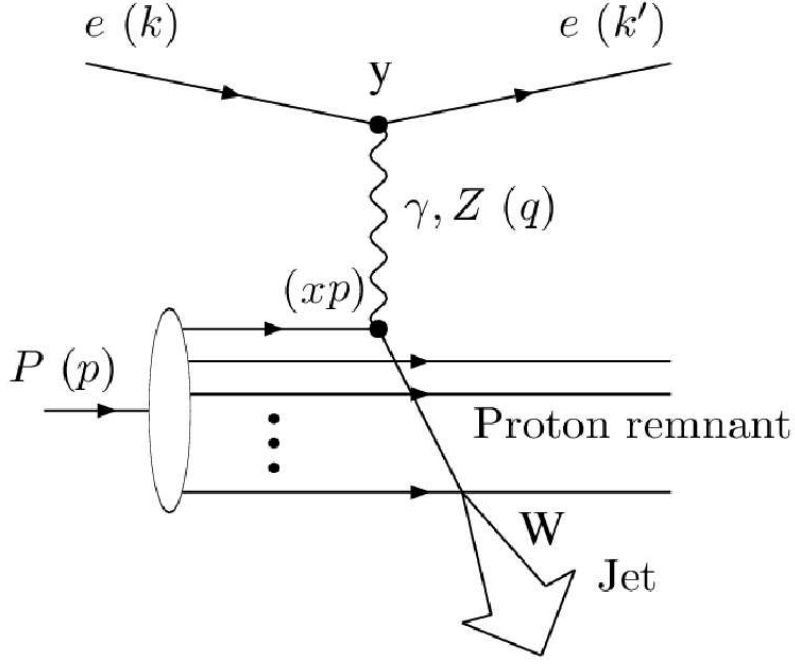


Figure 1.1: The lowest order Feynman diagram for neutral current electron proton scattering. Four momenta of incoming and outgoing particles and kinematic variables are shown. Note that a jet follows the direction of the struck quark.

invariant variables are most commonly used to define the kinematics of the interaction:

$$Q^2 \equiv -q^2 = -(k - k')^2, \quad (1.1)$$

$$x \equiv \frac{-q^2}{2p \cdot q}, \quad (1.2)$$

$$y \equiv \frac{p \cdot q}{p \cdot k}, \quad (1.3)$$

$$W^2 \equiv (p + q)^2. \quad (1.4)$$

Q^2 is the virtuality of the exchanged boson, i.e. $Q^2 = 0$ corresponds to a real photon. Q^2 gives the “scale” of the interaction: the wavelength of the photon and therefore the smallest distance scale the probe can resolve is given by $\lambda \approx \hbar c / \sqrt{Q^2}$. The Bjorken scaling variable x denotes the proton momentum fraction carried by the struck quark in the proton infinite momentum frame. The variable y gives the energy fraction transferred from the electron to the quark in the proton rest frame and is known as the inelasticity. Both x and y are constrained to lie between $0 \leq x, y \leq 1$. W^2 is the square of the invariant mass

of the hadronic final state. However, these four kinematic variables are not independent. The process is characterized by only two independent variables. Neglecting the masses of the electron and proton, Q^2 , x and y are related through:

$$Q^2 = sxy, \tag{1.5}$$

where s is the squared center-of-mass energy of the electron proton system and $W^2 = sy(1-x)$. So the maximum Q^2 and W^2 are limited by s . In this analysis, the two chosen variables are Q^2 and x .

1.3 DIS cross section

The inclusive $ep \rightarrow eX$ cross section can be factorized and written as the product of a lepton tensor and a hadronic tensor. The lepton tensor can be described by the electroweak theory [5]. For $Q^2 \ll M_Z^2$, quantum electrodynamics (QED) represents it well with just photon exchange. The cross section can be calculated from the Feynman diagrams [6]. The coupling strength at a QED vertex is proportional to $\sqrt{\alpha(\mu)}$ with $\sqrt{\alpha(0)} \approx \sqrt{137}$, where $\alpha(\mu)$ denotes the fine structure constant and μ is a renormalization scale. The dependence of α on μ is small. But Z^0 , which mediates weak neutral current interactions, can not be described by the massless vector-field, like the photon, in QED. The solution is called spontaneous symmetry-breaking [7–9], which makes it possible to generate masses for the W^\pm and Z^0 from the originally massless fields. The weak force is mediated by the exchange of the massive gauge boson and is unified with the electromagnetic force to the more fundamental electroweak force [10]. At distances 10^{-18} m, the electromagnetic force is much stronger than the weak force due to the massless gauge boson, the photon.

Because the proton is not point-like, the structure of the proton is described by the hadronic tensor which parametrizes our ignorance of the proton structure. It depends on the momentum of the probe, the momentum of the struck parton in the proton and the spin of both objects. Three out of eight structure functions, which come from the most general Lorentz-invariant ansatz (with restrictions of current conservation and time

reversal invariance), are spin independent and relevant for the unpolarized lepton nucleon scattering studied in this analysis. With the Lorentz-invariant variables described before, the NC electron-proton double differential scattering cross section at Born level (lowest order in QED theory) is typically written in terms of the three proton structure functions as:

$$\frac{d^2\sigma_{\text{Born}}(e^\pm p)}{dx dQ^2} = \frac{2\pi\alpha^2}{xQ^4} \left[\frac{y^2}{2} 2xF_1^{NC}(x, Q^2) + (1-y^2)F_2^{NC}(x, Q^2) \mp \left(y - \frac{y^2}{2}\right)x F_3^{NC}(x, Q^2) \right], \quad (1.6)$$

where α denotes the fine structure constant. The dependence on $1/Q^4$ reflects the photon exchange dominant at low momentum transfers. The effect of Z^0 boson exchange is included in the definitions of the structure function. The structure function $2xF_1^{NC}(x, Q^2)$ is proportional to the transverse component of the cross section, in which a transversely polarized boson is exchanged, while the structure function $F_2^{NC}(x, Q^2)$ includes the cross section of both transversely and longitudinally polarized boson. The difference between $2xF_1^{NC}(x, Q^2)$ and $F_2^{NC}(x, Q^2)$ gives the longitudinal part of the cross section. $x F_3^{NC}(x, Q^2)$ contains the parity violating part of the cross section, which can be neglected at low Q^2 . Photon exchange dominates in this region and parity is conserved for pure electro-magnetic coupling. For Q^2 high enough, $Q^2 \simeq M_Z^2$, the contribution of the weak interaction by exchanging of Z^0 becomes measurable in the cross section. As discussed above, the longitudinal structure function $F_L^{NC}(x, Q^2)$ is defined as:

$$F_L^{NC}(x, Q^2) = F_2^{NC}(x, Q^2) - 2xF_1^{NC}(x, Q^2), \quad (1.7)$$

which describes the absorption of a longitudinally polarized virtual photon. The $F_L^{NC}(x, Q^2)$ is suppressed, since the helicity is not conserved in the interaction between a quark and a longitudinally polarized virtual photon. Thus the cross section can be written as:

$$\frac{d^2\sigma_{\text{Born}}(e^\pm p)}{dx dQ^2} = \frac{2\pi\alpha^2}{xQ^4} \left[Y_+ F_2^{NC}(x, Q^2) \mp Y_- x F_3^{NC}(x, Q^2) - y^2 F_L^{NC}(x, Q^2) \right], \quad (1.8)$$

where $Y_\pm \equiv 1 \pm (1-y)^2$. An interpretation of the structure functions in terms of momentum distributions of parton inside the proton is given by the Quark-Parton-Model described in the next section.

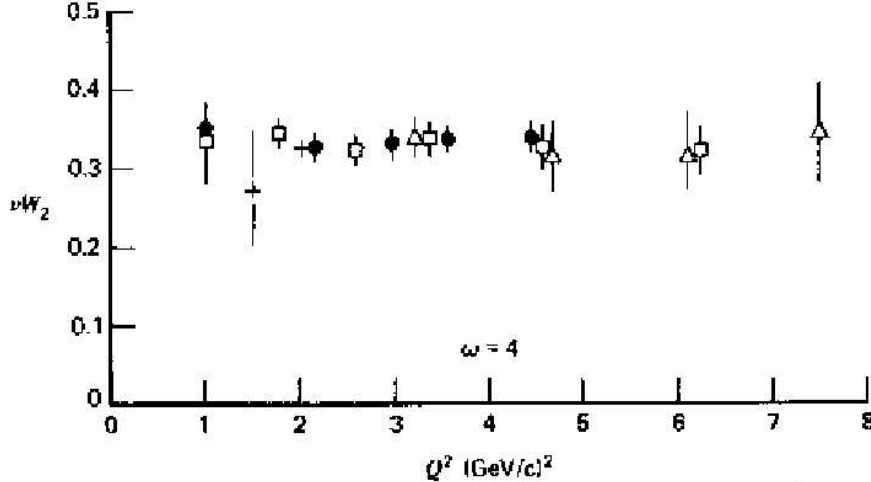


Figure 1.2: *Scaling behavior as seen by SLAC in 1969 in electron-proton scattering experiment [11]. The plot shows the structure function μW_2 as a function of Q^2 , for $\omega = 4$, where μW_2 is the structure function F_2 and the ω is the inverse of the momentum fraction carried by the struck quark, $1/x$.*

1.4 Parton densities and structure functions

1.4.1 Quark-Parton-Model

The first high energy measurement of the inelastic ep cross section at SLAC found the structure function $F_2(x, Q^2)$ to be only weakly dependent on Q^2 for values of $x \sim 0.25$ [11] (Fig. 1.2) in the region $1 < Q^2 < 8 \text{ GeV}^2$. This so called scaling behavior had been predicted by Bjorken [12]. A constant value of $F_2(x, Q^2)$ is the consequence of the fact that the probed parton has point-like structure. The Quark-Parton-Model [2], which assumes the proton is a static object with free (non-interacting), point-like partons (quarks) inside, explains this observation.

In addition to the scaling behavior, Callan and Gross [13] suggested that the structure functions are related:

$$2xF_1(x, Q^2) = F_2(x, Q^2), \quad (1.9)$$

a consequence of the fact that the charged partons inside the proton carry spin $1/2$ ($2xF_1/F_2 = 0$ for spin 0). This relation was approximately confirmed by experiment and together with the verification of scaling behavior gave early evidence of the existence of

quarks. In reality, F_L , defined in Eq. 1.7, is not equal to zero as expected from Eq.1.9. But it is close to zero at high x . So the proton does not just consist of free point-like quarks.

1.4.2 Parton densities

The assumption that quarks are free inside the proton leads to electron free quark elastic scattering, which is not exactly true from experiments. It was found that the scaling behavior, the independence of Q^2 , is violated at high Q^2 and low x . The observed facts can be explained by quantum chromodynamics (QCD), which describes the strong color force mediated by electrically neutral “gluons”. QCD led to the dynamic parton model. In this model, quarks inside the proton interact with each other via the exchange of gluons and the gluons can also interact with each other. Quarks and gluons carry a new quantum number, color, which is exchanged in their interaction. There are three colors, red, blue and green, and corresponding anticolors. Quarks carry one color and gluon carry a color and an anticolor. Colors are conserved in the QCD process and the hadron must be color neutral. There are six “flavors” of quarks, u , d , c , s , t and b . Table 1.1 shows their names and charges. The corresponding antiquarks have the electric charges with the reversed sign. The particles with one quark and one antiquark are called meson. The particles with three quarks are called baryons. Both mesons and baryons are hadrons. The quark composition for the proton is uud . In QCD, the quark cannot be observed as free particle because the energy between two bound quarks, stored in the gluon flux, increases as the distance between them increases. When the energy in the gluon flux is big enough, a quark-antiquark pair is generated. So in a proton, besides the three valence quarks (q_v) probed at low momentum transfer and high x , which are responsible for the quantum numbers, the proton contains many extra quark-antiquark pairs, called sea quarks. The number of quarks and gluons seen inside the proton changes as the scale of the interaction, Q^2 , changes. The larger the momentum scale, the more quarks and gluons are observed. At low Q^2 and high x , the valence quarks carry most of the proton momentum; at high Q^2 , the proton momentum is shared by many partons, and the probability of a quark

Quark			Charge (e_f)
u (up)	c (charm)	t (top)	2/3
d (down)	s (strange)	b (bottom)	-1/3

Table 1.1: *The six quark flavors and their charges.*

carrying a high x momentum fraction is lower. In contrast to QED, the coupling strength $\alpha_s(\mu)$ in QCD gets large for small momentum scales. The scale dependence of $\alpha_s(\mu)$ is determined in leading order by:

$$\alpha_s(\mu) = \frac{12\pi}{(11n - 2n_f)\ln(\frac{\mu^2}{\Lambda^2})}, \quad (1.10)$$

where n is the number of colors, n_f is the number of “active” quark flavors (3-5 at HERA, depending on the scale μ) and $\Lambda \approx 200\text{MeV}$. In ep scattering, μ^2 is chosen to be $\mu^2 = Q^2$.

The scaling violations observed in the data can be explained by the fact that parton distributions have a Q^2 dependence. The parton density function (PDF) is parametrized with a function, $q(x, Q^2)$, which is the differential probability that a parton q carries the momentum fraction x when observed with scale Q . So $u(x, Q^2)$ and $d(x, Q^2)$ give the probability densities for u and d quarks respectively. To make sure the quantum numbers of the proton, which has valence quarks uud , are correct, the quark densities must satisfy the following sum rules:

$$\int_0^1 dx(u(x, Q^2) - \bar{u}(x, Q^2)) = \int_0^1 dx u_v(x, Q^2) = 2, \quad (1.11)$$

$$\int_0^1 dx(d(x, Q^2) - \bar{d}(x, Q^2)) = \int_0^1 dx d_v(x, Q^2) = 1, \quad (1.12)$$

$$\int_0^1 dx(s(x, Q^2) - \bar{s}(x, Q^2)) = \int_0^1 dx s_v(x, Q^2) = 0. \quad (1.13)$$

The DGLAP (Dokshitzer-Gribov-Lipatov-Altarelli-Parisi) evolution equations [14] describe how quark ($q(x, Q^2)$) and gluon ($g(x, Q^2)$) density functions evolve with Q^2 . In the leading order, e.g.,

$$\frac{dq(x, Q^2)}{d \ln Q^2} = \frac{\alpha_s(Q^2)}{2\pi} \int_x^1 \frac{dy}{y} (q(y, Q^2) P_{qq}(\frac{x}{y}) + g(y, Q^2) P_{qg}(\frac{x}{y})), \quad (1.14)$$

$$\frac{dg(x, Q^2)}{d \ln Q^2} = \frac{\alpha_s(Q^2)}{2\pi} \int_x^1 \frac{dy}{y} \left(\sum_q q(y, Q^2) P_{gq}\left(\frac{x}{y}\right) + g(y, Q^2) P_{gg}\left(\frac{x}{y}\right) \right), \quad (1.15)$$

where x and y are the momentum fractions carried by the partons, $P_{ij}(\frac{x}{y})$ is the splitting function, which gives the probability for a parton j with momentum fraction y to create a parton i with the momentum fraction x . The four possible splitting processes are shown in Fig.1.3 and $P_{ij}(\frac{x}{y})$ can be calculated in QCD.

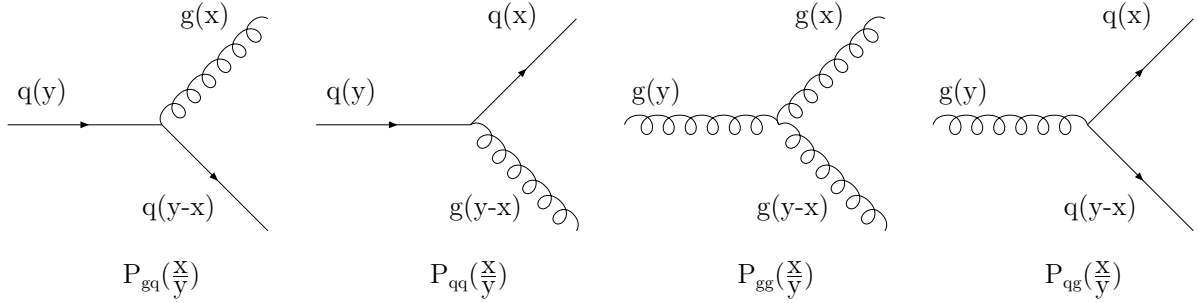


Figure 1.3: The four possible parton splitting process: P_{gq} , P_{qq} , P_{gg} and P_{qg} .

The DGLAP equations do not predict the x -dependence of the PDFs, but do give the Q^2 -dependence and allows PDFs at one Q^2 to be evolved to other Q^2 as described above. The PDFs were found experimentally to decrease very quickly for $x > 0.3$. At high x , the region this analysis is interested in, the shape of the parton densities is usually parametrized by $(1-x)^\eta$ as $x \rightarrow 1$. However, a direct confrontation with data has not been possible to date for $x \rightarrow 1$ due to limitations in beam energies and measurement techniques. The $x - Q^2$ phase space covered by different experiments including HERA is shown in Fig. 1.4. The high x region covered by the fixed target experiments is at low Q^2 . The highest measured points in the DIS regime are for $x = 0.75$ [15] by BCDMS. Data at higher x exist [16,17] but these are in the resonance production region and cannot be easily interpreted in terms of parton distributions. The structure functions measured by HERA [18–25] cover much large phase space than the the previous fixed target experiments. The Q^2 region increases substantially to 30000 GeV^2 and x reaches to the lowest point $x = 6.3 \cdot 10^{-5}$. But HERA did not extend the structure function measurement to the high x region. The highest x value for HERA structure function data reported until now is

$x = 0.65$. The structure function F_2 measured at ZEUS with 96-97 e^+p data as a function of Q^2 at different x values is shown in the Fig. 1.5. The values measured in the fixed target experiments are also shown. The behavior of the structure function at high x is still not well known. On the other hand, the differences between different PDFs increase very fast as x increases as seen in Fig. 1.6, even though they use similar data and have common parametrization for $x \rightarrow 1$. New data and new analysis techniques are needed to provide the necessary data in this domain.

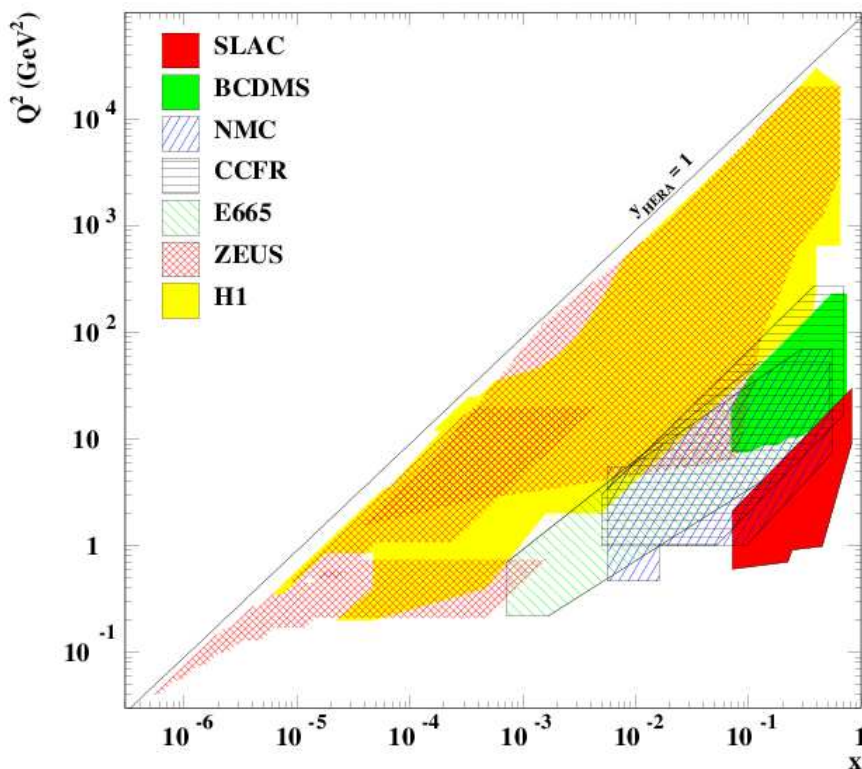


Figure 1.4: *DIS phase space covered by different experiments.*

1.4.3 Structure function

The structure functions parametrize the momentum carried by the charged partons. The structure functions are written in terms of the quark and anti-quark momentum densities

ZEUS

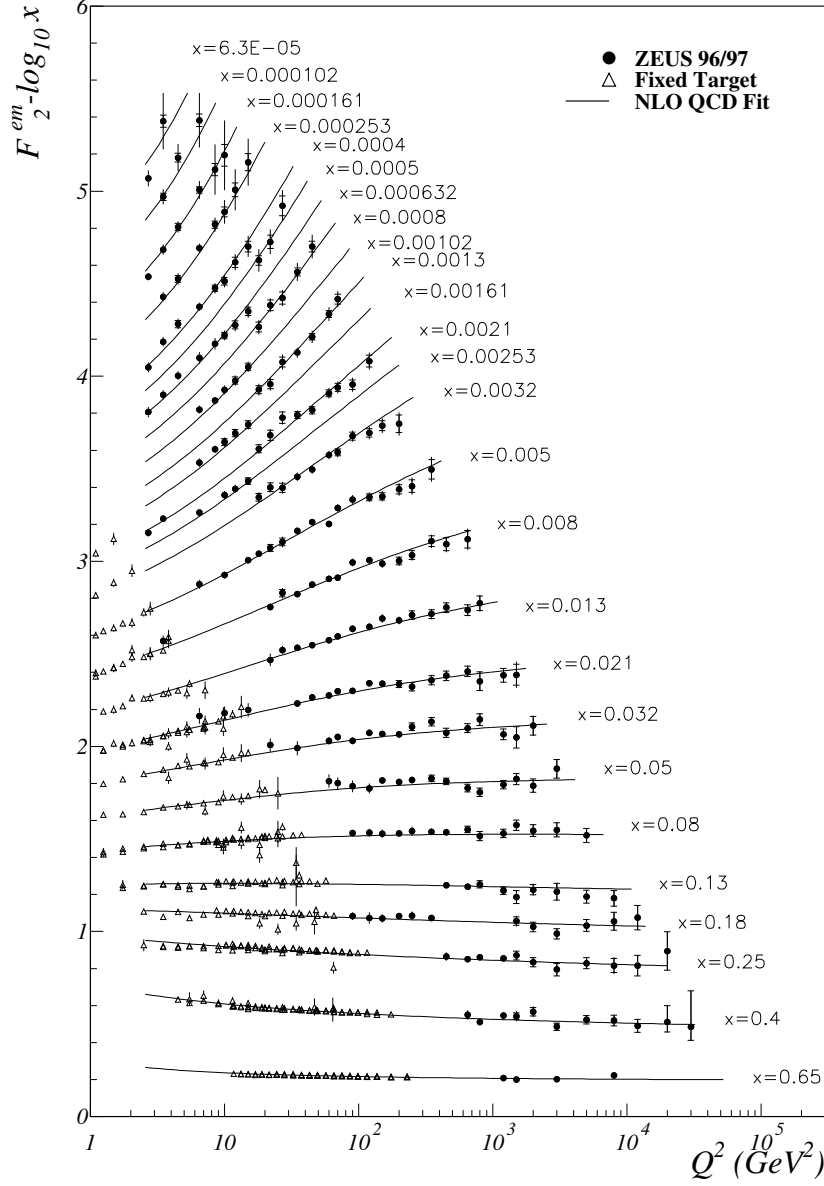


Figure 1.5: The structure function F_2 as a function of Q^2 at different x values [21]. The points are the results from ZEUS 96 – 97 data. The triangles are the results from the fixed target experiment: NMC, BCDMS and E665. The lines are the ZEUS-S fit.

at leading order (LO) α_s as follows:

$$F_2(x, Q^2) = x \sum_f A_f(Q^2) (q_f(x, Q^2) + \bar{q}_f(x, Q^2)) , \quad (1.16)$$

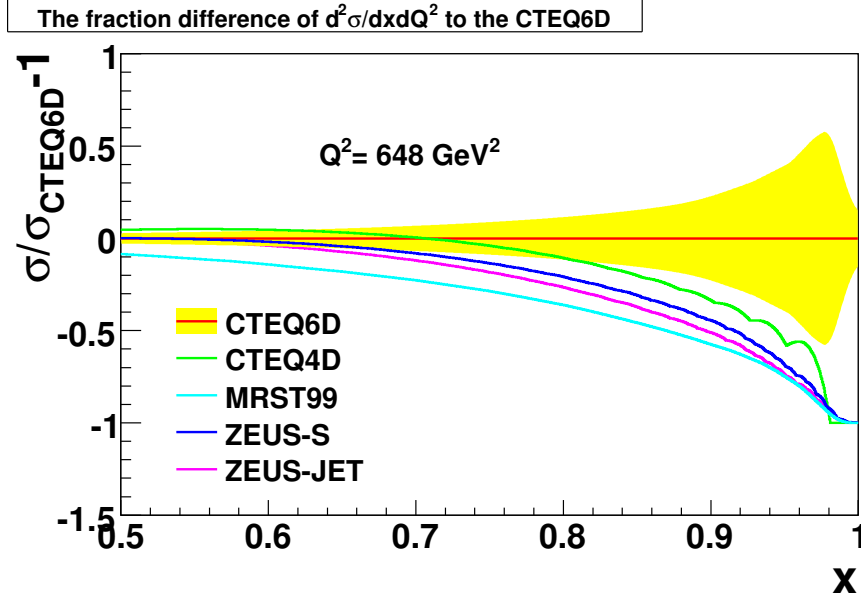


Figure 1.6: The ratio of the cross section calculated using different PDFs to that calculated from CTEQ6D is shown versus x for the PDF sets indicated in the figure. The yellow shaded band corresponds to the one sigma uncertainty from the CTEQ6D PDF.

$$xF_3(x, Q^2) = x \sum_f B_f(Q^2)(q_f(x, Q^2) - \bar{q}_f(x, Q^2)) , \quad (1.17)$$

where $xq_f(x, Q^2)$ are the quark and $x\bar{q}_f(x, Q^2)$ the anti-quark PDFs and f runs over the five active quark flavors; $A_f(x, Q^2)$ and $B_f(x, Q^2)$ contain products of electroweak couplings and ratios of photon and Z -boson propagators. The prefactor $A_f(x, Q^2)$ and $B_f(x, Q^2)$ are defined as:

$$A_f(Q^2) = q_f^2 - 2v_e v_f q_f P_z + (v_e^2 + a_e^2)(v_f^2 + a_f^2)P_z^2, \quad (1.18)$$

$$B_f(Q^2) = -2a_e a_f q_f P_z + 4v_e a_e v_f a_f P_z^2 \quad (1.19)$$

with

$$P_z = \frac{1}{4\sin^2\theta_W \cos^2\theta_W} \cdot \frac{Q^2}{Q^2 + M_Z^2} \quad (1.20)$$

and

$$\cos\theta_W = \frac{M_W}{M_Z}. \quad (1.21)$$

Here, q_f is the electric charge of the struck quark, (v_e, v_f) and (a_e, a_f) are the vector and axial-vector coupling-constants for the lepton e and the quark f . The term $A_f(Q^2)$

is unchanged by changing the polarity of either the electron or the quark. So $A_f(Q^2)$ conserves parity and $B_f(Q^2)$ does not. $F_2(x, Q^2)$ is proportional to the sum of all the quarks inside the proton, including the valence and sea quarks. $xF_3(x, Q^2)$ is the difference between the quarks and antiquarks inside the proton. $F_2(x, Q^2)$ dominates in the cross section and $xF_3(x, Q^2)$ probes the valence quarks. The sign of $xF_3(x, Q^2)$ is different in e^+p and e^-p (see Eq. 1.8), due to the parity violation intrinsic to the weak interaction. So the difference between the cross sections of e^+p and e^-p scattering is evidence of parity violation. At low Q^2 , the exchange of Z^0 can be neglected because the propagator is proportional to $1/Q^2$ for photon and $1/(Q^2 + M_Z^2)$ for Z^0 . As Q^2 increases and is comparable to M_Z^2 , the effect of the parity violation from the exchange of Z^0 included in xF_3 becomes measurable.

The $xq_f(x, Q^2)$ cannot be derived from the DGLAP equations, but they can be indirectly measured. The parametrization of the different PDFs, like CTEQ [26], MRST [27], ZEUS-S [17] and ZEUS-JET [28], have been chosen to conform to cross section measurements from different experiments at different energy scales. These are combined into fits based on the DGLAP evolution equations. The PDFs are commonly parametrized as a function of x at a fixed Q_0^2 value of a few GeV^2 . Then the evolution equations are applied to evolve the PDF to higher Q^2 values. Over the years, the CTEQ and the MRST groups have specialized in the extraction of PDF. Figure 1.7 shows the PDF obtained from these groups as well as from ZEUS.

1.5 Summary

As mentioned in the Sect. 1.4, the PDFs at high x are not predicted and are hard to measure. We designed a new method to measure the NC DIS cross section at $x \rightarrow 1$. The ZEUS data taken during 1996 to 2000 at HERA were analyzed with this new method and the results will be given in this thesis. A preliminary QCD fit shows that the new cross section gives new constraint on PDF at high x .

The thesis is organized as follows. This chapter gives the introduction of the NC DIS

ZEUS

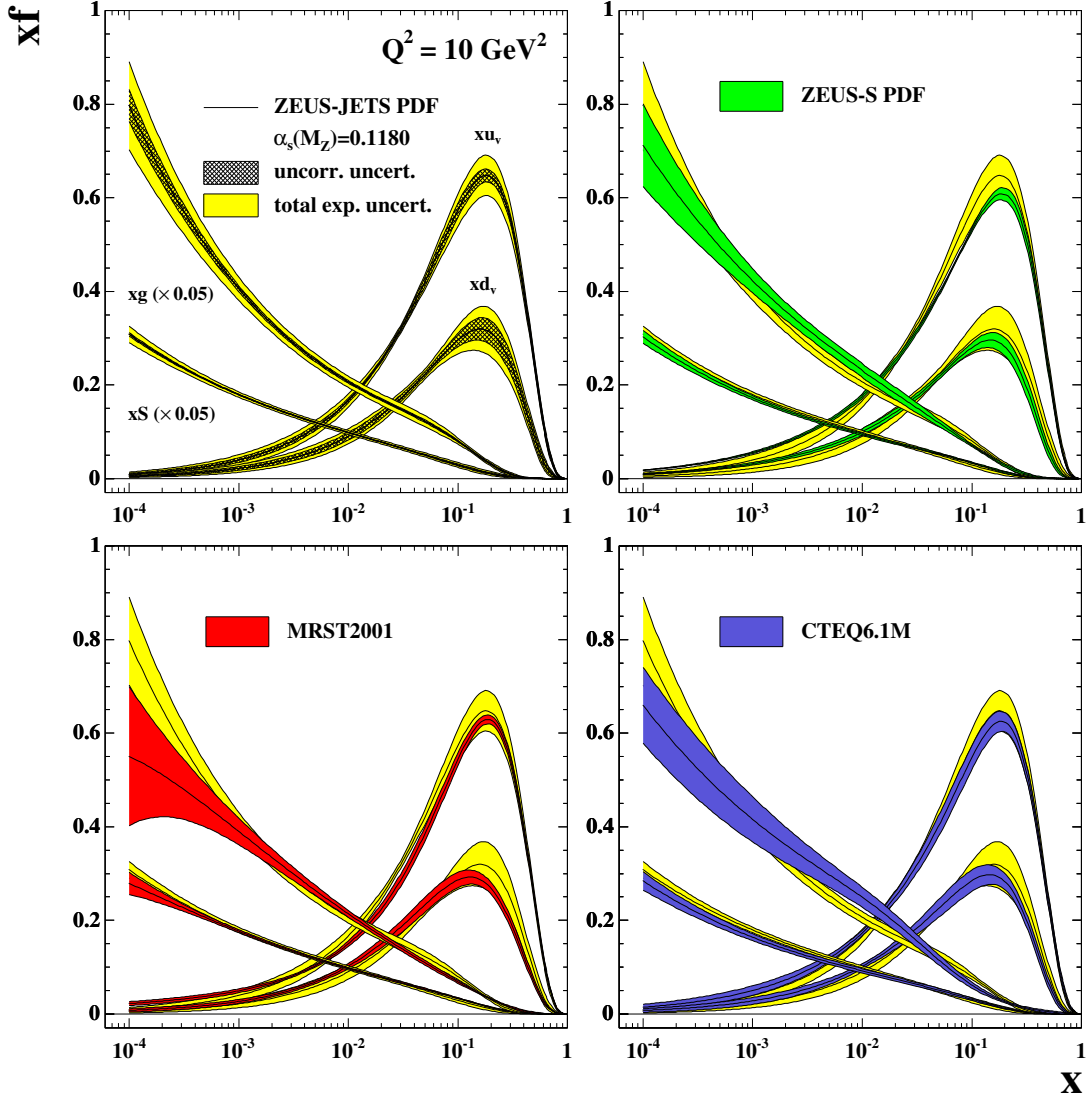


Figure 1.7: *The PDFs from ZEUS NLO, ZEUS-JET, MRST and CTEQ6 [28]. xu_v and xd_v show the valence quark, xg the gluon xS the sea quark and antiquark distributions. The shaded bands are the uncertainty on the PDF fit from data.*

structure function and the motivation of this analysis. Chapter 2 introduces the experiment setup, which includes the HERA collider and the ZEUS detector, and the Monte Carlo. Chapter 3 describes the features of NC DIS events, the new method used in this analysis and the reconstruction of the kinematics. Chapter 4 shows the background events which could be misidentified as DIS events and the selections applied online and offline. The last chapter describes the calculation of the cross sections and the systematic checks. The F_2 measured with the new method is also shown.

Chapter 2

The ZEUS experiment at HERA

2.1 HERA ep collider

The Hadron-Elektron-Ringanlage (HERA) is the world wide first lepton-proton storage ring, located at Deutsches Elektronen-Synchrotron (DESY) in Hamburg, Germany. The schematic layout of HERA with pre-accelerators is shown in Fig. 2.1. It has a circumference of 6.3 km and consists of two separate rings for electron¹ and proton beams. The electron beam uses conventional magnets and proton beam uses superconducting magnets.

The protons start as H^- ions in the linear accelerator (LINAC) and are accelerated to 50 MeV, then filled into DESY III and accelerated to 7.5 GeV in bunches with the time separated 96 ns. The bunches are then filled into PETRA and accelerated to 40 GeV before being filled into HERA. This procedure is repeated until all the bunches in HERA are filled. Only then the protons are accelerated to their final energy 820 GeV (920 GeV after 1998). The electrons follow a similar procedure. Electrons are accelerated to 450 MeV in LINAC II, then to 7.5 GeV in DESY II. Afterward they are transferred to PETRA and accelerated to 12 GeV. Finally the beam is injected into HERA and accelerated up to the full energy of 27.6 GeV.

The beam consists of 220 bunches with 96 ns separation between them. Not all the

¹ In the following, we use the term electron to represent both electrons and positrons unless specifically noted otherwise.

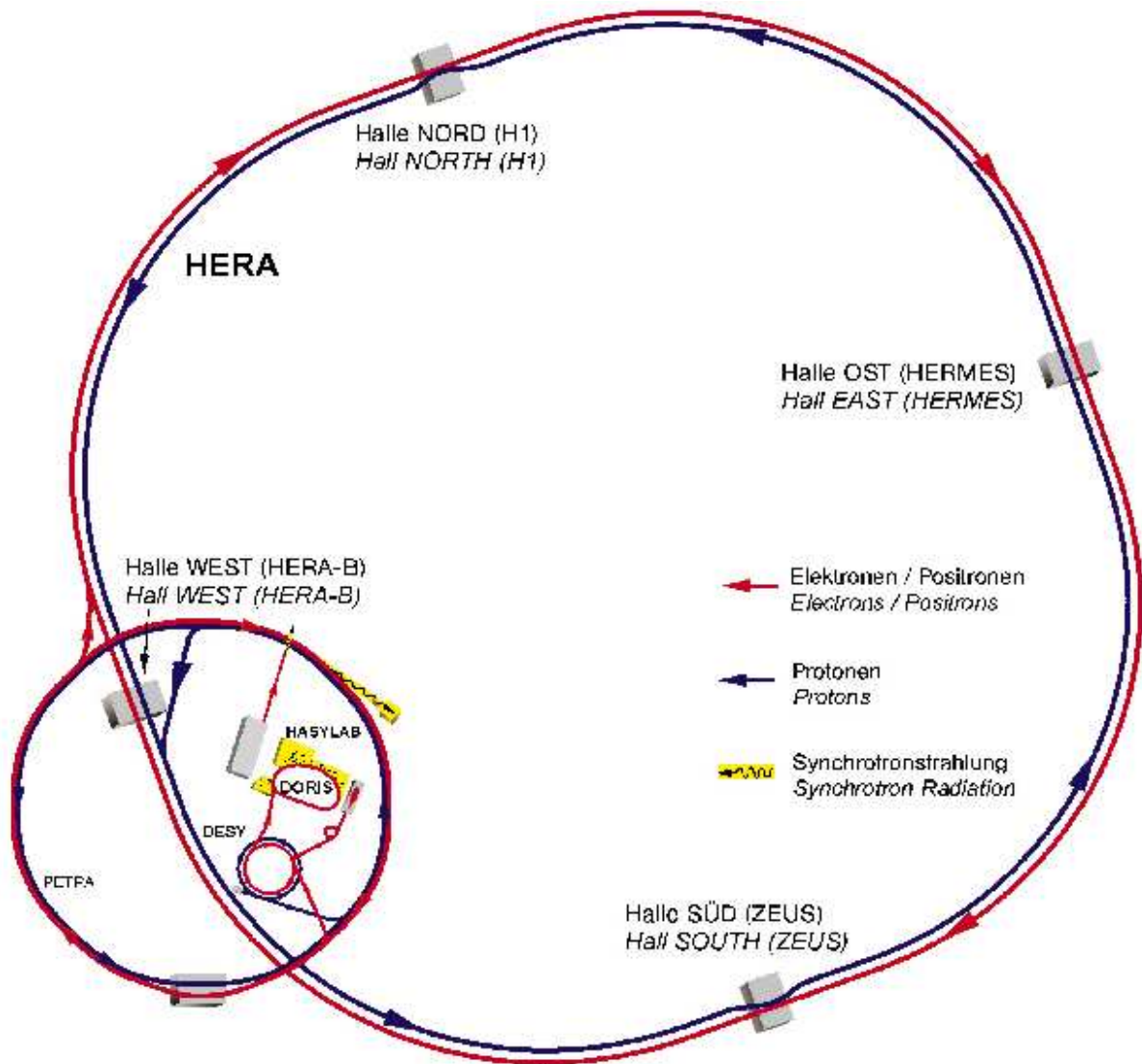


Figure 2.1: *The HERA accelerator complex at DESY, Hamburg.*

bunches are filled so that backgrounds can be monitored. The unpaired bunches (pilot bunches) can be used to study beam related backgrounds, while the empty bunches can be used for cosmic muon background study.

Four experiments have been using the HERA beams. ZEUS and H1 are general purpose experiments to study ep collisions. The other two experiments HERMES and HERA-B use only the electron or the proton beam, respectively. HERA-B has terminated operation.

After the first years of operation, positrons were accelerated instead of electrons in 1995,

Period	E_P (GeV)	E_e (GeV)	e charge	\mathcal{L}_{HERA} (pb ⁻¹)	\mathcal{L}_{ZEUS} (pb ⁻¹)	δ (%)
96-97	820	27.5	e^+	53.51	42.26	1.6
98-99	920	27.5	e^-	25.2	19.95	1.8
99-00	920	27.5	e^+	94.95	78.52	2.25

Table 2.1: 1996-2000 HERA running summary. The first column is the running period. The second and the third columns show the proton and electron beam energies. The fourth column gives the electron charge. The fifth and the sixth columns are the luminosity values delivered by HERA and gated by ZEUS in the running period. The last column gives the systematic uncertainty of the luminosity.

because positrons had longer life time². After the installation of new vacuum pumps in 1997/1998 the situation was improved and electrons were used until 1999. The integrated luminosity delivered by HERA as a function of days of operation is show in Fig.2.2. Table 2.1 summarizes the proton and electron beam energies, E_P and E_e , the e -beam charge, the HERA delivered luminosity and the ZEUS gated luminosity, which is used in this analysis, and the systematic uncertainty of the luminosity.

2.2 The ZEUS detector

The ZEUS collaboration is composed of about 450 physicists, and approximately the same number of technicians coming from about 50 institutes in 12 different countries. ZEUS is a multipurpose detector for studying physics processes occurring in high energy ep interactions. In 1992 the installation of the detector was finished in the South Hall of the HERA tunnel 30 m underground. However, new detector components were added continuously. The main detector has a size of 12m×11m×20m and a weight of 3600 ton. A detailed description of the detector can be found elsewhere [29].

An asymmetric design was implemented taking into account the large difference between electron and proton beam energies which results in the center-of-mass system moving in the proton beam direction with respect to the lab-frame. The ZEUS geometry is described by a right-handed coordinate system with its origin at the nominal interaction point. The

² The shorter life time of electron was caused by the capture of the positive charged dust originating from ion getter pumps from the HERA electron vacuum system.

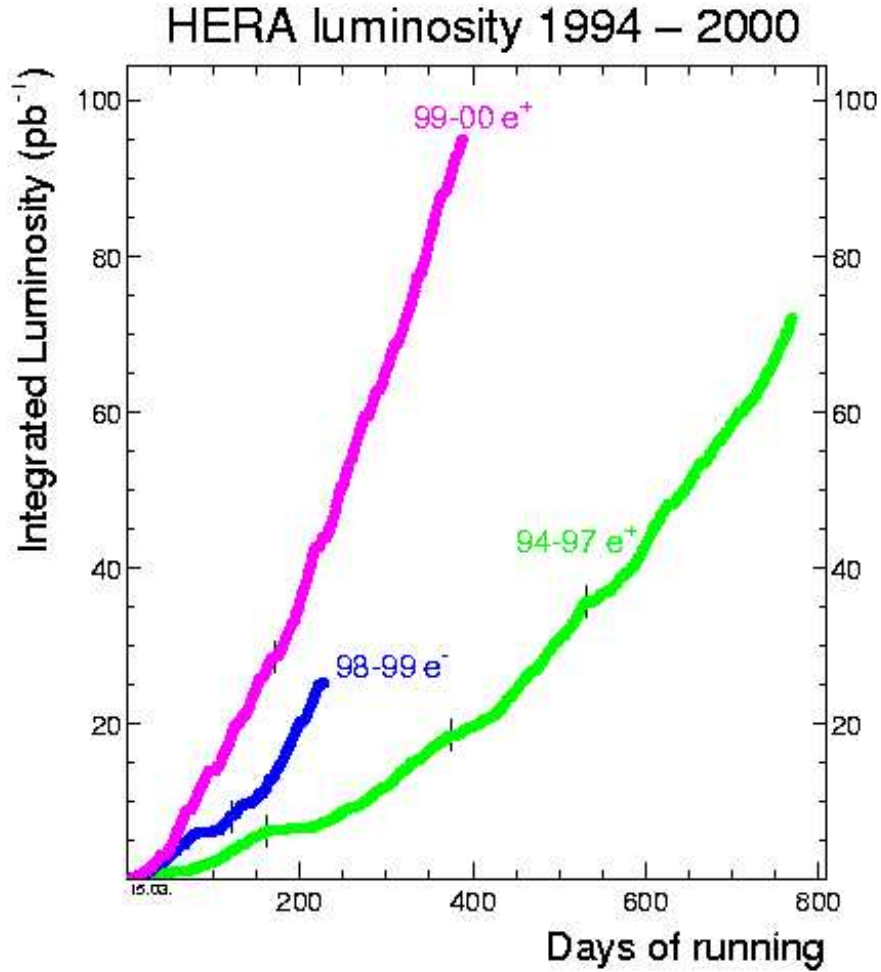


Figure 2.2: *Integrated Luminosity delivered by HERA. Positrons were used as colliding lepton in the years 1995-1997 and from summer 1999 till the end of the running period in September 2000.*

x -axis points horizontally to the center of HERA, the y -axis points upward while the z -axis points in the proton beam direction. The polar angle θ is determined relative to the z -axis. With this definition the angle of the incoming electron beam is $\theta = 180^\circ$. The proton beam direction is called *forward* and the electron beam direction is referred to as the *backward* or *rear* direction.

The xy and yz projection of the ZEUS detector are shown in Fig.2.3 and Fig.2.4 respectively. The most inner part of the ZEUS detector is the tracking detector, which consists of three parts: the central (CTD), the forward (FTD) and the real tracking detector(RTD),

*Overview of the ZEUS Detector
(cross section)*

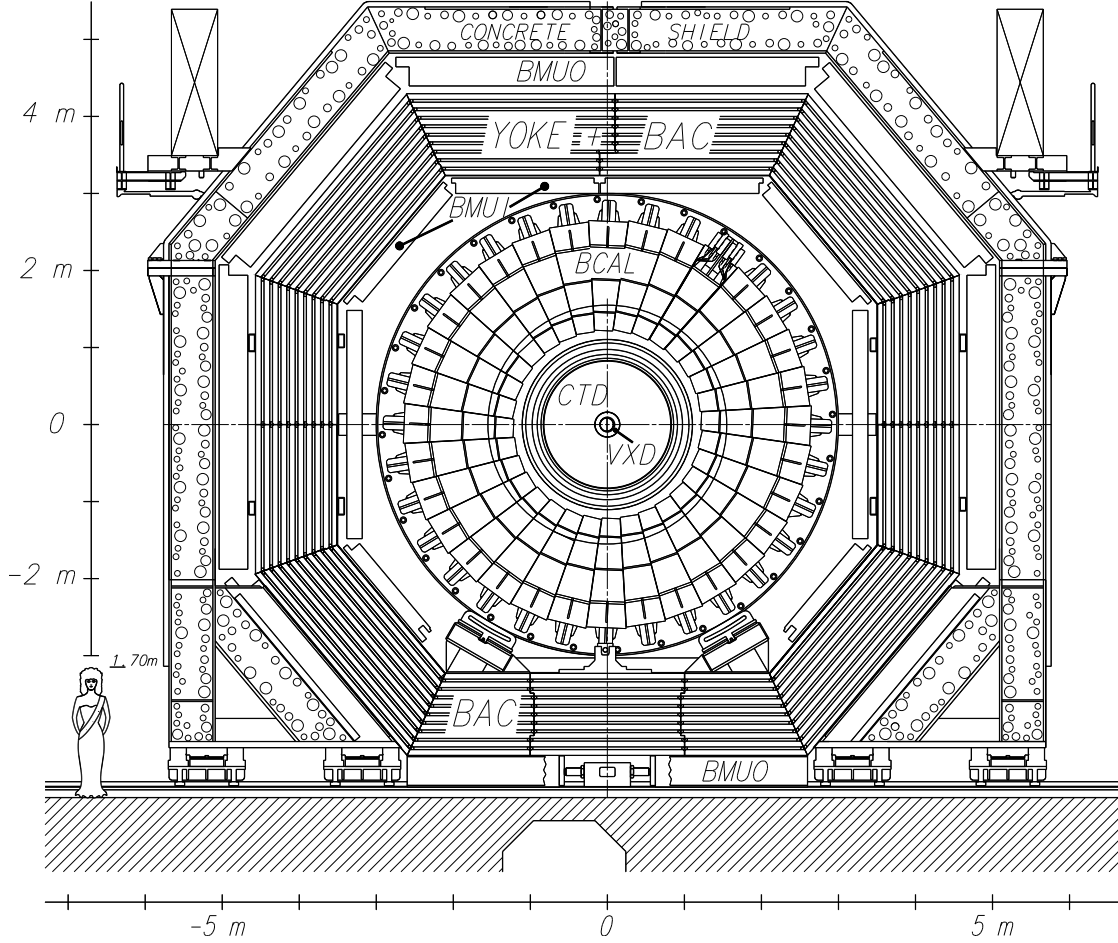


Figure 2.3: *The xy view of the ZEUS detector.*

surrounding the interaction point. The CTD is enclosed by a super-conducting toroidal magnet providing a paraxial field of 1.43 T. The tracking system is surrounded by a high resolution uranium-scintillator calorimeter (CAL), which is divided into three part: the forward (FCAL), the barrel (BCAL) and the rear calorimeter (RCAL). The small Angle Rear Tracking Detector (SRTD) [30] is attached to the front face of the RCAL to a radius of ~ 34 cm around the center of the beam pipe in order to get better measurement of electrons with small scattering angle. The Hadron Electron Separator (HES) [31] is located inside the R/FCAL, 7 cm below front the surface near the electromagnetic shower maximum and is used to identify electrons. The BAC (Backing-Calorimeter) surrounds the

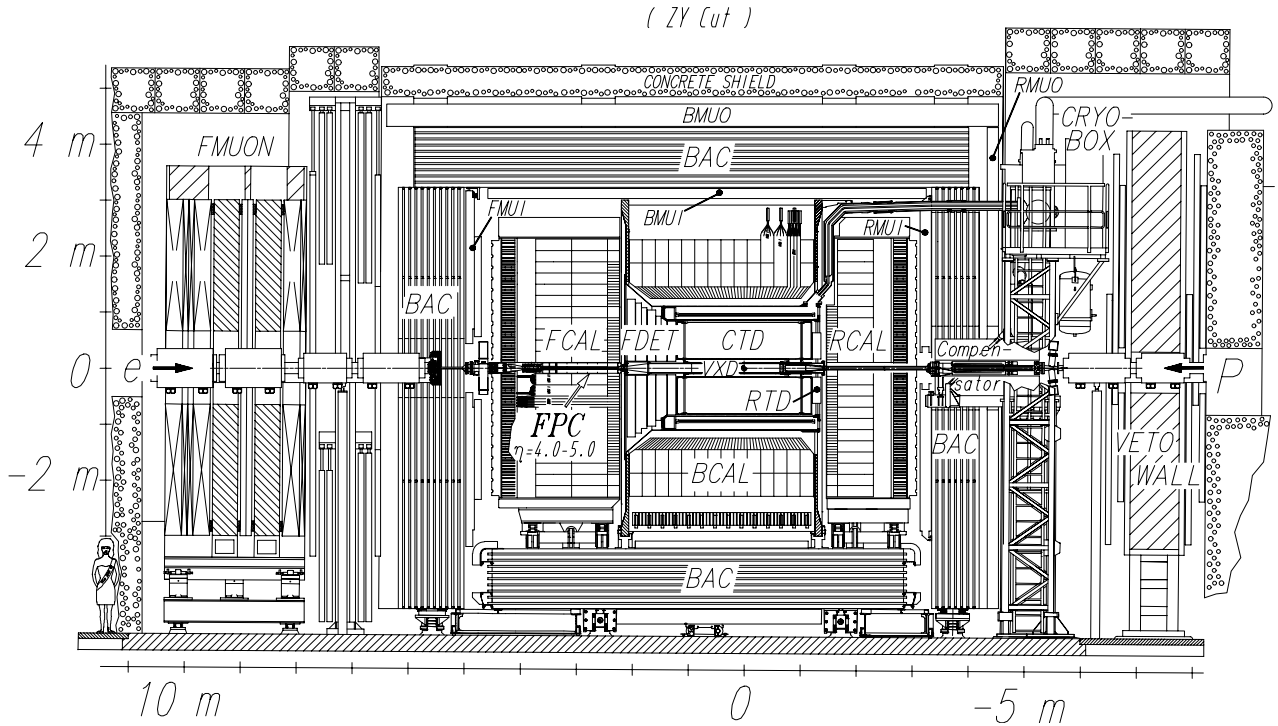


Figure 2.4: *The yz view of the ZEUS detector.*

main calorimeter and provides a measurement of energy leakage from the main calorimeter. The MUOn-chamber system consists of two layers of limited streamer tubes, one between CAL and BAC and the second outside the BAC. It is divided into three parts: the forward (FMUI, FMUO), the barrel (BMUI, BMUO) and the rear (RMUI, RMUO) parts.

2.2.1 The uranium calorimeter

The ZEUS CAL [32] is a compensating sampling calorimeter consisting of absorber plates made from depleted uranium and active plates of plastic scintillator. The CAL is used to measure the energy of final state particles and timing when energy is higher than a few GeV. It plays an important role in this analysis.

CAL consists of three parts. The FCAL covers the polar angle regions from 2.2° to 39.9° , the BCAL from 36.7° to 129.1° , and the RCAL from 128.1° to 176.5° . The spaces not covered are the beam hole in the forward ($20 \times 20 \text{ cm}^2$) and in the rear direction

($8 \times 20 \text{ cm}^2$). Each part is subdivided transversely into towers and longitudinally into one electromagnetic section (EMC) and either one (in RCAL) or two (in BCAL and FCAL) hadronic sections (HAC). The smallest subdivision is called a cell. The transverse dimension of HAC cells is $20 \times 20 \text{ cm}^2$. Each EMC section is transversely subdivided into four cells for F/BCAL and two cells for RCAL with rectangular surface of $5(10) \times 20 \text{ cm}^2$. Figure 2.5 shows the structure of the towers and cells in CAL. The towers in the FCAL closest to the beam hole are called the First Inner Ring (FIR) (Fig. 2.6).

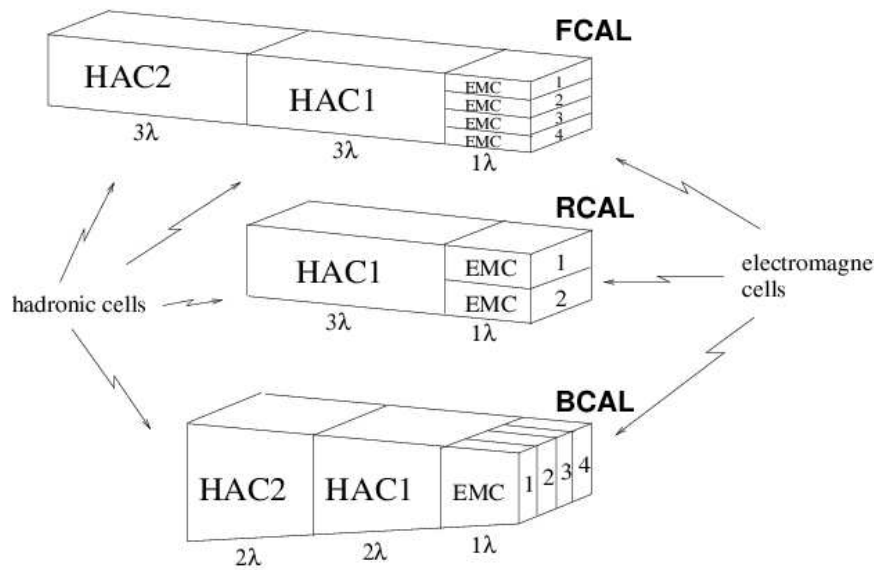


Figure 2.5: *The structure of CAL towers with EMC and HAC cells (not to scale). Cell depths are in units of interaction length.*

The calorimeter is compensating, i.e., the energy response to electrons and hadrons is equalized ($e/h = 1.00 \pm 0.02$) resulting in lower sensitivity to hadron shower development and better hadronic energy resolution. The cells are read out on two sides by wave length shifters coupled to photomultiplier tubes resulting in improved position measurement. The CAL energy resolutions, as measured under test-beam conditions, are $\sigma(E)/E = 0.18/\sqrt{E}$ for electrons and $\sigma(E)/E = 0.35/\sqrt{E}$ for hadrons (E in GeV). The natural radioactivity of U^{238} provides a very stable reference signal which is used to monitor

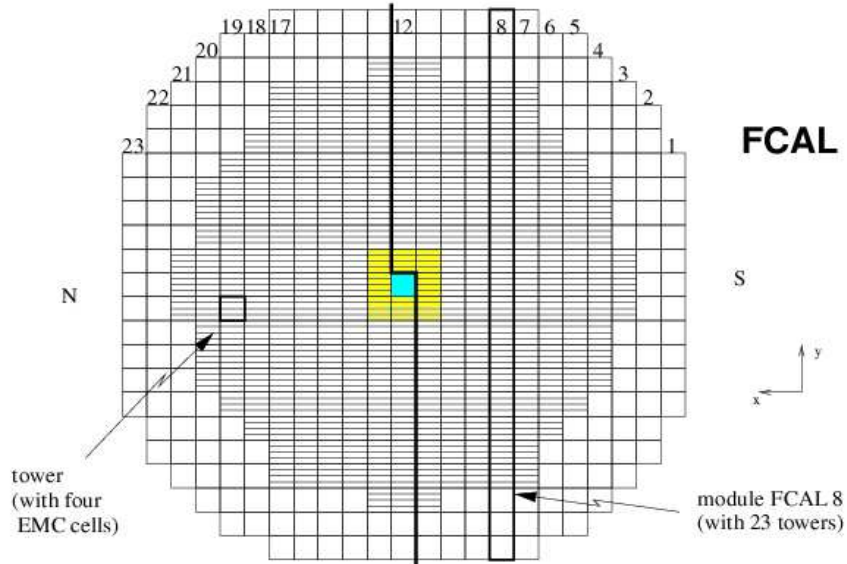


Figure 2.6: *The front view of FCAL seen from the interaction point. The blue region is the beam hole. The yellow region shows the FIR.*

the photomultiplier tubes to 0.2%. The position resolution is ~ 1 cm depending on the electron impact position. The timing measurement as well as electron identification is provided by the CAL.

2.2.2 The central tracking detector

Charged particles are tracked in the central tracking detector (CTD) [33], which operates in a magnetic field of 1.43 T. A measurement of the mean energy loss dE/dx within the chamber gas provides a means of particle identification. In addition the measurement of primary and secondary vertices is provided.

The CTD consists of 72 cylindrical drift chamber layers, organized in 9 superlayers covering the polar angle region $15^\circ < \theta < 164^\circ$. Its active volume has a length of 205 cm, an inner radius of 18.2 cm and an outer radius of 79.4 cm. The gas consists of a mixture of argon, CO_2 and ethane. The cross-section of an octant of the CTD is shown in Fig. 2.7.

The resolution of the CTD in $r - \phi$ plane is about $230 \mu\text{m}$. The transverse momentum resolution for full-length tracks is $\sigma(p_T)/p_T = 0.0058p_T \oplus 0.0065 \oplus 0.0014/p_T$, with p_T in

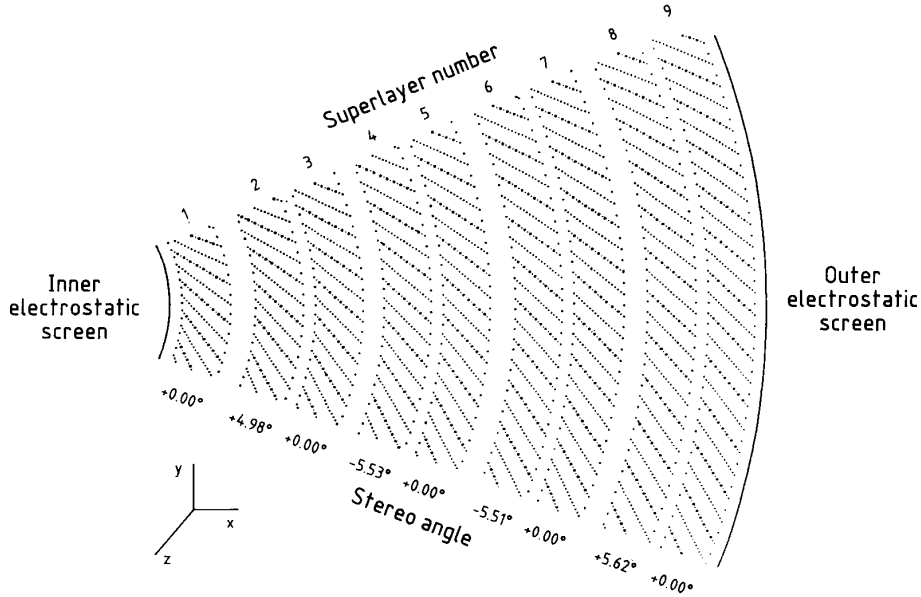


Figure 2.7: *Layout of a CTD octant. The stereo angle of each superlayer is indicated.*

GeV.

2.2.3 The presampler

The presampler detector (PRES) [34], which consists of 20×20 cm² single layers of scintillator plates, is installed in front of the RCAL and FCAL modules. The PRES measures the number of minimum ionizing particles produced by showers developing in front of the calorimeter. The PRES signal can be used to calculate lost energy in dead material since the lost energy is correlated with the number of generated shower particles. The energy resolution is improved by correcting the measured calorimeter electron energy event-by-event.

2.2.4 The luminosity measurement

At ZEUS the measurement of luminosity is done by measuring the QED Bremsstrahlung process (Bethe-Heitler-process) [35]

$$ep \rightarrow ep\gamma, \quad (2.1)$$

which has a large and well known cross section. The photon calorimeter [36] measures the rate of outgoing photons to decide the luminosity.

2.2.5 The trigger and data acquisition system

The electron and proton bunches cross at a rate of 10.4 MHz. In a fraction of these an ep -interaction takes place. ZEUS with its subcomponents has a total of ~ 250000 readout channels, which limits the event rate that can be written for off-line analysis to only a few Hz. In fact, the majority of events that leave detectable signals in the detector come from the proton beam interactions with residual gas in the beam pipe, occurring at a rate on the order of 10 – 100 kHz. Other background sources are cosmic rays, proton beam halo and electrons interacting with gas in the beam pipe. In addition, the rate of physics events is dominated by photoproduction (PHP) processes. In PHP process, a quasi-real photon is exchanged between electron and the proton (e.g. the process has $Q^2 \sim 0$) .

A sophisticated trigger decision is necessary to select ep event candidates in the presence of large backgrounds. ZEUS has a three-level trigger system adopting various selection techniques at each level [29]. At the first-level trigger (FLT), each component analyzes events in 25 clock cycles and sends data to the global first level trigger (GFLT). The GFLT issues a global trigger decision based on various logical combinations of inputs from individual components. This takes an additional 20 bunch crossings. In case of a positive trigger decision, the data stored in pipelines of each component are read out and processed further. The FLT is designed to reduce the event rates to below 1 kHz.

Each component has its own second-level trigger (SLT) which stores the data to be analyzed in a memory buffer. The component SLTs are based on a network of programmable transputers. Sophisticated algorithms can be used to identify and reject backgrounds. The results from the local SLTs are combined in the global second-level trigger (GSLT) and the rate is reduced to ~ 100 Hz.

Afterward the data are sent to the Event-builder which combines the component data into one single data set and makes the information accessible to the third-level trigger (TLT).

The TLT consists of a processor farm of CPUs. Part of the full off-line reconstruction code runs on this processor farm and the selected events are written to tape at a rate of few Hz.

2.3 Monte Carlo simulation

2.3.1 DIS event generator

Standard Model (SM) NC DIS events were simulated with the DJANGO version 1.1 [37] which includes an interface to the HERACLES 4.6.1 [38] program. HERACLES includes the corrections for the initial and final-state electroweak radiation, vertex and propagator corrections, and two-boson exchange. First- and second- generation quarks are simulated, while third-generation quarks are ignored because of the large mass of the top quark and the small values of the off-diagonal elements of the CKM matrix. The hadronic final state was simulated using the MEPS model of LEPTO 6.5 [39], which includes order- α_S matrix elements (ME) with a lower and upper cutoff on the soft and collinear divergences. Both the ME cut-offs and the parton evolutions are treated by parton showers based on the DGLAP evolution equations, which sum over all the higher order terms proportional to $\alpha_S \log Q^2$. The fragmentation of the scattered partons into observable hadrons is performed with the Lund string hadronization model by JETSET [40]. The CTEQ4D PDFs set [41] was used to evaluate the nominal Standard Model (SM) cross section.

As a systematic check for the strong interaction simulation, ARIADNE 4.08 [42] was used instead of MEPS. ARIADNE contains the color-dipole model (CDM).

2.3.2 Detector simulation

Generated events were input into the MOZART program, which has all ZEUS detector components taking into account the exact geometry and inactive material implemented using the GEANT 3.13 program [43]. MOZART was previously tuned with test beam data and later enhanced with performance studies of the ZEUS running. The trigger is

Q^2 cut (GeV ²)	x cut	num of events	cross section (pb/GeV ²)
>400	-	599504	1167.4
>1250	-	259836	197.69
>2500	-	119938	58.895
>5000	-	113056	14.809
>10000	-	119877	2.7922
>20000	-	119909	0.31026
>30000	-	59969	0.054457
>40000	-	59830	0.010864
>50000	-	59957	0.0021218
>1250	>0.3	19995	10.430
>1250	>0.4	19998	4.0921
>1250	>0.5	19990	1.4167
>1250	>0.6	19985	0.40054
>1250	>0.7	19996	0.081000
>1250	>0.8	19967	0.0088012
>1250	>0.9	19995	0.00021809

Table 2.2: *NC DIS MEPS Monte Carlo used in this analysis for 99-00 e^+p data. The first and the second column give the lower cut values for Q^2 and x . The third column shows the number of events in each MC sample. The last column is the corresponding luminosity in each MC sample.*

simulated with the ZGANNA package. The MC and data events are reconstructed with the ZEPHYR program resulting in the same format as the data output, which allows identical event reconstruction for data and simulated events.

2.3.3 Generated event sample

Tables 2.2, 2.3, 2.4 and 2.5 show the total amounts of MC events used for the 99-00 e^+p , 98-99 e^-p and 96-97 e^+p data analysis. Sufficient numbers of events were generated to ensure the statistical uncertainties from the MC samples were negligible compared to those in the data.

Q^2 cut (GeV ²)	x cut	num of events	cross section (pb/GeV ²)
>400	-	776181	1167.67
>1250	-	139785	197.5
>2500	-	39957	58.93

Table 2.3: *NC DIS ARIADNE Monte Carlo used as a systematic check in this analysis for 99-00 e^+p data. The first and the second column give the lower cut values for Q^2 and x . The third column shows the number of events in each MC sample. The last column is the corresponding luminosity in each MC sample.*

Q^2 cut (GeV ²)	x cut	num of events	cross section (pb/GeV ²)
>400	-	577116	1196.4
>1250	-	259876	217.22
>2500	-	119866	71.769
>5000	-	119941	21.671
>10000	-	119911	5.3655
>20000	-	119932	0.84694
>30000	-	59959	0.18511
>40000	-	59830	0.0042655
>50000	-	59987	0.00091918
>1250	>0.3	19995	11.616
>1250	>0.4	19994	4.5102
>1250	>0.5	20000	1.5486
>1250	>0.6	19980	0.43454
>1250	>0.7	19981	0.087359
>1250	>0.8	20000	0.0094198
>1250	>0.9	19960	0.00023224

Table 2.4: *NC DIS MEPS Monte Carlo used in this analysis for 98-99 e^-p data. The first and the second column give the lower cut values for Q^2 and x . The third column shows the number of events in each MC sample. The last column is the corresponding luminosity in each MC sample.*

Q^2 cut (GeV ²)	x cut	num of events	cross section (pb/GeV ²)
>400	-	599759	1096.7
>1250	-	259678	182.00
>2500	-	119975	53.176
>5000	-	119907	12.915
>10000	-	119943	2.2866
>20000	-	119992	0.22474
>30000	-	59971	0.034239
>40000	-	59974	0.0056424
>50000	-	59969	0.00084336

Table 2.5: *NC DIS MEPS Monte Carlo used in this analysis for 96-97 e^+p data. The first and the second column give the lower cut values for Q^2 and x . The third column shows the number of events in each MC sample. The last column is the corresponding luminosity in each MC sample.*

2.4 Data sample

All the data taken by ZEUS from 1996 to 2000 were used in this analysis. The data include three main samples as illustrated in Table 2.1. The runs with bad running condition were excluded either by the ZEUS data quality routine EVTAKKE or the data quality monitoring of the ZEUS structure function working group. The used data sets correspond to integrated luminosity of 38.62 pb⁻¹ of e^+p data at $\sqrt{s} = 300$ GeV, 16.68 pb⁻¹ of e^-p data and 65.1 pb⁻¹ of e^+p data at $\sqrt{s} = 318$ GeV respectively.

Chapter 3

Method and Event Reconstruction

3.1 Introduction

DIS neutral current events at high Q^2 are characterized by an isolated high energy electron. The experiment measures the scattered electron energy E' and polar angle θ_e . A precise cross section measurement depends on accurately reconstructed kinematic variables. Both Q^2 and x can be calculated in many ways, which are based on different quantities of the scattered electron and the hadronic final states and have different performance in different kinematic regions. Since this analysis deals with the high Q^2 and high x region, the scattered electron is measured precisely and the jet in this region has high enough energy to be well reconstructed and understood. The lines of constant E'_e , θ_e , E_{jet} and θ_{jet} in the (x, Q^2) plane are shown in Fig. 3.1.

Figure 3.2 includes a schematic depiction of a typical NC event in the ZEUS detector: the scattered electron and the jet are outlined in the CAL, while the proton remnant largely disappears down the forward beam pipe. As x increases, the jet is boosted in the forward direction and θ_{jet} decreases. When x is too high, $x > x_{\text{edge}}$, a part of the jet is lost in the beam pipe and becomes unobservable. This occurs typically for $\theta_{\text{jet}} < 0.12$ rad. The value of x at which this occurs is Q^2 dependent: the x value for which jets are well contained increases as Q^2 increases. At the Q^2 values considered in this analysis, the scattered electron is at large angles and well contained in the detector.

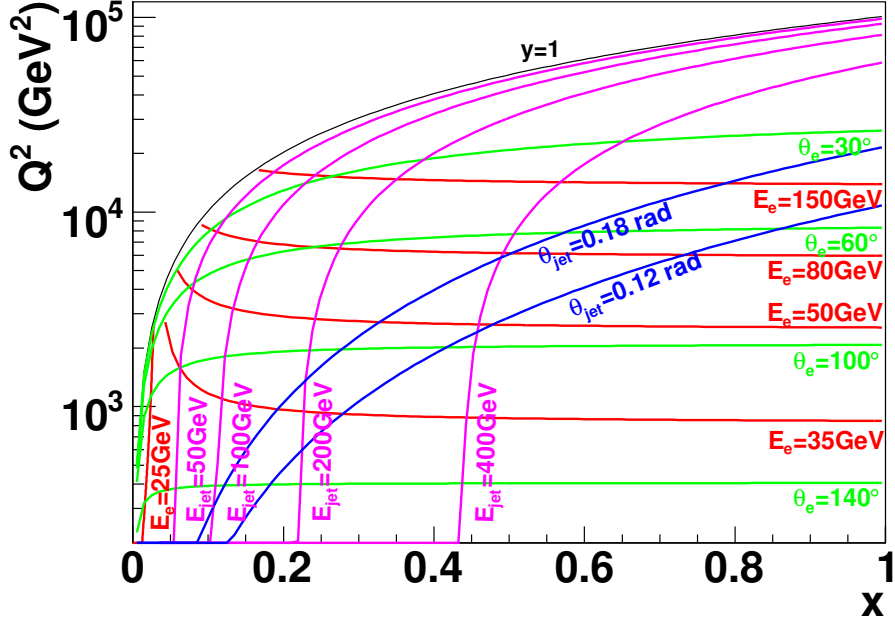


Figure 3.1: Contour lines of fixed E' , θ_e , E_{jet} and θ_{jet} in the (x, Q^2) plane.

The double angle method (DA) [44] was used in previous ZEUS neutral current cross section measurements. In this method, the CAL energy deposits were separated into those associated with the scattered electron and all other energy deposits. The sum of all other energy deposits is referred to as the hadronic energy. The spatial distribution of the hadronic energy, together with the reconstructed vertex position, were used to evaluate the hadronic polar angle, γ_h . γ_h corresponds to the polar angle of the struck quark in the naive quark-parton mode and is calculated as:

$$P_{T,h}^2 = P_X^2 + P_Y^2 = \left(\sum_i^h E_i \sin \theta_i \cos \phi_i \right)^2 + \left(\sum_i^h E_i \sin \theta_i \sin \phi_i \right)^2, \quad (3.1)$$

$$\delta_h = \sum_i^h (E - p_Z)_i = \sum_i^h (E_i - E_i \cos \theta_i), \quad (3.2)$$

$$\cos \gamma_h = \frac{P_{T,h}^2 - \delta_h^2}{P_{T,h}^2 + \delta_h^2}, \quad (3.3)$$

where the sums run over all the deposit energy not associated with the scattered electron. The DA method uses the polar angles of the electron, θ_e , and the hadronic system, γ_h :

$$Q_{DA}^2 = 4E_e^2 \frac{\sin \gamma_h (1 + \cos \theta_e)}{\sin \gamma_h + \sin \theta_e - \sin(\theta_e + \gamma_h)}, \quad (3.4)$$

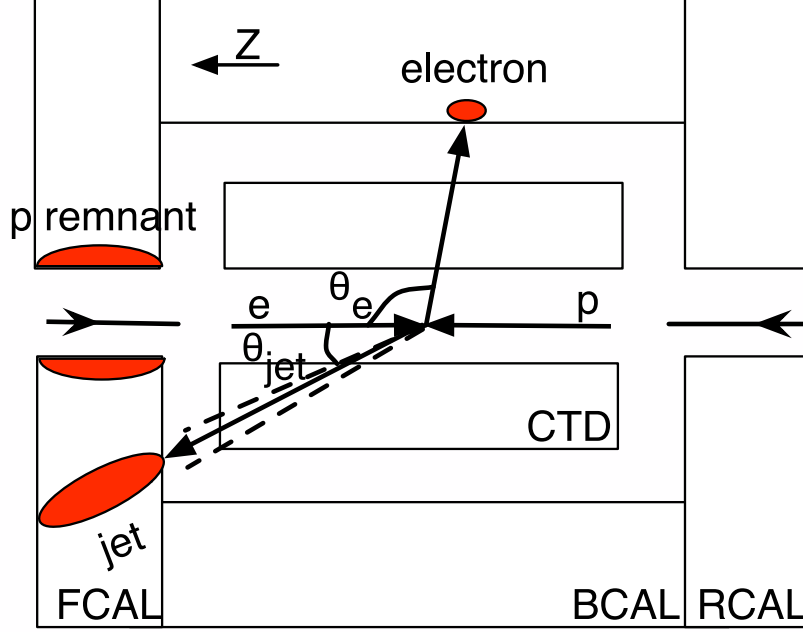


Figure 3.2: A schematic depiction of the ZEUS detector with the main components used in this analysis labeled. Also shown is a typical topology for events studied in this analysis. The electron is scattered at large angles and is reconstructed using the central tracking detector (CTD) and the barrel calorimeter (BCAL), while the scattered jet is typically reconstructed in the forward calorimeter (FCAL). The jet of particles from the proton remnant largely disappears down the beam pipe.

$$x_{DA} = \frac{E_e \sin \gamma_h + \sin \theta_e + \sin(\theta_e + \gamma_h)}{E_p \sin \gamma_h + \sin \theta_e - \sin(\theta_e + \gamma_h)}, \quad (3.5)$$

where E_e and E_p are the electron and proton beam energies. The advantage of this method is that it is not sensitive to uncertainties in the overall energy scale of the calorimeter. But it is sensitive to the accurate simulations of all kinds of effects in CAL, like backsplash and noise which are very hard to simulate accurately. When x is too high, most of the hadronic energy is lost in the beam hole and there is little hadronic energy deposit in CAL, the reconstructed γ_h is no longer the polar angle of the struck quark. So this method does not work well as $x \rightarrow 1$, as we have therefore developed a new method for this kinematic region.

3.2 New method

The new method employed in this analysis combines electron and jet information to allow a measurement of the differential cross section up to $x = 1$. Events are first sorted into Q^2 bins using information from the electron only:

$$Q^2 = 2E_e E'_e (1 + \cos\theta_e), \quad (3.6)$$

where E_e is the electron beam energy. The jet information is then used to calculate x for events with a well reconstructed jet:

$$x = \frac{E_{jet}(1 + \cos\theta_{jet})}{2E_p(1 - \frac{E_{jet}(1 - \cos\theta_{jet})}{2E_e})}, \quad (3.7)$$

where E_p is the proton beam energy. These events are sorted into x bins using the jet information to allow a measurement of the double differential cross section $d^2\sigma_{\text{Born}}/dx dQ^2$. Events with no jet reconstructed within the fiducial volume are assumed to be characterized by large x and are collected in a bin with $x_{\text{edge}} < x < 1$. Since these bins are often large and the form of the PDF is not well known in this region, a cross section integrated over the bin is calculated: $\int_{x_{\text{edge}}}^1 (d^2\sigma_{\text{Born}}/dx dQ^2) dx$. Events with more than one high energy jet are discarded.

The features of this method are:

- the fractional resolution in Q^2 for all x is about 5% as shown in Fig. 5.1 since the electron is always well reconstructed in the whole region;
- the fractional resolution in x varies from 15% to 4% as x increases in events where a jet can be reconstructed as shown in Fig. 5.2. At high x , where θ_{jet} is small, $x = E_{jet}/E_p$, and E_{jet} has good resolution;
- cross section measurements are obtained up to $x = 1$.

3.3 The scattered electron

The major initial task for NC event reconstruction is the identification and reconstruction of the scattered electron. The presence of an isolated energetic electron is the most

important feature to distinguish NC events from potential background processes. So the electron energy and scattered angle are not only used for the calculation of Q^2 , but are also important for the offline selection.

3.3.1 Electron finder

The identification of the electron with the detector information is performed by a software tool called the electron finder. There are several different programs that emphasize different purposes. The electron finder used in this analysis is EM [45], which was specially developed to identify electrons in the high Q^2 regime and to suppress background in the relevant detector regions. The finders give a list of electron candidates for the “true” scattered electron. This list is sorted by probability as calculated by the finder. The electron candidate with the highest probability is selected as the “true” scattered electron if its probability lies above a certain threshold.

After it groups energy deposits in calorimeter cells, the EM finder combines calorimeter and track information of the detector to determine if this cluster is an electron candidate. The four variables for CAL are the shower spread, shower depth and the isolation of the candidate. The three variables for matching the CTD track to a calorimeter cluster are the differences between the polar angle and azimuthal angle and the energy momentum match.

Compared to hadrons, the electron deposits a large fraction of its energy in the EMC section and less in HAC. The electron shower energy is well isolated from hadronic deposits. In addition, there should be a spatially matched track from the CTD in its good acceptance region. EM also contains an algorithm which appropriately merges nearby energy deposits by the electron, including most of those due to final state radiation (FSR) from the electron.

3.3.2 Energy measurement

If an electron candidate is identified as the scattered electron, its properties are calculated. The total energy is the sum over the energies of the cells belonging to the electron cluster.

The following corrections [46] are applied to the electron energy:

- **Dead-material correction.** On the way from the interaction point to CAL, the electron loses energy due to the interaction with (mostly non-active) material in the detector. The dead-material map is obtained from the detector geometry data and the Monte Carlo (MC) simulation. The correction was determined from the test beam data.
- **Non-uniformity correction.** Due to the inactive material of shielding and support structures and the wavelength shifter for the signal read out between the modules, the calorimeter is not homogeneous. The electrons hitting the inactive material in gaps between cells have a lower energy response while the electrons hitting the wavelength shifter between modules have a higher response. This correction is determined for data and MC separately using tracking information.
- **Dead-photomultiplier correction.** If one of the two PMTs in a cell is not operating, the common procedure has been to double the energy of the working channel. This technique could measure the energy badly. To improve it, the tracking information or the imbalance information from neighboring cells are used to make corrections, where the imbalance is the difference between the values measured by the two PMTs in a cell divided by the sum of the values.

After applying the corrections described above, the electron energy resolution was 5% for $E'_e > 20$ GeV. The scale uncertainty on the energy of the scattered electron is $\pm 1\%$ in BCAL and FCAL and $\pm 3\%$ in RCAL [21,47].

3.3.3 Angle measurement

The position of the electron in the CAL is calculated from the momentum of the electron and the event vertex and is used to make sure that potential FSR photons are taken into

account. The scattering angle of the electron, θ_e , can be calculated in two ways: (1) combination of the electron position in the CAL and the reconstructed vertex; and (2) the polar angle of the track matched to the electron at the vertex. The second method is always used if there is a well reconstructed matched track since it has a better resolution. The BCAL is aligned to precisions of ± 0.3 mm in the Z direction and ± 0.6 mrad in the azimuthal angle, ϕ . The electron angular resolution was 2 mrad for $\theta_e < 23^\circ$, 3 mrad for $23^\circ < \theta_e < 156^\circ$ and 5 mrad for $\theta_e > 156^\circ$ [21].

3.4 The jet

In this analysis, the jet is not only essential for the x calculation, as mentioned in Eq. 3.7, but its absence is essential to identify those events that do not have a well reconstructed jet in the detector and therefore can only be assigned to a large x bin.

3.4.1 Jet finder

All the jet finder algorithms are based on the assumption that the parton fragmentation and hadronization should produce particles close to the jet axis. The jet finder algorithm specifies how to combine those hadrons within a specified phase space centered in the jet axis.

The k_T algorithm [48] is used in this analysis. The energy deposits in the CAL cells were grouped into islands by the software routine CORANDCUT, which includes corrections for dead material and rejects the back-splashing of hadrons from the FCAL into the BCAL or RCAL. Then the jet was reconstructed by the k_T cluster algorithm in the inclusive mode [49]. k_T is the relative transverse momentum of two islands, which is defined as:

$$k_T^2 = 2\min(E_i^2, E_j^2)(\Delta\eta^2 + \Delta\phi^2).$$

If k_T is smaller than $0.8Q$, these two islands are merged together. The procedure is repeated for the remaining islands until no further merging. A cone algorithm [50] is also used as a way to estimate the systematic uncertainty associated with hadronic final

state simulation. The cone jet finder is applied to hadronic energy deposits characterized by pseudo-rapidity, η and azimuthal angle around the interaction axis, ϕ , where $\eta = -\ln \tan \frac{\theta}{2}$ and θ is the angle to the interaction axis. This jet finder is applied on all the energy cells above a certain energy threshold (300 MeV in ZEUS). The candidate energy cell with the highest transverse energy is taken as the center of a cone for the beginning of the jet finder. All the energies with radius $R = \sqrt{(\Delta\eta)^2 + \Delta\phi^2}$ smaller than 0.7 around this cone center are assigned to a jet. And the energy cells belonging to this jet are removed from the candidates. The procedure is repeated until no energy deposit higher than the threshold.

3.4.2 Energy and angle measurement

Once identified, the variables used to characterize jets are the transverse energy, $E_{T,jet}$, and the pseudorapidity η_{jet} . They are defined according to the Snowmass convention [50] which give the jet energy, E_{jet} , and jet angle θ_{jet} :

$$E_{T,jet} = \sum_i E_{T,i}, \quad \eta_{jet} = \frac{\sum_i E_{T,i} \eta_i}{E_{T,jet}}, \quad (3.8)$$

$$\theta_{jet} = 2 \tan^{-1}(e^{-\eta_{jet}}), \quad E_{jet} = \frac{E_{T,jet}}{\sin \theta_{jet}},$$

where $E_{T,i}$ and η_i are the transverse energy and pseudorapidity of the objects. The sum are over all the CAL cells, as identified from the jet algorithm to belonging to the jet.

3.5 Vertex

The Z -vertex is the position along the beam, or Z -axis, of the interaction point. This is used to determine the electron angle θ_e and jet angle θ_{jet} . The X and Y positions of the interaction point are set to be zero, since the resolution of the transverse vertex reconstruction is larger than the size of real beam spot, which is $\sim 300 \times 100 \mu\text{m}^2$. The Z position of the interaction point is determined from the CTD tracks. The reconstruction of tracks and the procedure followed to reconstruct vertices are described in detail in [51,52].

The vertex reconstruction procedure can do multi-vertex fitting, with both the primary vertex (interaction point) and secondary vertex found at the same time. Below is a brief description of the vertex reconstruction procedure based on the CTD tracks.

- First, each pair of tracks is tested for loose compatibility with forming a common vertex. And by doing so, several track clusters are found.
- Second, the weighted center of each track cluster is calculated. A track which contributes a very high χ^2 to the track cluster is removed from that cluster.
- Then a score is calculated based on the assumption for each track cluster center to be the primary vertex. The score is mainly based on the fitting probability and the proximity in the $X - Y$ plane to the origin (beam spot). The track cluster with the highest score will be chosen as the primary vertex.
- Finally a full fit is performed on the primary vertex and all the tracks associated with it, with the vertex position obtained so far as starting input, and all the associated track parameters are then updated. The iteration proceeds and is stopped when the vertex position reconstructed has converged.

Some special considerations have been taken in the Z -vertex reconstruction for this analysis. In some events, especially high- x events, the majority of the CTD tracks proceed forward with very small polar angles. Thus the reconstructed Z position of the primary vertex will not be satisfactory if all the tracks were assigned the same weight in the position calculation. We use the track identified as the scattered electron to find the starting primary vertex, and subsequently assign it a higher weight in the Z position calculation. This technique has been shown to improve the reconstruction resolution.

Chapter 4

Event selection

In this chapter, we discuss the broad features of the signal events, (Sect. 4.1), the origins of the principal background processes and their features (Sect. 4.2), and the application of both online (Sect. 4.3) and offline (Sect. 4.4) selection cuts. In the final section, we compare the relevant section parameters for selected events with prediction of the MC.

4.1 Characteristics of neutral current events

As mentioned in Sect. 3.2, a DIS NC event is characterized by an isolated electron. At high Q^2 , the scattered electron has large polar angle and high energy in BCAL or FCAL. For the hadronic system, the struck quark is hadronized into a jet. The energy and polar angle of the jet are reconstructed in the CAL. Figure 4.1 shows a high Q^2 DIS NC event. In this event, the scattered electron is well reconstructed in the BCAL with a track in the CTD and the jet is detected in FCAL.

The transverse momentum of the scattered electron balances that of the jet since the transverse momenta of the electron and proton beams are zero before the interaction. The proton remnant may carry a significant fraction $(1 - x)$ of the proton beam momentum which is in the forward beam hole, but the transverse momentum it carries is negligible. The net transverse momentum is defined as:

$$P_T^2 = P_X^2 + P_Y^2 = \left(\sum_i E_i \sin \theta_i \cos \phi_i \right)^2 + \left(\sum_i E_i \sin \theta_i \sin \phi_i \right)^2, \quad (4.1)$$

where the sums run over all calorimeter energy deposits, E_i , with polar and azimuthal angles θ_i and ϕ_i with respect to the event vertex, respectively. So the net transverse momentum is close to zero.

The variable $E - p_Z$ is defined as:

$$E - p_Z \equiv \sum_i (E - p_Z)_i = \sum_i E_i (1 - \cos \theta_i) \quad (4.2)$$

where the sum runs over all cells in the calorimeter. Since both total energy and total momentum are conserved, $E - p_Z$ does not change before and after interaction. Neglecting the electron and proton masses, $E - p_Z = (E_p + E_e) - (E_p - E_e) = 2E_e = 55 \text{ GeV}$. Particles escaping down the forward beam hole contribute negligibly to $E - p_Z$ since the longitudinal momentum cancels energy¹. So the unmeasured proton remnant does not substantially affect $E - p_Z$. It should be noted that these the particles lost in the rear beam hole could reduce the $E - P_Z$ a lot, since the contribution for these particles is the twice of their energy. But such particles are likely associated with the beam electron and the electron is at large angle in high Q^2 events; it follows that initial state radiation (relatively unlikely) will produce anomalously small value of $E - P_Z$.

4.2 Background

The selection of NC DIS events is mainly based on detection of the scattered electron. The main background events usually get selected when particles are falsely identified as the scattered electrons in γp interactions (photoproduction) and beam gas interactions. We discuss in this section the nature of all the backgrounds and their features that permit their removal.

¹ Note that the other linear combination, $E + p_Z$, is not a useful parameter because of the substantial final state energy in proton beam direction.

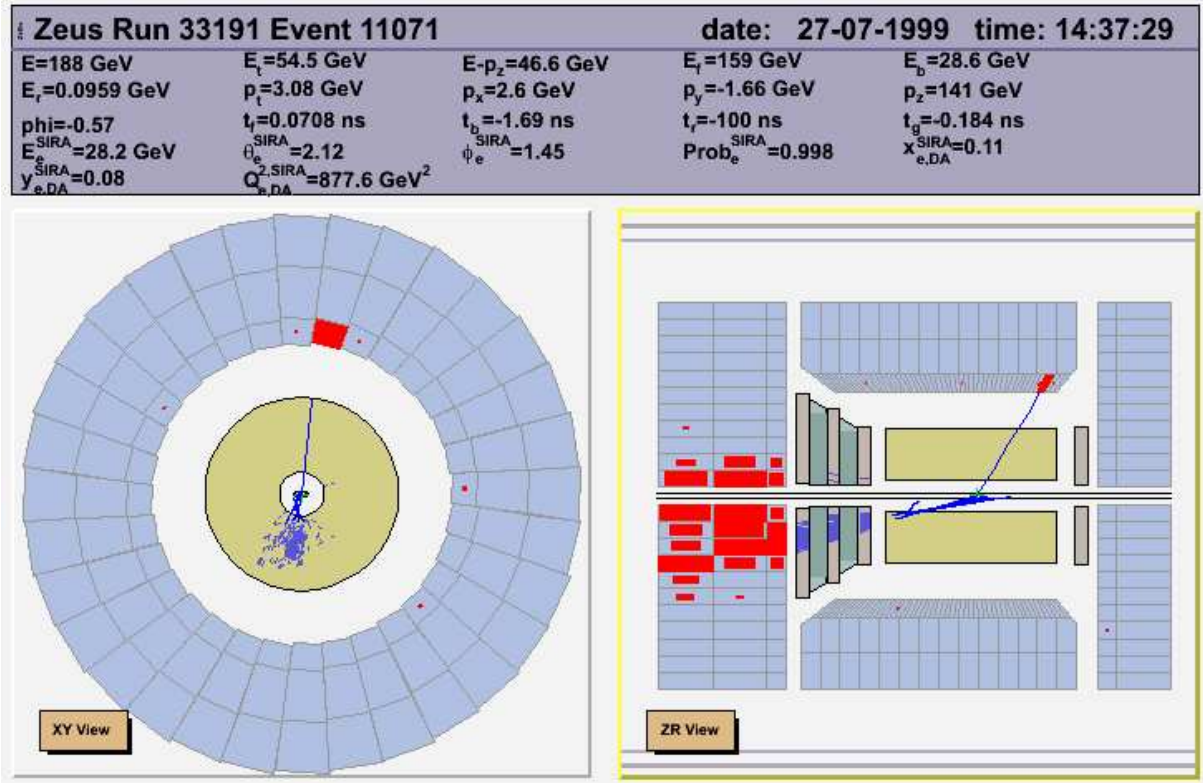


Figure 4.1: An example of high Q^2 event. The scattered electron deposits energy in BCAL and leaves a track in CTD. A jet is in FCAL and leaves several tracks in CTD.

4.2.1 Photoproduction

As mentioned in Sect. 2.2.5 photoproduction (PHP) events are defined as events with $Q^2 \approx 0$ with an exchanged photon almost on mass-shell. Since the square of the exchanged 4-momentum is very small, the electron goes practically undeflected and is lost in the rear beamhole. In background PHP events, a photon or a pion is misidentified as an electron and passes the selection. Since the cross section is large, PHP events are the biggest source of DIS background. The quantity $E - p_z$ is used to reject photoproduction. If the scattered electron escapes in the rear beam-hole, as discussed in the Sect. 4.1, the measured $E - p_z$ will be smaller than 55 GeV. In addition the cuts on the probability and energy from the electron finder can further reduce the photoproduction background. An example of a typical PHP event is shown in Fig. 4.2.

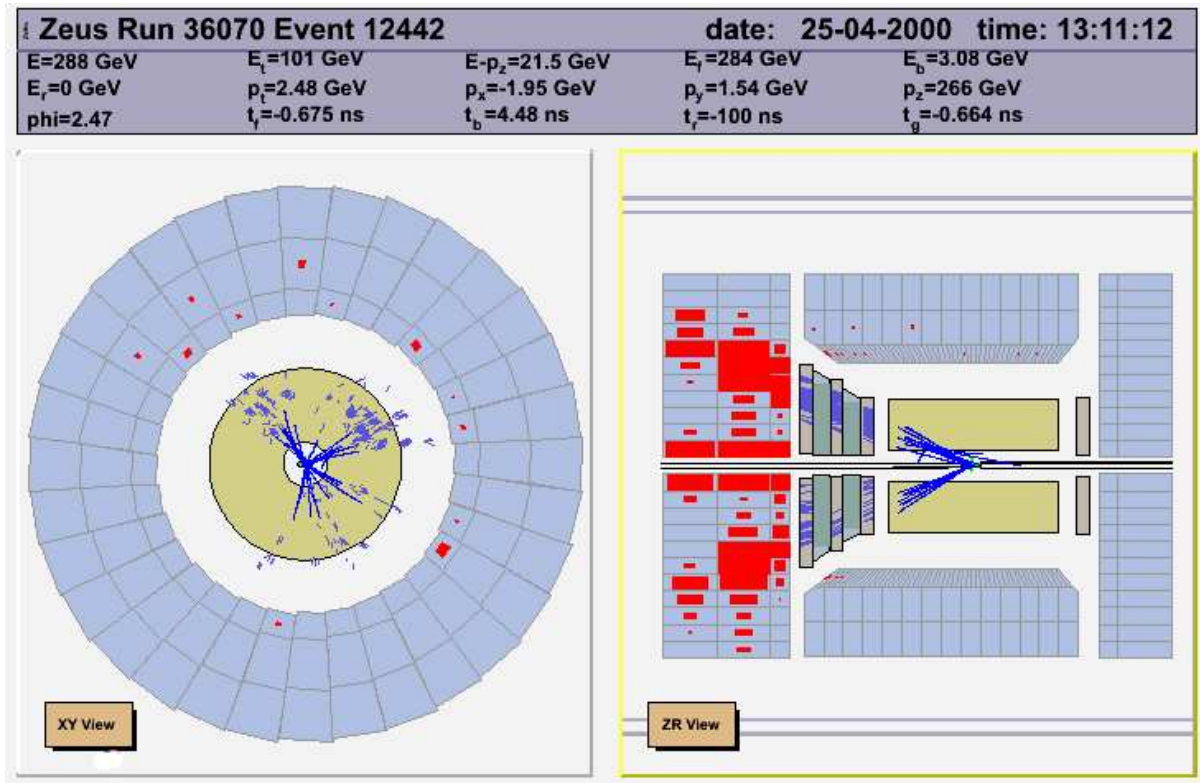


Figure 4.2: A photoproduction event showing a two-jet structure. The transverse momentums of these two jets are balanced. The electron escapes through the rear beam hole.

4.2.2 Cosmic and halo muons

Cosmic rays, mainly high energy protons, produce pions in the upper atmosphere often in large shower of particles. These pions then decay into muons. Energetic muons penetrate through the atmosphere of the earth and arrive to the detector. When passing through the BCAL, the high energy muon can deposit substantial energy in the EMC through an electromagnetic process. Combined with the track left by the muon in the CTD, this energy can be misidentified as an electron. Such events are usually rejected in the trigger by comparing the timing in the top and bottom halves of the BCAL. Note that the ep beam interaction deposits energies simultaneously in the two halves while cosmic muon events do not. Figure 4.3 shows a typical cosmic shower detected.

Similar to cosmic muons, the interaction between the protons and residential gas or elements of the accelerator optics upstream of the detector creates high energy muons

through the decay of charged pions. These penetrating muons are almost parallel to the beam axis and create a fake electron candidate if they deposit enough energy in the EMC. The timing of the energy deposit of such an event is earlier in RCAL and later in FCAL compared to an ep scattering event.

In both cases, the total transverse momentum p_T is typically not zero in contrast to the DIS events, since the muons leave very different energies in the two halves of the CAL.

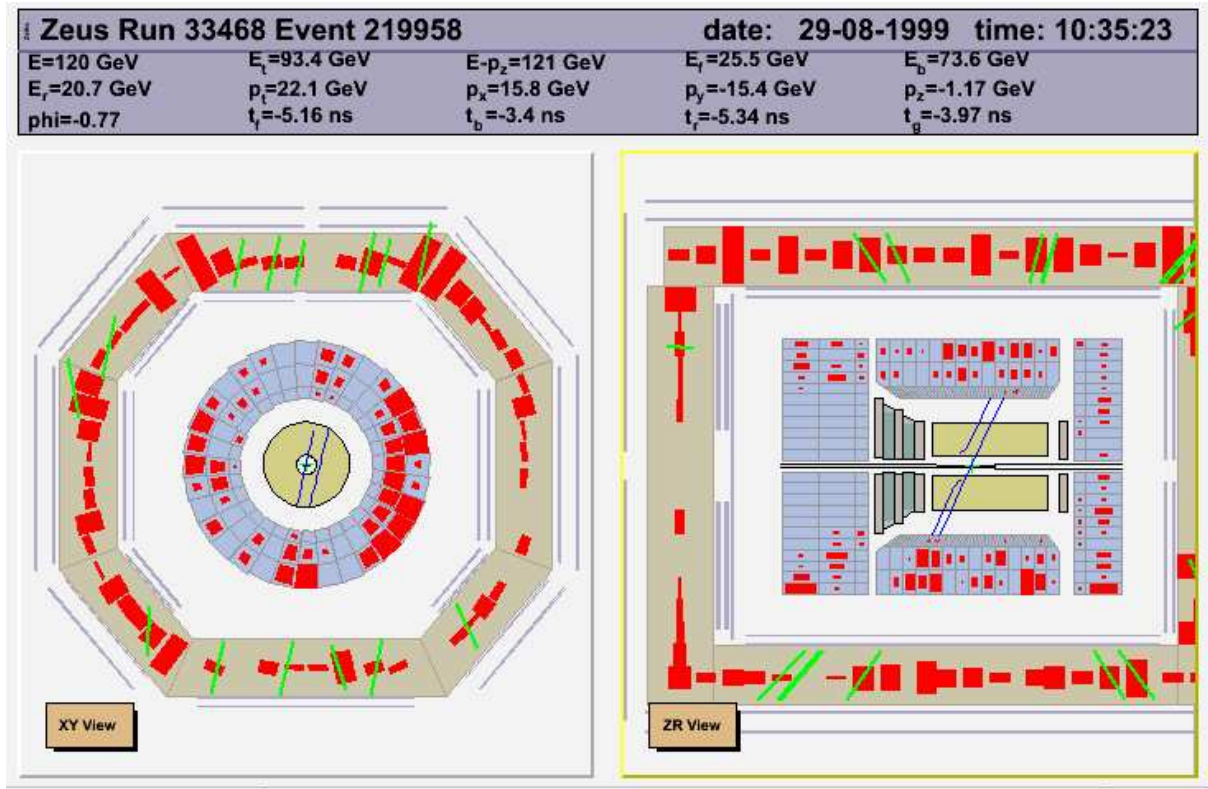


Figure 4.3: A cosmic shower, with muon tracks in CTD. Particles leave signals in CAL, CTD, BAC and muon chambers.

4.2.3 Proton beam gas interaction

Protons in the beam can interact with gas molecules in the beampipe or in beampipe wall and produce events that are sometimes misidentified as NC DIS events. Proton beam gas interactions have a very different topology from DIS events and are characterized by one or more of following features:

- low $E - p_Z$ value since most particles in proton beam gas events are in the forward direction;
- an erroneous Z -vertex position since the interaction can happen anywhere;
- early energy deposit in the RCAL, a feature that permits rejection efficiently in the trigger;
- large missing p_T , if the off-beam-axis proton interacts with the beampipe wall.

Due to the very high rate of beam gas collisions compared to the rate of physics events, proton beam gas events can also occur at the same time as a NC DIS event. Such events, known as overlay events, have an anomalously high $E - p_Z$.

4.2.4 QED Compton scattering

Together with initial- and final-state bremsstrahlung, QED Compton scattering $ep \rightarrow e\gamma X$ are all the processes involving the radiation of a hard photon from the initial or scattered electron. Relevant here is the feature that final state photon has large p_T . Compton scattering is the case of an emission of a hard photon not collinear with the emitting electron. If the photon is confused with the hadronic final state in reconstruction, a severely biased measurement of the kinematic variables would result. In inelastic Compton scattering, the proton breaks up producing a final state with hadrons. This process has a well known cross section and is included in the MC simulation. Such inelastic events are not rejected in this analysis, but the number is small and well understood. In the elastic Compton scattering process ($ep \rightarrow e\gamma p$), the proton stays intact and does not deposit any energy in the FCAL. Only the scattered electron and emitted photon are detected. Such elastic events are easily rejected. Figure 4.4 shows an elastic Compton scattering event with clearly reconstructed electron and photon. The photon is easily identified as such and not confused with a hadronic jet.

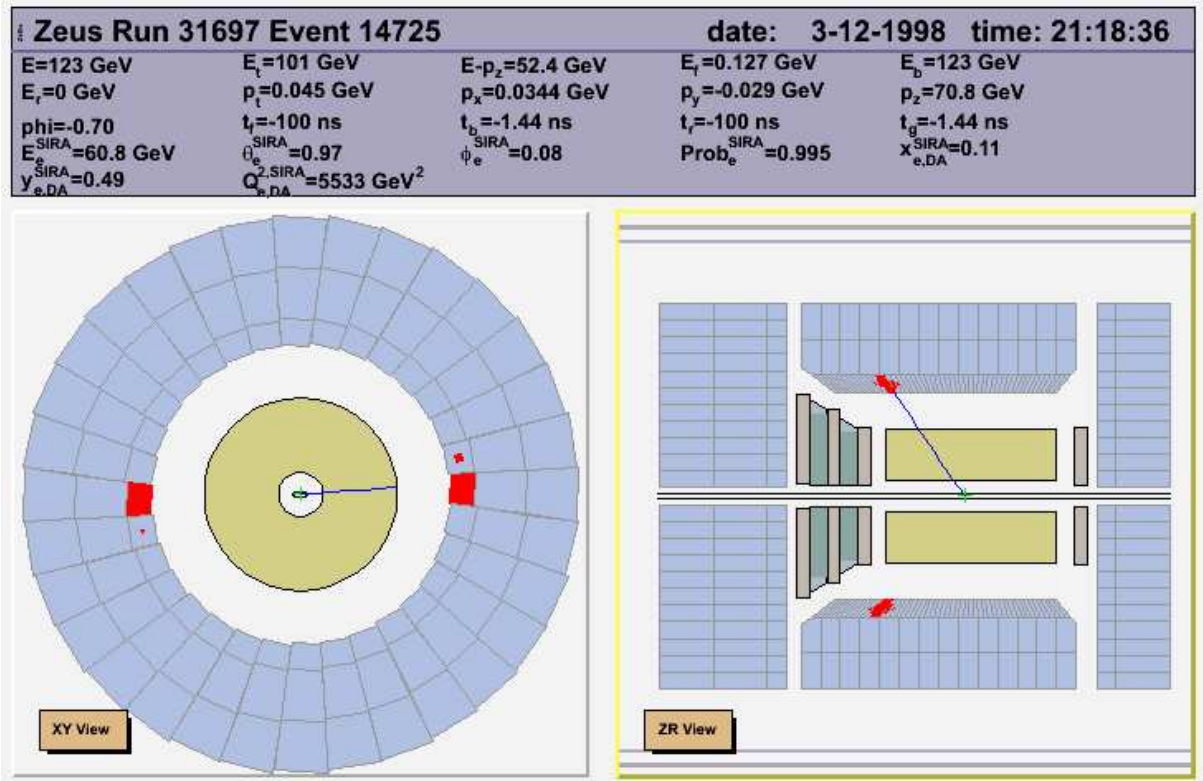


Figure 4.4: A QED Compton elastic event with a well reconstructed electron in CTD and BCAL. A photon is detected in BCAL.

4.2.5 Calorimeter sparks

Electrical discharges sometimes occur between the photocathode and shielding of the CAL photomultipliers (PMTs). It can also occur in unstable or defective PMT bases, which supply the PMT high voltage. These discharges are called calorimeter sparks, which can be misidentified as scattered electrons in EMC cells. Since two operating PMTs read the signal from one CAL cell, a large energy deposit in only one of them is anomalous. So a big difference between the signals from the two PMTs, combined with the cell history and the signals from surrounding PMTs, are used to reject the spark events in the triggering.

4.3 Trigger preselection

At the first-level trigger, only coarse calorimeter and tracking information are available. NC DIS events are selected using criteria involving the energy deposits in the CAL. The

BCAL EMC energy is required to be bigger than 4.78 GeV. Since the electron must pass through the CTD, a track visible there is also required. For the FCAL, the event is triggered by either a high transverse energy $E_T > 30$ GeV (or $E_T > 11.6$ GeV with a track in the CTD) or the total electromagnetic energy in the FCAL EMC is larger than 10 GeV.

At the second level, a more sophisticated trigger selection is possible since the full calorimeter information is available. A requirement on $E - p_Z$ is used here to select NC DIS events. And timing information from the calorimeter is used to reject events characterized by energy deposits inconsistent with the bunch-crossing time. Particles from upstream proton beam gas interactions will hit the RCAL 10 ns before secondaries from the protons reaching the interaction point. Cosmic rays will hit top half of the BCAL 12 ns earlier than bottom.

At the third level, events are fully reconstructed on a computer farm. Several electron finder algorithms are run to identify the scattered electron and CTD tracks are reconstructed to find the Z -vertex position, which helps to calculate $E - p_Z$ more accurately. The requirements are similar to, but looser than, the offline cuts described below. The electron finder used online should be simpler and more efficient (but less pure).

The main uncertainty in the trigger efficiency comes from the first level. The efficiency in data and MC simulation agree to within $\sim 0.5\%$ and the overall efficiency in the kinematic region of interest is above 95%. This three-level trigger system is simulated in Monte Carlo with exact same algorithm in data.

4.4 Offline event-selection

Offline selections used in this analysis are described here, including the scattered electron selection, jet selection and background suppression. Offline cuts are more stringent than the third level trigger described above. All the selections are applied to data and MC. To ensure that the data is well described by both event generator and the detector simulation, all the essential variables before the offline selection applied are compared between data

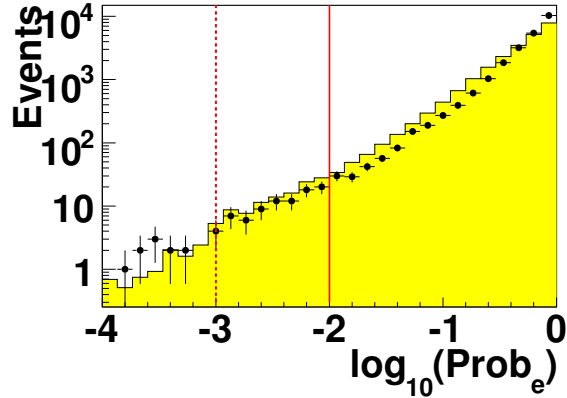


Figure 4.5: Comparison of NC MC simulated events (histograms) with 99-00 e^+p data (points) on the electron probability selection. The MC distributions are normalized to the luminosity of the data. The dashed line shows the cut for electron with a matched track and solid line is the tighter cut for electron in FCAL without a track.

and MC where MC is normalized to the luminosity of the data. Each variable is in a separate plot, which shows the events pass through all other selections except this variable. Overall MC describes data quite well.

4.4.1 Electron selection

The main tag of DIS NC events is an isolated electron in the CAL. So an electron finder with high efficiency and purity is essential for the offline selection. The following criteria are imposed to select the electron.

- **Electron finder:** As mentioned in Sect. 3.3.1, in this analysis, the EM electron finder [45] is used to find the scattered electron. The electron candidate with the highest “probability” is selected. The cut is applied on this probability to get the DIS sample with high purity. In the CTD acceptance region, $\theta_e > 0.3$ rad, the probability is required higher than $1 \cdot 10^{-3}$; outside that region, the probability cut increases to $1 \cdot 10^{-2}$. Figure 4.5 shows the comparison between data and MC on the electron probability in log scale. The events around the cut region are three orders of magnitude less than the events with probability close to 1.

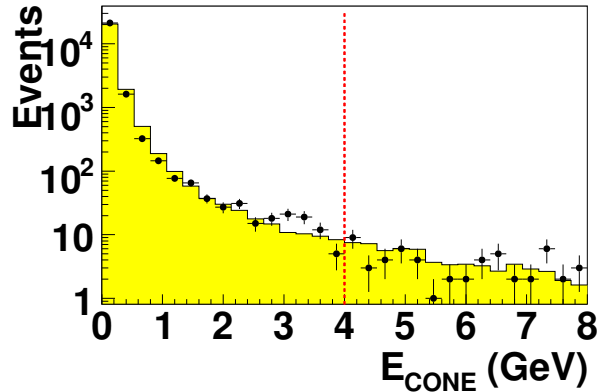


Figure 4.6: *The comparison of NC MC simulated events (histograms) with 99-00 e^+p data (points) on the energy not belonging to the electron in a cone around the electron E_{CONE} . The MC distributions are normalized to the luminosity of the data. The dashed line shows the 4 GeV cut.*

- **Isolation:** The energy deposits by the scattered electron must be well isolated in the CAL compared to electrons within jets. To increase the purity, the energy deposit in calorimeter cells within an η - ϕ cone of radius $R_{\text{CONE}} = 0.8$ centered on the scattered electron and not associated with this electron must be less than 4 GeV. Figure 4.6 shows the comparison between data and MC in log scale.
- **Track matching:** For those electrons in the CTD acceptance region, a track extrapolated to the shower maximum is required to pass within 10 cm of the cluster center. The matched track is required to traverse at least four of the nine superlayers of the CTD. The momentum of the track, p_{trk} , is required to be at least 10 GeV; Figure 4.7 and 4.8 show the comparisons between data and MC on the distance of closest approach between track and calorimeter and the momentum of the track in log scale. MC describes the momentum of track quite well.
- **Electron energy:** For the electron in CTD acceptance, the electron energy is required to be bigger than 25 GeV for a pure NC sample; for electrons outside the forward tracking acceptance of the CTD, the tracking requirement is replaced by a cut on the transverse momentum of the electron, $E_{T,e} > 30$ GeV; Figure 4.9 shows the good agreement between data and MC on the electron energy in log scale.

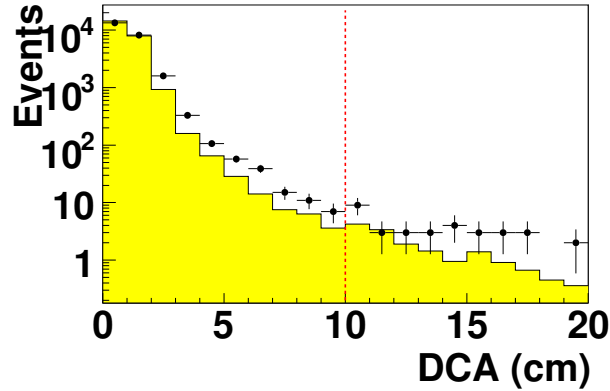


Figure 4.7: *The comparison of NC MC simulated events (histograms) with 99-00 e^+p data (points) on the distance of closest approach between track and calorimeter. The MC distributions are normalized to the luminosity of the data . The dashed line shows the 10 cm cut.*

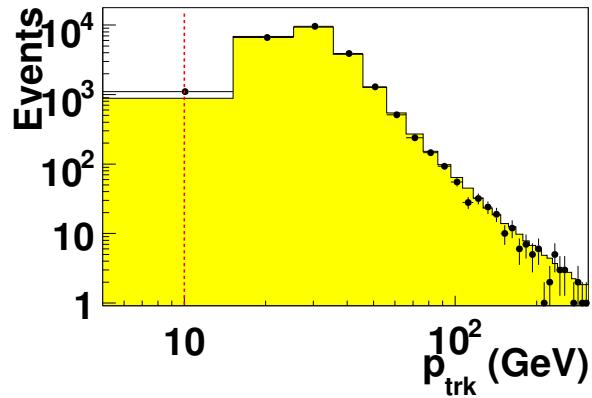


Figure 4.8: *The comparison of NC MC simulated events (histograms) with 99-00 e^+p data (points) on the momentum of the matched track. The MC distributions are normalized to the luminosity of the data . The dashed line shows the 10 GeV cut. MC describes the track momentum quite well in the whole track region.*

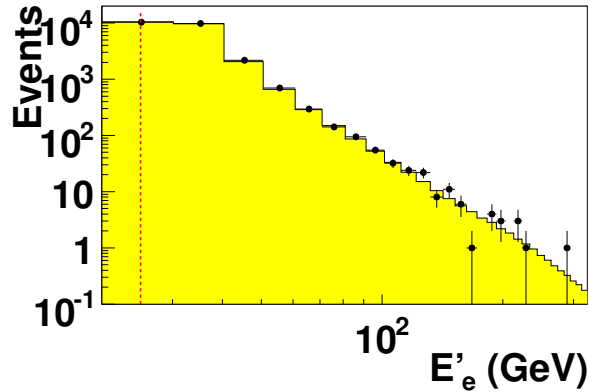


Figure 4.9: *The comparison of NC MC simulated events (histograms) with 99-00 e^+p data (points) on the electron energy. The MC distributions are normalized to the luminosity of the data. The dashed line shows the 25 GeV cut.*

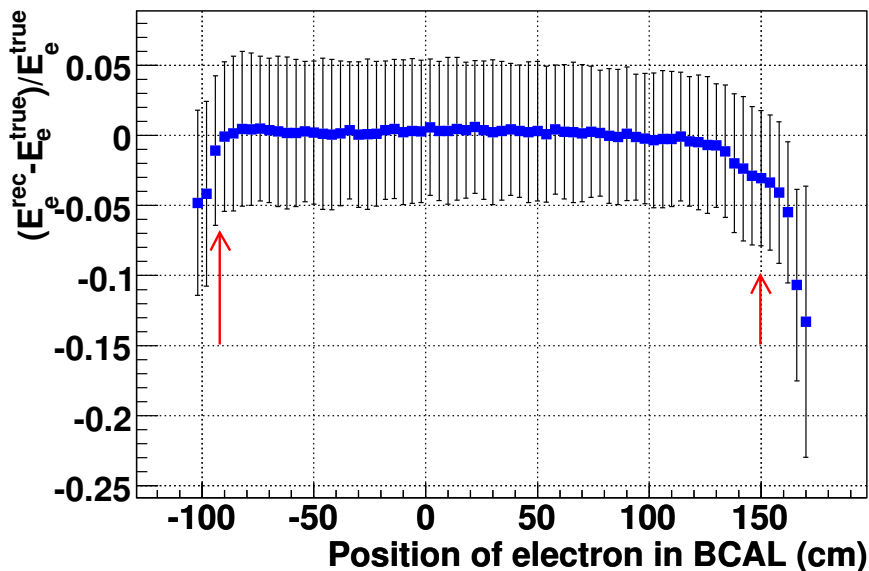


Figure 4.10: *Relative difference of BCAL electron energy compared with true energy versus the longitudinal impact position as determined from the matched track for 99-00 MC, where the error bar is sigma of Gaussian fit. The arrows show the fiducial cut to reject the events in the region between main parts of CAL.*

- **Geometrical cut:** A fiducial-volume cut is applied to the electron to guarantee it is within a region in which the experimental acceptance is well understood. It excludes the transition regions between FCAL and BCAL [53] (Fig. 4.10). It also excludes the region within 1.5 cm of the module gap in BCAL (Fig. 4.11). Because the kinematic region emphasizes in this analysis is at high Q^2 , electrons in RCAL are not considered.

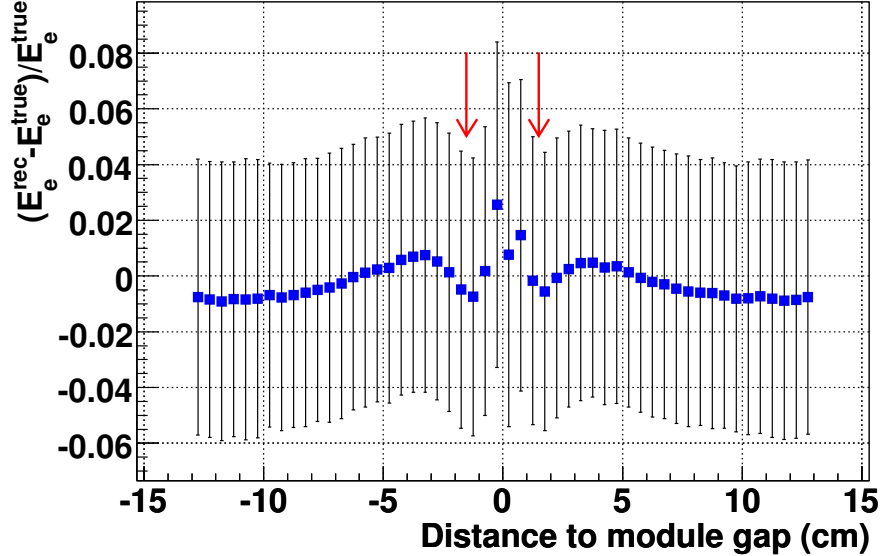


Figure 4.11: *Relative difference of BCAL electron energy compared with true energy versus the distance to the CAL module gap which determined from the matched track for 99-00 MC, where the error bar is sigma of Gaussian fit. The arrows show the fiducial cut to reject the events in the module gap in BCAL.*

4.4.2 Jet selection

Jet reconstruction is accomplished as described in Sect. 3.4. The following cuts on the reconstructed jets are used to select events for this analysis:

- **Jet energy and angle:** $E_{T,jet} > 10$ GeV and $\theta_{jet} > 0.12$ rad. The angle cut removes jets found too close to the beam hole. This cut excludes the inner most FCAL towers, the so-called “first inner ring” (FIR), which is a square of 60×60 cm² centered on the beam hole (Fig. 2.6). Jets with $\theta_{jet} < 0.12$ rad lose energy in the forward beam hole, so the reconstructed E_{jet} and θ_{jet} are not reliable. Also jets that close to the beam hole could include extra energy from the proton remnant since it is hard to tell jets from the proton remnant in this region. Figure 4.12 and 4.13 show the comparison between data and MC on the jet transverse energy and angle before the jet selection. MC generally describes the data quite well. Figure 4.14 shows the very good agreement between data and MC on the number of jets which pass the jet energy and angle selection. The comparison of data and MC on the number of jets in different x_{DA}

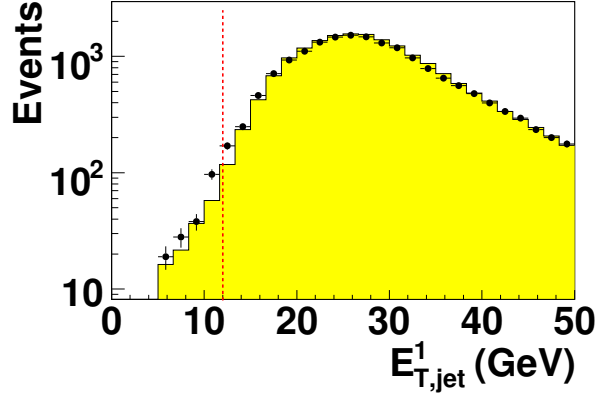


Figure 4.12: The comparison of NC MC simulated events (histograms) with 99-00 e^+p data (points) on $E_{T,jet}$. The MC distributions are normalized to the luminosity of the data. The dashed line shows the cut.

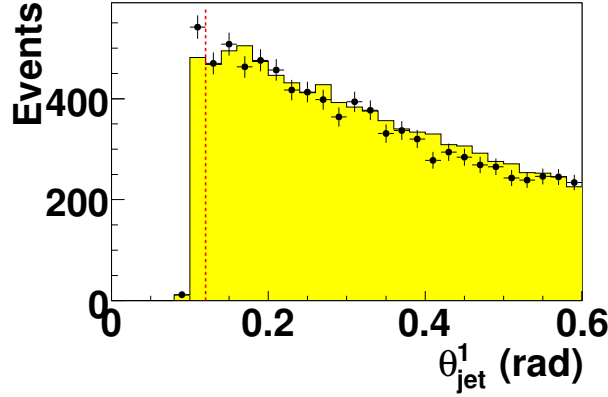


Figure 4.13: The comparison of NC MC simulated events (histograms) with 99-00 e^+p data (points) on θ_{jet} . The MC distributions are normalized to the luminosity of the data. The dashed line shows the cut.

bins is shown in Fig. 4.15. MC describes data quite well on one and two jets events in the whole x_{DA} region. As described in Sect. 3.2, zero jet events are in the higher x region. So zero jet events are used to measure the cross section at high x in this analysis. Due to poorer x resolution, as shown in Fig. 4.16, events with more than one jet that satisfies the jet selection are discarded. The correction to the cross section for discarding multi-jet events is taken from the Monte Carlo simulation, and ranged from 9% at $x = 0.1$ to 1% at $x = 0.6$. The systematic uncertainty associated with this cut is discussed in Sect. 5.4.

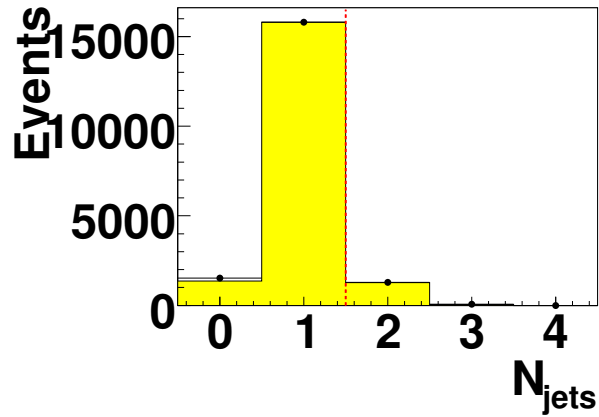


Figure 4.14: *The comparison of NC MC simulated events (histograms) with 99-00 e^+p data (points) on the number of jets. The MC distributions are normalized to the luminosity of the data. The dashed line shows the $n_{jet} = 1$ cut. Only zero and one jet events are used in this analysis. MC describes the number of zero, one and two jets events quite well.*

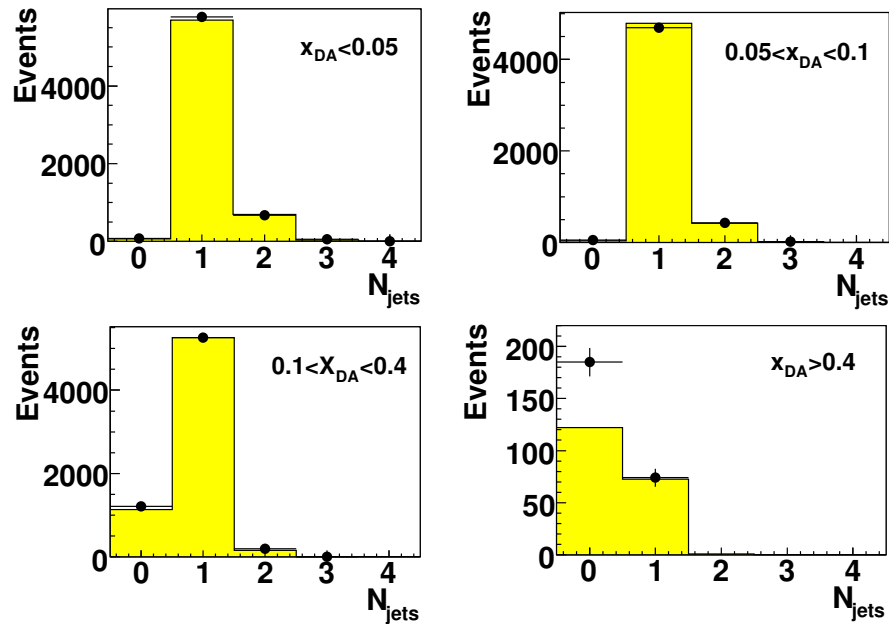


Figure 4.15: *The comparison of NC MC simulated events (histograms) with 99-00 e^+p data (points) on the number of jets in different x_{DA} bins. The MC distributions are normalized to the luminosity of the data. MC describes the number jets events quite well in the whole x_{DA} region.*

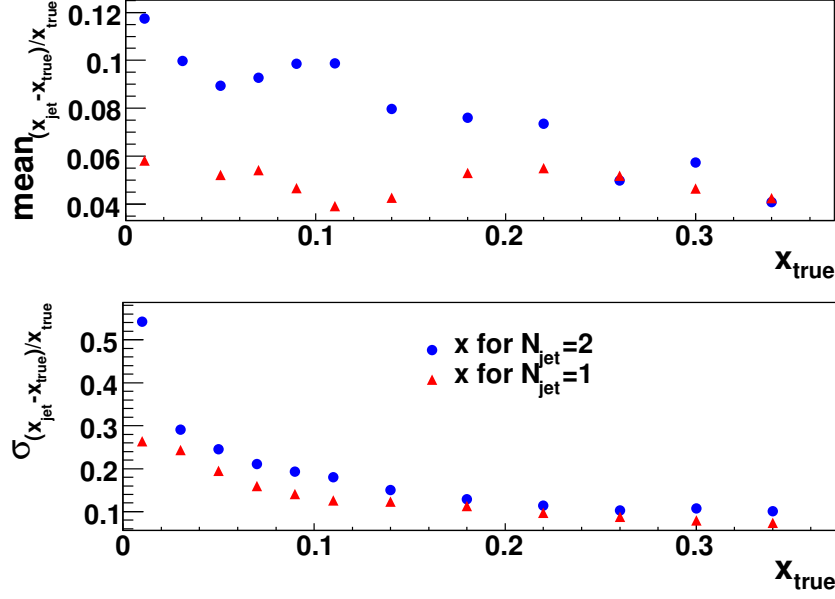


Figure 4.16: *The resolution of x which is reconstructed from jet energy and angle for one and two jets events for 99-00 e^+p MC. The mean and the sigma of the Gaussian fit are shown. The triangle is the x calculated from one jet and the square is for the two jets events. The x resolution is better for one jet events.*

4.4.3 Background suppression

After the electron and jet selections, the DIS event sample is clean since we require high energy electrons and high E_T jets, which exclude most of the background. To further reduce the background, the following kinematic cuts are used to select an essentially background free and well reconstructed event sample:

- **z -vertex cut:** A cut on the reconstructed z -position of the vertex with $-50 < Z < 50$ cm, the range of the ep interaction region. A small fraction of the proton-beam current is contained in satellite bunches, which are shifted by ± 4.8 ns with respect to the nominal bunch-crossing time, resulting in a few % of the ep interactions occurring ± 72 cm from the nominal interaction point. Though this cut rejects ep events from these regions, the effect is small ($\sim 6\%$) and well-understood. Figure 4.17 shows the good agreement between data and MC on the z -vertex in log scale even in the region outside the cut.

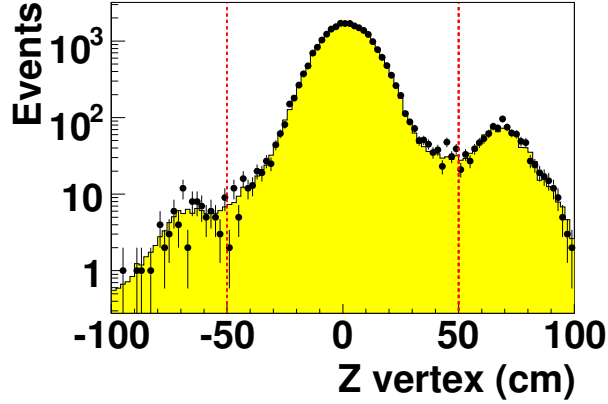


Figure 4.17: The comparison of NC MC simulated events (histograms) with 99-00 e^+p data (points) on the z -vertex. The MC distributions are normalized to the luminosity of the data. The dashed lines show the ± 50 cm cut.

- **$E - p_Z$ cut:** $E - p_Z > 40$ GeV to suppress events with large QED initial state radiation, described in Sect. 4.2.4. This cut also rejected remaining PHP events. The lower cut value is increased to 47 GeV for events in the highest x bins, where the jet is not reconstructed. The additional requirement $E - p_Z < 65$ GeV removed a small number of “overlay” events in which a normal DIS event coincided with additional energy deposits in the RCAL from some other reaction. This requirement had a negligible effect on the efficiency for selecting NC DIS events. Figure 4.18 shows the good agreement between data and MC on the $E - p_Z$ in log scale even in the region outside the cut.
- **y_e cut:** PHP events which fake a DIS event accumulate at high y values. For example: a π^0 , often occurring in the proton remnant, decays into two photons and can easily be misidentified as the scattered electron. Such a fake electron usually has a low energy and small $(E - P_Z)_e$, which leads to high y_e ($(E - P_Z)_e = E'_e(1 - \cos\theta_e)$), where y_e is defined as:

$$y_e = 1 - \frac{E'_e}{2E_e}(1 - \cos\theta_e). \quad (4.3)$$

Therefore, we require $y_e < 0.95$ to further reduce background from PHP events, Figure 4.19 shows the good agreement between data and MC on the y_e in log scale and only several events are removed.

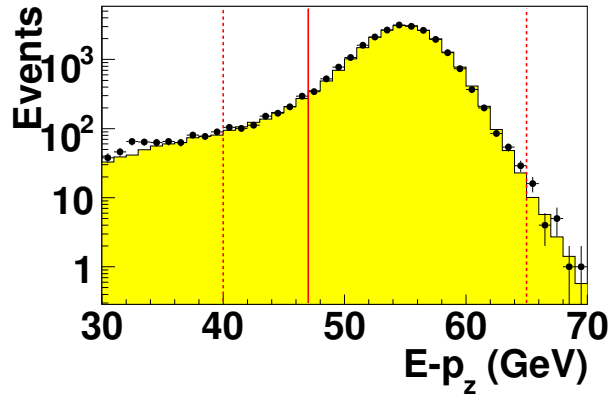


Figure 4.18: *The comparison of NC MC simulated events (histograms) with 99-00 e^+p data (points) on the $E - p_z$. The MC distributions are normalized to the luminosity of the data. The dashed lines show the $40 \text{ GeV} < E - p_z < 65 \text{ GeV}$ cut and the solid line shows the tighter lower cut 47 GeV .*

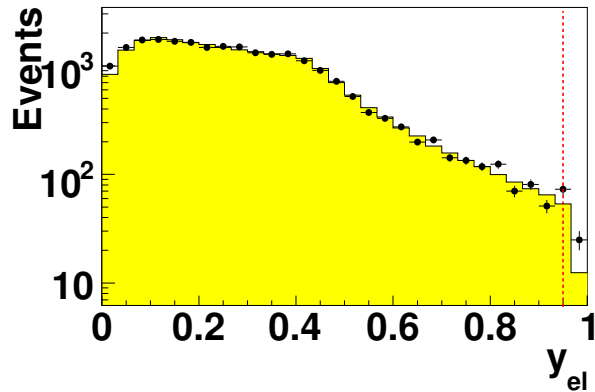


Figure 4.19: *The comparison of NC MC simulated events (histograms) with 99-00 e^+p data (points) on y_e . The MC distributions are normalized to the luminosity of the data. The dashed line shows the cut.*

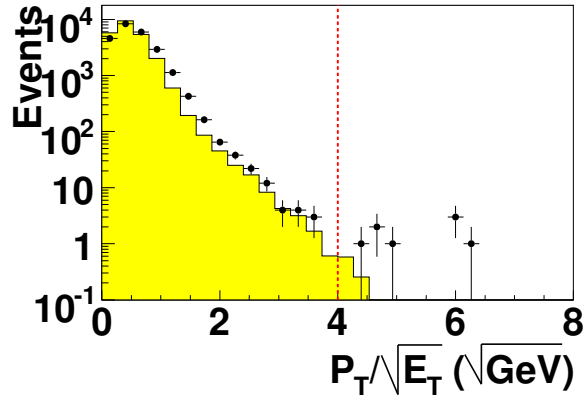


Figure 4.20: The comparison of NC MC simulated events (histograms) with 99-00 e^+p data (points) on $P_T/\sqrt{E_T}$. The MC distributions are normalized to the luminosity of the data. The dashed line shows the cut.

- **$P_T/\sqrt{E_T}$ cut:** If a DIS event is perfectly reconstructed, the total transverse momentum P_T should be 0. P_T is calculated from the individual energy deposits in CAL and the uncertainty of measured energy in CAL is approximately proportional to $\sqrt{E_T}$, which is defined as:

$$E_T = \sum_i E_i \sin \theta_i, \quad (4.4)$$

where the sums run over all calorimeter energy deposits, E_i , with polar and azimuthal angles θ_i and ϕ_i with respect to the event vertex, respectively, which means the ratio of P_T to $\sqrt{E_T}$ should be close to zero. So $P_T/\sqrt{E_T}$ is required to be smaller than $4 \text{ GeV}^{1/2}$ to remove cosmic rays and beam related background; Figure 4.20 shows the good agreement between data and MC on the $P_T/\sqrt{E_T}$ in log scale. Only several events are removed by this cut.

- **Elastic Compton scattering rejection:** Their very clean topology make the rejection straightforward. More than 4 HAC cells with energy above 110 MeV is required to remove background from Compton scattering events ($ep \rightarrow e\gamma p$). Totally 68 events, $\sim 0.4\%$, removed in 99-00 data. are All are QED elastic events, which were checked by eye scan.
- **Migration from low x rejection for zero jet events:** There is a small fraction of low x events, which have struck quark at large angle, can be counted as zero jet

events when no jet passes through the jet requirement. Since Q^2 is reconstructed accurately, these low x events have higher y compared to the true high x events. The cut $y_{\text{JB}} < 1.3 \cdot Q_{\text{upperedge}}^2 / (s \cdot x_{\text{edge}})$ is required to limit event migration from small x to large x for zero jet events, where y_{JB} is calculated with the Jacquet-Blondel method [54]:

$$y_{\text{JB}} = \frac{\delta_h}{2E_e} \quad (4.5)$$

and $Q_{\text{upperedge}}^2$ and x_{edge} are the edges of the $x - Q^2$ bins defined for the cross section measurement (see Sect. 5.2). Figure 4.21 shows the x_{true} distribution of zero jet events in each Q^2 bins before and after this cut. The x_{edge} is shown too. Most of the zero jet events are at high x region. Also there are small number of events at low x which have no “good” reconstructed jet. The figure shows that this cut removes those low x events and keeps the true high x events.

4.4.4 Comparison of data and Monte Carlo

After all the selection, 17101 events remained in the 99-00 e^+p data, 4462 in the 98-99 e^-p data and 8679 events in the 96-97 e^+p data. The numbers of PHP background events are estimated ~ 2 events in 99-00 data and less than 1 event in 98-99 and 96-97 data. MC distributions are compared with those from data for several variables in Fig. 4.22, 4.23 and 4.24 as described below. The MC distributions are normalized to the measured luminosity. Only the comparison to 99-00 e^+p data is shown; the comparisons of 98-99 e^-p and 96-97 e^+p data with MC distributions showed similar features and are shown in Fig. A.1 to Fig. A.6. The first set of plots, Fig. 4.22, shows general properties for the full sample of events. Good agreement between data and MC simulation is observed, and there is no indication of residual backgrounds. Figure 4.23 shows distributions related to the scattered electron. Figure 4.24 presents a series of control plots for jet quantities. The MC reproduces the data distribution for the number of reconstructed jets to high accuracy. This is important since the MC is used to correct for the inefficiency resulting from the requirement of less than two reconstructed jets. The remaining distributions in

ZEUS

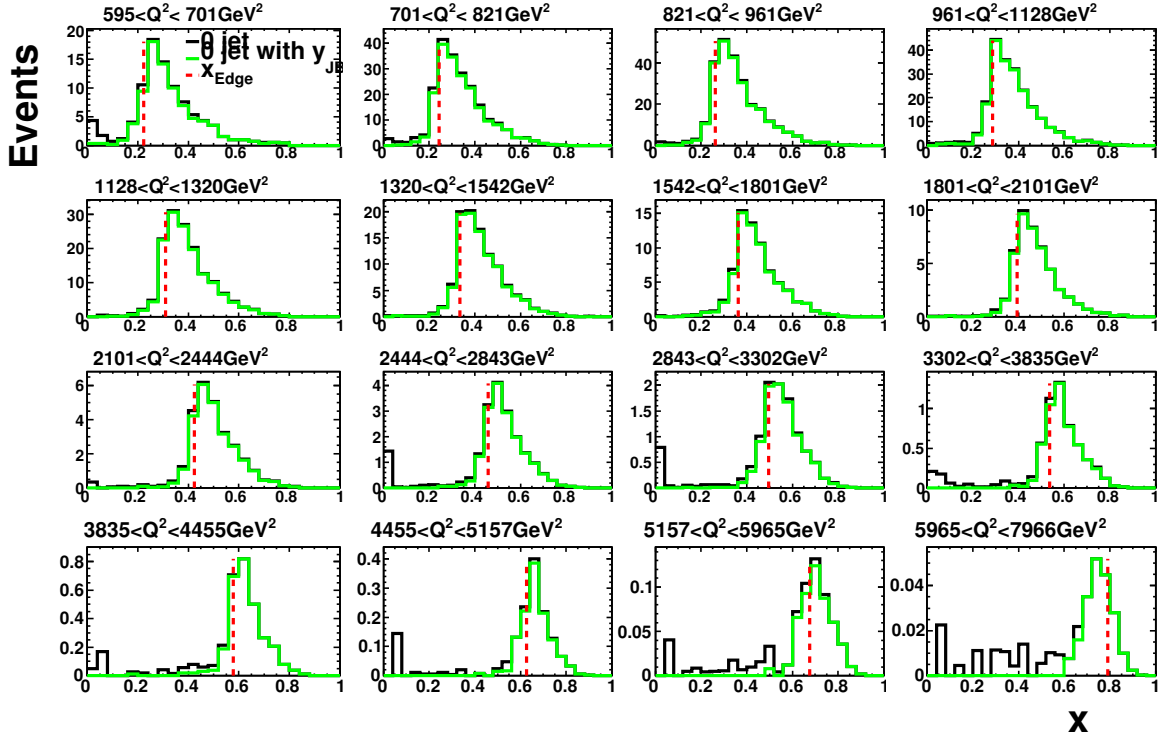


Figure 4.21: *The true x distribution for zero jet events from 99-00 e^+p MC simulations in different Q^2 bins before and after y_{JB} cut. The black line is the distribution before applying y_{JB} cut and the gray line is the distribution after. The dashed lines represent the lower edge of the bins, x_{edge} . The MC distributions are normalized to the luminosity of the data.*

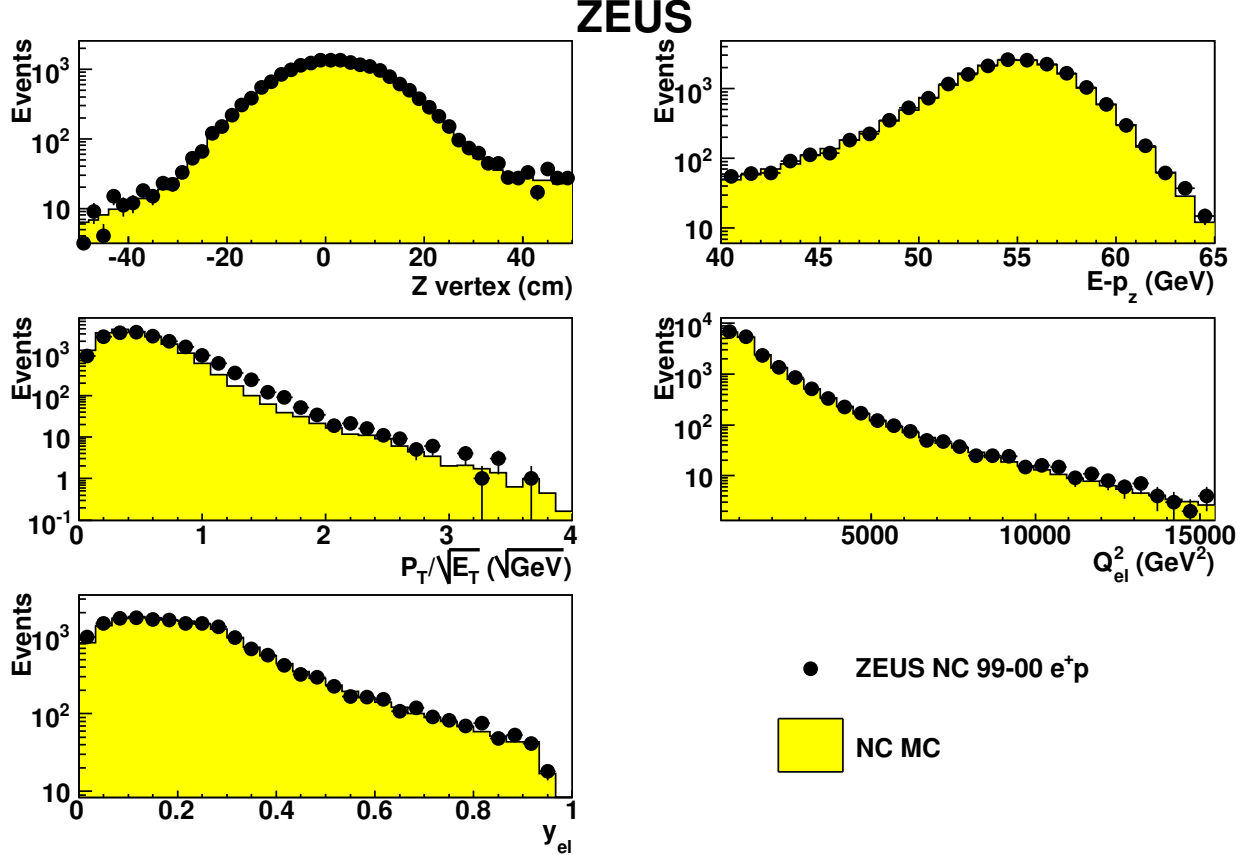


Figure 4.22: Comparison of NC MC simulated events (histograms) with 99-00 e^+p data (points) for: the Z coordinate of the event vertex; $E - p_z$; $P_T/\sqrt{E_T}$; Q_{el}^2 and y_e . The MC distributions are normalized to the luminosity of the data.

this figure are for the jet quantities in one jet events.

4.4.5 Comparison of data and Monte Carlo for zero jet events

Among all the events pass through the selections, the numbers of events in the zero jet bins are 1292, 293 and 493 in 99-00, 98-99 and 96-97 data respectively. Figure 4.25 shows distributions for the smaller class of events with zero jets. Overall, 13 % more data events for 99-00 e^+p , 2 % more data events for 98-99 e^-p and 5 % more data events for 96-97 e^+p are observed for zero jet events than expected in the simulation. The distributions for 96-98 are shown in Fig. A.7 to Fig. A.8. An offset in the $E - p_z$ data distribution is also seen. Many possible sources for this discrepancy were investigated, but no obvious

ZEUS

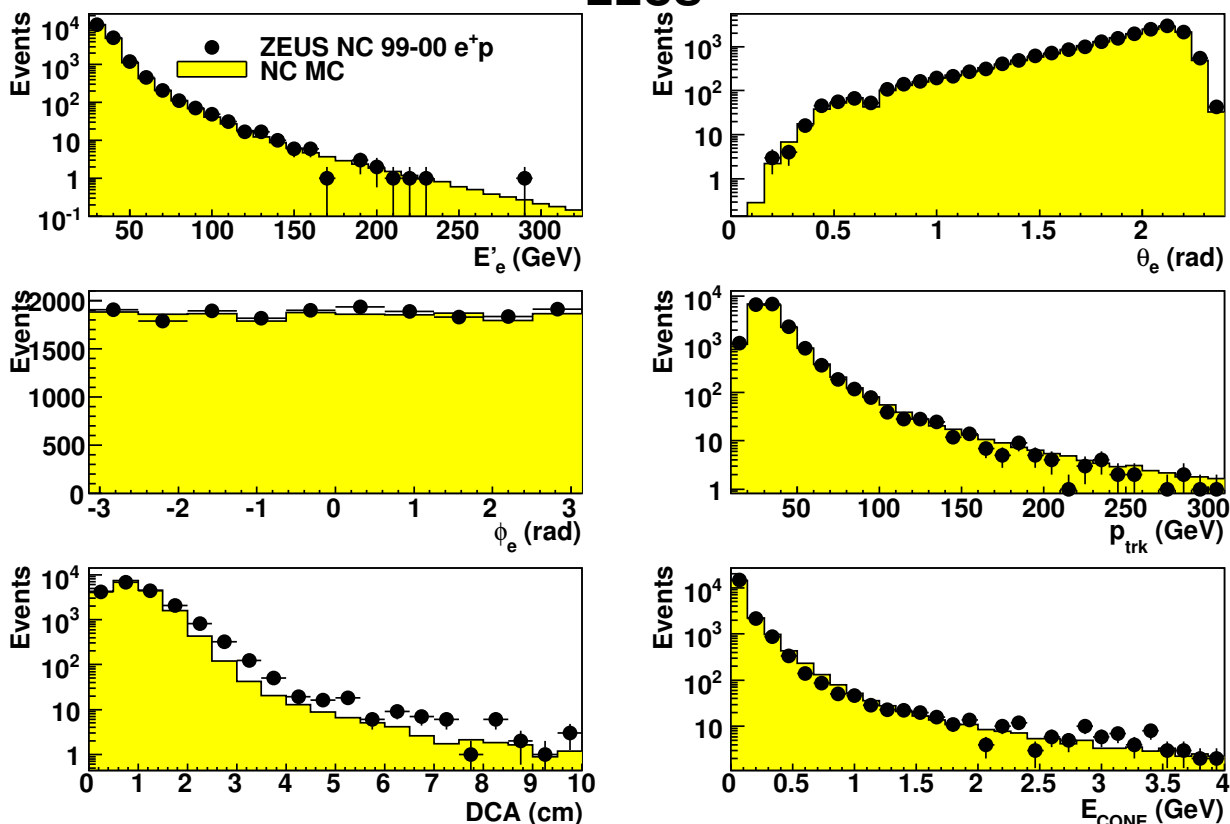


Figure 4.23: Comparison of NC MC distributions (histograms) with 99-00 e^+p data (points) for: E'_e ; polar angle of scattered electron θ_e ; azimuthal angle ϕ_e ; P_{trk} ; DCA and E_{CONE} , the momentum of the track associated with the scattered electron. The MC distributions are normalized to the luminosity of the data.

candidate was found. This discrepancy can be explained by shifting the electron energy scale by 1%, which is within the estimated uncertainty (Fig. 4.26) and included in quoted systematic uncertainty.

As mentioned in Sect. 3.2, the zero jets are critical to this analysis in high x region. The selection of zero jet depends on where the jet is, which is calculated from the energy weighted cell positions. The wrong energy scale in one cell could change the jet position a lot, especially in the FCAL FIR. If the energy scale is underestimated in FIR, one “bad” jet could be taken as one “good” jet since the reconstructed jet position is moved out and it passes the jet angle cut. While if energy scale is higher than true value in FIR,

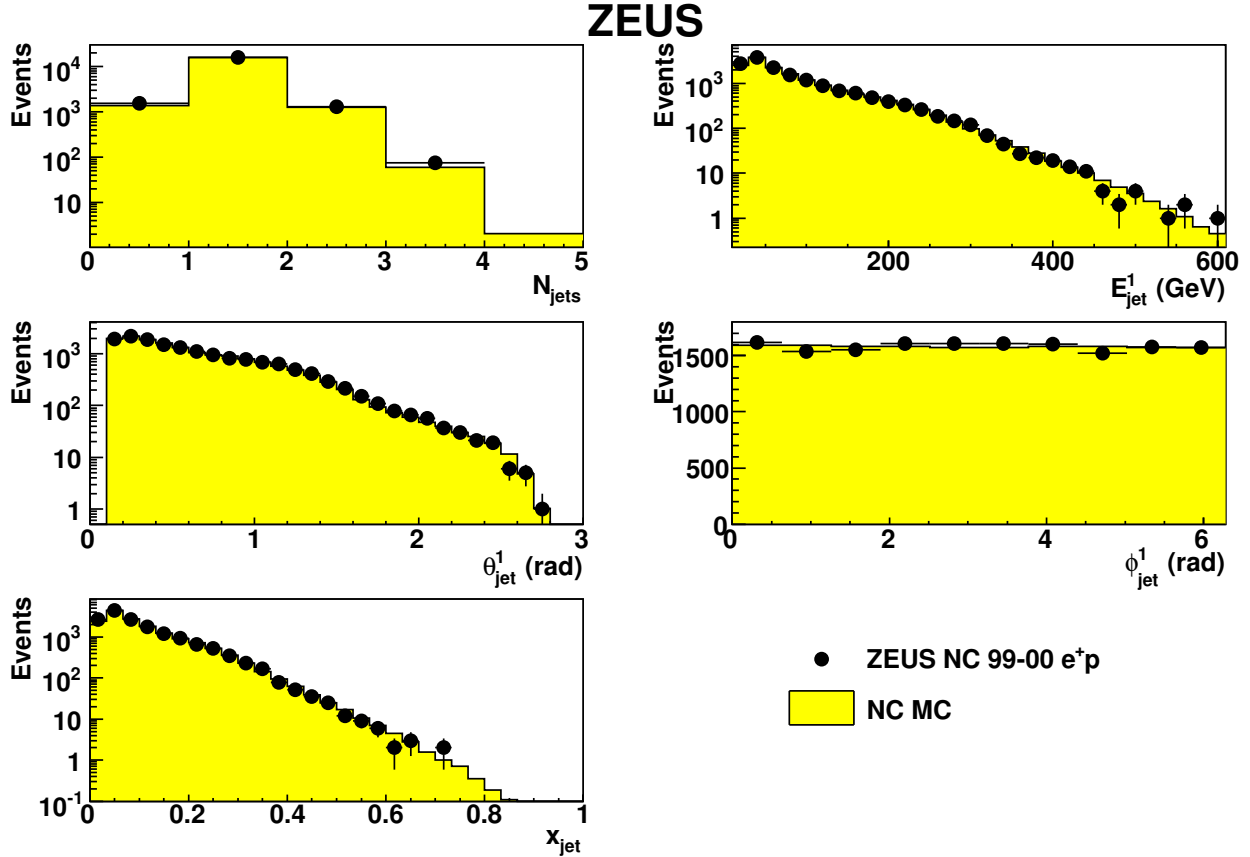


Figure 4.24: Comparison of NC MC distributions (histograms) with 99-00 e^+p data (points) for: the number of reconstructed jets N_{jets} ; the energy of the leading jet E_{jet} ; the polar angle of the leading jet θ_{jet} ; azimuthal angle ϕ_{jet} and x calculated from the jet x_{jet} . The jet distributions are for one jet events. The MC distributions are normalized to the luminosity of the data.

a “good” jet could be pulled into the FIR and counted as zero jet. So it is important that MC simulates the energy deposits in the FCAL FIR correctly. Figure 4.27 shows the comparison between data and MC for θ_{jet} in different E_{jet} region in the very forward direction, $\theta_{\text{jet}} < 0.3$ rad. Comparison shows that MC simulates the energy scale in FCAL FIR well.

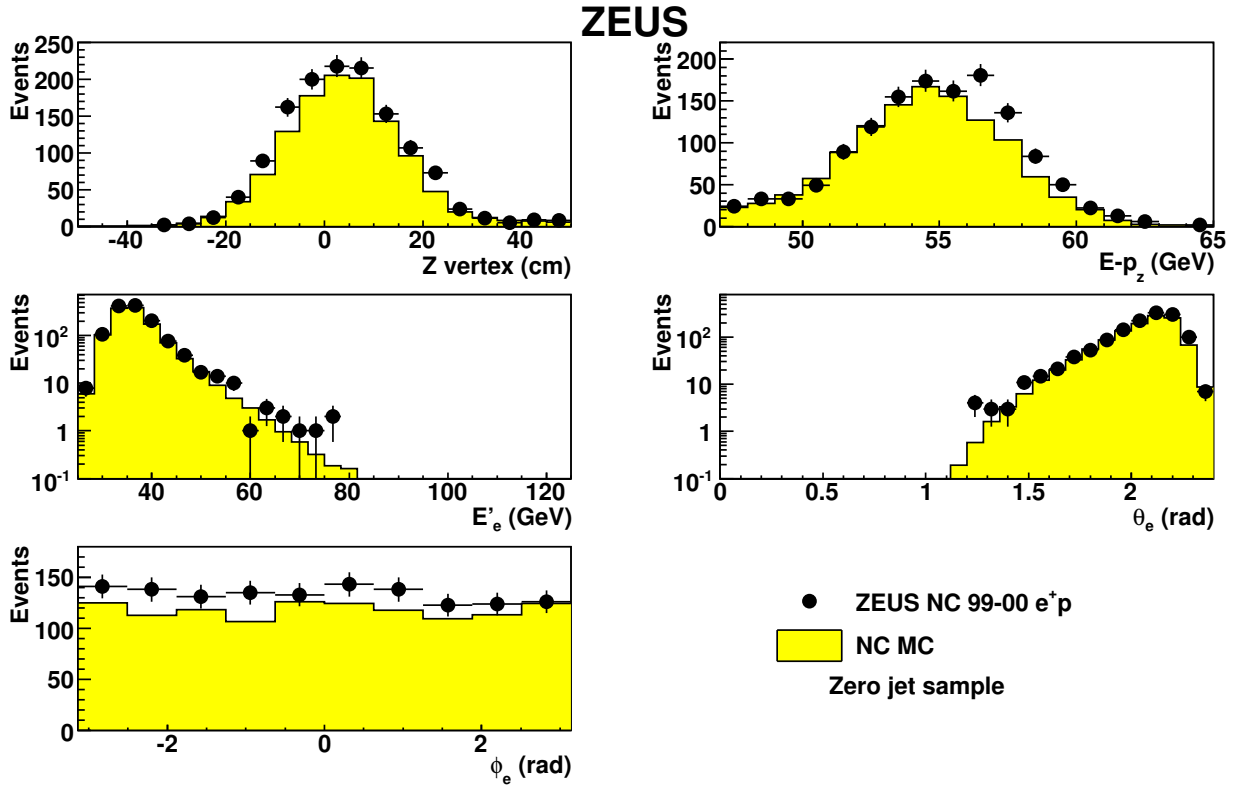


Figure 4.25: Comparison of NC MC distributions (histograms) with 99-00 e^+p data (points) for events with zero jets. The plots show: the Z coordinate of the event vertex; $E - p_z$; E'_e ; θ_e and ϕ_e . The MC distributions are normalized to the luminosity of the data.

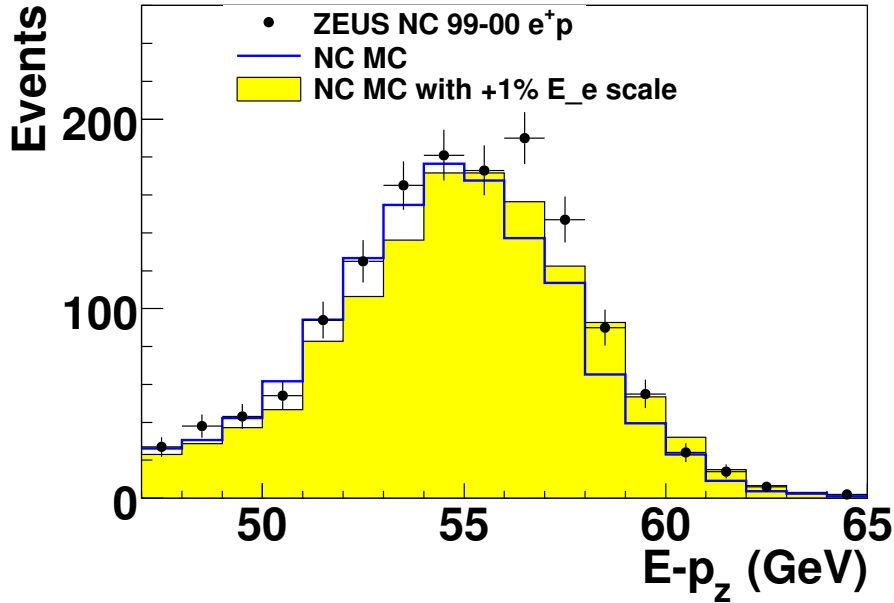


Figure 4.26: Comparison of NC MC distribution (shaded histogram) with electron energy scale +1% with 99-00 e^+p data (points) for $E - p_z$ for zero jet events. The line shows the original MC distribution. The MC distributions are normalized to the luminosity of the data. MC describes data better with +1% electron energy scale.

4.4.6 Comparison of data and ARIADNE Monte Carlo in jet

As mentioned in Sect. 2.3.1, ARIADNE was used to check the strong interaction simulation between the struck quark and the proton remnant. The number of jets is compared between data, MEPS, which is used in this analysis, and ARIADNE. Figure 4.28 shows much better agreement between MEPS and data on the number of two jets events and ARIADNE expects about 20% less two jets events. Since MC is used to correct the multijets and ARIADNE does not simulate the multijets well ARIADNE is not used as a systematic check on the simulation of the hadronic final state.

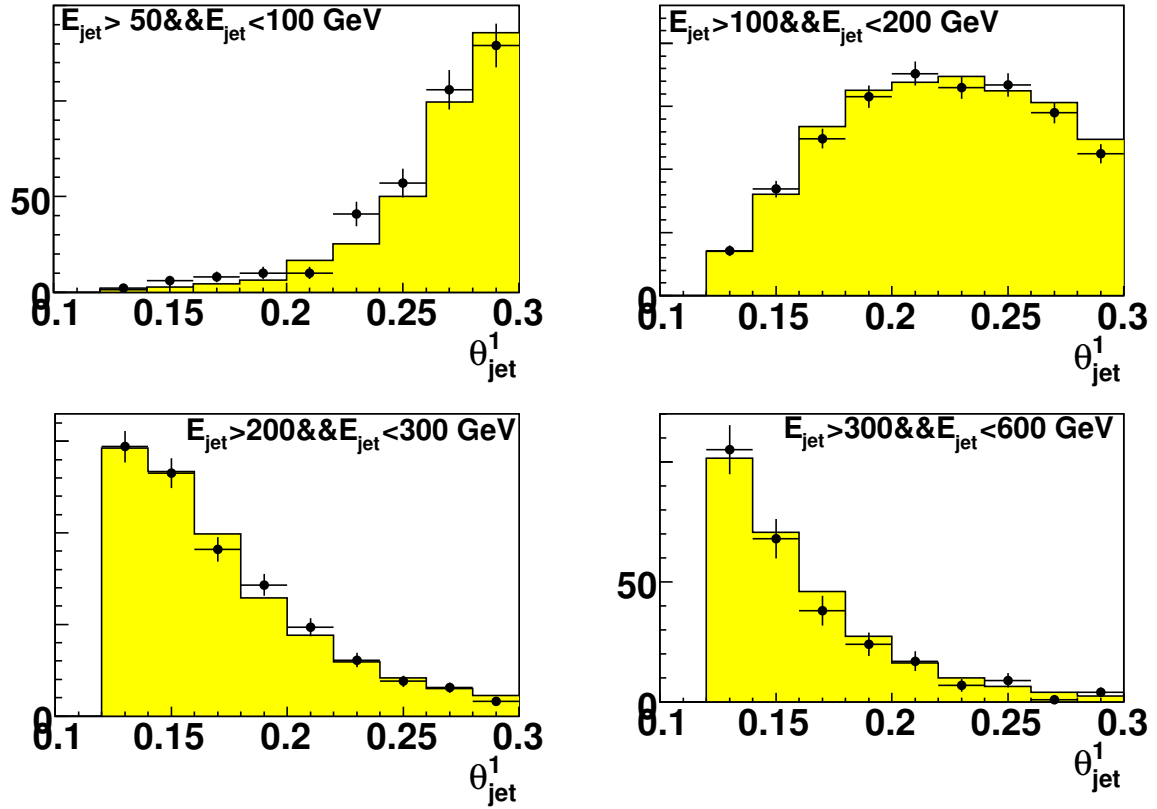


Figure 4.27: Comparison of NC MC distributions (histograms) with 99-00 e^+p data (points) for θ_{jet} in different E_{jet} bins in the forward region. The MC distributions are normalized to the luminosity of the data. MC describes data well.

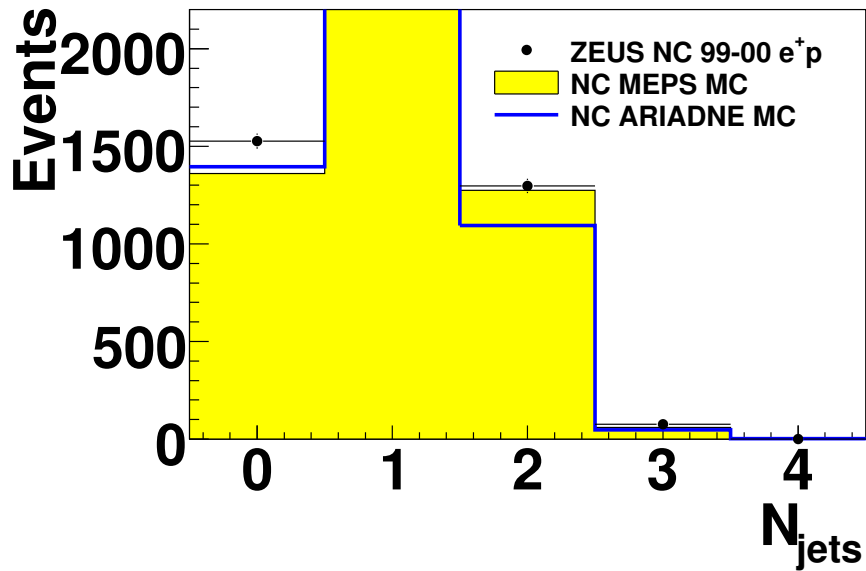


Figure 4.28: Comparison of NC MCs distributions (histograms) with 99-00 e^+p data (points) for the number of reconstructed jets N_{jets} . The histogram is for MEPS MC and the line is for ARIADNE MC. The MC distributions are normalized to the luminosity of the data. ARIADNE MC expects about 20% less events in two jets events.

Chapter 5

The cross section measurement

5.1 Cross section unfolding method

In a perfect detector with 100% acceptance over the accepted fiducial region and no background, the measured cross section σ would simply be:

$$\sigma = \frac{N}{\mathcal{L}}, \quad (5.1)$$

where N is the number of detected events and \mathcal{L} is the integrated luminosity of the data sample. However, in reality, the detector has limited resolution and acceptance. Also there are background events, so the cuts are used to remove them. Due to the limited acceptance of detector and the analysis selection, only a subset of the true events is used for the cross section measurement. In addition, the finite resolution leads to smearing of calculated kinematic variables and hence migration of variables to different value.

So the number of measured data events is not equal to the number of true events. The method used to estimate the true quantities from the measured quantities is called unfolding, a process that relate the measured probability density function to the true one with a transfer function. In practice, the kinematic region is divided into bins. If the net event migrations from or into a bin are small and bin to bin correlations are negligible, the numbers of reconstructed data events N_i^{data} and number of true data events N_i^{true} in a bin are simply related by a constant A_i

$$N_i^{data} = A_i \cdot N_i^{true}. \quad (5.2)$$

Equation 5.2 holds for MC as well:

$$N_{rec,i}^{MC} = A_i \cdot N_{gen,i}^{MC}, \quad (5.3)$$

where $N_{rec,i}^{MC}$ is the number of MC events reconstructed in this bin and $N_{gen,i}^{MC}$ is the number of MC events generated in this bin. Note that the A_i is taken to be the same as in Eq. 5.2. I.e., the Monte Carlo simulation is assumed to be reproduce the detector acceptance and resolution correctly. So Eq. 5.2 is written as:

$$N_i^{true} = N_i^{data} \cdot \frac{N_{gen,i}^{MC}}{N_{rec,i}^{MC}}. \quad (5.4)$$

This method is the so called bin-by-bin unfolding method used in this analysis. It has the advantage of being simple, but it does not take the information from neighbor bins to derive the cross section for a given bin. So the cross section in bin i is given by

$$\sigma_i = \frac{N_i^{true}}{\mathcal{L}} = \frac{N_i^{data}}{\mathcal{L}} \cdot \frac{N_{gen,i}^{MC}}{N_{rec,i}^{MC}}. \quad (5.5)$$

As mentioned in Sect. 2.3.1, the electroweak radiative effect is already included in the MC. To get the Born level cross section σ_i^{Born} , another correction must be applied:

$$\sigma_i^{Born} = \sigma_i \cdot \frac{N_{gen,i}^{MC,Born}}{N_{gen,i}^{MC}} = \frac{N_i^{data}}{\mathcal{L}} \cdot \frac{N_{gen,i}^{MC,Born}}{N_{rec,i}^{MC}}, \quad (5.6)$$

where $N_{gen,i}^{MC,Born}$ is the number of events generated in this bin by a MC generated with the Born level cross section. With the assumption that the MC describes the measured cross section shape very well, the differential cross section can be calculated at a certain specified quoted value X_{quote} (this parameter can be Q^2 , x or y in either the single or double differential cross section) in the bin, usually in the bin center, by correcting the σ_i^{Born} :

$$\frac{d\sigma^{Born}}{dX}(X_{quote}) = \sigma_i^{Born} \cdot \frac{\frac{d\sigma^{SM,Born}}{dX}(X_{quote})}{\int_{bini} \frac{d\sigma^{SM,Born}}{dX}(\tilde{X})d\tilde{X}}. \quad (5.7)$$

The ratio of the differential cross section to the integral cross section at the Born level is thus obtained from the Standard Model (SM). The SM predicted cross section must use

the same parton density function as in the of MC simulation. Since the MC is always reweighted to the data luminosity \mathcal{L} ,

$$\int_{bini} \frac{d\sigma^{SM,Born}}{dX}(\tilde{X})d\tilde{X} = \frac{N_{gen,i}^{MC,Born}}{\mathcal{L}}. \quad (5.8)$$

It follows from Eq. 5.6 and 5.7, the measured cross section is most simply unfolded as:

$$\frac{d\sigma^{Born}}{dX}(X_{quote}) = \frac{N_i^{data}}{N_{rec,i}^{MC}} \cdot \frac{d\sigma^{SM,Born}}{dX}(X_{quote}). \quad (5.9)$$

One advantage of this method is that the cross section measured from the integral over the bin can be quoted at a single value of X_{quote} if the dependence of the theoretical cross section agrees well with measured cross section, so long as the quoted value is within the bin. As mentioned before, this unfolding method neglects the correlations between bins. These bin to bin correlations are estimated in the systematic uncertainty checks.

5.2 Binning definition

In the unfolding method, the cross section is measured in a set of bins throughout the kinematic region. The maximum amount of information on the shape of a PDF is obtained by making as many bins as possible. On the other hand, very small bin size leads to the large migrations from neighboring bins because of the finite resolution. Thus a balance must be reached between the cross section in many bins with large bin-to-bin migrations and too few bins with limited knowledge of the cross section shape in binning definition. Here we choose bin widths about three times the resolution except for large x , which are defined separately.

The two kinematic variable used in this analysis are Q^2 and x . The reconstructed Q^2 and x are compared with the true values in Monte Carlo to estimate the reconstruction resolution. The Q_{true}^2 and x_{true} values are calculated from the MC true information. The Q_{rec}^2 and x_{rec} values are the MC reconstructed value following the same method mention in Sect. 3.2. The differences between the true and reconstructed values are shown as a function of the true values. The error bar is the RMS of the distribution in

each true value bin. The points in Fig. 5.1 show that the bias of the reconstructed Q^2 is within 1% of the true Q^2 and the error bars give $\approx 5\%$ resolution in the whole Q^2 region of this analysis. Figure 5.2 shows that the bias of x is about 3%. The resolution is big at $x < 0.04$ and decreases to 5% at $x = 0.6$. The bias is much smaller than the resolution for Q^2 and x .

Due to different proton beam energies in different running periods (820 GeV before 1998 and 920 GeV after), the kinematic regions for the cross section measurements are different. Figure 5.3 shows the isolines for $y = 1$, $E'_e = 25$ GeV and $\theta_{\text{jet}} = 0.12$ rad for 96-97 and 98-00 data. The kinematic region shifts to higher x for the 96-97 data. So different bin sets for 96-97 and 98-00 data are required. The bin definitions used in this analysis are given in Fig 5.4. The Q^2 bin widths were chosen to correspond to three times the resolution of the reconstructed Q^2 . The minimum value of Q^2 corresponds roughly to the acceptance of the BCAL. The lower x edge of the bin for zero jet events, x_{edge} , is determined from the condition $\theta_{\text{jet}} > 0.12$ rad where a jet is expected to be observed. For the bins where a jet is reconstructed, the x bin widths were chosen to correspond to three times the resolution of the reconstructed x . The lowest x bin edge is at 0.04 to avoid the poor x resolution.

Care was taken to understand these cases where the jet was unobserved, and so only a lower limit could be placed on the x variable. The MC simulation was used to study the x distribution of the zero jet events assigned to the highest x bin. We showed in Fig. 4.21 the true x distribution for the zero jet 99-00 e^+p MC events in different Q^2 bins, which should be in the high x bins for a perfect detector. Similar distributions are observed in the 98-99 e^-p and 96-97 e^+p MC. As can be seen in this figure, the zero jet events predominantly originate from the interval $x_{\text{edge}} < x < 1$. We note that these distributions depend somewhat on the particular PDF chosen and that there are some uncertainties at large x .

The quality of the bins can be expressed in terms of efficiency and purity. The efficiency is defined as the number of events generated and reconstructed in a bin after all selection cuts divided by the number of events that were generated in that bin. The efficiency

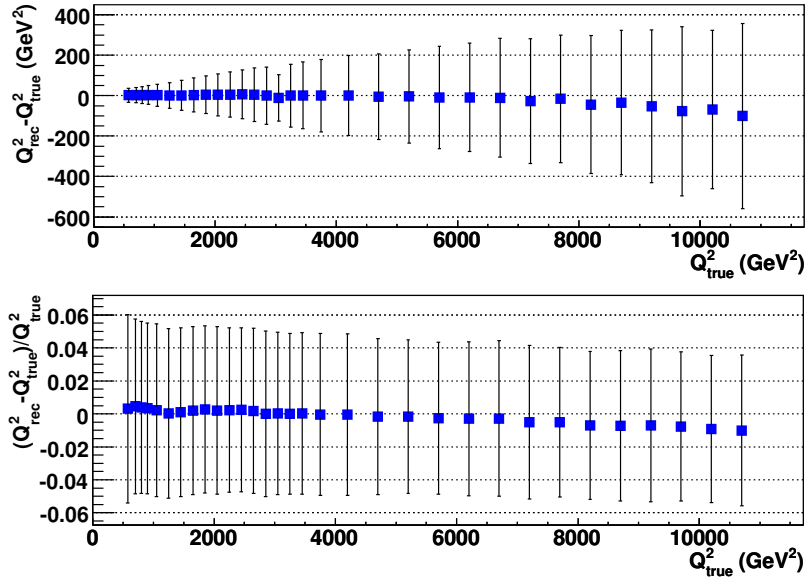


Figure 5.1: The resolution of Q^2 which is reconstructed from the electron energy and angle for 99-00 MC, the error bar is the RMS of Gaussian fit. The resolution of Q^2 calculated from electron method is about 5% in all Q^2 region.

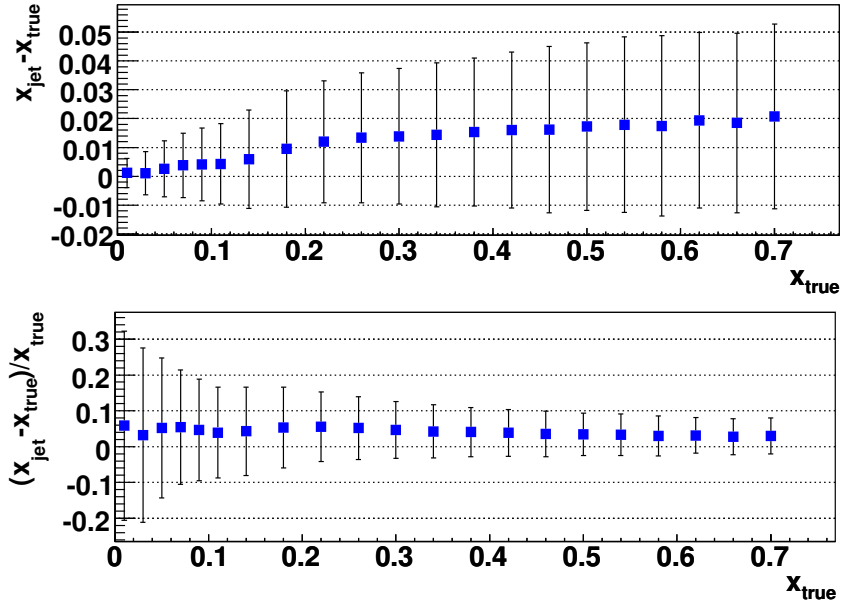


Figure 5.2: The resolution of x which is reconstructed from jet energy and angle for 99-00 MC, the error bar is the RMS of Gaussian fit. As x increases, the resolution is better.

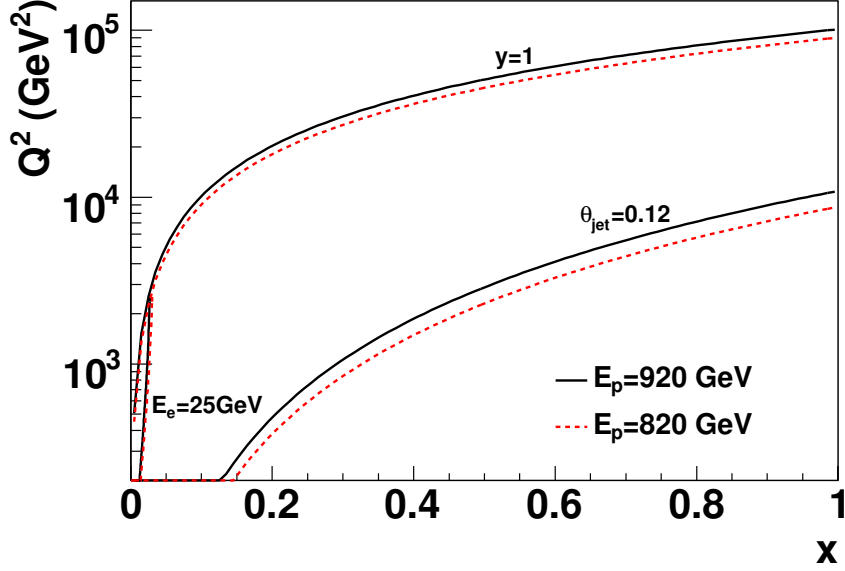


Figure 5.3: *Isoline for $y = 1$, $E'_e = 25$ GeV and $\theta_{\text{jet}} = 0.12$ rad for $E_p = 820$ GeV and $E_p = 920$ GeV in $x - Q^2$ plane. At same Q^2 , the jet with same jet angle θ_{jet} has higher x for $E_p = 820$ GeV.*

in a single bin can be reduced by the acceptance of the detector, the trigger, the offline selection or migration to other bins. The purity is defined as the number of events generated and reconstructed in a bin after all selection cuts divided by the total number of events reconstructed in that bin. Purity is strongly correlated to bin to bin migration. Low purity means most of events reconstructed in the bin were generated elsewhere. The MC is used to estimate both efficiency and purity. The efficiency varied between 35% and 60%. In some low- Q^2 bins, where the electron is scattered into the RCAL or the B/RCAL transition region and often removed by the fiducial cut, the efficiency decreases to around 12%. The purity ranges from 40% to 60%, a range quite reasonable for bin sizes chosen to be of order of the resolution. The efficiency and purity in $x - Q^2$ bins for 99-00 e^+p are shown in Fig. 5.5. The 96-97 e^+p and 98-99 e^-p simulation yield similar values. The efficiency and purity in the zero jet bins are comparable to the mid- x bins.

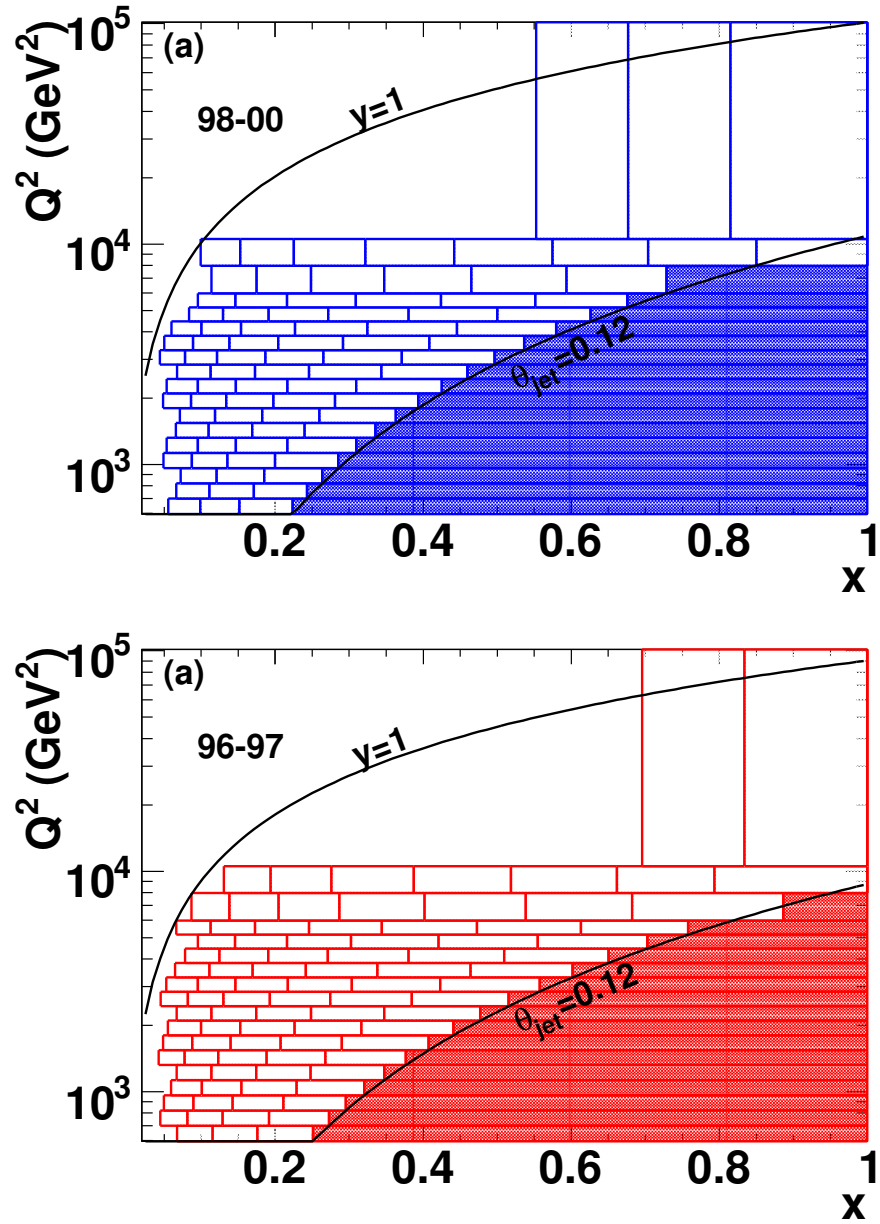


Figure 5.4: Definition of the bins as used in this analysis for: (a) 98-00 data with $E_p = 920 \text{ GeV}$ and (b) 96-97 data with $E_p = 820 \text{ GeV}$. The shaded bins extending to $x = 1$ are for the zero jet events. The $y = 1$ lines shows the kinematic limit. The $\theta_{\text{jet}} = 0.12$ rad shows the selection cut for jets.

ZEUS

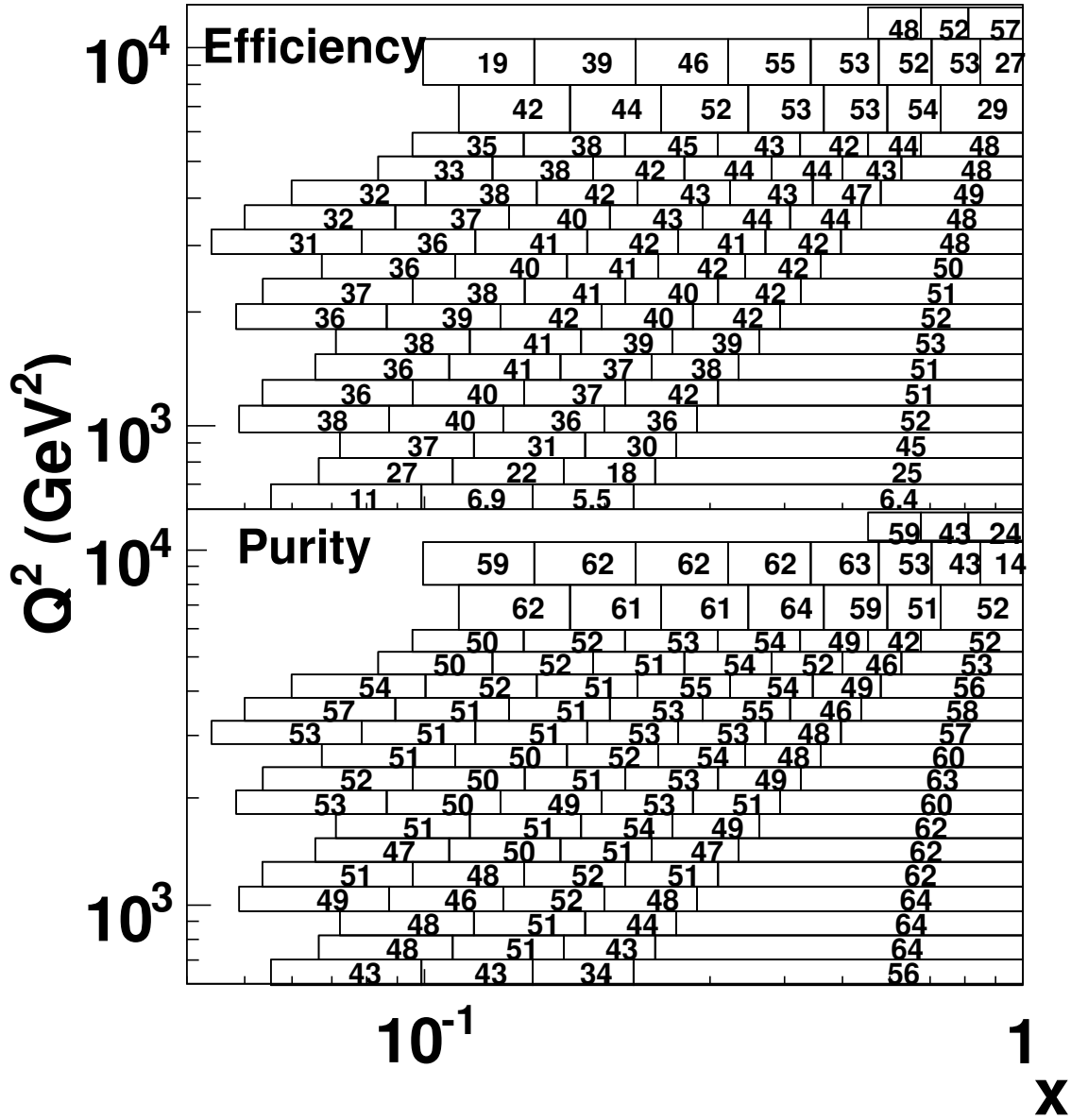


Figure 5.5: The efficiency and purity in % for each bin for 99 – 00 e^+p are shown.

5.3 Cross section measurement

From Eq.5.9 the double differential cross section for the bins at low x was determined as:

$$\frac{d^2\sigma_{\text{Born}}(x, Q^2)}{dx dQ^2} = \frac{N_{\text{data}}(\Delta x, \Delta Q^2)}{N_{\text{MC}}(\Delta x, \Delta Q^2)} \frac{d^2\sigma_{\text{Born}}^{\text{SM}}}{dx dQ^2} (1 + \delta(Q^2)), \quad (5.10)$$

and the integrated cross section in the wide highest x bins was determined as:

$$\int_{x_{\text{edge}}}^1 \frac{d^2\sigma_{\text{Born}}(x, Q^2)}{dx dQ^2} dx = \frac{N_{\text{data}}(\Delta x, \Delta Q^2)}{N_{\text{MC}}(\Delta x, \Delta Q^2)} \int_{x_{\text{edge}}}^1 \frac{d^2\sigma_{\text{Born}}^{\text{SM}}}{dx dQ^2} dx (1 + \delta(Q^2)), \quad (5.11)$$

where $N_{\text{data}}(\Delta x, \Delta Q^2)$ is the number of data events in a bin $(\Delta x, \Delta Q^2)$ and $N_{\text{MC}}(\Delta x, \Delta Q^2)$ is the number of signal MC events normalized to the luminosity of the data. The SM prediction, $d^2\sigma_{\text{Born}}^{\text{SM}}(x, Q^2)/dx dQ^2$, was evaluated according to (1.8) with the same PDF as used in the MC simulation and using the PDG values [55] for the fine-structure constant, the mass of the Z boson and the weak mixing angle. As mentioned before, this procedure corrects for the acceptance, bin-centering and leading order radiative corrections with the MC simulation. The small dependence of the cross sections resulting on different choices of PDF in the MC are described in the next section.

The parameter $\delta(Q^2)$ corrects for orders of the radiative correction higher than used in MC. Studies indicated that the radiative corrections generally do not affect the evaluation of x for the kinematic reconstruction method used here. Figure 5.6 shows that the difference of the cross section calculated from the MC, including the leading radiative correction $0(\alpha)$, relative to the Born cross section as a function of x for different Q^2 . The plot shows no significant dependence on the x calculated from jet information, as we use. With the assumption that higher order effects, not in our standard MC, also do not depend dramatically on x , $\delta(Q^2)$ can be calculated directly from HECTOR [56]. HECTOR includes two different programs to calculate the radiative correction: HELIOS and TERAD. HELIOS calculates QED radiative correction in the leading logarithm approximation in the $0(\alpha)$ and higher order including the soft photon exponentiation. TERAD calculates the complete QED and weak radiative correction in the leading order. The leading order

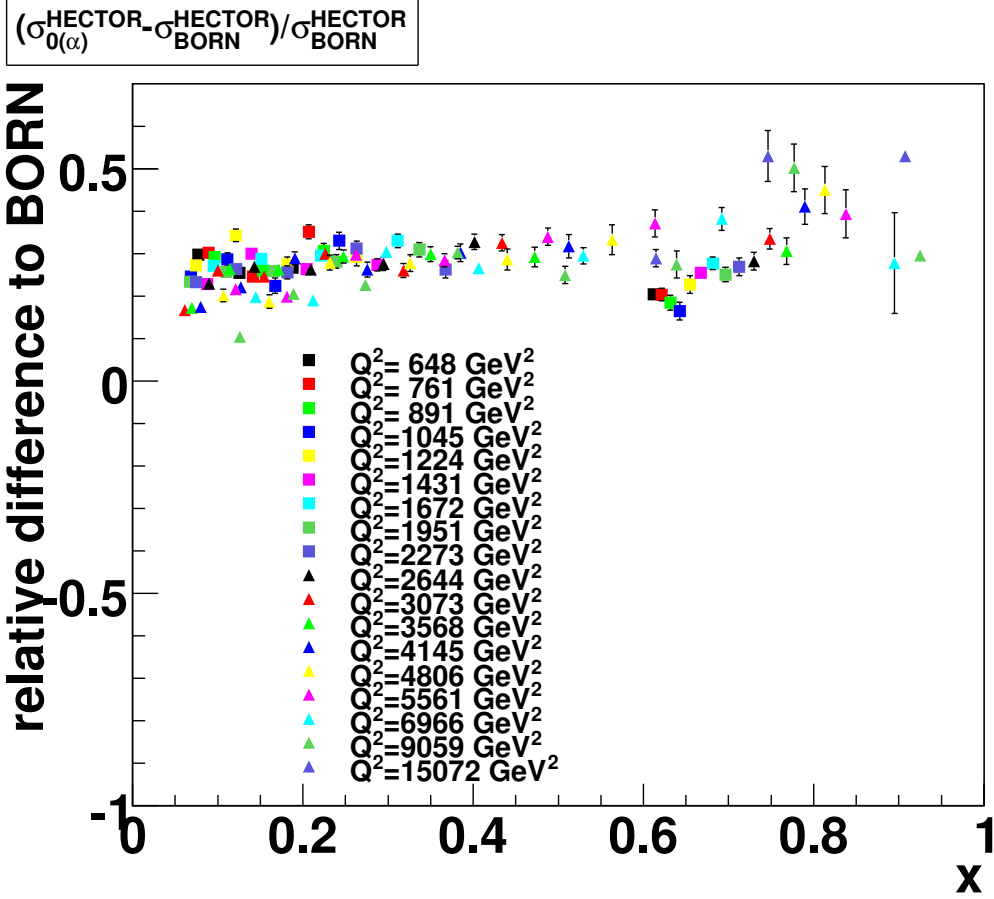


Figure 5.6: *The relative difference of cross section calculated from HERACLES MC to the Born cross section in all the bins as a function of x . The HERACLES includes the leading order radiative correction. The HERACLES cross section was calculated on MC true electron and jet information, where exact same reconstruction method as in the analysis was used. The true jet finder was done on the final state particles. For the event with zero or two jets, x is calculated from the struck quark. This study shows no dramatic dependence of radiation correction on x from jet method.*

radiative correction calculated from two programs agrees quite well. Figure 5.7 shows that the correction varied from 3% at low Q^2 to 0% at high Q^2 . The remaining x difference between higher order calculations seen in Fig. 5.6 were taken as a correlative systematic uncertainty and included in Sect. 5.4.2.

The statistical uncertainty of the measured cross section is given by the statistical uncertainty of the number of data events $N_{\text{data}}(\Delta x, \Delta Q^2)$ since the statistical uncertainty of the number of MC events $N_{\text{MC}}(\Delta x, \Delta Q^2)$ is negligible. The statistical uncertainty on the

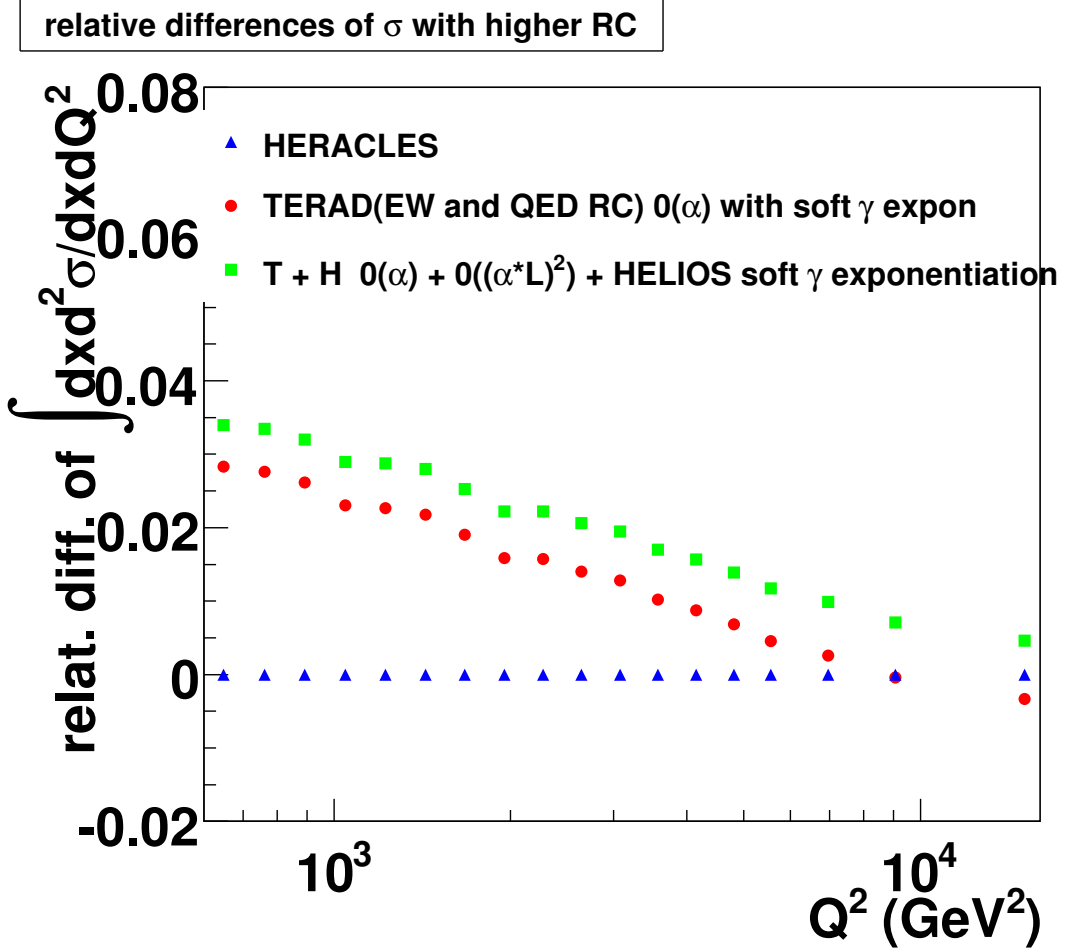


Figure 5.7: *The relative difference of cross section in higher radiation correction orders to the HERACLES cross section as a function of Q^2 . The first and the second order radiation correction with soft photon exponentiation calculated from HECTOR compared with cross section from HERACLES. Soft photon exponentiation is not included in HERACLES.*

cross section is calculated with the Bayesian approach:

$$P(\sigma|N_{data}) = \frac{P(N_{data}|\sigma)P_0(\sigma)}{\int P(N_{data}|\sigma)P(\sigma)d\sigma} \quad (5.12)$$

with the probability function $P_0(\sigma)$, the prior distribution, chosen to be flat:

$$P(\sigma) = constant, \quad (5.13)$$

where σ is the true cross section and N_{data} is the reconstructed number of events. The probability function $P(N_{data}|\sigma)$ gives the probability of measuring N_{data} events when the

true cross section is σ and $\int P(N_{\text{data}}|\sigma)P_0(\sigma)d\sigma$ is the normalization constant. Equation 5.12 shows how to calculate the probability of the true cross section with N_{data} reconstructed events. A Gaussian probability function for $P(N_{\text{data}}|\sigma)$ is used for bins with $N_{\text{data}}(\Delta x, \Delta Q^2) > 100$:

$$P(N_{\text{data}}|\sigma) = \frac{1}{\sqrt{2\pi N_{\text{true}}}} e^{-\frac{(N_{\text{data}} - N_{\text{true}})^2}{2N_{\text{true}}}}, \quad (5.14)$$

where N_{true} is the true number of events in this bin. N_{true} is calculated from the true cross section $N_{\text{true}} = K \cdot \sigma$, where K is a constant in this bin including the acceptance and luminosity effects. Similarly the Poisson function was used for bins with $N_{\text{data}}(\Delta x, \Delta Q^2) < 100$:

$$P(N_{\text{data}}|\sigma) = \frac{e^{-K \cdot \sigma} (K \cdot \sigma)^{N_{\text{data}}}}{N_{\text{data}}!}. \quad (5.15)$$

The uncertainties are calculated by taking the central 68% probability interval level (CL) for the bin with more than zero reconstructed events:

$$0.16 = \int_0^{\sigma_L} P(\sigma|N_{\text{data}})d\sigma = \int_{\sigma_U}^{\infty} P(\sigma|N_{\text{data}})d\sigma. \quad (5.16)$$

The central value σ_c is taken to be the mode of the probability distribution. The statistical uncertainties are $\sigma_U - \sigma_c$ and $\sigma_c - \sigma_L$ for this bin. For the bin with zero reconstructed event, the 68% upper limit σ_{UL} is calculated with the Poisson probability function by:

$$0.68 = \int_0^{\sigma_{UL}} P(\sigma|N_{\text{data}})d\sigma. \quad (5.17)$$

Note that typically statistical uncertainties on data range from 5% to 20%.

5.4 Systematic uncertainties

Systematic uncertainties associated with the MC simulations were estimated by re-calculating the cross section after modifying the input parameter to the simulation by amount corresponding to the known uncertainty. Where this method was not applicable, cut values

were appropriately varied. In general, the analysis was repeated for each source of systematic uncertainty, with the difference between the cross section from the check and the normal one taken as the systematic uncertainty.

5.4.1 Uncorrelated systematic uncertainties

The following systematic uncertainties are either small or exhibit no bin-to-bin correlations. Figure 5.8 and 5.9 show the uncorrelated systematic uncertainties from different checks as the functions of x in one jet bins, and zero jet bins, respectively. The sources of uncertainty in this category are:

- electron energy resolution in the MC simulation: the effect on the cross sections was evaluated by changing the resolution by about 1% in the MC. It resulted in $\sim \pm 1\%$ effects over almost the full kinematic range. The effect increased to about $\pm 2\%$ for double differential cross section in several low Q^2 bins and integral cross section in several of the highest x bins;
- electron angle: uncertainties in the electron scattering angle determination are known to be at most 1 mrad [19]. The resulting systematic effects to the cross section measurement were at most 2%;
- electron isolation requirement: variation of the electron isolation energy in the cone around the electron direction, E_{cone} by ± 2 GeV caused negligible effects in the low Q^2 region and typically 2.5% or less in the high Q^2 region on the cross section;
- FCAL alignment: the FCAL jet position was varied by ± 0.5 cm in both the x and y directions. The resulting changes in the cross sections were negligible;
- background estimation: the cut on the reconstructed Z vertex was changed by ± 2 cm. The uncertainties in the cross sections associated with this variation were negligible over the full kinematic range.

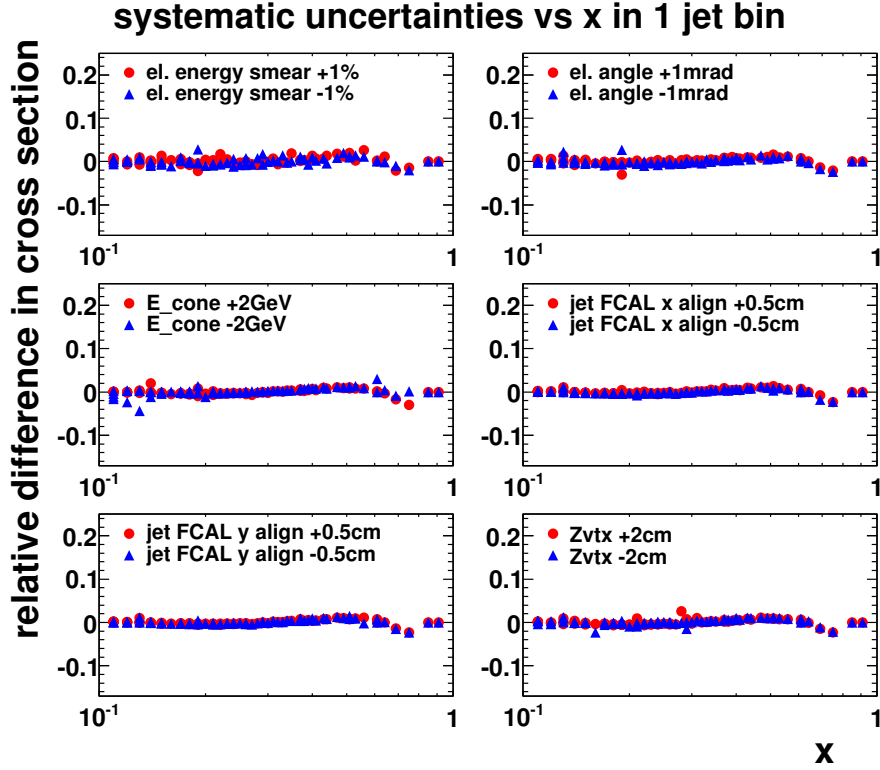


Figure 5.8: *The uncorrelated systematic uncertainties versus x for one jet bins in different checks. All these uncertainties are small.*

5.4.2 Correlated systematic uncertainties

The following systematic uncertainties are correlated from bin-to-bin. They are labeled for further reference. δ_1 to δ_3 are shown in Fig. 5.13 and 5.14.

The correlated systematic uncertainties are:

- $\{\delta_1\}$ electron energy scale: As mentioned in Sect.3.3.2, the uncertainty of the electron energy scale is 1% in BCAL and FCAL. The systematic uncertainty resulting from uncertainty in the electron energy scale was checked by changing the energy scale by $\pm 1\%$ in the MC. This resulted in 0 – 5% systematic variations in the cross section from $Q^2 = 600 \text{ GeV}^2$ to $Q^2 = 7000 \text{ GeV}^2$;
- $\{\delta_2\}$ jet energy scale: the relative uncertainty on the hadronic energy scale was found to be 1% in FCAL and BCAL and 2% in RCAL [20]. In the kinematic region this analysis focuses on, the jets are all in BCAL or FCAL. So the uncertainty in the cross

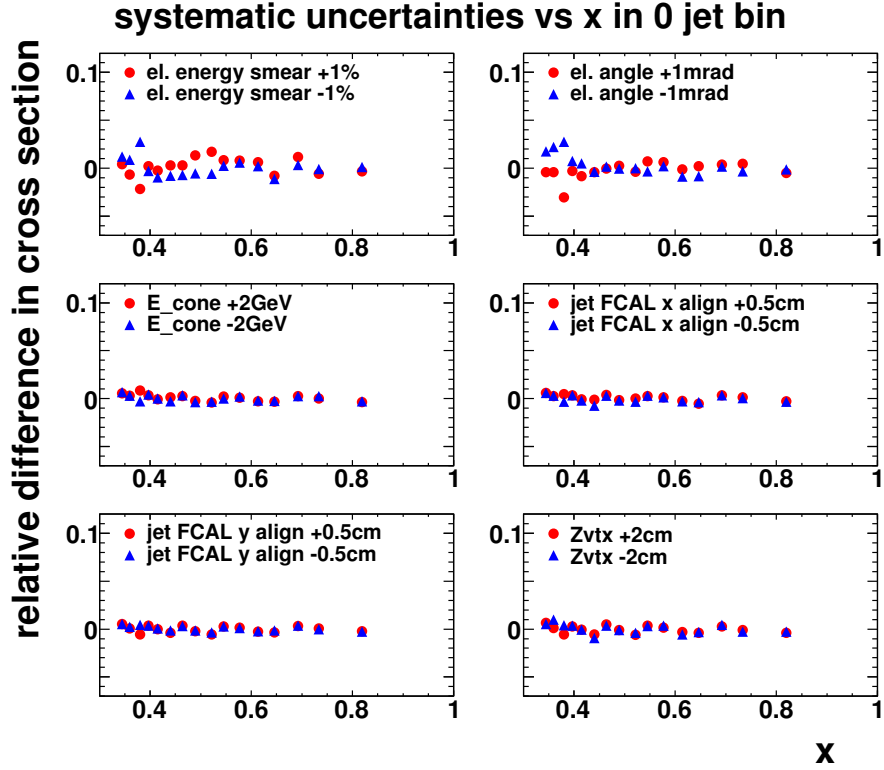


Figure 5.9: *The uncorrelated systematic uncertainties versus x for zero jet bins in different checks. All these uncertainties are small.*

sections arising from the measurement of the jet energy was checked by changing the energy scale by $\pm 1\%$ in the MC. The effect in the highest x bins is negligible over the full Q^2 region. The uncertainty in the double differential cross section bins is from 0 – 7% as x ranges from 0 to 0.7;

- $\{\delta_3\}$ FCAL first inner ring (FIR) EMC energy scale: The halo muon study [57] shows that the FIR EMC uncertainty is about 5%. The effect of the FIR EMC energy scale uncertainty on the cross section was checked by changing the energy scale by $\pm 5\%$, which gives 0 – 3.5% uncertainty as x increases from 0 to 0.9;
- $\{\delta_4\}$ different PDFs: the uncertainty in the extracted cross section resulting from uncertainties in the PDF at high x was checked by comparing the Born cross section calculated from different PDFs, CTEQ4D, CTEQ6D, MRST99, ZEUS-S and ZEUS-JET. The effect is less than 1% at low x and increased to 5% at high x ;

- $\{\delta_5\}$ simulation of the hadronic final state and jet selection procedure. The invariant k_T jet algorithm was replaced with the cone algorithm [50] with cone radius 0.7, and cross sections were re-evaluated. The comparisons between data and MC for jet variables with cone algorithm are shown in Fig. 5.10, 5.11 and 5.11. MC describes data as well as k_T algorithm for events with zero, one and two jets. The uncertainty was found to be $\pm 1.6\%$ in the highest x bins and $\pm 2.5\%$ in the lower x bins. In addition, the analysis was redone under the following conditions: including multijet events for the events with $x < x_{\text{edge}}$; choosing different jet E_T and θ_{jet} cuts for the jet selection; and varying the y_{JB} cut. These checks produced small differences consistent with expected statistical variations;

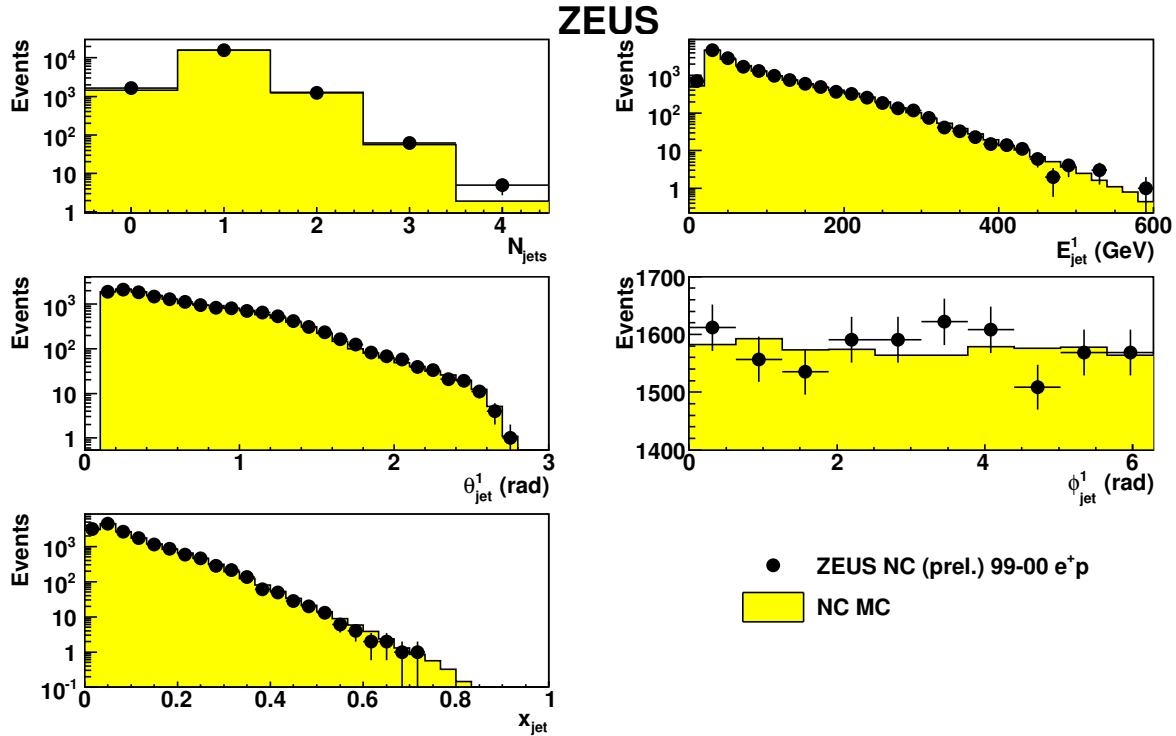


Figure 5.10: Comparison of NC MC distributions (histograms) with 99 – 00 e^+p data (points) with cone algorithm for: the number of reconstructed jets N_{jets} ; the energy of the leading jet E_{jet} ; the polar angle of the leading jet θ_{jet} ; azimuthal angle ϕ_{jet} and x calculated from the jet x_{jet} . The jet distributions are for one jet events. The MC distributions are normalized to the luminosity of the data.

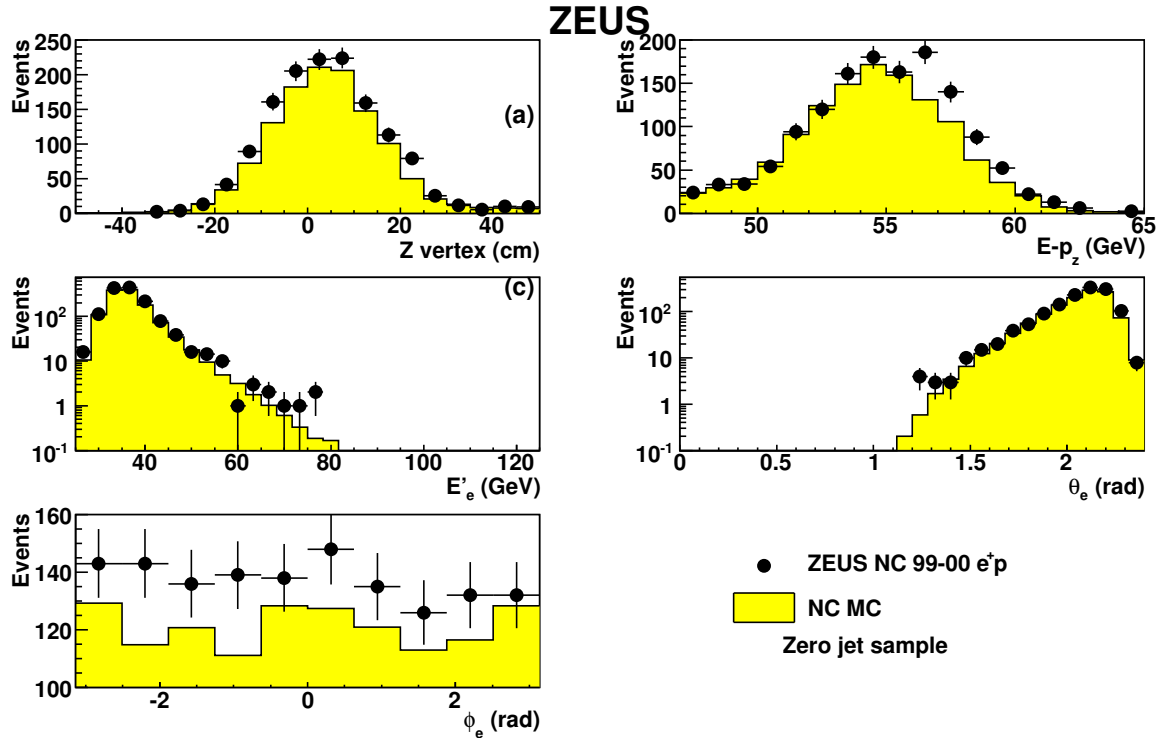


Figure 5.11: Comparison of NC MC distributions (histograms) with 99 – 00 e^+p data (points) for events with zero jets with cone algorithm. The plots show: the Z coordinate of the event vertex; $E - p_z$; E'_e ; θ_e and ϕ_e . The MC distributions are normalized to the luminosity of the data.

- $\{\delta_6\}$ higher order radiative corrections and a possible dependence on x : as discussed in Sect. 5.3, the uncertainty was estimated to be about 2% at low x increasing to 12% at $x > 0.8$;
- $\{\delta_7\}$ the uncertainties on the luminosity: the uncertainties for the 1996 e^+p sample, 1997 e^+p sample, 1998-1999 e^-p sample and 1999-2000 e^+p sample are 1.1%, 1.8%, 1.8% and 2.25% respectively.

All these systematic uncertainties are often much smaller or comparable to the statistical uncertainty. Figure. 5.15 and 5.16 show all the systematic uncertainties mentioned above in color points and the statistical uncertainty in solid lines.

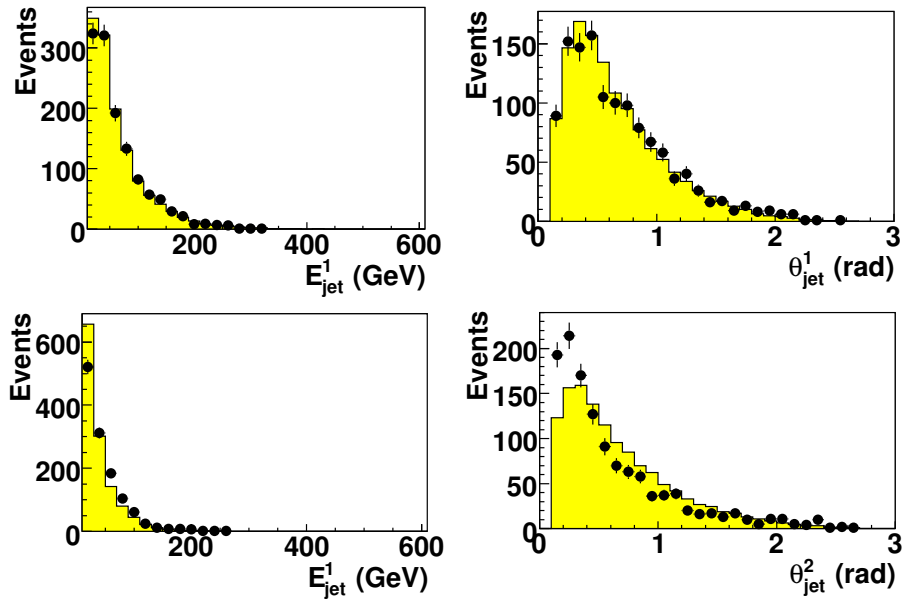


Figure 5.12: Comparison of NC MC distributions (histograms) with 99 – 00 e^+p data (points) with cone algorithm for E_{jet} and θ_{jet} for two jets events. E_{jet}^1 and θ_{jet}^1 are for the leading jet and E_{jet}^2 and θ_{jet}^2 are for the second jet. The MC distributions are normalized to the luminosity of the data. MC describes leading jet quite well.

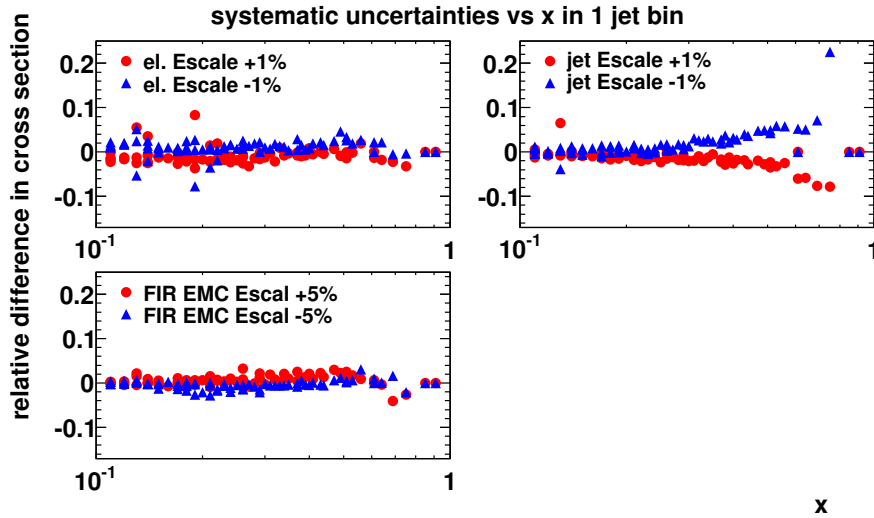


Figure 5.13: The correlated systematic uncertainties versus x for one jet bins in different checks.

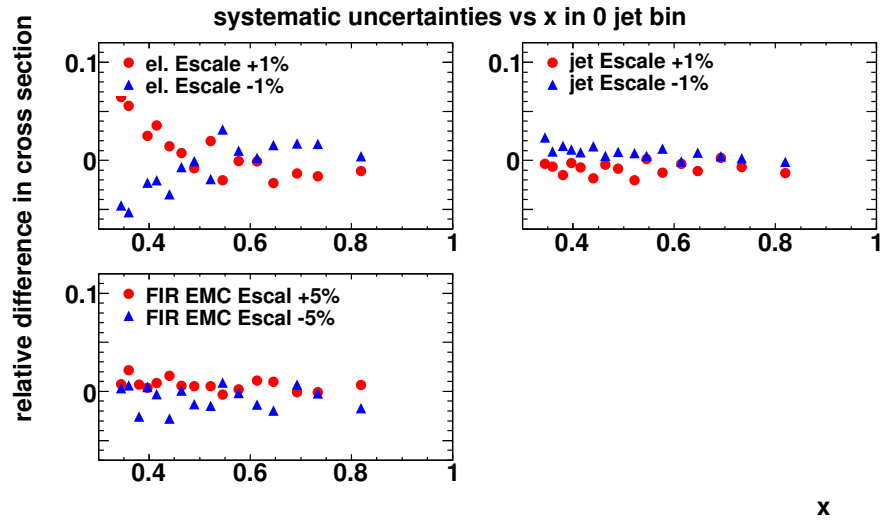


Figure 5.14: The correlated systematic uncertainties versus x for zero jet bins in different checks.

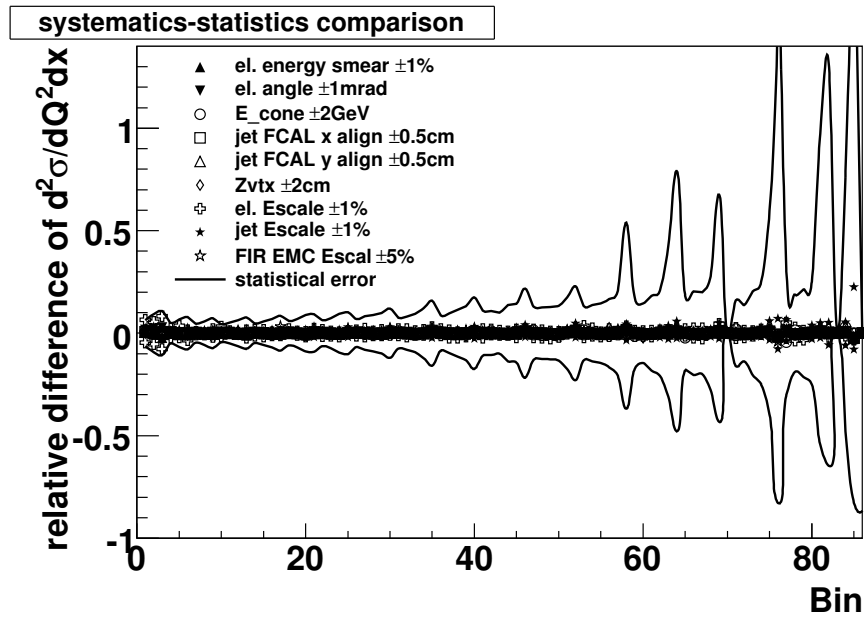


Figure 5.15: The systematic and statistical uncertainties in all the one jet bins. The color points are all the systematic uncertainties and the solid lines are the statistical uncertainty. Except several bins in the lowest Q^2 region, all the systematic uncertainties are smaller than the statistical uncertainties. The bin number is defined in Fig. 5.17.

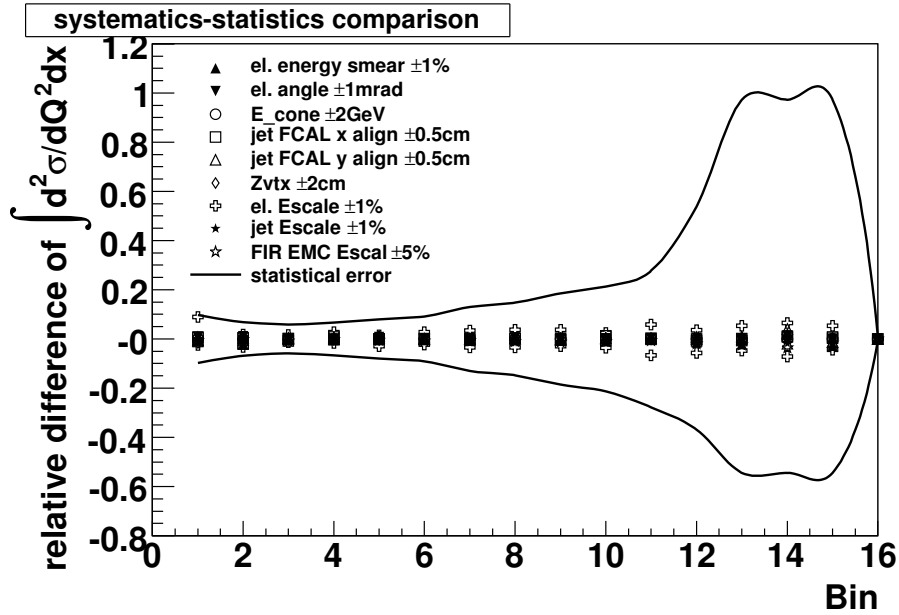


Figure 5.16: The systematic and statistical uncertainties in all the zero jet bins. The color points are all the systematic uncertainties and the solid lines are the statistical uncertainty. All the systematic uncertainties are smaller than the statistical uncertainties. The bin number is defined in Fig. 5.17.

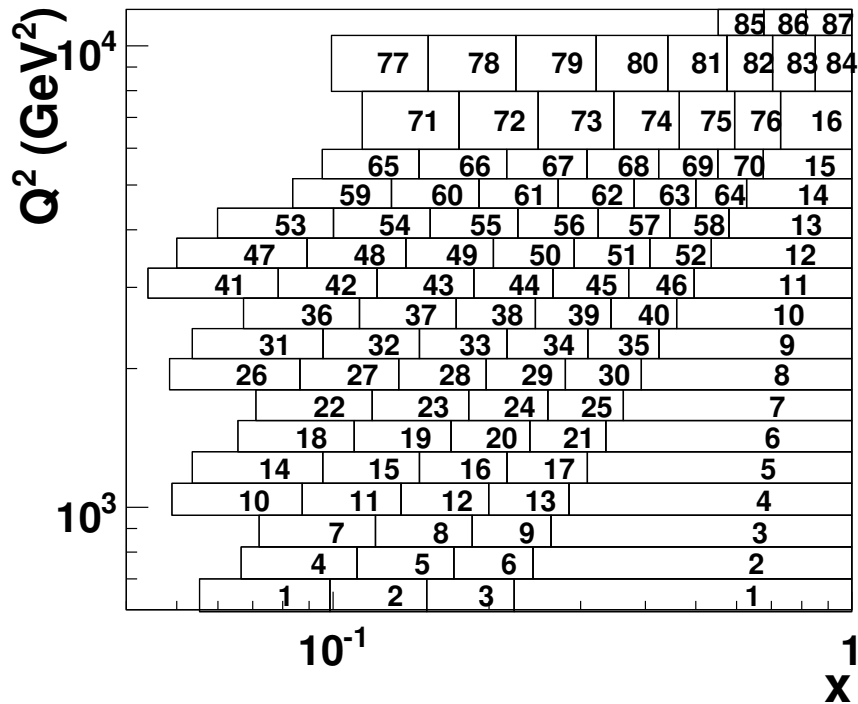


Figure 5.17: The definition of the cross section bin number.

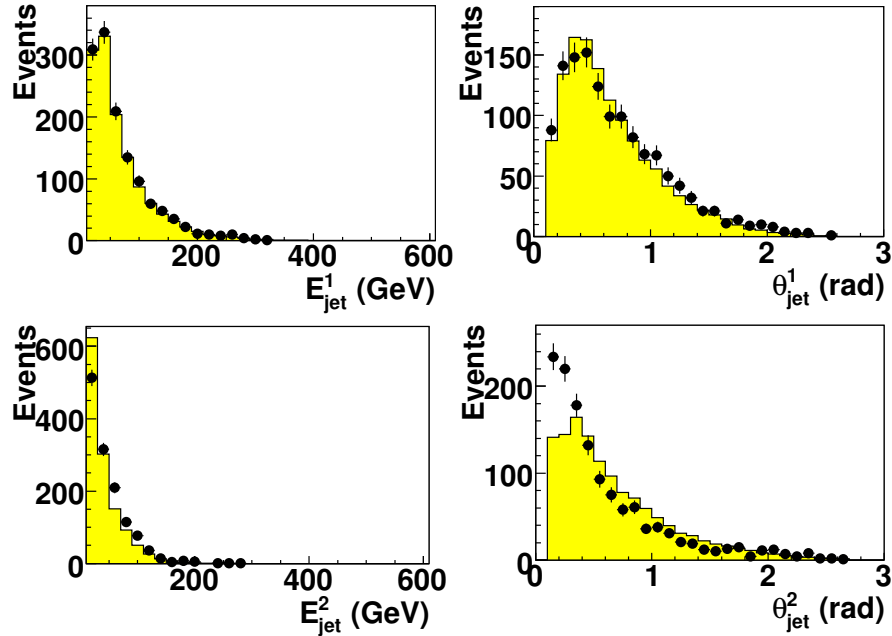


Figure 5.18: Comparison of NC MC distributions (histograms) with 99 – 00 e^+p data (points) for E_{jet} and θ_{jet} for two jets events. E_{jet}^1 and θ_{jet}^1 are for the leading jet and E_{jet}^2 and θ_{jet}^2 are for the second jet. The MC distributions are normalized to the luminosity of the data. MC describes leading jet quite well.

5.5 Other checks

5.5.1 Two jets events

As mention in Sect. 4.4.2, in the low x region, only one jet events are included to measure the cross section and this correction is done by MC. Figure. 4.24 shows that the number of jets is simulated very well by MC. The one jet events dominate in the whole DIS events sample and the number of two jets events are about ten times smaller. Since the events with more than two jets can be neglected, the correction for this should be tiny. The correction for the one jet events is mainly from the two jets. The properties of the two jet events are studied. Figure 5.18 show the energies and angles of the jets for the two jets events. MC describes the leading jet quite well. The cross section calculated with one and two jets events is compared to the original one. Figure 5.19 shows that the relative difference in cross section is typically smaller or comparable to the statistical uncertainty and there is no systematic trend.

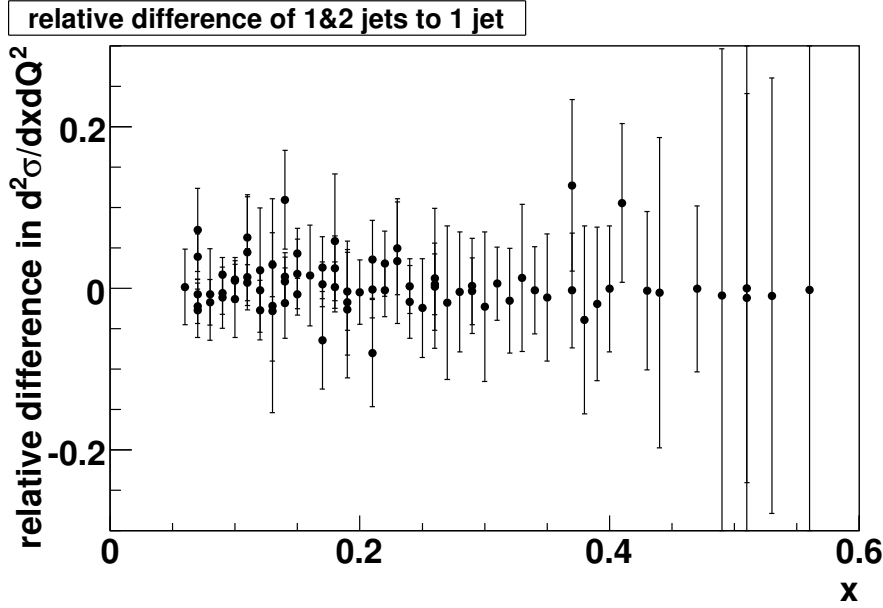


Figure 5.19: *The relative difference in cross section with one and two jets events compared to one jet events. The error bar is the relative statistical uncertainty due to including the two jets events, which is about 10% more events. The cross section fluctuation is typically smaller or comparable to the statistical uncertainty.*

5.5.2 Cut of y_{JB} on zero jet events

For the highest x bins, where the zero jet events are counted, the migration from low x is removed the $y_{JB} < 1.3 \cdot Q_{upperedge}^2 / (s \cdot x_{edge})$ cut mentioned in Sect. 4.4.3. This cut is the most significant cut to clean the purity up. The systematic check on this cut was done by varying 1.3 to 1.35 and 1.25. The effect in cross section is almost neglected as shown in Fig. 5.20.

5.5.3 Compare with the ZEUS published result

As a check, the reduced cross section, which is defined as:

$$\tilde{\sigma} = \frac{x Q^4}{2\pi\alpha^2 Y_+} \frac{d^2 \sigma_{\text{Born}}}{dx dQ^2} \quad (5.18)$$

was calculated using the new reconstruction in this method in the same bin structure as ZEUS previous published reduced cross section [18] in the overlapping kinematic region. Figure 5.21 shows the result and the ZEUS published value as a comparison. The reduced

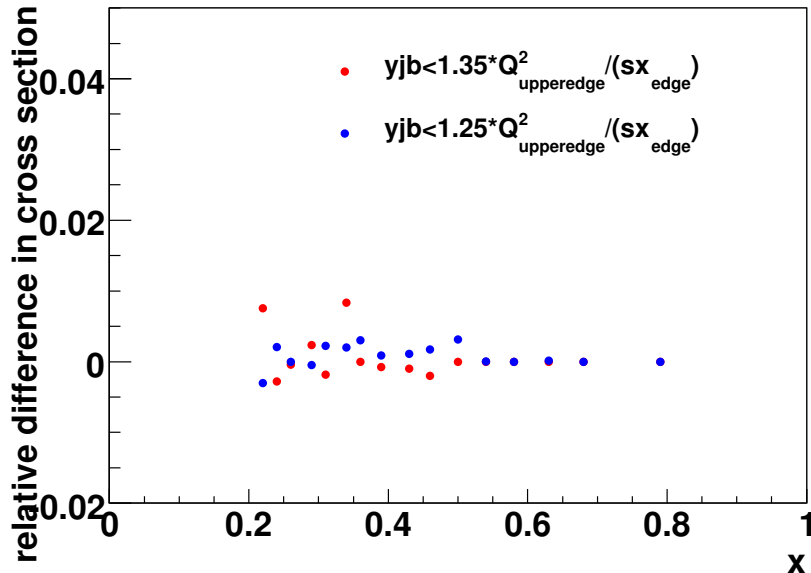


Figure 5.20: *The relative difference in cross section by changing 1.3 to 1.35 and 1.25 in y_{JB} cut.*

cross section in the two methods agree very well.

5.6 Results

5.6.1 Cross section

The measured Born level cross sections for 99-00 e^+p , 98-99 e^-p and 96-97 e^+p and their systematic uncertainties are collected in Tables B.1-B.6. The statistical errors on the cross sections have been evaluated using a Bayesian approach with flat prior distribution. For bins with zero measured events, a 68% probability limit, calculated including the uncorrelated systematic uncertainty, is given. The cross sections are shown in Fig. 5.22, Fig. 5.23 and Fig. 5.24 respectively and compared to SM expectations at NLO using the CTEQ6D PDFs [58]. The double differential cross sections are represented by solid points, and generally agree well with the expectations. The cross section in the highest x bin is plotted at the bin center as

$$\frac{1}{1 - x_{\text{edge}}} \int_{x_{\text{edge}}}^1 \frac{d^2\sigma_{\text{Born}}}{dx dQ^2} dx .$$

ZEUS

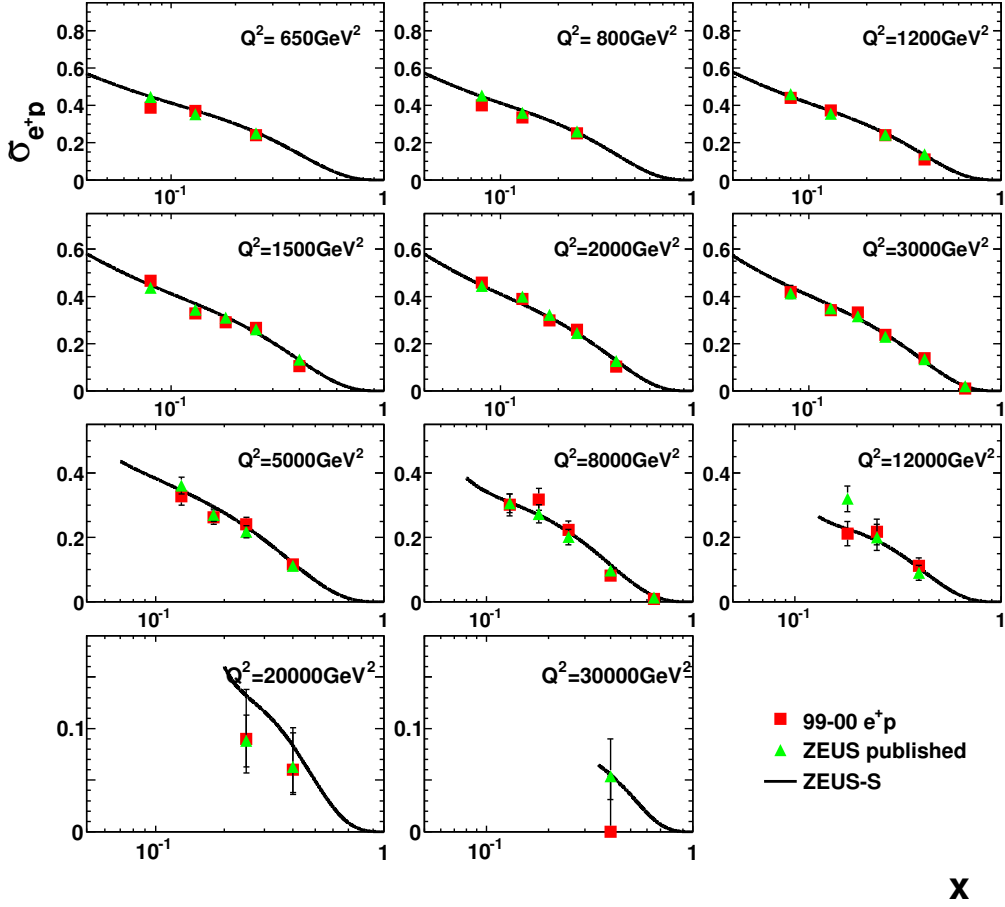


Figure 5.21: *The NC DIS reduced cross section for 99 – 00 e^+p calculated with the selection and reconstruction in the new method (square) compared to the value published by ZEUS (triangles) in the bin structure ZEUS published. The Standard Model expectations are evaluated with ZEUS-S PDF (lines). Only the statistical uncertainty is shown here. The two method agree quite well.*

In this bin, the expected cross section is drawn as a horizontal line, while the measured cross section is displayed as the open symbol. Though the measured data is plotted at the center of the bin, it should be understood to be an integrated cross section for the bin. The error bars represent the quadratic sum of the systematic and statistical uncertainties. For the bin with zero reconstructed event, the limit is drawn as an arrow downward and the tail is at the upper limit value.

The ratios of the measured cross sections to SM expectation using the CTEQ6D PDFs

for 96-97 e^+p , 98-99 e^-p and 99-00 e^+p are shown in Fig. 5.25, Fig. 5.26 and Fig. 5.27 respectively. The ratio of the expectation using the ZEUS-S PDFs [59] and ZEUS-JET PDFs [60] to that using CTEQ6D are also shown. The measured double differential cross sections generally agree well with all three sets of expectations. For the highest x bins, which are in previously unmeasured kinematic ranges, the data has a slight tendency to lie above the expectations.

The data presented here, specifically the “0-jet” data at high x , extend the kinematic coverage for DIS. An initial QCD fit [61] was performed using these new data to evaluate the impact on the PDFs at high x . The best fit cross sections are compared to the data in Fig. 5.28, and the comparison of the PDFs to previous ZEUS fits are shown in Fig. 5.29. These new data clearly have a significant effect, and pull the u_v density outside the previously estimated uncertainty band.

5.6.2 The structure function F_2

The measured NC DIS cross section in e^+p and e^-p can be used to extract the structure function. From Eq. 1.8, F_2 is written in the subtraction of the cross of e^+p and e^-p :

$$F_2 = \frac{xQ^4}{2\pi\alpha^2} \frac{1}{2Y_+} \left[\frac{d^2\sigma_{\text{Born}}(e^-p)}{dx dQ^2} + \frac{d^2\sigma_{\text{Born}}(e^+p)}{dx dQ^2} \right], \quad (5.19)$$

while combined with Eq. (5.10) $\int_{x_{\text{edge}}}^1 F_2 dx$ can be expressed as:

$$\int_{x_{\text{edge}}}^1 F_2 dx = \int_{x_{\text{edge}}}^1 \frac{1}{2} \left[F_2 + \frac{Y_-}{Y_+} x F_3 \right] dx \frac{N_{\text{data}}^{e^-}}{N_{\text{MC}}^{e^-}} + \int_{x_{\text{edge}}}^1 \frac{1}{2} \left[F_2 - \frac{Y_-}{Y_+} x F_3 \right] dx \frac{N_{\text{data}}^{e^+}}{N_{\text{MC}}^{e^+}}, \quad (5.20)$$

Note that the formula only holds when both data sets were recorded at the same center-of-mass energy. Figure 5.30 shows the combined F_2 calculated from 98–99 e^-p and 99–00 e^+p cross section plotted as a function of x in different Q^2 bins. The F_2 is represented by solid points, and in the highest x bin,

$$\frac{1}{1 - x_{\text{edge}}} \int_{x_{\text{edge}}}^1 F_2 dx$$

ZEUS

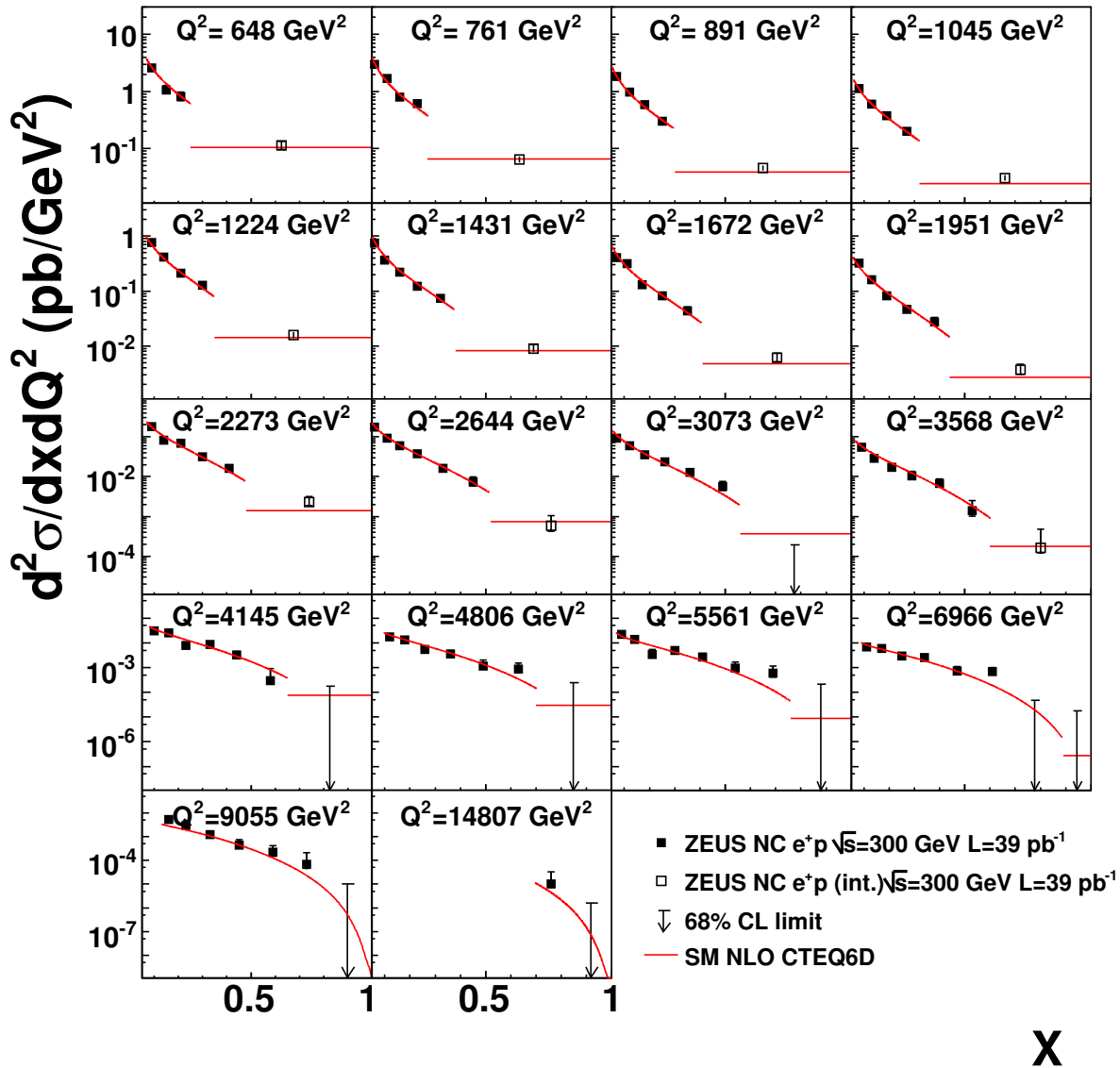


Figure 5.22: The double differential cross section for 96-97 e^+p NC scattering at $\sqrt{s} = 318$ GeV (solid squares) and the integral of the double differential cross section divided by the bin width (open squares) compared to the Standard Model expectations evaluated using CTEQ6D PDFs (lines). The inner error bars show the statistical uncertainty, while the outer ones show the statistical and systematic uncertainties added in quadrature. For bins with zero measured events, the 68% CL upper limit is given.

ZEUS

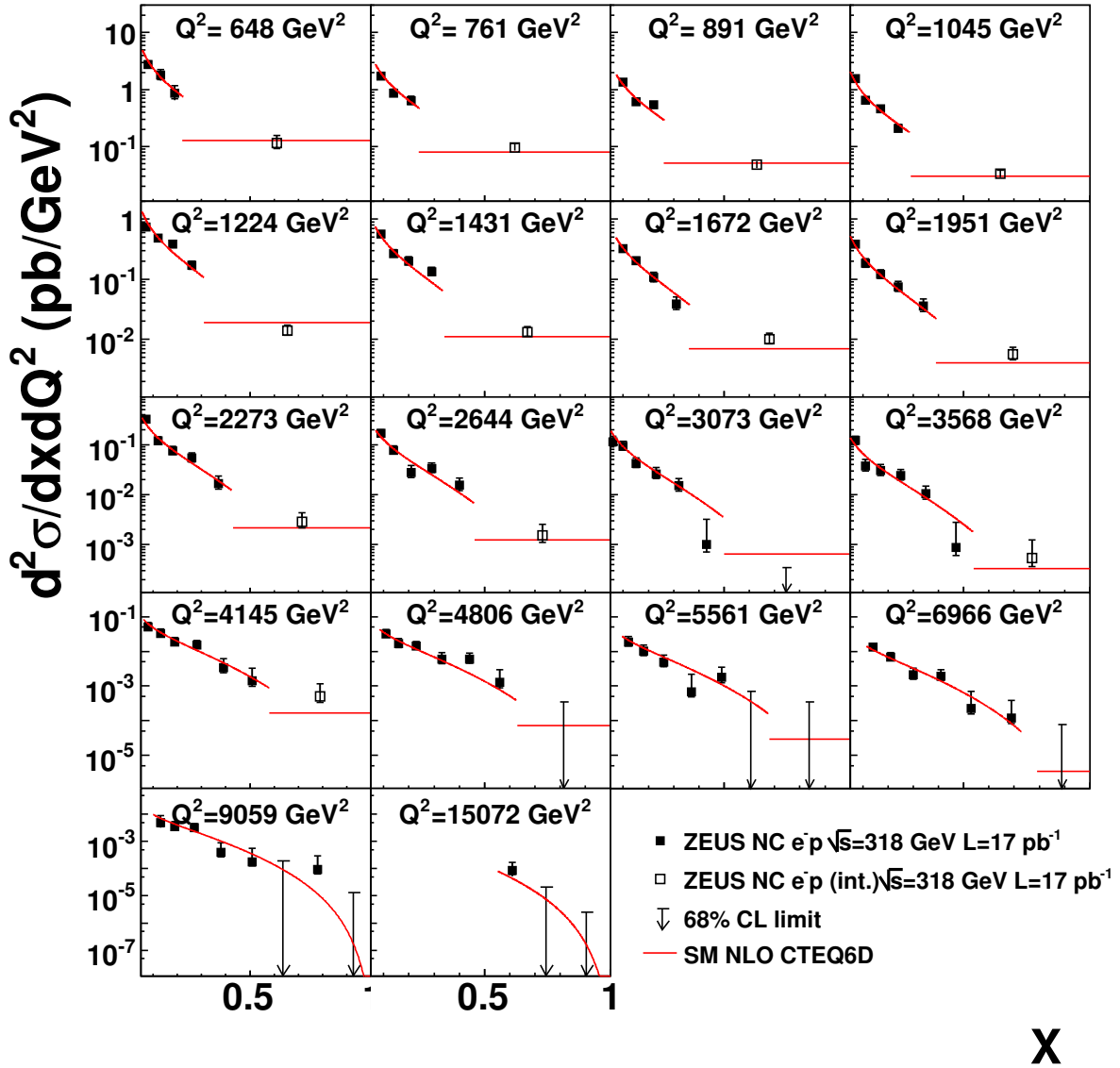


Figure 5.23: The double differential cross section for 98 – 99 e^-p NC scattering at $\sqrt{s} = 318$ GeV (solid squares) and the integral of the double differential cross section divided by the bin width (open squares) compared to the Standard Model expectations evaluated using CTEQ6D PDFs (lines). The inner error bars show the statistical uncertainty, while the outer ones show the statistical and systematic uncertainties added in quadrature. For bins with zero measured events, the 68% CL upper limit is given.

ZEUS

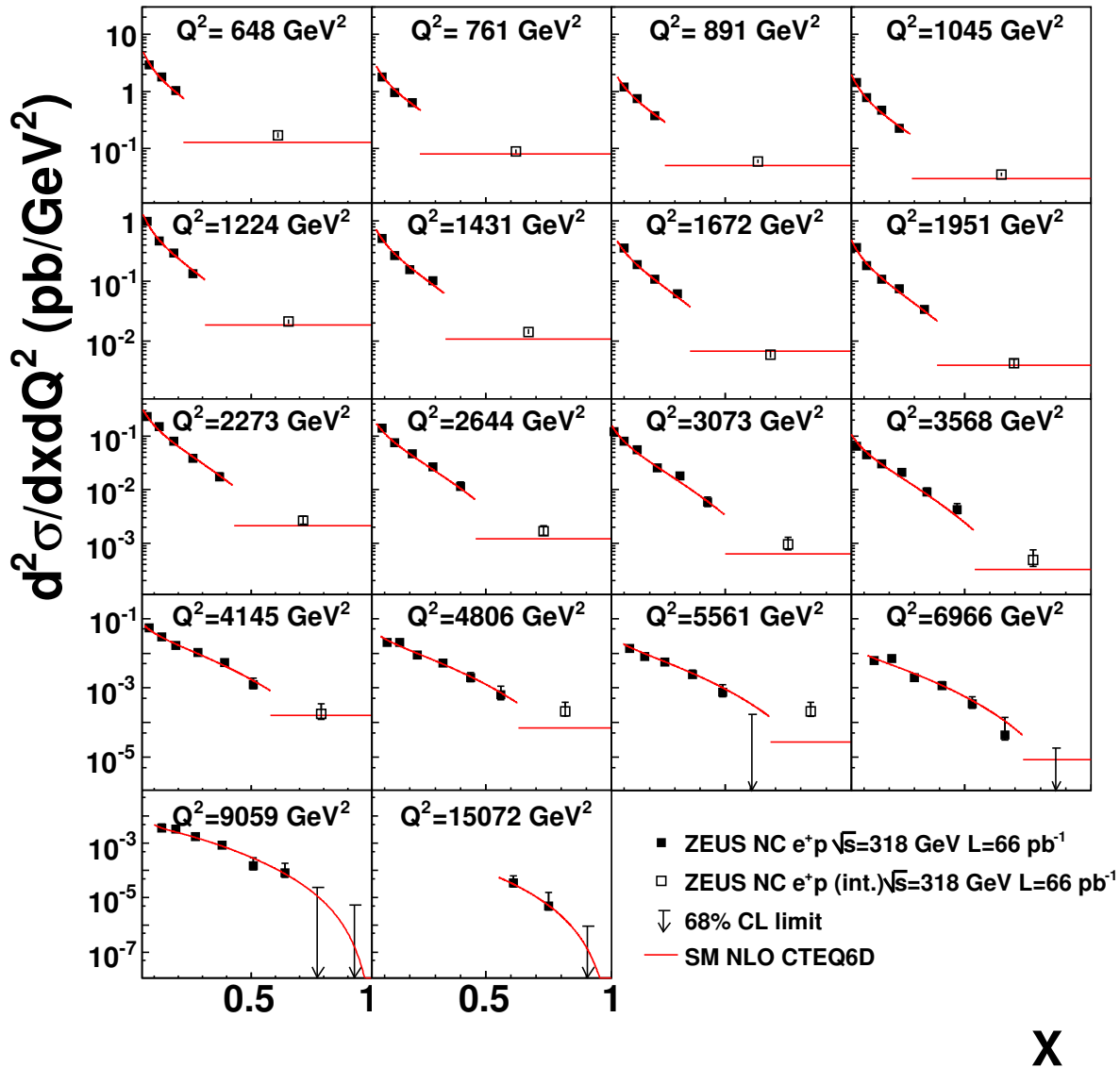
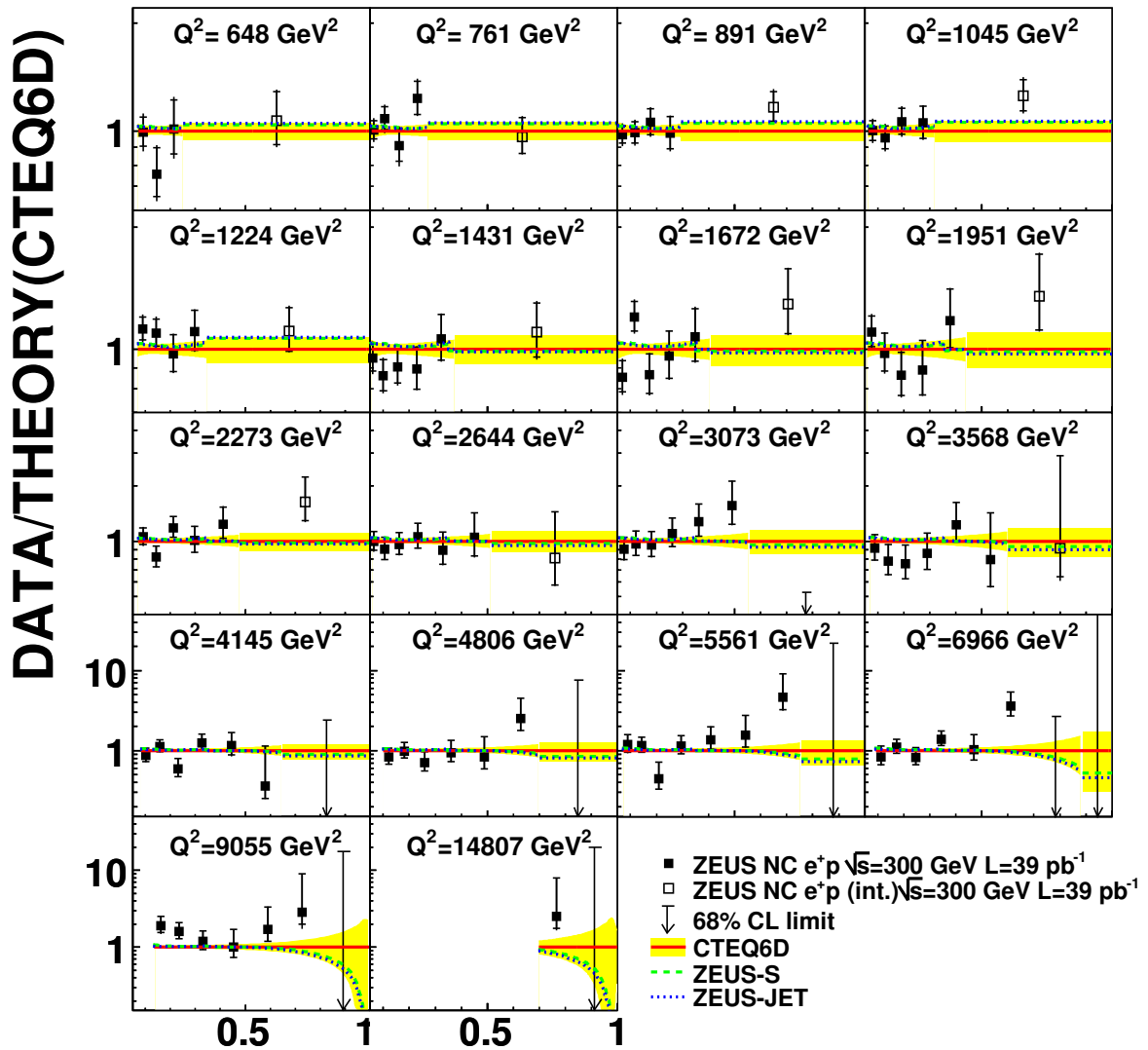


Figure 5.24: The double differential cross section for 99 – 00 e^+p NC scattering at $\sqrt{s} = 318$ GeV (solid squares) and the integral of the double differential cross section divided by the bin width (open squares) compared to the Standard Model expectations evaluated using CTEQ6D PDFs (lines). The inner error bars show the statistical uncertainty, while the outer ones show the statistical and systematic uncertainties added in quadrature. For bins with zero measured events, the 68% CL upper limit is given.

ZEUS



X

Figure 5.25: Ratio of the double differential cross section for 96 – 97 e^+p NC scattering (solid squares) and the integral of the double differential cross section divided by x bin width (open squares) to the Standard Model expectation evaluated using the CTEQ6D PDFs. The inner error bars show the statistical uncertainty, while the outer ones show the statistical and systematic uncertainties added in quadrature. The ratio of the expectations using the ZEUS-S and ZEUS-JET PDFs to those using the CTEQ6D predictions are also shown. For bins with zero measured events, the 68% CL upper limit is given.

ZEUS

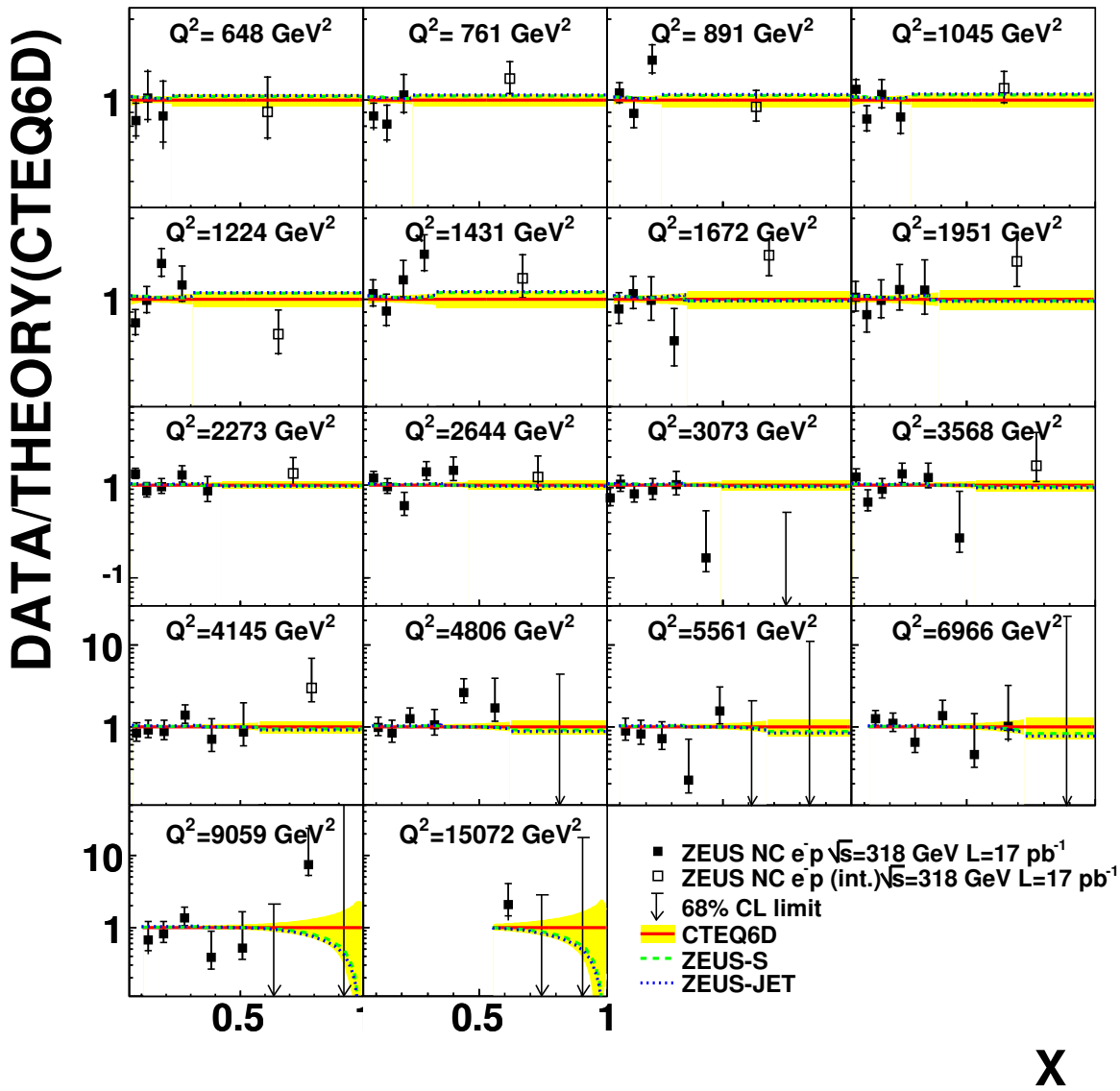


Figure 5.26: Ratio of the double differential cross section for 98 – 99 e^-p NC scattering (solid squares) and the integral of the double differential cross section divided by x bin width (open squares) to the Standard Model expectation evaluated using the CTEQ6D PDFs. The inner error bars show the statistical uncertainty, while the outer ones show the statistical and systematic uncertainties added in quadrature. The ratio of the expectations using the ZEUS-S and ZEUS-JET PDFs to those using the CTEQ6D predictions are also shown. For bins with zero measured events, the 68% CL upper limit is given.

ZEUS

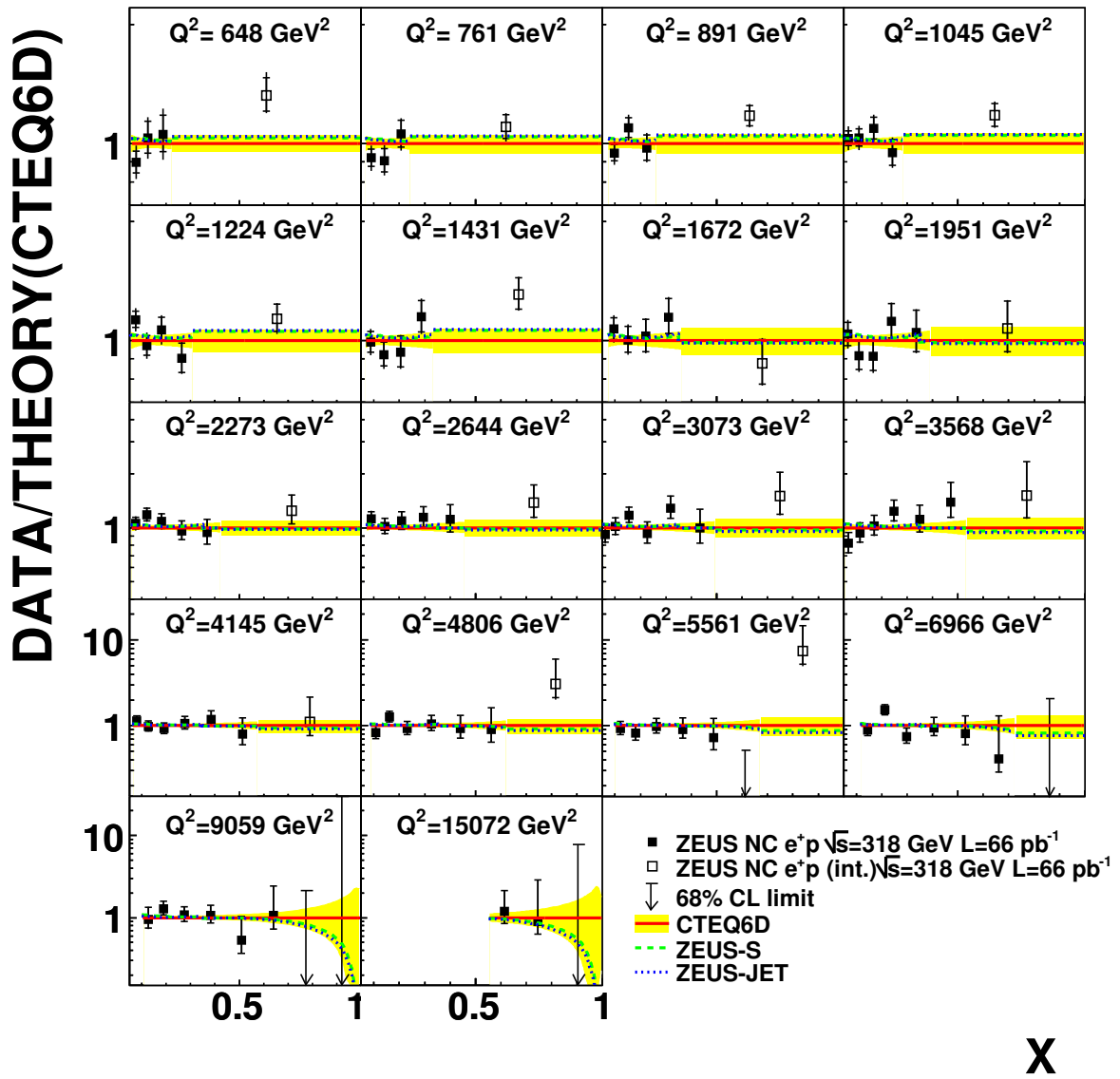


Figure 5.27: Ratio of the double differential cross section for 99 – 00 e^+p NC scattering (solid squares) and the integral of the double differential cross section divided by x bin width (open squares) to the Standard Model expectation evaluated using the CTEQ6D PDFs. The inner error bars show the statistical uncertainty, while the outer ones show the statistical and systematic uncertainties added in quadrature. The ratio of the expectations using the ZEUS-S and ZEUS-JET PDFs to those using the CTEQ6D predictions are also shown. For bins with zero measured events, the 68% CL upper limit is given.

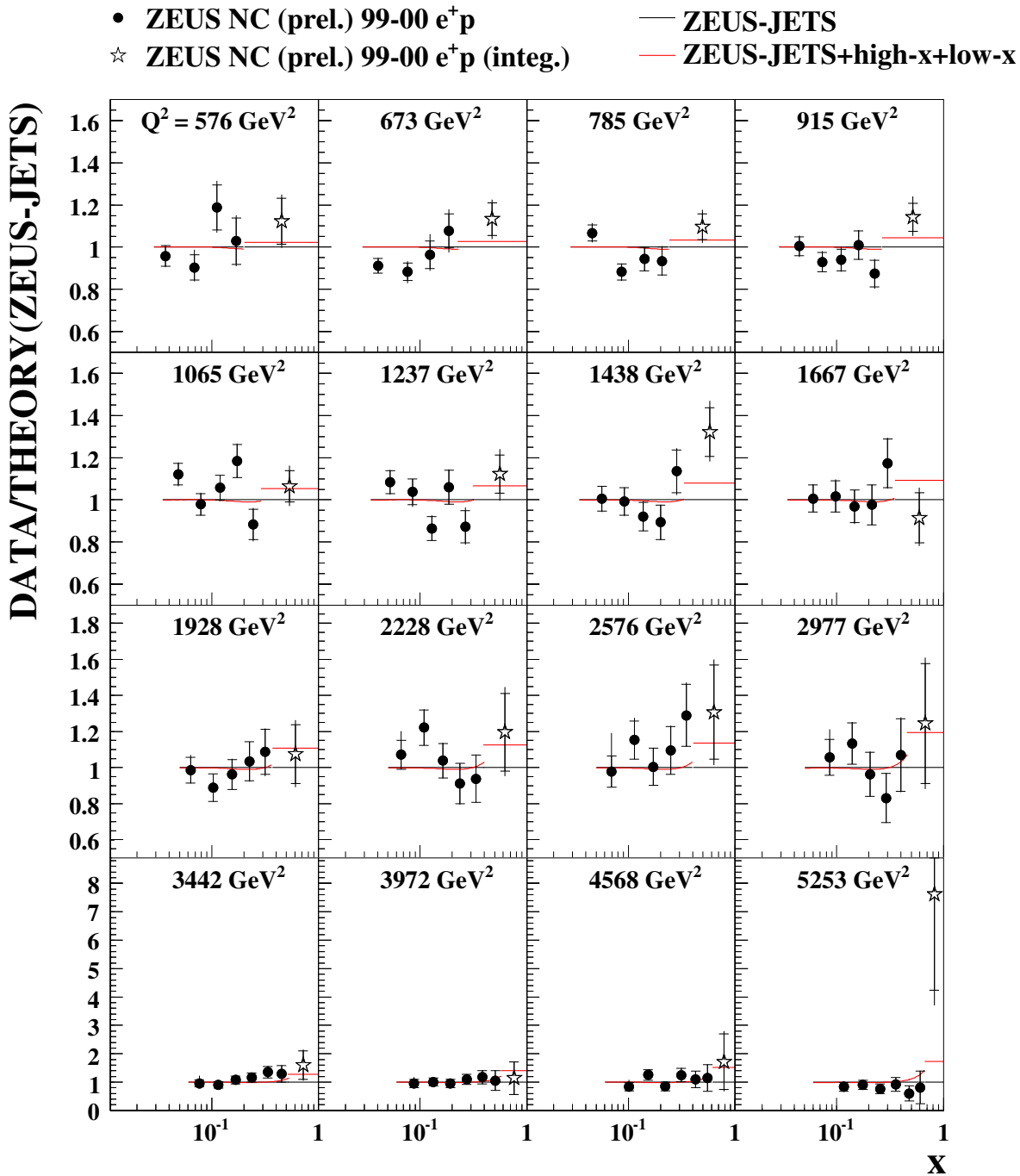


Figure 5.28: Ratio of the double differential cross section for 99 – 00 e^+p NC scattering (solid squares) and the integral of the double differential cross section divided by x bin width (open triangles) to the expectation evaluated using the ZEUS-JET and the PDF fit from this new measurement. The ZEUS-JET is also shown as a comparison. The main difference is at high x . The expectation using the PDF with the new measurement is higher than the old ZEUS-JET PDF at high x and shows better agreement to the data.

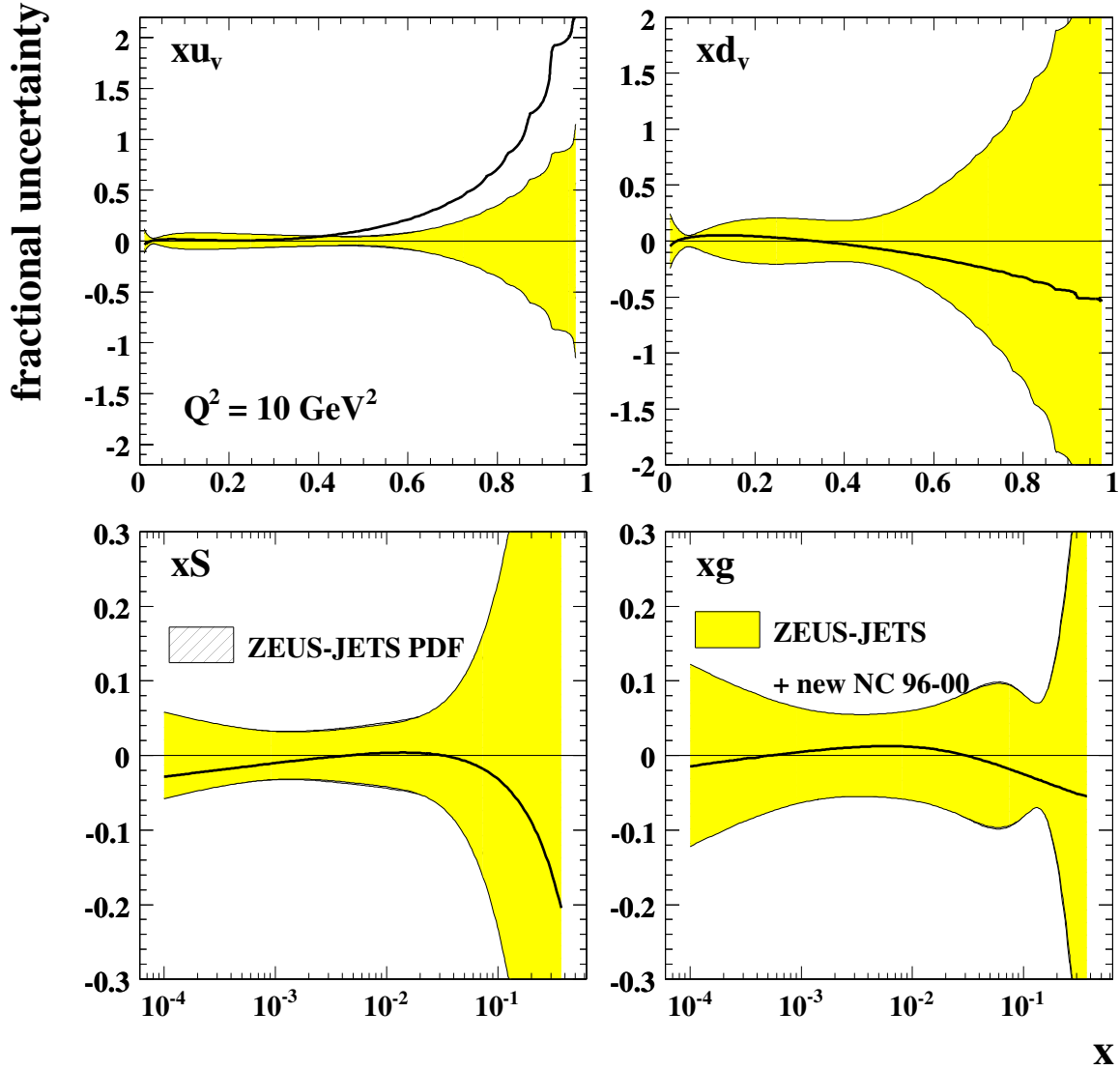


Figure 5.29: The fractional differences of the PDFs from the new fit combining the result from this analysis and ZEUS-JET to the ZEUS-JET PDFs for: valence quarks u and d , sea quark and gluon. The yellow band shows the uncertainty and the solid line shows the fractional difference.

is given as open points in the weighted center. The predictions obtained using the ZEUS-S and CTEQ6D PDFs are also shown. In the highest x bins, the expected F_2 is drawn as a horizontal line. The results agree well with predictions. The measured F_2 at different Q^2 values, ranged from $Q^2 = 648 \text{ GeV}^2$ to $Q^2 = 15072 \text{ GeV}^2$, as a function of x are shown in Fig. 5.31. The bins with zero reconstructed event are not included in this plot. The F_2 measured by the fixed target experiment BCDMS [15] from $Q^2 = 8.75 \text{ GeV}^2$ to $Q^2 = 230 \text{ GeV}^2$ is shown as a comparison. The new method reaches higher x and Q^2 region.

5.7 Summary

This thesis presented a reanalysis of previously published ZEUS data with a new method designed to measure the neutral current cross section up to Bjorken- x values equal to one. The data were taken with the ZEUS detector at HERA with an integrated luminosity of 65.1 pb^{-1} for e^+p collisions and of 16.7 pb^{-1} for e^-p collisions at $\sqrt{s} = 318 \text{ GeV}$ and 38.6 pb^{-1} for e^+p at $\sqrt{s} = 300 \text{ GeV}$.

The new technique reconstructs Q^2 with electron energy and polar angle in the whole kinematic region. In the lower x region, x is reconstructed with the jet energy and polar angle for events with one jet; at high x , the number of events without any observed jet is counted since the jet is boosted into the beam hole for x high enough. The Monte Carlo simulation shows good precision on the reconstructed electron and jet variables in the low x region. At the highest x , slightly more data events were reconstructed without a jet than predicted by the MC.

The bin-by-bin unfolding method was applied to measure the cross sections: double differential cross sections for low x bins and integral cross sections for the highest x bins. The cross sections have been extracted for $Q^2 > 648 \text{ GeV}^2$ and are compared to predictions using different parton density functions. The higher order radiative correction is applied to the cross sections. The systematic uncertainties relative to the detectors, electron and jet reconstruction, different PDFs and radiative corrections were studied and estimated.

ZEUS

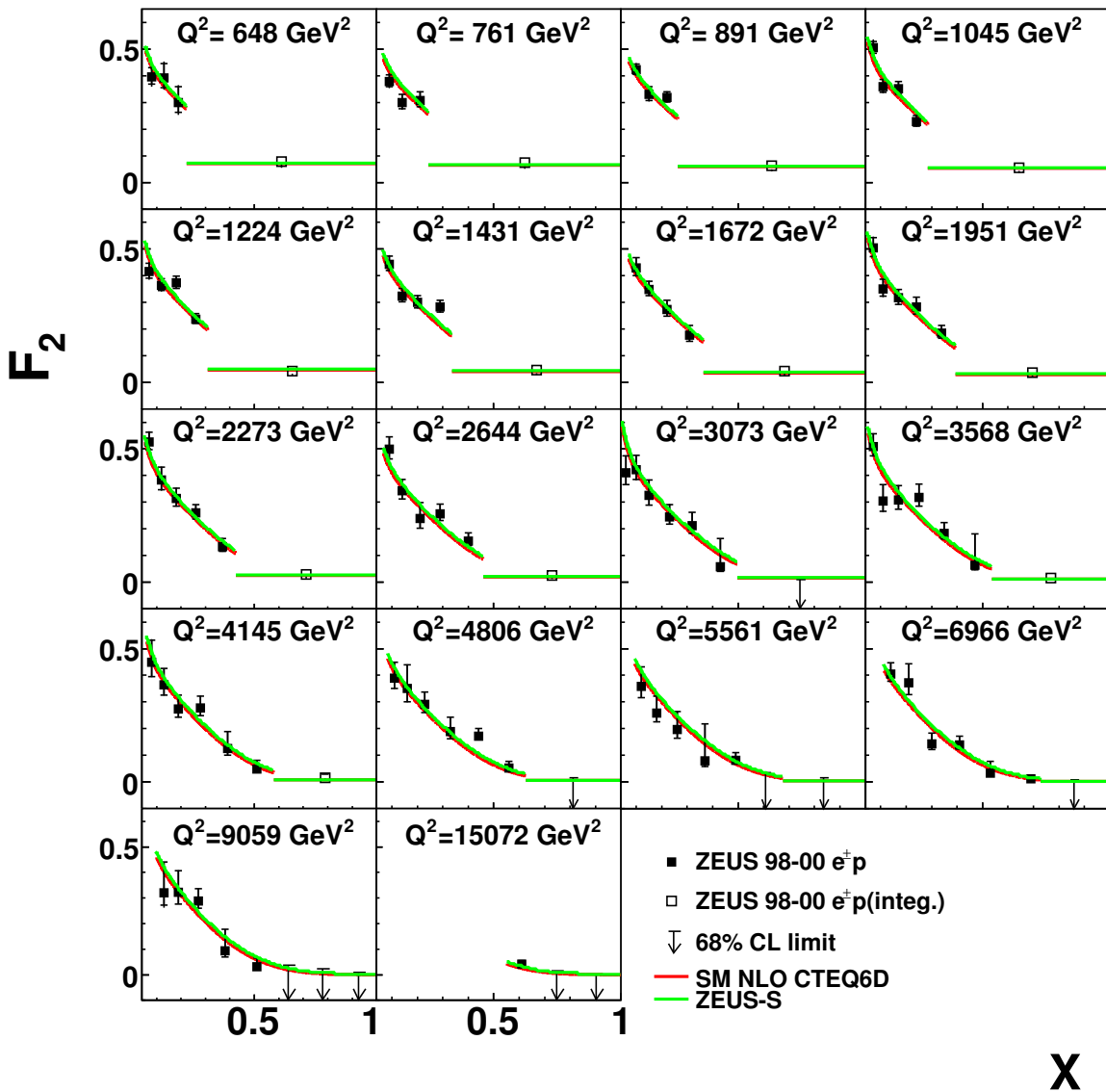


Figure 5.30: The structure function F_2 (solid squares) and the integral of the F_2 divided by the bin width (open squares) calculated from 98 – 99 e^-p and 99 – 00 e^+p NC data. The Standard expectation are evaluated with CTEQ6D (red lines) and ZEUS-S (green lines) are shown. The inner error bars show the statistical uncertainty, while the outer ones show the statistical and systematic uncertainties added in quadrature. For bins with zero measured events, the 68% CL upper limit is given.

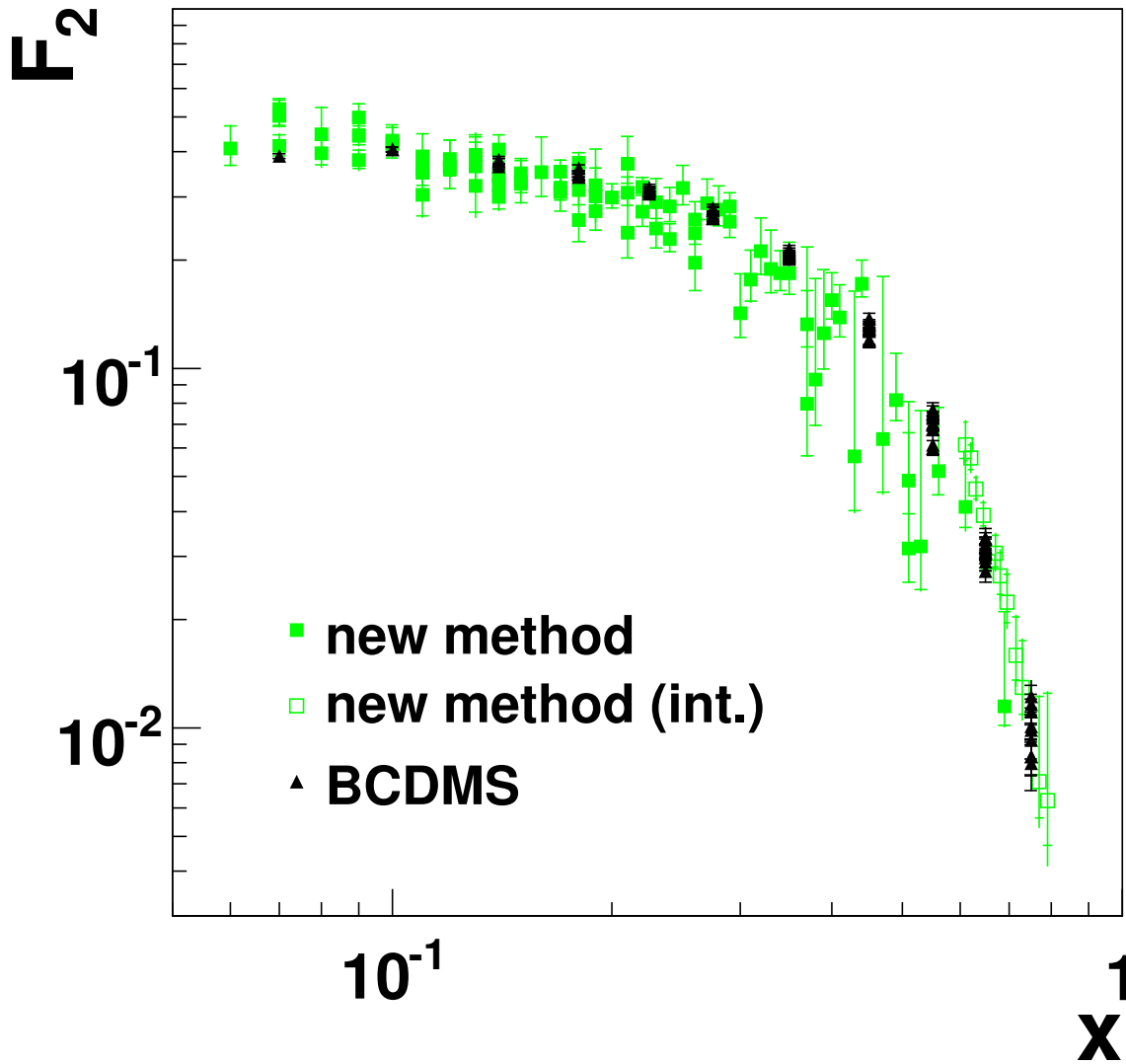


Figure 5.31: *The structure function F_2 (solid squares) and the integral of the F_2 divided by the bin width (open squares) calculated from 98–99 e^-p and 99–00 e^+p NC data as a function of x . The bins with zero reconstructed event are not included. The results from BCDMS at different Q^2 are shown in triangles. The error bars for both measurements, the inner error bars show the statistical uncertainty, while the outer ones show the statistical and systematic uncertainties added in quadrature.*

In the kinematic region where ZEUS previously analyzed these data, there is good agreement with the published data. Also, the data and SM prediction based on the CTEQ6D PDF are in good agreement. At the highest x , the Standard Model predictions based on CTEQ6D and other recent PDFs tend to slightly underestimate the data. A preliminary QCD fit shows that the new data provides important constraint on the form of the PDF at the highest values of x .

HERA began a high luminosity phase HERA II, in 2003. The data sets will be about five times larger than those analyzed for this thesis, and should bring considerably more information on the high x parton density functions.

Appendix A

Control plots for 96-97 e^+p and 98-99 e^-p data

In this appendix, the comparisons between MC and data for the distribution of reconstructed variables for 96-97 e^+p and 98-99 e^-p are shown. The MC distributions are normalized to the measured luminosities. As shown in Sect. 4.4.4 for 99-00 e^+p , the comparisons include the general kinematic variables for DIS, the scattered electron, the reconstructed jet and the general variables for the zero jet events. In general MC describes data quite well.

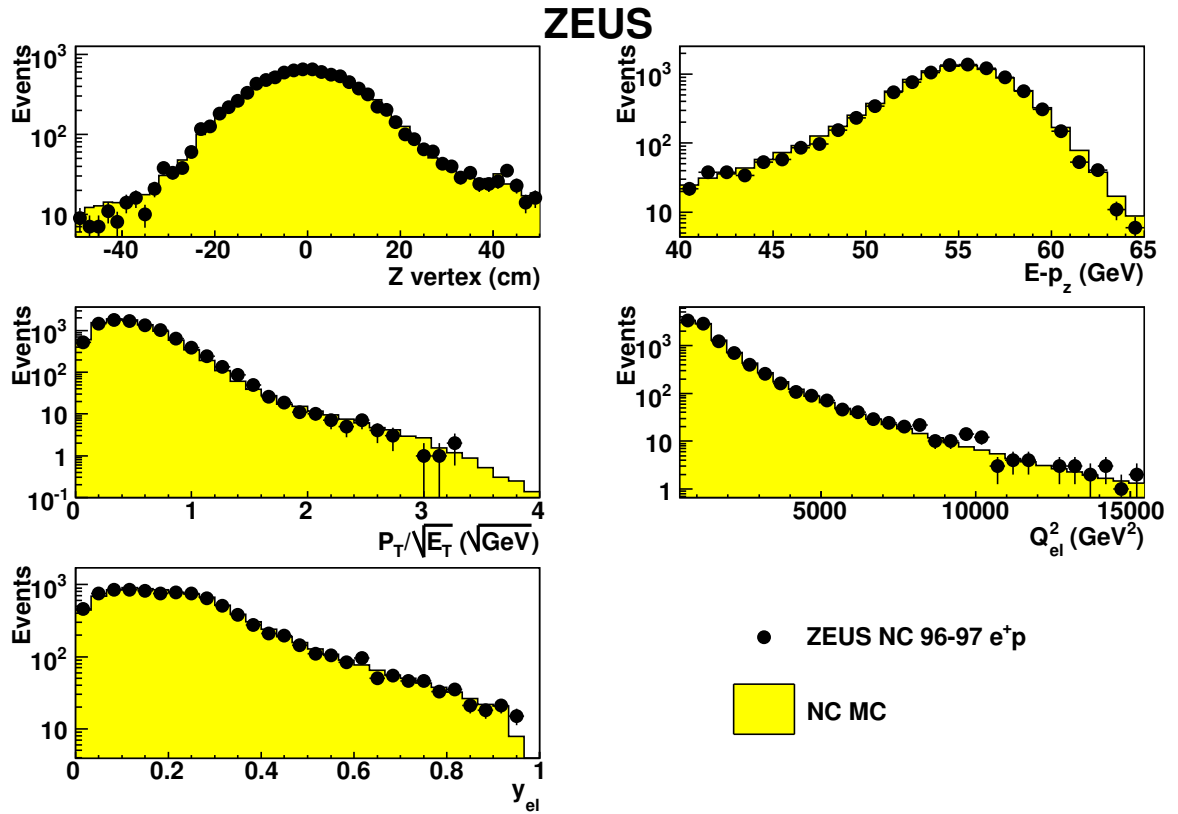


Figure A.1: Comparison of NC MC simulated events (histograms) with 96 – 97 e^+p data (points) for: the Z coordinate of the event vertex; $E - p_z$; $P_T/\sqrt{E_T}$; Q_{el}^2 and y_e . The MC distributions are normalized to the luminosity of the data.

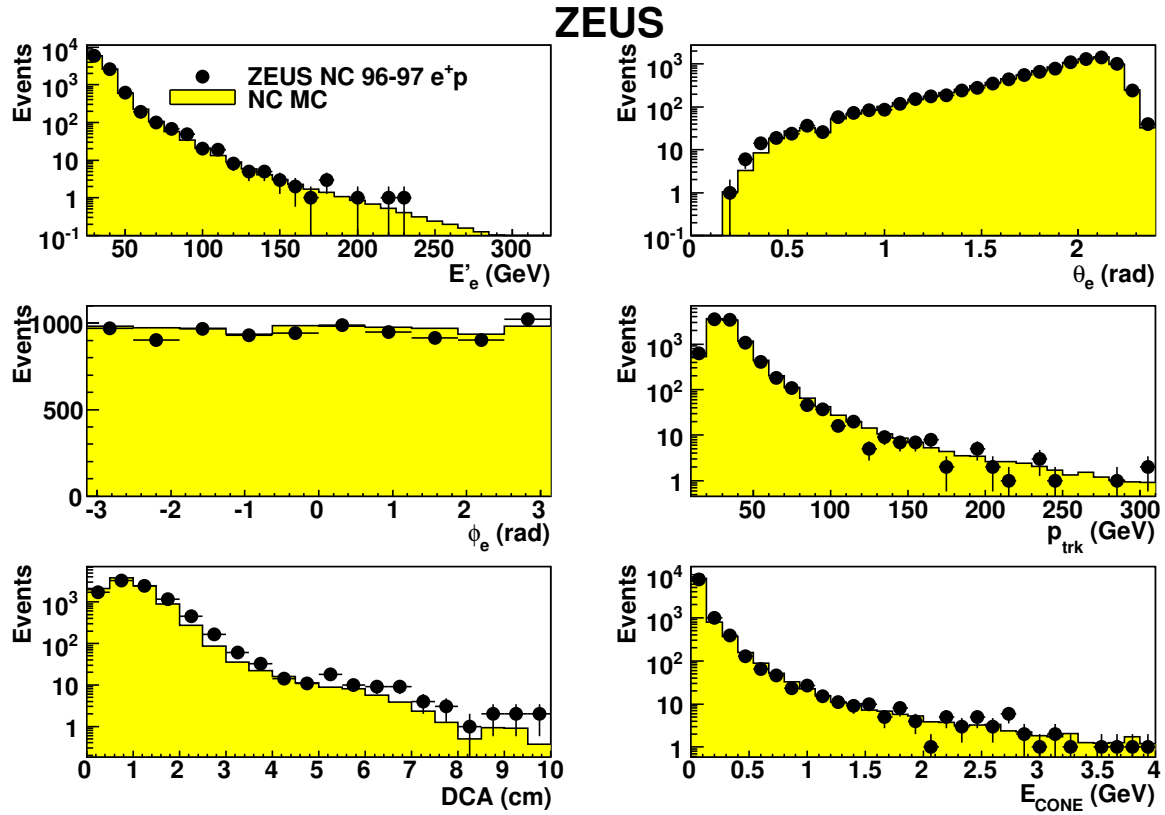


Figure A.2: Comparison of NC MC distributions (histograms) with 96 – 97 e^+p data (points) for: E'_e ; polar angle of scattered electron θ_e ; azimuthal angle ϕ_e ; P_{trk} ; DCA and E_{CONE} , the momentum of the track associated with the scattered electron. The MC distributions are normalized to the luminosity of the data.

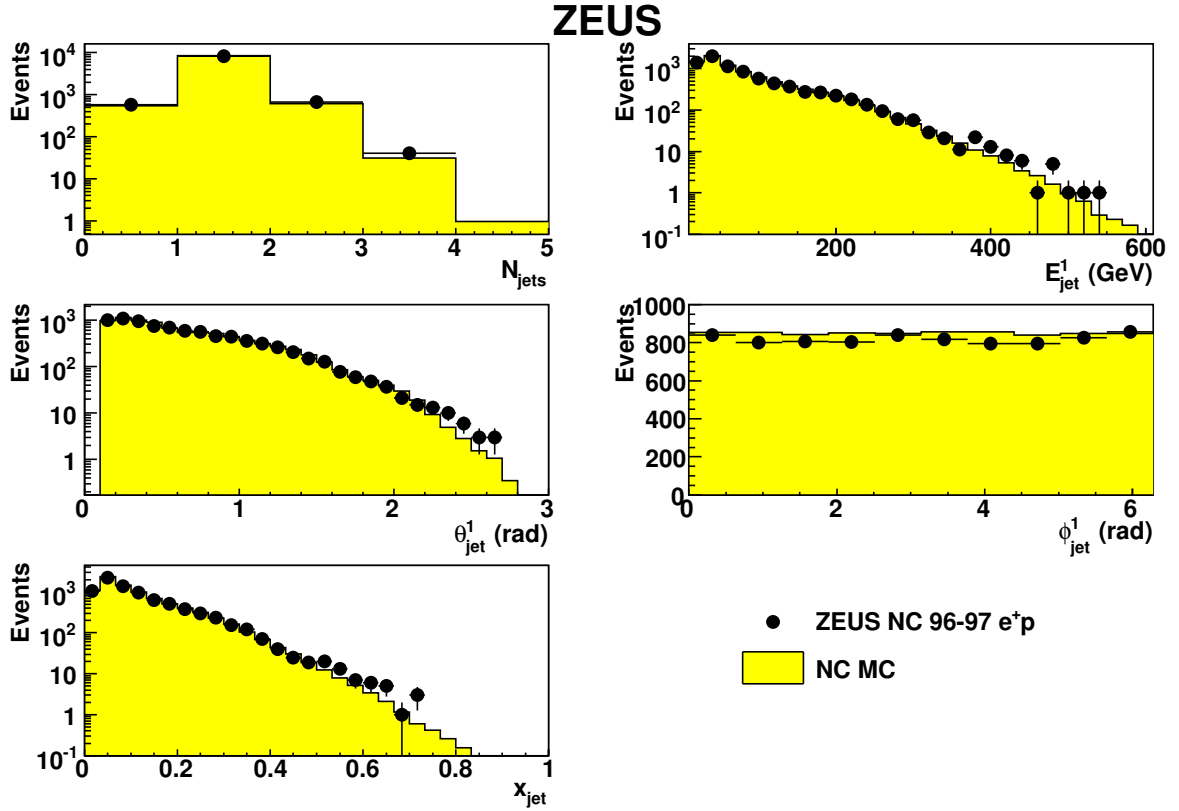


Figure A.3: Comparison of NC MC distributions (histograms) with 96 – 97 e^+p data (points) for: the number of reconstructed jets N_{jets} ; the energy of the leading jet E_{jet} ; the polar angle of the leading jet θ_{jet} ; azimuthal angle ϕ_{jet} and x calculated from the jet x_{jet} . The jet distributions are for one jet events. The MC distributions are normalized to the luminosity of the data.

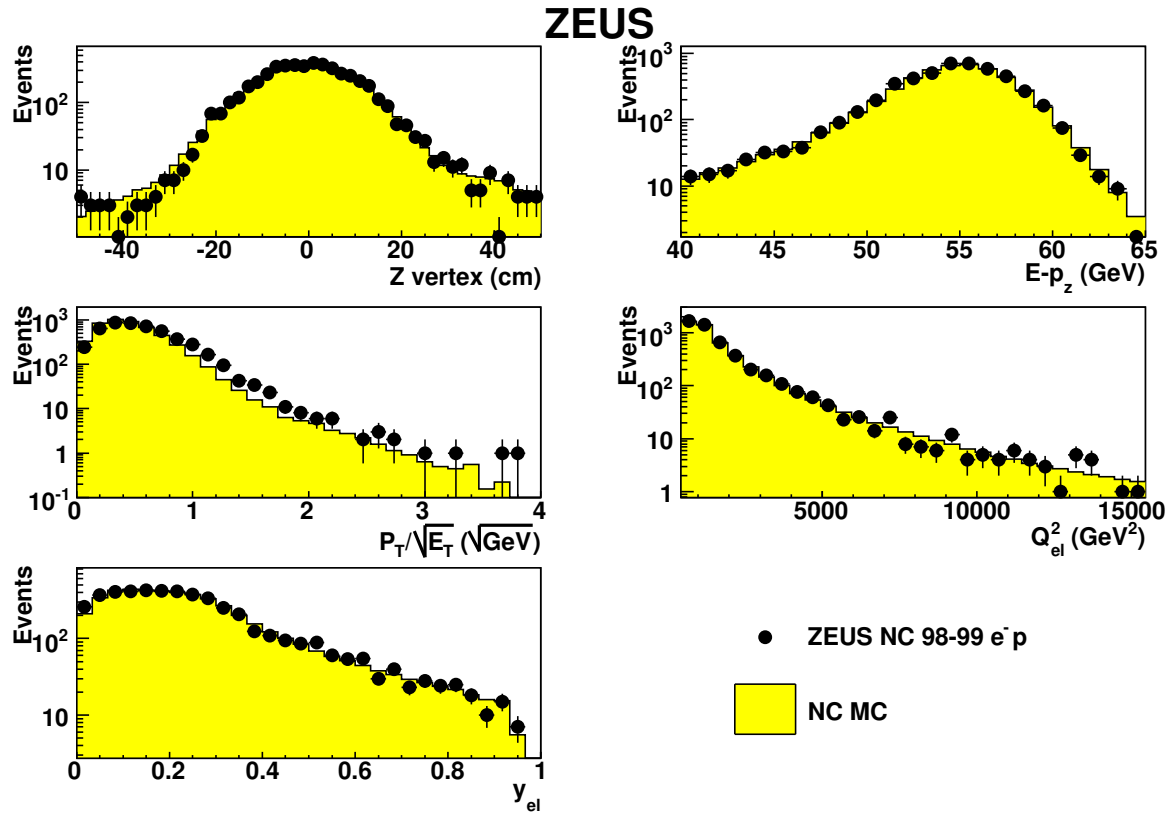


Figure A.4: Comparison of NC MC simulated events (histograms) with 98 – 99 e^-p data (points) for: the Z coordinate of the event vertex; $E - p_z$; $P_T / \sqrt{E_T}$; Q_{el}^2 and y_e . The MC distributions are normalized to the luminosity of the data.

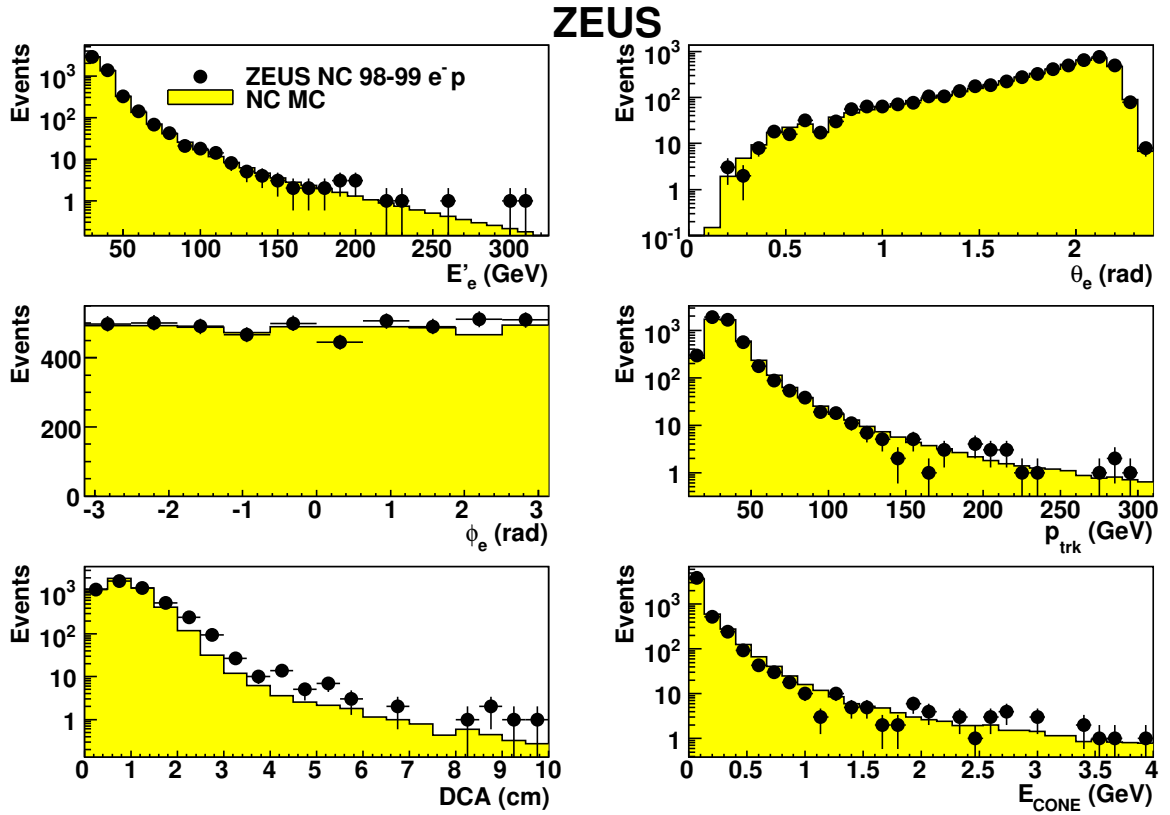


Figure A.5: Comparison of NC MC distributions (histograms) with 98 – 99 e^-p data (points) for: E'_e ; polar angle of scattered electron θ_e ; azimuthal angle ϕ_e ; P_{trk} ; DCA and E_{CONE} , the momentum of the track associated with the scattered electron. The MC distributions are normalized to the luminosity of the data.

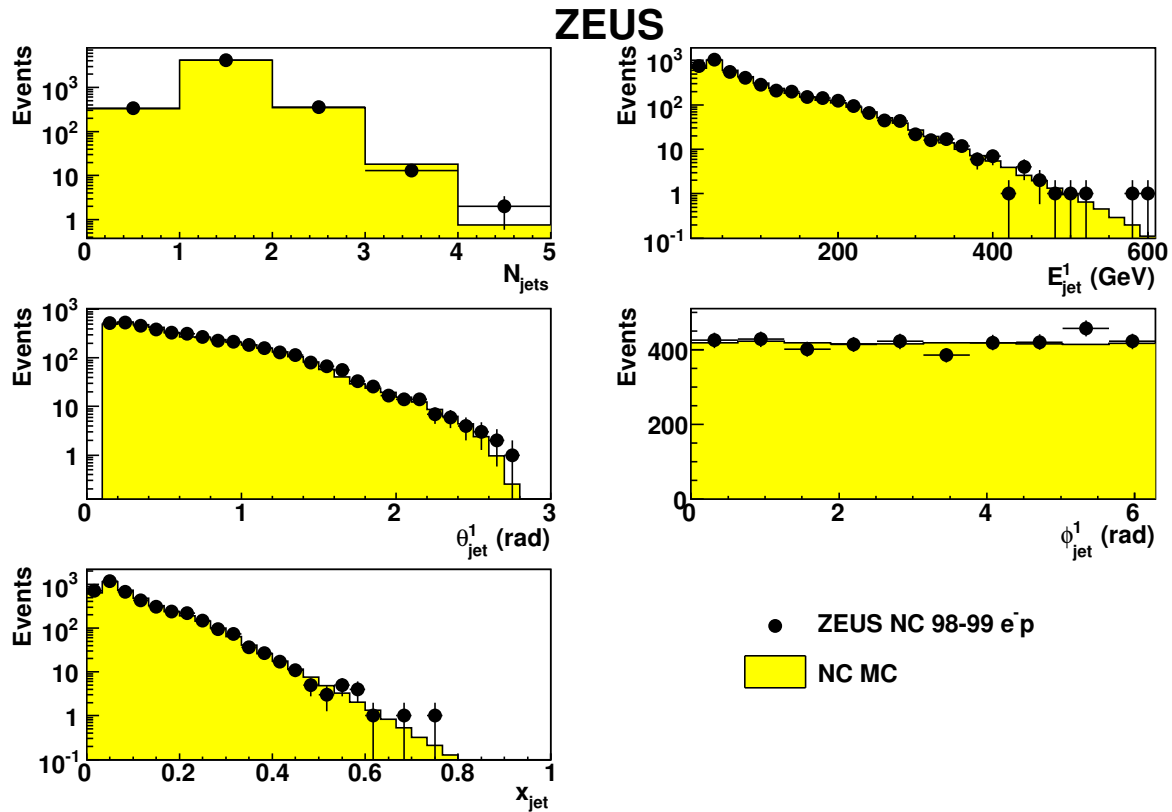


Figure A.6: Comparison of NC MC distributions (histograms) with 98 – 99 e^-p data (points) for: the number of reconstructed jets N_{jets} ; the energy of the leading jet E_{jet} ; the polar angle of the leading jet θ_{jet} ; azimuthal angle ϕ_{jet} and x calculated from the jet x_{jet} . The jet distributions are for one jet events. The MC distributions are normalized to the luminosity of the data.

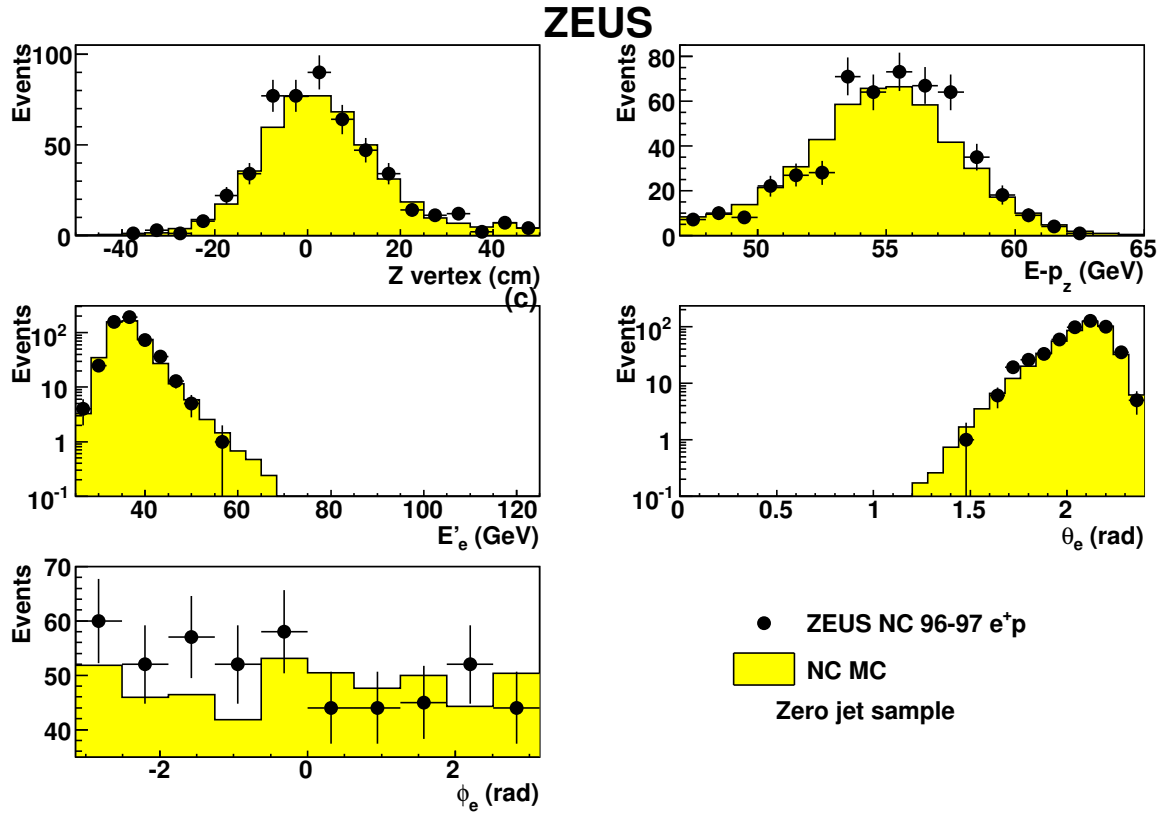


Figure A.7: Comparison of NC MC distributions (histograms) with 96 – 97 e^+p data (points) for events with zero jets. The plots show: the Z coordinate of the event vertex; $E - p_z$; E'_e ; θ_e and ϕ_e . The MC distributions are normalized to the luminosity of the data.

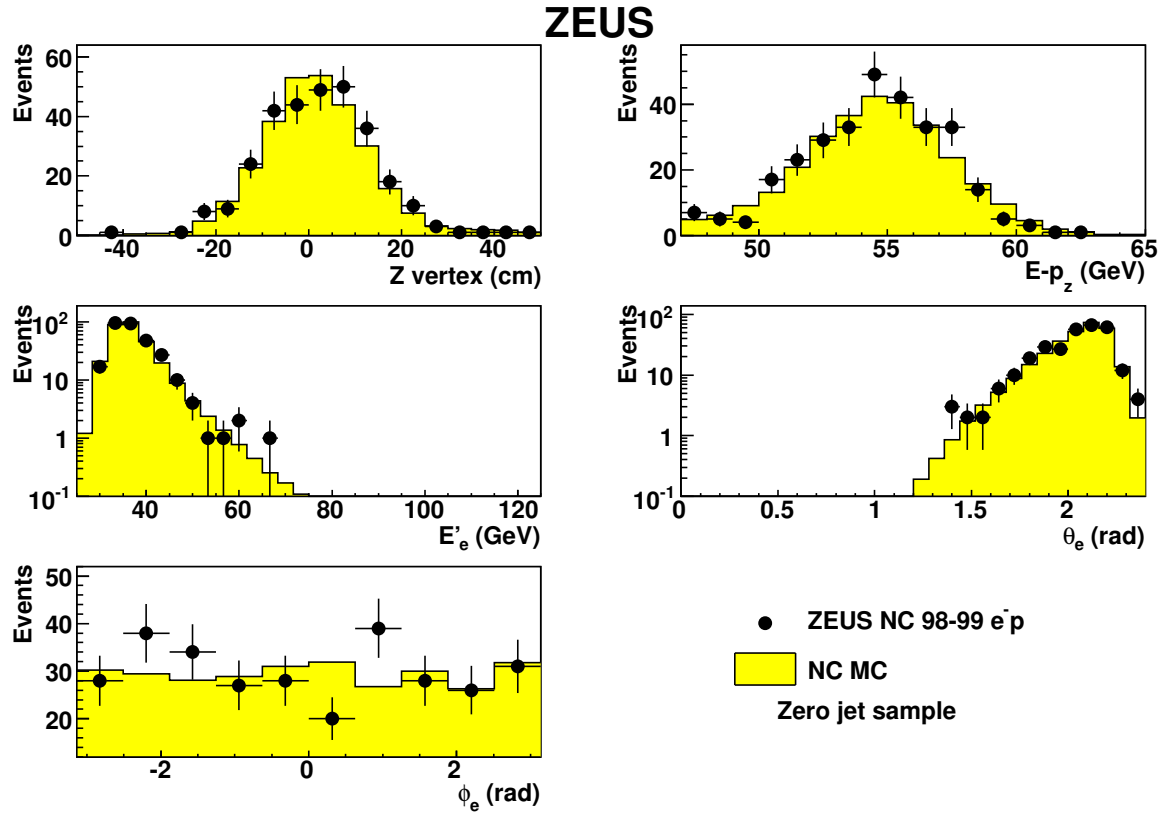


Figure A.8: Comparison of NC MC distributions (histograms) with 98 – 99 e^-p data (points) for events with zero jets. The plots show: the Z coordinate of the event vertex; $E - p_z$; E'_e ; θ_e and ϕ_e . The MC distributions are normalized to the luminosity of the data.

Appendix B

Cross section tables

In this appendix, the cross section value and the related uncertainties are shown in tables. All the low x tables, B.1, B.3 and B.5 have the same format. The first two columns give Q^2 and x where the cross section is quoted. The third column is the measured double differential cross section. The fourth column shows the number of reconstructed events used in the cross section calculation. The fifth column gives the 68% CL upper limit for the bins with zero reconstructed event. The sixth column is the statistical uncertainty calculated by Bayes approach. The seventh column is the total systematic uncertainty for the cross section, which is the sum of all the systematic uncertainties in quadrature. The ninth column gives the sum of all the uncorrelated systematic uncertainties described in Sect.5.4.1 in quadrature. The rest columns are the correlated systematic uncertainties δ_1 to δ_6 as explained in Sect.5.4.2. For the bin with zero reconstructed event, all these uncertainty columns are blank. The highest x cross section tables, B.2, B.4 and B.6 have similar arrangement, but the second column shows the lower x bin edge, x_{edge} , the cross section and the upper limit are the integration over the x bin.

Q^2 (GeV ²)	x	$d^2\sigma/dxdQ^2$ (pb/GeV ²)	Nevt.	upper limit (pb/GeV ²)	stat. (%)	total sys. (%)	uncor. sys. (%)	δ_1 (%)	δ_2 (%)	δ_3 (%)	δ_4 (%)	δ_5 (%)	δ_6 (%)
648	0.09	$2.66 \cdot 10^0$	114		+10.3 -8.5	+7.9 -7.8	+2.0 -1.6	+6.0 -6.1	-0.3 +1.2	-0.2 +0.1	+1.4 -1.4	+2.4 -2.4	+3.3 -3.3
	0.15	$1.08 \cdot 10^0$	40		+18.5 -13.4	+8.3 -8.7	+2.1 -2.2	+6.4 -6.7	-1.3 +0.4	+1.6 -2.1	+0.9 -0.9	+2.4 -2.4	+3.3 -3.3
	0.21	$7.97 \cdot 10^{-1}$	33		+20.5 -14.6	+11.0 -8.9	+3.6 -2.0	+9.2 -8.1	-0.4 +2.5	+2.7 -0.2	+0.5 -0.5	+2.4 -2.4	+1.0 -1.0
761	0.06	$3.06 \cdot 10^0$	299		+6.1 -5.4	+5.0 -4.8	+1.3 -0.7	+1.0 -0.6	-0.4 -0.1	-0.4 +0.2	+1.7 -1.7	+2.4 -2.4	+3.3 -3.3
	0.11	$1.72 \cdot 10^0$	187		+7.9 -6.8	+5.3 -5.6	+0.2 -1.0	+2.4 -3.0	-0.9 +1.5	-0.0 -0.3	+1.3 -1.3	+2.4 -2.4	+3.3 -3.3
	0.16	$8.11 \cdot 10^{-1}$	92		+11.6 -9.4	+6.2 -8.2	+0.8 -2.1	+4.2 -6.1	-1.4 -0.3	+0.3 -2.0	+0.8 -0.8	+2.4 -2.4	+3.3 -3.3
891	0.23	$6.09 \cdot 10^{-1}$	88		+11.8 -9.6	+6.7 -4.5	+0.9 -1.5	+4.8 -2.8	-0.6 +2.6	+1.9 +0.5	+0.6 -0.6	+2.4 -2.4	+1.0 -1.0
	0.07	$1.89 \cdot 10^0$	314		+6.0 -5.4	+4.8 -4.7	+1.0 -0.3	-0.8 +0.8	-0.3 +0.3	-0.3 +0.3	+1.6 -1.6	+2.4 -2.4	+3.3 -3.3
	0.12	$9.96 \cdot 10^{-1}$	214		+7.3 -6.4	+4.8 -4.6	+1.2 -0.6	+1.1 +0.2	-0.9 +0.2	+0.0 -0.3	+1.2 -1.2	+2.4 -2.4	+3.3 -3.3
1045	0.18	$5.96 \cdot 10^{-1}$	145		+9.1 -7.6	+4.8 -4.7	+1.4 -0.8	+0.4 +0.4	-1.1 +0.9	+0.9 -1.1	+0.7 -0.7	+2.4 -2.4	+3.3 -3.3
	0.25	$2.92 \cdot 10^{-1}$	91		+11.6 -9.4	+4.0 -5.3	+0.7 -1.1	+0.5 -3.0	-1.9 +1.5	+1.6 -2.0	+0.8 -0.8	+2.4 -2.4	+1.0 -1.0
1045	0.08	$1.16 \cdot 10^0$	251		+6.8 -5.9	+4.8 -4.8	+0.6 -0.4	-1.2 +1.0	-0.5 +0.2	-0.2 +0.5	+1.6 -1.6	+2.4 -2.4	+3.3 -3.3

Table B.1: The cross section table for 96-97 e^+p NC scattering. The first two columns of the table contain the Q^2 and x values at which the cross section is quoted, the third contains the measured cross section $d^2\sigma/dxdQ^2$ corrected to the electroweak Born level, the fourth contains the number of events reconstructed in the bin, the fifth contains the upper limit in case of zero observed events, the sixth contains the statistical uncertainty and the seventh contains the total systematic uncertainty. The right part of the table lists the total uncorrelated systematic uncertainty followed by the bin-to-bin correlated systematic uncertainties δ_1 - δ_6 defined in the text. For the latter, the upper (lower) numbers refer to the variation of the cross section, whereas the signs of the numbers reflect the direction of change in the cross sections. Note that the normalization uncertainty, δ_7 is not listed.

Table B.1 (continued):

Q^2 (GeV ²)	x	$d^2\sigma/dxdQ^2$ (pb/GeV ²)	Nevt.	upper limit (pb/GeV ²)	stat. (%)	total sys. (%)	uncor. sys. (%)	δ_1 (%)	δ_2 (%)	δ_3 (%)	δ_4 (%)	δ_5 (%)	δ_6 (%)
1224	0.13	$6.10 \cdot 10^{-1}$	182		+8.0 -6.9	+4.6 -4.8	+0.7 -1.1	-0.8 +0.2	-1.0 +0.8	-0.2 -0.3	+1.1 -1.1	+2.4 -2.4	+3.3 -3.3
	0.19	$3.79 \cdot 10^{-1}$	143		+9.1 -7.7	+5.4 -4.9	+1.3 -0.8	-1.7 +2.1	+0.2 +0.7	+1.9 -1.2	+0.6 -0.6	+2.4 -2.4	+3.3 -3.3
	0.27	$1.94 \cdot 10^{-1}$	94		+11.4 -9.3	+4.4 -4.4	+2.0 -0.5	-0.3 +1.1	-2.9 +1.8	+1.0 -1.0	+0.9 -0.9	+2.4 -2.4	+1.0 -1.0
	0.09	$7.98 \cdot 10^{-1}$	233		+7.0 -6.2	+4.8 -5.0	+0.0 -0.7	-1.6 +1.3	-0.2 -0.0	-0.5 +0.3	+1.6 -1.6	+2.4 -2.4	+3.3 -3.3
	0.14	$4.26 \cdot 10^{-1}$	169		+8.3 -7.2	+5.1 -4.6	+1.0 -0.4	-0.4 +2.2	-1.1 +0.9	+0.1 -0.4	+0.9 -0.9	+2.4 -2.4	+3.3 -3.3
	0.21	$2.04 \cdot 10^{-1}$	91		+11.6 -9.4	+3.9 -3.9	+1.8 -0.4	+1.0 +0.2	-0.4 -0.6	+1.1 -2.2	+0.6 -0.6	+2.4 -2.4	+1.0 -1.0
1431	0.30	$1.25 \cdot 10^{-1}$	78		+12.7 -10.1	+4.7 -4.1	+0.6 -1.7	-1.7 +0.6	-0.7 +2.7	+1.8 -0.1	+1.1 -1.1	+2.4 -2.4	+1.0 -1.0
	0.06	$7.68 \cdot 10^{-1}$	170		+8.3 -7.1	+5.0 -5.0	+1.0 -0.5	-1.1 +1.4	-0.8 -0.3	-0.2 -0.4	+1.8 -1.8	+2.4 -2.4	+3.3 -3.3
	0.10	$3.83 \cdot 10^{-1}$	126		+9.7 -8.1	+5.1 -4.8	+1.0 -1.2	-0.7 +1.6	+1.0 +0.4	-0.1 +0.5	+1.5 -1.5	+2.4 -2.4	+3.3 -3.3
	0.16	$2.27 \cdot 10^{-1}$	112		+10.4 -8.6	+4.6 -5.0	+0.5 -0.3	-1.0 +0.5	-1.8 +0.8	-0.2 -0.6	+0.8 -0.8	+2.4 -2.4	+3.3 -3.3
	0.23	$1.19 \cdot 10^{-1}$	70		+13.4 -10.6	+4.3 -3.7	+1.9 -0.9	-1.0 +2.0	-0.0 -0.2	+1.1 -1.3	+0.7 -0.7	+2.4 -2.4	+1.0 -1.0
	0.32	$7.17 \cdot 10^{-2}$	59		+14.8 -11.5	+4.6 -4.1	+0.8 -0.4	-0.3 +0.6	-2.0 +2.3	+1.8 -1.1	+1.4 -1.4	+2.4 -2.4	+1.0 -1.0
1672	0.07	$4.21 \cdot 10^{-1}$	126		+9.7 -8.1	+5.3 -5.0	+1.6 -0.5	-1.6 +1.9	-0.1 +0.1	-0.1 -0.1	+1.8 -1.8	+2.4 -2.4	+3.3 -3.3
	0.11	$3.25 \cdot 10^{-1}$	144		+9.1 -7.7	+5.0 -5.0	+0.6 -0.7	-2.0 +2.0	-0.3 +0.3	-0.3 +0.1	+1.3 -1.3	+2.4 -2.4	+3.3 -3.3
	0.17	$1.35 \cdot 10^{-1}$	80		+12.5 -10.0	+4.5 -4.9	+0.4 -1.4	-1.3 -0.2	-0.8 +0.5	+0.2 -0.1	+0.7 -0.7	+2.4 -2.4	+3.3 -3.3
	0.25	$7.96 \cdot 10^{-2}$	55		+15.4 -11.7	+3.3 -4.8	+0.3 -2.4	-2.0 -0.1	-1.5 +0.6	+0.6 -1.2	+0.8 -0.8	+2.4 -2.4	+1.0 -1.0
	0.35	$4.27 \cdot 10^{-2}$	45		+17.3 -12.8	+6.4 -4.8	+4.1 -1.0	-1.7 +1.5	-2.1 +2.7	+1.5 -1.5	+1.8 -1.8	+2.4 -2.4	+1.0 -1.0
	0.08	$3.32 \cdot 10^{-1}$	130		+9.6 -8.1	+4.9 -5.4	+0.5 -1.5	-2.2 +1.2	-0.5 +0.6	-0.1 -0.1	+1.8 -1.8	+2.4 -2.4	+3.3 -3.3
1951	0.13	$1.66 \cdot 10^{-1}$	86		+12.0 -9.7	+4.7 -4.8	+0.9 -0.9	-1.2 +1.1	-0.6 -0.6	-0.3 +0.1	+1.2 -1.2	+2.4 -2.4	+3.3 -3.3
	0.19	$8.47 \cdot 10^{-2}$	66		+13.9 -10.8	+5.3 -4.9	+0.9 -1.4	-1.6 +2.6	-0.7 +0.9	+0.1 -0.2	+0.7 -0.7	+2.4 -2.4	+3.3 -3.3

Table B.1 (continued):

Q^2 (GeV ²)	x	$d^2\sigma/dxdQ^2$ (pb/GeV ²)	Nevt.	upper limit (pb/GeV ²)	stat. (%)	total sys. (%)	uncor. sys. (%)	δ_1 (%)	δ_2 (%)	δ_3 (%)	δ_4 (%)	δ_5 (%)	δ_6 (%)
2273	0.27	$4.53 \cdot 10^{-2}$	41		+18.1 -13.3	+4.2 -3.4	+1.6 -0.4	-0.3 +1.9	-0.6 +0.8	+0.9 -0.6	+1.0 -1.0	+2.4 -2.4	+1.0 -1.0
	0.38	$2.69 \cdot 10^{-2}$	35		+19.9 -14.2	+4.8 -4.8	+0.3 -1.4	-1.3 -0.3	-1.8 +2.4	+1.8 -1.4	+2.2 -2.2	+2.4 -2.4	+1.0 -1.0
	0.09	$1.88 \cdot 10^{-1}$	88		+11.8 -9.6	+4.8 -5.4	+0.3 -1.5	-2.0 +1.1	-0.9 +0.4	-0.4 -0.0	+1.7 -1.7	+2.4 -2.4	+3.3 -3.3
	0.14	$8.43 \cdot 10^{-2}$	60		+14.6 -11.4	+5.0 -5.0	+0.4 -0.7	-2.1 +2.1	+0.8 -0.5	-0.2 +0.2	+1.0 -1.0	+2.4 -2.4	+3.3 -3.3
	0.21	$6.76 \cdot 10^{-2}$	59		+14.8 -11.5	+3.5 -3.9	+0.4 -1.0	-0.9 +0.1	-1.9 +1.4	+0.1 -0.4	+0.7 -0.7	+2.4 -2.4	+1.0 -1.0
	0.30	$3.05 \cdot 10^{-2}$	37		+19.2 -13.8	+4.0 -3.8	+1.4 -0.7	-0.3 +0.9	-1.3 +1.3	+0.6 -1.1	+1.2 -1.2	+2.4 -2.4	+1.0 -1.0
2644	0.41	$1.56 \cdot 10^{-2}$	25		+24.2 -16.2	+6.9 -5.2	+2.2 -0.7	+1.4 +1.0	-1.8 +2.6	+3.1 -0.5	+2.7 -2.7	+2.4 -2.4	+2.7 -2.7
	0.06	$1.78 \cdot 10^{-1}$	71		+13.3 -10.6	+5.4 -5.5	+0.5 -1.3	-2.1 +2.5	-0.5 +0.0	-0.1 -0.6	+2.0 -2.0	+2.4 -2.4	+3.3 -3.3
	0.11	$9.53 \cdot 10^{-2}$	53		+15.7 -12.0	+4.7 -4.8	+0.6 -0.7	-1.2 +0.4	+0.0 +0.7	-0.2 +0.1	+1.6 -1.6	+2.4 -2.4	+3.3 -3.3
	0.16	$6.08 \cdot 10^{-2}$	53		+15.7 -12.0	+4.9 -4.8	+0.8 -0.5	-1.5 +1.8	-0.6 +0.5	-0.4 -0.1	+0.9 -0.9	+2.4 -2.4	+3.3 -3.3
	0.23	$3.70 \cdot 10^{-2}$	41		+18.1 -13.3	+3.4 -3.7	+0.7 -0.7	-0.6 +0.6	-1.6 +0.7	+0.3 -0.4	+0.7 -0.7	+2.4 -2.4	+1.0 -1.0
	0.33	$1.54 \cdot 10^{-2}$	24		+24.9 -16.5	+5.6 -4.9	+3.9 -1.9	-2.3 +1.1	-0.5 +1.2	+1.4 -1.7	+1.6 -1.6	+2.4 -2.4	+1.0 -1.0
3073	0.45	$7.21 \cdot 10^{-3}$	13		+36.0 -20.8	+5.9 -7.8	+0.8 -3.0	-2.5 +0.6	-4.4 +2.5	-0.3 +1.2	+3.3 -3.3	+2.4 -2.4	+2.7 -2.7
	0.07	$9.55 \cdot 10^{-2}$	51		+16.1 -12.2	+5.5 -5.2	+1.7 -1.6	-1.1 +2.1	-0.1 -0.1	+0.1 -0.5	+2.0 -2.0	+2.4 -2.4	+3.3 -3.3
	0.12	$6.15 \cdot 10^{-2}$	42		+17.9 -13.1	+5.1 -5.3	+1.9 -1.4	-2.0 +1.0	-1.0 +0.6	-0.6 +0.0	+1.4 -1.4	+2.4 -2.4	+3.3 -3.3
	0.18	$3.67 \cdot 10^{-2}$	40		+18.5 -13.4	+4.9 -5.2	+0.6 -0.9	-2.4 +2.0	-0.4 -0.8	-0.2 -0.1	+0.8 -0.8	+2.4 -2.4	+3.3 -3.3
	0.26	$2.30 \cdot 10^{-2}$	31		+21.4 -14.9	+4.0 -3.9	+0.6 -0.6	-1.2 +0.6	-1.8 +2.3	+0.3 +0.2	+0.9 -0.9	+2.4 -2.4	+1.0 -1.0
	0.36	$1.25 \cdot 10^{-2}$	24		+24.9 -16.5	+4.5 -4.3	+0.7 -0.8	-1.1 +0.6	-1.4 +2.1	+1.0 -0.9	+2.1 -2.1	+2.4 -2.4	+1.0 -1.0
3568	0.49	$5.38 \cdot 10^{-3}$	13		+36.0 -20.8	+6.5 -7.2	+0.7 -1.3	+0.6 -0.5	-4.0 +3.2	-0.2 -1.9	+3.8 -3.8	+2.4 -2.4	+2.7 -2.7
	0.09	$5.61 \cdot 10^{-2}$	39		+18.7 -13.6	+5.8 -5.1	+2.3 -0.7	-1.7 +2.2	+0.4 +0.7	+0.3 -0.8	+1.9 -1.9	+2.4 -2.4	+3.3 -3.3
	0.14	$2.97 \cdot 10^{-2}$	27		+23.1 -15.8	+4.9 -6.1	+0.6 -3.5	-1.2 +1.6	-1.8 +0.7	-0.6 +0.7	+1.1 -1.1	+2.4 -2.4	+3.3 -3.3
	0.21	$1.67 \cdot 10^{-2}$	22		+26.2 -17.2	+3.8 -3.4	+0.7 -0.7	-1.1 +1.8	-0.1 +0.7	-0.1 -0.1	+0.7 -0.7	+2.4 -2.4	+1.0 -1.0
	0.29	$1.04 \cdot 10^{-2}$	19		+28.6 -18.0	+4.2 -3.4	+1.1 -0.4	+0.6 +1.9	-0.9 +1.3	+0.1 -0.3	+1.2 -1.2	+2.4 -2.4	+1.0 -1.0

Table B.1 (continued):

Q^2 (GeV ²)	x	$d^2\sigma/dxdQ^2$ (pb/GeV ²)	Nevt.	upper limit (pb/GeV ²)	stat. (%)	total sys. (%)	uncor. sys. (%)	δ_1 (%)	δ_2 (%)	δ_3 (%)	δ_4 (%)	δ_5 (%)	δ_6 (%)
4145	0.40	$6.43 \cdot 10^{-3}$	16		+31.8 -19.2	+6.6 -5.7	+1.3 -0.1	-1.2 +4.1	-2.7 +1.6	+0.8 -1.0	+2.6 -2.6	+2.4 -2.4	+2.7 -2.7
	0.53	$1.37 \cdot 10^{-3}$	4		+78.5 -28.9	+7.8 -7.5	+1.5 -0.6	-0.2 +1.6	-4.6 +4.5	+0.8 -0.3	+4.3 -4.3	+2.4 -2.4	+2.7 -2.7
	0.10	$3.18 \cdot 10^{-2}$	26		+23.7 -16.1	+5.2 -6.5	+0.4 -3.5	-2.6 +2.2	-1.0 +0.2	+0.2 -0.5	+1.7 -1.7	+2.4 -2.4	+3.3 -3.3
	0.16	$2.61 \cdot 10^{-2}$	32		+21.0 -14.7	+5.6 -5.2	+3.1 -1.0	-2.5 +1.5	-0.3 +0.5	-0.4 +0.3	+0.9 -0.9	+2.4 -2.4	+3.3 -3.3
	0.23	$7.72 \cdot 10^{-3}$	14		+34.6 -20.1	+7.6 -4.4	+6.8 -1.1	-2.5 +0.7	-1.3 +1.3	-0.2 -0.4	+0.7 -0.7	+2.4 -2.4	+1.0 -1.0
	0.33	$8.50 \cdot 10^{-3}$	20		+27.7 -17.8	+4.3 -4.6	+0.7 -1.1	-2.3 +1.8	-1.7 +1.5	+0.4 +0.3	+1.6 -1.6	+2.4 -2.4	+1.0 -1.0
	0.44	$3.03 \cdot 10^{-3}$	9		+45.6 -23.5	+5.3 -13.0	+0.0 -10.9	-1.6 -0.7	-4.0 +1.0	+0.5 -2.1	+3.3 -3.3	+2.4 -2.4	+2.7 -2.7
4806	0.58	$2.96 \cdot 10^{-4}$	1		+218.6 -29.8	+10.9 -7.4	+1.3 -2.4	+0.0 -2.0	-2.6 +7.7	-0.9 +4.4	+4.7 -4.7	+2.4 -2.4	+2.7 -2.7
	0.12	$1.76 \cdot 10^{-2}$	18		+29.6 -18.5	+4.8 -7.0	+0.6 -5.0	-1.6 +1.3	+0.4 -0.4	+0.3 -0.3	+1.5 -1.5	+2.4 -2.4	+3.3 -3.3
	0.18	$1.36 \cdot 10^{-2}$	20		+27.7 -17.8	+5.2 -4.8	+1.1 -0.6	-0.4 +1.2	-1.6 +2.2	-0.9 +0.3	+0.7 -0.7	+2.4 -2.4	+3.3 -3.3
	0.26	$5.44 \cdot 10^{-3}$	12		+38.1 -21.3	+3.7 -3.6	+0.6 -0.8	-0.8 +1.6	-1.4 +0.8	+0.1 +0.0	+0.9 -0.9	+2.4 -2.4	+1.0 -1.0
	0.36	$3.48 \cdot 10^{-3}$	10		+42.7 -22.6	+5.1 -4.5	+1.6 -0.5	-1.2 +2.8	-2.1 +1.3	-0.2 -0.7	+2.1 -2.1	+2.4 -2.4	+1.0 -1.0
	0.49	$1.12 \cdot 10^{-3}$	4		+78.5 -28.9	+7.6 -6.5	+1.8 -0.6	-1.6 +2.8	-2.8 +3.9	+1.0 -0.5	+3.9 -3.9	+2.4 -2.4	+2.7 -2.7
	0.63	$9.18 \cdot 10^{-4}$	4		+78.5 -29.0	+12.2 -8.1	+1.0 -2.0	-2.3 -0.3	-4.8 +9.6	-1.0 +4.8	+4.9 -4.9	+2.4 -2.4	+0.1 -0.1
5561	0.09	$2.26 \cdot 10^{-2}$	15		+33.1 -19.8	+6.9 -9.6	+1.8 -6.5	-4.1 +3.5	+3.1 -3.1	-0.1 -0.5	+1.9 -1.9	+2.4 -2.4	+3.3 -3.3
	0.14	$1.42 \cdot 10^{-2}$	21		+26.9 -17.4	+5.2 -5.2	+0.7 -1.4	-2.2 +2.5	-0.3 +0.6	-0.1 -0.4	+1.1 -1.1	+2.4 -2.4	+3.3 -3.3
	0.21	$3.41 \cdot 10^{-3}$	6		+59.7 -26.4	+3.5 -4.2	+0.6 -0.9	-2.0 +1.5	-1.4 -0.3	-0.7 +0.3	+0.7 -0.7	+2.4 -2.4	+1.0 -1.0
	0.30	$4.92 \cdot 10^{-3}$	14		+34.6 -20.1	+4.3 -4.4	+0.4 -0.7	-2.4 +1.1	-1.7 +2.5	+0.1 -0.3	+1.2 -1.2	+2.4 -2.4	+1.0 -1.0
	0.41	$2.56 \cdot 10^{-3}$	9		+45.6 -23.5	+5.0 -5.8	+0.7 -1.5	-1.8 +0.0	-2.1 +1.0	+0.4 -0.2	+2.8 -2.8	+2.4 -2.4	+2.7 -2.7
	0.54	$9.13 \cdot 10^{-4}$	4		+78.5 -28.9	+8.0 -8.0	+0.4 -2.2	-1.8 -0.1	-4.2 +5.1	-0.3 -1.1	+4.6 -4.6	+2.4 -2.4	+2.7 -2.7
	0.69	$6.11 \cdot 10^{-4}$	3		+96.3 -30.4	+12.7 -9.9	+5.8 -2.1	+0.3 +1.8	-7.3 +9.2	-3.1 +3.1	+4.6 -4.6	+2.4 -2.4	+0.1 -0.1
6966	0.11	$6.88 \cdot 10^{-3}$	13		+36.0 -20.8	+6.3 -9.9	+0.4 -6.6	-4.2 +2.3	+3.5 -3.6	-0.1 -1.5	+1.8 -1.8	+2.4 -2.4	+3.3 -3.3
	0.17	$6.24 \cdot 10^{-3}$	25		+24.2 -16.2	+4.7 -7.8	+0.0 -5.3	-2.9 +1.7	-2.0 +0.3	-0.6 -0.2	+0.8 -0.8	+2.4 -2.4	+3.3 -3.3

Table B.1 (continued):

Q^2 (GeV ²)	x	$d^2\sigma/dxdQ^2$ (pb/GeV ²)	Nevt.	upper limit (pb/GeV ²)	stat. (%)	total sys. (%)	uncor. sys. (%)	δ_1 (%)	δ_2 (%)	δ_3 (%)	δ_4 (%)	δ_5 (%)	δ_6 (%)	
9055	0.25	$2.85 \cdot 10^{-3}$	15	$< 4.42 \cdot 10^{-5}$	+33.1 -19.8	+3.7 -3.7	+0.6 -0.8	-1.6 +1.8	-0.4 +0.8	-0.5 +0.0	+0.7 -0.7	+2.4 -2.4	+1.0 -1.0	
	0.34	$2.52 \cdot 10^{-3}$	22		+26.2 -17.2	+4.3 -4.3	+0.7 -0.8	-1.3 +1.9	-1.9 +1.3	+0.1 -0.1	+1.8 -1.8	+2.4 -2.4	+1.0 -1.0	
	0.47	$6.97 \cdot 10^{-4}$	7		+53.7 -25.2	+7.1 -6.4	+1.1 -0.4	-0.7 +1.3	-3.3 +4.2	+0.3 -0.5	+3.7 -3.7	+2.4 -2.4	+2.7 -2.7	
	0.61	$6.75 \cdot 10^{-4}$	8		+49.2 -24.4	+9.4 -9.9	+1.3 -0.6	-1.1 +3.0	-7.9 +6.6	-0.5 -0.1	+5.0 -5.0	+2.4 -2.4	+0.1 -0.1	
	0.78	0	0											
	0.16	$5.35 \cdot 10^{-3}$	16		+31.9 -19.2	+6.5 -12.4	+0.4 -9.9	-4.6 +3.8	+2.6 -3.4	+0.6 -1.4	+1.0 -1.0	+2.4 -2.4	+3.3 -3.3	
	0.23	$2.96 \cdot 10^{-3}$	17		+30.5 -18.8	+3.8 -4.9	+1.3 -1.7	-2.6 +1.2	-1.9 +1.2	-1.1 +0.3	+0.4 -0.4	+2.4 -2.4	+1.0 -1.0	
	0.33	$1.23 \cdot 10^{-3}$	12		+38.1 -21.3	+4.0 -4.5	+0.6 -0.7	-2.2 +1.6	-1.7 +1.4	-0.3 -0.1	+1.5 -1.5	+2.4 -2.4	+1.0 -1.0	
	0.45	$4.31 \cdot 10^{-4}$	5		+67.3 -27.5	+6.3 -6.9	+0.4 -0.7	-1.3 +0.4	-4.2 +3.4	+0.1 -0.3	+3.4 -3.4	+2.4 -2.4	+2.7 -2.7	
	0.59	$2.12 \cdot 10^{-4}$	3		+96.3 -30.4	+9.8 -7.0	+0.6 -0.7	-1.4 -0.4	-2.3 +7.3	+0.1 +0.3	+5.1 -5.1	+2.4 -2.4	+2.7 -2.7	
	0.73	$6.86 \cdot 10^{-5}$	1		+218.6 -29.8	+10.2 -24.7	+1.1 -6.2	-2.3 -2.5	-23.0 +8.3	-0.9 +2.2	+4.6 -4.6	+2.4 -2.4	+0.1 -0.1	
14807	0.90	0	0	$< 8.12 \cdot 10^{-6}$										
	0.76	$1.03 \cdot 10^{-5}$	1	+218.6 -29.8	+14.5 -15.9	+2.1 -2.6	-2.7 +1.6	-14.9 +13.7	-1.5 +0.7	+2.5 -2.5	+2.4 -2.4	+0.1 -0.1		
	0.92	0	0	$< 1.28 \cdot 10^{-6}$										

Q^2 (GeV ²)	x_{edge}	$\int_{x_{edge}}^1 d^2\sigma/dxdQ^2$ (pb/GeV ²)	Nevt.	upper limit (pb/GeV ²)	stat. (%)	total sys. (%)	uncor. sys. (%)	δ_1 (%)	δ_2 (%)	δ_3 (%)	δ_4 (%)	δ_5 (%)	δ_6 (%)
648	0.25	$8.49 \cdot 10^{-2}$	34		+20.2 -14.4	+8.5 -6.7	+4.9 -2.7	+6.1 -5.2	+0.6 +0.6	-0.8 +1.1	+2.0 -2.0	+1.6 -1.6	+0.1 -0.1
761	0.27	$4.66 \cdot 10^{-2}$	74		+13.0 -10.3	+5.1 -3.6	+1.8 -1.1	+3.0 -0.6	+0.9 +0.9	-0.7 +0.7	+2.5 -2.5	+1.6 -1.6	+0.1 -0.1
891	0.30	$3.19 \cdot 10^{-2}$	109		+10.5 -8.7	+6.5 -3.7	+4.6 -0.1	+2.2 +0.5	+1.1 +1.1	-1.0 +1.1	+2.7 -2.7	+1.6 -1.6	+0.1 -0.1
1045	0.32	$2.08 \cdot 10^{-2}$	101		+10.9 -9.1	+6.9 -5.8	+3.8 -0.6	-4.4 +4.2	+0.9 +0.9	-1.0 +0.7	+2.9 -2.9	+1.6 -1.6	+0.1 -0.1
1224	0.35	$1.03 \cdot 10^{-2}$	65		+14.0 -10.9	+6.0 -3.9	+3.0 -0.2	+0.6 +3.2	+0.7 +0.7	-0.4 +0.7	+3.1 -3.1	+1.6 -1.6	+0.1 -0.1
1431	0.38	$5.65 \cdot 10^{-3}$	42		+17.9 -13.1	+7.2 -6.0	+2.3 -0.1	-4.3 +5.3	+0.8 +0.8	-1.1 +0.7	+3.4 -3.4	+1.6 -1.6	+0.1 -0.1
1672	0.41	$3.66 \cdot 10^{-3}$	29		+22.3 -15.4	+5.8 -4.6	+2.2 -0.2	-1.3 +2.8	+0.5 +0.5	-0.7 +1.5	+3.7 -3.7	+1.6 -1.6	+0.1 -0.1
1951	0.44	$2.07 \cdot 10^{-3}$	21		+26.9 -17.4	+6.8 -5.5	+2.3 -0.6	-2.5 +4.1	+0.6 +0.6	-1.1 +1.0	+4.1 -4.1	+1.6 -1.6	+0.1 -0.1
2273	0.48	$1.22 \cdot 10^{-3}$	13		+36.0 -20.8	+7.3 -8.3	+4.1 -1.1	-5.7 +2.9	+0.4 +0.4	-2.9 +0.9	+4.6 -4.6	+1.6 -1.6	+0.1 -0.1

Table B.2: *The integral cross section table for 96-97 e^+p NC scattering. The first two columns of the table contain the Q^2 and x_{edge} values for the bin, the third contains the measured cross section $\int_{x_{edge}}^1 d^2\sigma/dxdQ^2$ corrected to the electroweak Born level, the fourth contains the number of events reconstructed in the bin, the fifth contains the upper limit in case of zero observed events, the sixth contains the statistical uncertainty and the seventh contains the total systematic uncertainty. The right part of the table lists the total uncorrelated systematic uncertainty followed by the bin-to-bin correlated systematic uncertainties δ_1 – δ_6 defined in the text. For the latter, the upper (lower) numbers refer to the variation of the cross section, whereas the signs of the numbers reflect the direction of change in the cross sections. Note that the normalization uncertainty, δ_7 is not listed.*

Table B.2 (continued):

Q^2 (GeV ²)	x_{edge}	$\int_{x_{edge}}^1 d^2\sigma/dxdQ^2$ (pb/GeV ²)	Nevt.	upper limit (pb/GeV ²)	stat. (%)	total sys. (%)	uncor. sys. (%)	δ_1 (%)	δ_2 (%)	δ_3 (%)	δ_4 (%)	δ_5 (%)	δ_6 (%)
2644	0.52	$2.87 \cdot 10^{-4}$	4		+78.5 -29.0	+8.7 -6.8	+2.2 -3.0	-2.1 +6.5	+0.5 +0.5	-2.3 +0.9	+4.7 -4.7	+1.6 -1.6	+0.1 -0.1
3073	0.56	0	0	$< 8.32 \cdot 10^{-5}$									
3568	0.60	$6.04 \cdot 10^{-5}$	1		+218.6 -29.8	+16.0 -15.3	+4.5 -3.1	-6.1 +6.1	+1.4 +1.4	-2.1 +3.7	+4.7 -4.7	+1.6 -1.6	+12.5 -12.5
4145	0.65	0	0	$< 5.30 \cdot 10^{-5}$									
4806	0.70	0	0	$< 5.79 \cdot 10^{-5}$									
5561	0.76	0	0	$< 3.87 \cdot 10^{-5}$									
6966	0.89	0	0	$< 1.61 \cdot 10^{-6}$									

Q^2 (GeV ²)	x	$d^2\sigma/dxdQ^2$ (pb/GeV ²)	Nevt.	upper limit (pb/GeV ²)	stat. (%)	total sys. (%)	uncor. sys. (%)	δ_1 (%)	δ_2 (%)	δ_3 (%)	δ_4 (%)	δ_5 (%)	δ_6 (%)
648	0.08	$2.76 \cdot 10^0$	51		+16.1 -12.2	+8.3 -9.0	+0.7 -0.4	-7.0 +5.6	-1.1 +1.1	-3.0 +3.6	+0.1 -0.1	+2.4 -2.4	+3.4 -3.4
	0.13	$1.78 \cdot 10^0$	23		+25.4 -16.9	+9.1 -11.9	+3.6 -3.3	-8.4 +6.0	-1.3 +0.1	-6.1 +3.3	+0.0 -0.0	+2.4 -2.4	+3.4 -3.4
	0.19	$8.63 \cdot 10^{-1}$	14		+34.6 -20.1	+11.0 -14.9	+1.0 -9.2	-9.2 +8.8	-1.4 +1.3	-5.4 +4.3	+0.0 +0.0	+2.4 -2.4	+3.4 -3.4
761	0.09	$1.71 \cdot 10^0$	92		+11.6 -9.4	+6.1 -5.8	+1.0 -1.4	-2.5 +3.6	-0.9 +0.8	-1.6 +1.2	+0.1 -0.1	+2.4 -2.4	+3.3 -3.3
	0.14	$8.70 \cdot 10^{-1}$	44		+17.5 -13.0	+6.5 -6.5	+1.1 -1.1	-4.3 +4.2	-0.4 +0.3	-0.7 +1.4	+0.1 -0.1	+2.4 -2.4	+3.3 -3.3
	0.21	$6.10 \cdot 10^{-1}$	38		+19.0 -13.8	+6.8 -6.7	+1.3 -1.1	-4.0 +2.8	-1.4 +2.8	-2.0 +2.8	+0.0 -0.0	+2.4 -2.4	+3.3 -3.3
891	0.10	$1.36 \cdot 10^0$	137		+9.3 -7.9	+4.8 -4.7	+0.6 -0.2	+0.0 -0.4	-0.6 +1.2	-0.2 -0.1	+0.1 -0.1	+2.4 -2.4	+3.2 -3.2
	0.15	$6.16 \cdot 10^{-1}$	61		+14.5 -11.3	+5.0 -4.8	+0.5 -0.2	-0.2 +0.6	-1.4 +0.2	+0.0 +1.7	+0.1 -0.1	+2.4 -2.4	+3.2 -3.2
	0.22	$5.20 \cdot 10^{-1}$	68		+13.7 -10.7	+5.5 -5.3	+2.2 -2.2	-1.3 +1.7	+0.4 +1.2	-0.2 -0.2	+0.0 +0.0	+2.4 -2.4	+3.2 -3.2
1045	0.07	$1.56 \cdot 10^0$	148		+9.0 -7.6	+4.9 -5.2	+0.1 -0.6	+1.9 -2.4	+0.2 +0.2	+0.8 -1.1	+0.0 -0.0	+2.4 -2.4	+2.9 -2.9

Table B.3: *The cross section table for 98-99 e^-p NC scattering. The first two columns of the table contain the Q^2 and x values at which the cross section is quoted, the third contains the measured cross section $d^2\sigma/dxdQ^2$ corrected to the electroweak Born level, the fourth contains the number of events reconstructed in the bin, the fifth contains the upper limit in case of zero observed events, the sixth contains the statistical uncertainty and the seventh contains the total systematic uncertainty. The right part of the table lists the total uncorrelated systematic uncertainty followed by the bin-to-bin correlated systematic uncertainties δ_1 – δ_6 defined in the text. For the latter, the upper (lower) numbers refer to the variation of the cross section, whereas the signs of the numbers reflect the direction of change in the cross sections. Note that the normalization uncertainty, δ_7 is not listed.*

Table B.3 (continued):

Q^2 (GeV ²)	x	$d^2\sigma/dxdQ^2$ (pb/GeV ²)	Nevt.	upper limit (pb/GeV ²)	stat. (%)	total sys. (%)	uncor. sys. (%)	δ_1 (%)	δ_2 (%)	δ_3 (%)	δ_4 (%)	δ_5 (%)	δ_6 (%)
1224	0.11	$6.53 \cdot 10^{-1}$	84		+12.1 -9.7	+4.6 -4.6	+0.3 -0.4	+0.2 -0.2	-1.3 +1.3	+0.4 -0.6	+0.1 -0.1	+2.4 -2.4	+2.9 -2.9
	0.17	$4.61 \cdot 10^{-1}$	67		+13.8 -10.8	+4.6 -4.8	+1.0 -1.4	+1.0 -0.2	-0.1 -0.2	-0.6 -1.2	+0.1 -0.1	+2.4 -2.4	+2.9 -2.9
	0.24	$2.02 \cdot 10^{-1}$	43		+17.7 -13.1	+4.8 -5.4	+1.1 -0.9	+0.4 -2.5	-1.5 +1.4	-0.4 +0.1	+0.1 -0.1	+2.4 -2.4	+2.9 -2.9
	0.07	$7.47 \cdot 10^{-1}$	87		+11.9 -9.6	+4.7 -4.9	+0.3 -1.1	+1.4 -1.7	+0.0 -0.4	+0.6 -0.4	+0.0 -0.0	+2.4 -2.4	+2.9 -2.9
	0.12	$4.90 \cdot 10^{-1}$	80		+12.5 -10.0	+4.7 -4.7	+0.3 -0.3	+0.9 -1.5	-0.9 +1.3	+0.5 -0.1	+0.1 -0.1	+2.4 -2.4	+2.9 -2.9
	0.18	$3.83 \cdot 10^{-1}$	70		+13.4 -10.6	+4.8 -4.6	+1.5 -0.2	-0.5 -1.0	-0.9 +0.3	+1.1 +0.2	+0.1 -0.1	+2.4 -2.4	+2.9 -2.9
1431	0.26	$1.63 \cdot 10^{-1}$	44		+17.5 -13.0	+5.1 -4.9	+1.0 -1.7	+0.5 +0.0	-0.7 +1.8	+1.6 -1.0	+0.1 -0.1	+2.4 -2.4	+2.9 -2.9
	0.09	$5.65 \cdot 10^{-1}$	79		+12.6 -10.0	+4.8 -4.8	+0.3 -0.7	+1.7 -1.4	+0.6 +0.3	+0.7 -1.3	+0.1 -0.1	+2.4 -2.4	+2.8 -2.8
	0.14	$2.69 \cdot 10^{-1}$	55		+15.4 -11.7	+4.6 -4.9	+1.0 -0.5	+0.9 -1.9	-1.1 +0.9	+0.4 +0.0	+0.1 -0.1	+2.4 -2.4	+2.8 -2.8
	0.20	$1.92 \cdot 10^{-1}$	41		+18.1 -13.3	+5.0 -5.3	+1.1 -0.7	+2.1 -1.7	-1.3 +0.7	+0.8 -2.0	+0.0 -0.0	+2.4 -2.4	+2.8 -2.8
	0.29	$1.29 \cdot 10^{-1}$	41		+18.1 -13.3	+4.8 -4.7	+1.0 -0.9	+0.9 -1.5	-0.6 +1.6	-0.1 -0.1	+0.2 -0.2	+2.4 -2.4	+2.8 -2.8
	0.10	$3.25 \cdot 10^{-1}$	57		+15.1 -11.5	+4.3 -4.2	+0.3 -0.5	+1.2 -0.7	-0.3 -0.2	+0.4 -0.2	+0.1 -0.1	+2.4 -2.4	+2.5 -2.5
1672	0.15	$2.04 \cdot 10^{-1}$	52		+15.9 -12.1	+4.6 -4.5	+0.4 -0.5	+1.3 -0.5	-1.2 +1.6	+0.3 -1.0	+0.1 -0.1	+2.4 -2.4	+2.5 -2.5
	0.22	$1.03 \cdot 10^{-1}$	28		+22.7 -15.5	+4.2 -4.6	+0.1 -0.5	+0.9 -1.6	-0.1 -0.6	+0.3 -0.8	+0.0 -0.0	+2.4 -2.4	+2.5 -2.5
	0.31	$3.74 \cdot 10^{-2}$	16		+31.8 -19.2	+5.1 -5.3	+1.2 -1.5	+1.0 -1.9	-2.0 +2.5	+0.1 -1.1	+0.3 -0.3	+2.4 -2.4	+2.5 -2.5
	0.07	$3.91 \cdot 10^{-1}$	60		+14.6 -11.4	+4.1 -4.3	+0.3 -0.7	+1.0 -0.8	-1.1 +0.5	+0.2 -0.9	+0.0 -0.0	+2.4 -2.4	+2.2 -2.2
	0.11	$1.86 \cdot 10^{-1}$	39		+18.7 -13.6	+4.9 -4.4	+0.7 -0.6	+2.4 -1.3	+1.2 -0.7	+0.7 -1.0	+0.1 -0.1	+2.4 -2.4	+2.2 -2.2
	0.17	$1.22 \cdot 10^{-1}$	37		+19.2 -13.8	+4.1 -4.9	+0.2 -2.7	+0.3 +0.2	-1.2 +0.5	+0.6 +0.7	+0.1 -0.1	+2.4 -2.4	+2.2 -2.2
1951	0.24	$7.22 \cdot 10^{-2}$	26		+23.7 -16.1	+5.0 -4.5	+0.9 -0.8	+2.6 -0.4	-1.9 +1.1	+0.2 -0.6	+0.1 -0.1	+2.4 -2.4	+2.2 -2.2
	0.34	$3.48 \cdot 10^{-2}$	18		+29.6 -18.5	+4.8 -4.7	+1.8 -1.8	-0.3 -0.2	-1.1 +1.9	-0.6 -1.0	+0.4 -0.4	+2.4 -2.4	+2.2 -2.2

Table B.3 (continued):

Q^2 (GeV ²)	x	$d^2\sigma/dxdQ^2$ (pb/GeV ²)	Nevt.	upper limit (pb/GeV ²)	stat. (%)	total sys. (%)	uncor. sys. (%)	δ_1 (%)	δ_2 (%)	δ_3 (%)	δ_4 (%)	δ_5 (%)	δ_6 (%)
2273	0.07	$3.25 \cdot 10^{-1}$	62		+14.4 -11.2	+4.5 -4.7	+0.5 -1.2	+1.6 -2.0	-0.9 +0.2	+1.2 -0.5	+0.0 +0.0	+2.4 -2.4	+2.2 -2.2
	0.12	$1.19 \cdot 10^{-1}$	31		+21.4 -14.9	+4.2 -4.8	+0.6 -1.0	+0.7 -2.4	+0.5 -0.6	+0.9 -0.5	+0.1 -0.1	+2.4 -2.4	+2.2 -2.2
	0.18	$7.59 \cdot 10^{-2}$	29		+22.3 -15.4	+4.2 -4.5	+0.3 -0.9	+0.6 -1.1	-1.6 +1.3	+0.5 -0.6	+0.1 -0.1	+2.4 -2.4	+2.2 -2.2
	0.26	$5.21 \cdot 10^{-2}$	23		+25.4 -16.9	+4.6 -4.5	+0.6 -0.7	+0.7 -1.9	-0.5 +1.1	+1.8 -0.2	+0.1 -0.1	+2.4 -2.4	+2.2 -2.2
	0.37	$1.60 \cdot 10^{-2}$	10		+42.7 -22.6	+6.0 -4.4	+2.5 -0.8	+2.0 -0.8	-1.6 +2.5	+1.7 -0.1	+0.5 -0.5	+2.4 -2.4	+2.2 -2.2
2644	0.09	$1.70 \cdot 10^{-1}$	41		+18.1 -13.3	+4.7 -4.6	+0.6 -1.8	+2.1 -1.3	-0.9 +0.8	+1.0 -0.8	+0.1 -0.1	+2.4 -2.4	+2.1 -2.1
	0.14	$7.79 \cdot 10^{-2}$	29		+22.3 -15.4	+4.2 -4.5	+0.2 -0.6	+1.4 -1.7	+0.3 +0.3	+0.7 -1.2	+0.1 -0.1	+2.4 -2.4	+2.1 -2.1
	0.21	$2.68 \cdot 10^{-2}$	12		+38.1 -21.3	+4.1 -4.5	+0.4 -0.2	+0.9 -0.4	-2.1 +0.7	+0.0 +0.0	+0.0 -0.0	+2.4 -2.4	+2.1 -2.1
	0.29	$3.26 \cdot 10^{-2}$	19		+28.6 -18.0	+4.9 -4.1	+2.0 -0.3	+1.0 -0.9	+0.3 +2.0	-0.5 -0.8	+0.2 -0.2	+2.4 -2.4	+2.1 -2.1
3073	0.40	$1.47 \cdot 10^{-2}$	11		+40.2 -22.0	+4.7 -6.3	+1.1 -2.1	+0.9 -1.7	-3.9 +2.2	+0.2 -1.2	+0.5 -0.5	+2.4 -2.4	+2.1 -2.1
	0.06	$1.16 \cdot 10^{-1}$	20		+27.7 -17.8	+4.9 -4.7	+0.4 -1.3	+2.3 -2.3	+1.3 -0.3	+1.5 -0.7	+0.1 -0.1	+2.4 -2.4	+2.0 -2.0
	0.10	$9.39 \cdot 10^{-2}$	25		+24.2 -16.2	+4.1 -5.8	+0.9 -3.8	+0.8 -1.5	-1.5 +0.7	+0.1 -0.4	+0.0 -0.0	+2.4 -2.4	+2.0 -2.0
	0.15	$4.29 \cdot 10^{-2}$	19		+28.6 -18.0	+4.6 -4.2	+0.6 -0.4	+2.0 -1.6	+0.4 +0.1	+1.2 -0.4	+0.1 -0.1	+2.4 -2.4	+2.0 -2.0
	0.23	$2.53 \cdot 10^{-2}$	14		+34.6 -20.1	+7.7 -4.9	+6.5 -0.3	+0.6 -1.6	-2.5 +1.6	+0.3 -0.8	+0.0 -0.0	+2.4 -2.4	+2.0 -2.0
3568	0.32	$1.46 \cdot 10^{-2}$	11		+40.2 -22.0	+4.0 -4.1	+0.4 -0.6	+0.0 -0.4	-1.3 +0.1	+0.3 +0.9	+0.2 -0.2	+2.4 -2.4	+2.0 -2.0
	0.43	$9.60 \cdot 10^{-4}$	1		+218.6 -29.8	+6.8 -4.5	+1.4 -1.7	-0.8 +0.0	-1.2 +5.4	+0.4 -0.4	+0.5 -0.5	+2.4 -2.4	+2.0 -2.0
	0.07	$1.22 \cdot 10^{-1}$	28		+22.7 -15.5	+4.0 -4.6	+0.9 -1.2	+1.1 -2.3	-0.0 -0.2	+0.7 -0.7	+0.0 -0.0	+2.4 -2.4	+1.7 -1.7
	0.11	$3.80 \cdot 10^{-2}$	14		+34.6 -20.1	+4.1 -8.2	+0.4 -7.1	+0.9 -1.4	+0.2 +1.3	+0.5 -0.8	+0.1 -0.1	+2.4 -2.4	+1.7 -1.7
	0.17	$3.06 \cdot 10^{-2}$	16		+31.8 -19.2	+4.1 -4.4	+0.2 -0.7	+1.7 -1.8	-0.9 -0.1	+0.7 -1.2	+0.1 -0.1	+2.4 -2.4	+1.7 -1.7
4145	0.25	$2.37 \cdot 10^{-2}$	17		+30.5 -18.8	+4.7 -4.2	+0.2 -0.4	+1.5 -1.3	-1.4 +2.3	+1.1 -0.5	+0.0 -0.0	+2.4 -2.4	+1.7 -1.7
	0.35	$1.02 \cdot 10^{-2}$	10		+42.7 -22.6	+4.6 -4.6	+1.9 -0.9	+0.8 -2.0	-0.9 +1.7	+0.8 -1.4	+0.3 -0.3	+2.4 -2.4	+1.7 -1.7
	0.47	$8.33 \cdot 10^{-4}$	1		+218.6 -29.8	+7.5 -5.7	+2.9 -1.9	+3.7 -2.5	-2.8 +4.3	+1.2 +0.1	+0.6 -0.6	+2.4 -2.4	+1.7 -1.7
	0.08	$5.23 \cdot 10^{-2}$	15		+33.1 -19.8	+7.8 -4.0	+6.5 -1.2	+2.0 -0.6	+1.3 -0.2	+0.6 -0.9	+0.0 -0.0	+2.4 -2.4	+1.6 -1.6

Table B.3 (continued):

Q^2 (GeV ²)	x	$d^2\sigma/dxdQ^2$ (pb/GeV ²)	Nevt.	upper limit (pb/GeV ²)	stat. (%)	total sys. (%)	uncor. sys. (%)	δ_1 (%)	δ_2 (%)	δ_3 (%)	δ_4 (%)	δ_5 (%)	δ_6 (%)
4806	0.13	$3.39 \cdot 10^{-2}$	16		+31.9 -19.2	+4.1 -4.2	+0.3 -0.8	+1.3 -0.3	-1.8 +1.1	+0.3 -0.6	+0.1 -0.1	+2.4 -2.4	+1.6 -1.6
	0.19	$1.88 \cdot 10^{-2}$	13		+36.0 -20.8	+4.0 -4.2	+0.8 -0.5	+1.3 -1.6	-0.7 +0.4	+0.2 -0.9	+0.1 -0.1	+2.4 -2.4	+1.6 -1.6
	0.28	$1.49 \cdot 10^{-2}$	14		+34.6 -20.1	+4.0 -4.2	+0.3 -0.6	+0.4 -1.1	-1.3 +1.4	+0.2 -1.0	+0.1 -0.1	+2.4 -2.4	+1.6 -1.6
	0.39	$3.33 \cdot 10^{-3}$	4		+78.5 -29.0	+5.6 -3.8	+2.5 -0.3	+1.8 +0.0	-0.7 +2.5	+0.6 +1.3	+0.4 -0.4	+2.4 -2.4	+1.6 -1.6
	0.51	$1.36 \cdot 10^{-3}$	2		+129.5 -32.0	+5.9 -8.9	+3.3 -2.6	+1.5 -0.6	-6.2 +2.9	-4.1 -1.7	+0.7 -0.7	+2.4 -2.4	+1.6 -1.6
	0.11	$3.28 \cdot 10^{-2}$	14		+34.6 -20.1	+4.5 -4.4	+0.2 -0.7	+1.5 -2.4	+1.1 +1.1	+1.8 -0.4	+0.0 +0.0	+2.4 -2.4	+1.4 -1.4
	0.16	$1.70 \cdot 10^{-2}$	10		+42.7 -22.6	+4.5 -4.5	+0.3 -0.8	+0.6 -1.2	-2.2 +2.6	+0.9 -0.9	+0.1 -0.1	+2.4 -2.4	+1.4 -1.4
	0.23	$1.38 \cdot 10^{-2}$	13		+36.0 -20.8	+4.1 -4.1	+0.6 -0.3	+1.7 +0.5	-1.6 -0.6	+0.6 -0.9	+0.0 -0.0	+2.4 -2.4	+1.4 -1.4
	0.33	$5.78 \cdot 10^{-3}$	7		+53.7 -25.2	+4.1 -5.2	+1.1 -0.3	+1.3 -2.2	-2.4 +1.0	+0.4 -1.8	+0.2 -0.2	+2.4 -2.4	+1.4 -1.4
	0.44	$5.73 \cdot 10^{-3}$	8		+49.2 -24.4	+5.0 -5.4	+1.2 -2.8	+0.7 -0.7	-2.6 +3.2	+0.2 -1.2	+0.4 -0.4	+2.4 -2.4	+1.4 -1.4
5561	0.56	$1.23 \cdot 10^{-3}$	2		+129.5 -32.0	+7.8 -11.7	+4.3 -1.1	-3.2 -3.9	-9.8 +3.3	+4.3 +0.1	+0.4 -0.4	+2.4 -2.4	+1.4 -1.4
	0.12	$1.90 \cdot 10^{-2}$	10		+42.7 -22.6	+4.1 -4.5	+0.2 -1.3	+1.8 -1.2	-1.7 -0.5	+1.2 -1.4	+0.0 -0.0	+2.4 -2.4	+1.2 -1.2
	0.18	$1.03 \cdot 10^{-2}$	8		+49.2 -24.4	+5.8 -3.7	+0.3 -0.4	+0.8 -1.1	+1.0 +4.5	+0.1 -0.1	+0.1 -0.1	+2.4 -2.4	+1.2 -1.2
	0.26	$4.73 \cdot 10^{-3}$	6		+59.7 -26.4	+4.0 -4.0	+0.5 -0.3	+1.2 -1.2	-1.5 +1.5	+0.0 -0.4	+0.1 -0.1	+2.4 -2.4	+1.2 -1.2
	0.37	$6.69 \cdot 10^{-4}$	1		+218.6 -29.8	+4.2 -4.3	+1.2 -0.6	+0.8 -0.4	-2.4 +1.3	+0.6 +0.8	+0.3 -0.3	+2.4 -2.4	+1.2 -1.2
	0.49	$1.70 \cdot 10^{-3}$	3		+96.3 -30.4	+5.6 -7.2	+1.7 -3.5	-2.1 -4.0	-2.4 +3.9	+0.9 -0.5	+0.6 -0.6	+2.4 -2.4	+1.2 -1.2
	0.61	0	0	$< 6.44 \cdot 10^{-4}$									
6966	0.14	$1.37 \cdot 10^{-2}$	22		+26.2 -17.2	+4.1 -5.2	+0.9 -3.1	+1.8 -2.1	-0.9 +0.1	+0.8 -0.7	+0.0 -0.0	+2.4 -2.4	+1.0 -1.0
	0.21	$6.68 \cdot 10^{-3}$	14		+34.6 -20.1	+4.1 -4.2	+0.4 -0.8	+1.5 -1.5	-1.8 +1.3	+0.7 -0.5	+0.0 -0.0	+2.4 -2.4	+1.0 -1.0
	0.30	$2.06 \cdot 10^{-3}$	7		+53.7 -25.2	+4.6 -4.1	+0.3 -0.5	+1.8 -0.9	-2.0 +2.3	+0.7 -0.6	+0.2 -0.2	+2.4 -2.4	+1.0 -1.0
	0.41	$1.87 \cdot 10^{-3}$	7		+53.7 -25.2	+4.7 -4.4	+0.8 -0.3	+1.7 -0.8	-2.4 +2.5	+0.6 -0.8	+0.4 -0.4	+2.4 -2.4	+1.0 -1.0
	0.53	$2.14 \cdot 10^{-4}$	1		+218.6 -29.8	+6.1 -4.9	+0.3 -0.7	+1.6 -0.8	-3.2 +4.7	+0.6 -1.0	+0.5 -0.5	+2.4 -2.4	+1.0 -1.0
	0.69	$1.17 \cdot 10^{-4}$	1		+218.6 -29.8	+18.1 -16.7	+13.7 -14.7	+4.2 +4.5	-7.0 +9.5	-0.5 -1.4	+0.6 -0.6	+2.4 -2.4	+1.0 -1.0

Table B.3 (continued):

Q^2 (GeV ²)	x	$d^2\sigma/dxdQ^2$ (pb/GeV ²)	Nevt.	upper limit (pb/GeV ²)	stat. (%)	total sys. (%)	uncor. sys. (%)	δ_1 (%)	δ_2 (%)	δ_3 (%)	δ_4 (%)	δ_5 (%)	δ_6 (%)	
9059	0.13	$5.13 \cdot 10^{-3}$	4		+78.5 -29.0	+8.1 -22.5	+0.9 -21.8	+2.8 -3.4	+6.6 -2.8	+1.7 -1.5	+0.0 -0.0	+2.4 -2.4	+0.7 -0.7	
	0.19	$3.64 \cdot 10^{-3}$	8		+49.2 -24.4	+4.4 -5.0	+0.7 -2.1	+2.3 -2.5	-1.0 +1.1	+1.1 -1.5	+0.1 -0.1	+2.4 -2.4	+0.7 -0.7	
	0.27	$3.10 \cdot 10^{-3}$	11		+40.2 -22.0	+4.0 -4.3	+0.5 -1.0	+1.1 -1.6	-1.8 +1.8	+0.6 -0.7	+0.1 -0.1	+2.4 -2.4	+0.7 -0.7	
	0.38	$3.84 \cdot 10^{-4}$	2		+129.5 -32.0	+4.5 -5.7	+0.8 -0.6	+0.8 +0.3	-4.5 +2.7	+0.5 -0.3	+0.4 -0.4	+2.4 -2.4	+0.7 -0.7	
	0.51	$1.73 \cdot 10^{-4}$	1		+218.6 -29.8	+5.5 -4.9	+1.5 -1.2	+1.2 -1.0	-3.1 +3.8	+0.6 -0.7	+0.6 -0.6	+2.4 -2.4	+0.7 -0.7	
	0.64	0	0	$< 1.83 \cdot 10^{-4}$										
	0.78	$9.12 \cdot 10^{-5}$	1		+218.6 -29.8	+9.9 -12.8	+1.8 -1.1	+1.0 -1.6	-12.0 +8.8	+0.4 -0.3	+2.2 -2.2	+2.4 -2.4	+0.7 -0.7	
	0.93	0	0	$< 1.08 \cdot 10^{-5}$										
15072	0.61	$8.57 \cdot 10^{-5}$	3		+96.3 -30.4	+21.7 -25.0	+18.3 -20.2	-5.9 -9.5	-8.9 +11.1	+0.4 -1.1	+0.9 -0.9	+2.4 -2.4	+0.5 -0.5	
	0.75	0	0	$< 1.97 \cdot 10^{-5}$										
	0.91	0	0	$< 2.04 \cdot 10^{-6}$										

Q^2 (GeV ²)	x_{edge}	$\int_{x_{edge}}^1 d^2\sigma/dxdQ^2$ (pb/GeV ²)	Nevt.	upper limit (pb/GeV ²)	stat. (%)	total sys. (%)	uncor. sys. (%)	δ_1 (%)	δ_2 (%)	δ_3 (%)	δ_4 (%)	δ_5 (%)	δ_6 (%)
648	0.22	$8.74 \cdot 10^{-2}$	14		+34.6 -20.1	+8.7 -8.2	+3.7 -1.9	-5.9 +5.6	+0.0 +0.0	-3.0 +3.4	+0.3 -0.3	+1.6 -1.6	+3.4 -3.4
761	0.24	$7.12 \cdot 10^{-2}$	54		+15.5 -11.8	+5.5 -6.0	+0.5 -0.5	-3.7 +2.7	+0.0 -0.1	-1.9 +2.1	+0.2 -0.2	+1.6 -1.6	+3.3 -3.3
891	0.26	$3.44 \cdot 10^{-2}$	56		+15.2 -11.6	+4.5 -4.4	+1.3 -0.6	+0.3 -0.6	+0.0 -0.1	+0.6 -0.6	+0.2 -0.2	+1.6 -1.6	+3.2 -3.2
1045	0.29	$2.29 \cdot 10^{-2}$	54		+15.5 -11.8	+4.5 -4.5	+1.3 -0.9	+1.5 -1.5	+0.0 -0.2	+0.7 -1.0	+0.3 -0.3	+1.6 -1.6	+2.9 -2.9
1224	0.31	$9.38 \cdot 10^{-3}$	28		+22.7 -15.5	+4.9 -5.5	+0.2 -0.5	+2.4 -3.6	-0.2 -0.2	+1.4 -1.1	+0.2 -0.2	+1.6 -1.6	+2.9 -2.9
1431	0.34	$8.51 \cdot 10^{-3}$	29		+22.3 -15.4	+5.4 -5.5	+0.2 -0.1	+3.6 -2.9	+0.3 +0.2	+0.6 -2.4	+0.2 -0.2	+1.6 -1.6	+2.8 -2.8
1672	0.36	$6.31 \cdot 10^{-3}$	25		+24.2 -16.2	+4.4 -4.5	+0.8 -0.3	+1.4 -1.9	-0.4 -0.5	+1.7 -1.6	+0.2 -0.2	+1.6 -1.6	+2.5 -2.5
1951	0.39	$3.34 \cdot 10^{-3}$	16		+31.9 -19.2	+6.9 -4.3	+1.8 -1.6	+5.1 -1.6	+1.1 +1.0	+2.0 -0.9	+0.2 -0.2	+1.6 -1.6	+2.2 -2.2
2273	0.43	$1.61 \cdot 10^{-3}$	8		+49.2 -24.4	+5.6 -7.5	+3.1 -2.0	+2.9 -5.4	-0.5 -0.5	+1.0 -3.1	+0.2 -0.2	+1.6 -1.6	+2.2 -2.2

Table B.4: *The integral cross section table for 98-99 e^-p NC scattering. The first two columns of the table contain the Q^2 and x_{edge} values for the bin, the third contains the measured cross section $\int_{x_{edge}}^1 d^2\sigma/dxdQ^2$ corrected to the electroweak Born level, the fourth contains the number of events reconstructed in the bin, the fifth contains the upper limit in case of zero observed events, the sixth contains the statistical uncertainty and the seventh contains the total systematic uncertainty. The right part of the table lists the total uncorrelated systematic uncertainty followed by the bin-to-bin correlated systematic uncertainties δ_1 – δ_6 defined in the text. For the latter, the upper (lower) numbers refer to the variation of the cross section, whereas the signs of the numbers reflect the direction of change in the cross sections. Note that the normalization uncertainty, δ_7 is not listed.*

Table B.4 (continued):

Q^2 (GeV ²)	x_{edge}	$\int_{x_{edge}}^1 d^2\sigma/dxdQ^2$ (pb/GeV ²)	Nevt.	upper limit (pb/GeV ²)	stat. (%)	total sys. (%)	uncor. sys. (%)	δ_1 (%)	δ_2 (%)	δ_3 (%)	δ_4 (%)	δ_5 (%)	δ_6 (%)
2644	0.46	$8.11 \cdot 10^{-4}$	5		+67.3 -27.5	+6.3 -5.6	+2.1 -0.2	+3.9 -4.0	+1.4 +1.4	+1.9 -1.8	+0.2 -0.2	+1.6 -1.6	+2.1 -2.1
3073	0.50	0	0	$< 1.62 \cdot 10^{-4}$									
3568	0.54	$2.43 \cdot 10^{-4}$	2		+129.5 -32.0	+7.6 -4.5	+3.3 -0.5	+5.3 -2.5	+1.1 +0.8	+2.5 -1.9	+0.2 -0.2	+1.6 -1.6	+1.7 -1.7
4145	0.58	$2.06 \cdot 10^{-4}$	2		+129.5 -32.0	+6.2 -4.6	+0.7 -0.7	+3.6 -1.7	+0.1 +0.1	+3.9 -2.8	+0.1 -0.1	+1.6 -1.6	+1.6 -1.6
4806	0.63	0	0	$< 1.02 \cdot 10^{-4}$									
5561	0.68	0	0	$< 8.95 \cdot 10^{-5}$									
6966	0.79	0	0	$< 1.38 \cdot 10^{-5}$									
9059	1.00	0	0	$< 3.97 \cdot 10^{-1}$									

Q^2 (GeV ²)	x	$d^2\sigma/dxdQ^2$ (pb/GeV ²)	Nevt.	upper limit (pb/GeV ²)	stat. (%)	total sys. (%)	uncor. sys. (%)	δ_1 (%)	δ_2 (%)	δ_3 (%)	δ_4 (%)	δ_5 (%)	δ_6 (%)
648	0.08	$3.02 \cdot 10^0$	255		+6.6 -5.9	+7.8 -7.1	+1.3 -1.0	+5.8 -5.2	-0.9 +1.8	+0.2 -0.3	+0.3 -0.3	+2.4 -2.4	+3.3 -3.3
	0.13	$1.86 \cdot 10^0$	116		+10.2 -8.4	+7.5 -7.5	+2.1 -1.3	+5.2 -5.6	-1.0 +0.6	+1.8 +0.3	+0.2 -0.2	+2.4 -2.4	+3.3 -3.3
	0.19	$1.05 \cdot 10^0$	87		+11.9 -9.6	+11.1 -9.7	+4.7 -3.4	+8.6 -7.4	-1.2 +1.8	+1.0 -2.3	+0.1 -0.1	+2.4 -2.4	+3.3 -3.3
761	0.09	$1.85 \cdot 10^0$	403		+5.2 -4.7	+5.2 -5.5	+0.4 -0.9	+2.1 -2.6	-0.6 +0.7	+0.0 +0.1	+0.2 -0.2	+2.4 -2.4	+3.3 -3.3
	0.14	$9.89 \cdot 10^{-1}$	216		+7.3 -6.3	+6.0 -5.2	+0.6 -1.2	+3.6 -2.0	-0.7 +0.9	+0.9 -0.2	+0.0 -0.0	+2.4 -2.4	+3.3 -3.3
	0.21	$6.18 \cdot 10^{-1}$	161		+8.5 -7.3	+4.9 -5.4	+1.0 -0.7	+1.9 -3.1	-1.4 +1.8	+2.0 -2.4	+0.2 -0.2	+2.4 -2.4	+1.0 -1.0
891	0.10	$1.23 \cdot 10^0$	471		+4.8 -4.4	+4.7 -4.9	+0.3 -1.1	+0.5 -1.0	-0.7 +0.2	+0.3 -0.2	+0.1 -0.1	+2.4 -2.4	+3.3 -3.3
	0.15	$7.65 \cdot 10^{-1}$	301		+6.1 -5.4	+5.1 -4.9	+1.6 -0.4	-0.6 +0.1	-0.7 +1.1	+0.7 -1.1	+0.1 -0.1	+2.4 -2.4	+3.3 -3.3
	0.22	$3.64 \cdot 10^{-1}$	189		+7.9 -6.8	+4.9 -4.3	+2.2 -0.3	+2.4 -1.5	-1.7 +1.1	+0.9 -1.1	+0.2 -0.2	+2.4 -2.4	+1.0 -1.0
1045	0.07	$1.49 \cdot 10^0$	532		+4.5 -4.2	+5.5 -5.2	+0.7 -0.6	-2.3 +2.9	-0.1 +0.2	-0.6 +0.6	+0.1 -0.1	+2.4 -2.4	+3.3 -3.3

Table B.5: *The cross section table for 99-00 e^+p NC scattering. The first two columns of the table contain the Q^2 and x values at which the cross section is quoted, the third contains the measured cross section $d^2\sigma/dxdQ^2$ corrected to the electroweak Born level, the fourth contains the number of events reconstructed in the bin, the fifth contains the upper limit in case of zero observed events, the sixth contains the statistical uncertainty and the seventh contains the total systematic uncertainty. The right part of the table lists the total uncorrelated systematic uncertainty followed by the bin-to-bin correlated systematic uncertainties δ_1 – δ_6 defined in the text. For the latter, the upper (lower) numbers refer to the variation of the cross section, whereas the signs of the numbers reflect the direction of change in the cross sections. Note that the normalization uncertainty, δ_7 is not listed.*

Table B.5 (continued):

Q^2 (GeV ²)	x	$d^2\sigma/dxdQ^2$ (pb/GeV ²)	Nevt.	upper limit (pb/GeV ²)	stat. (%)	total sys. (%)	uncor. sys. (%)	δ_1 (%)	δ_2 (%)	δ_3 (%)	δ_4 (%)	δ_5 (%)	δ_6 (%)
1224	0.11	$7.98 \cdot 10^{-1}$	388		+5.3 -4.8	+4.9 -4.9	+0.9 -0.1	-0.2 +0.8	-1.4 +1.0	+0.0 -0.3	+0.1 -0.1	+2.4 -2.4	+3.3 -3.3
	0.17	$4.82 \cdot 10^{-1}$	253		+6.7 -5.9	+4.9 -4.8	+0.9 -0.7	+0.1 +0.5	-0.1 +0.1	+1.3 -1.1	+0.1 -0.1	+2.4 -2.4	+3.3 -3.3
	0.24	$2.21 \cdot 10^{-1}$	173		+8.2 -7.1	+4.3 -4.5	+0.6 -1.1	-2.0 +1.9	-0.8 +1.1	+1.3 -1.6	+0.2 -0.2	+2.4 -2.4	+1.0 -1.0
	0.07	$1.03 \cdot 10^0$	444		+5.0 -4.5	+4.9 -5.0	+0.8 -0.2	-1.7 +1.4	-0.1 +0.1	-0.4 +0.4	+0.2 -0.2	+2.4 -2.4	+3.3 -3.3
	0.12	$4.81 \cdot 10^{-1}$	294		+6.2 -5.5	+4.9 -5.1	+0.4 -0.9	-1.7 +1.6	-0.7 +0.1	-0.1 -0.3	+0.0 -0.0	+2.4 -2.4	+3.3 -3.3
	0.18	$2.99 \cdot 10^{-1}$	208		+7.4 -6.4	+4.8 -5.0	+0.5 -0.5	-0.8 +0.7	-1.0 +0.1	+0.9 -1.4	+0.1 -0.1	+2.4 -2.4	+3.3 -3.3
1431	0.26	$1.31 \cdot 10^{-1}$	139		+9.2 -7.8	+5.3 -3.8	+0.4 -0.6	-0.9 +0.9	-0.2 +1.9	+3.4 -1.2	+0.1 -0.1	+2.4 -2.4	+1.0 -1.0
	0.09	$5.29 \cdot 10^{-1}$	278		+6.4 -5.6	+5.0 -4.7	+0.5 -0.3	-0.4 +1.7	-0.0 -0.4	-0.2 +0.2	+0.1 -0.1	+2.4 -2.4	+3.3 -3.3
	0.14	$2.74 \cdot 10^{-1}$	212		+7.3 -6.4	+5.0 -4.8	+0.6 -0.3	-0.8 +0.9	-0.9 +1.4	-0.0 -0.1	+0.0 -0.0	+2.4 -2.4	+3.3 -3.3
	0.20	$1.51 \cdot 10^{-1}$	126		+9.7 -8.1	+3.8 -4.3	+0.8 -1.2	-1.4 +0.9	-0.6 +0.4	+1.0 -1.7	+0.2 -0.2	+2.4 -2.4	+1.0 -1.0
1672	0.29	$0.99 \cdot 10^{-1}$	119		+10.1 -8.3	+5.2 -4.5	+1.9 -0.1	-0.2 +2.2	-1.8 +1.5	+2.2 -2.1	+0.0 -0.0	+2.4 -2.4	+1.0 -1.0
	0.10	$3.71 \cdot 10^{-1}$	249		+6.8 -6.0	+4.9 -5.0	+0.6 -0.6	-1.6 +1.5	-0.1 +0.3	-0.2 +0.2	+0.1 -0.1	+2.4 -2.4	+3.3 -3.3
	0.15	$1.93 \cdot 10^{-1}$	183		+8.0 -6.9	+4.8 -4.9	+0.5 -0.7	-1.1 +1.1	-0.7 +0.7	+0.2 -0.1	+0.1 -0.1	+2.4 -2.4	+3.3 -3.3
	0.22	$1.05 \cdot 10^{-1}$	113		+10.3 -8.6	+3.7 -4.1	+0.2 -0.8	-1.3 +0.8	-0.3 +0.1	+1.0 -1.4	+0.1 -0.1	+2.4 -2.4	+1.0 -1.0
1951	0.31	$6.10 \cdot 10^{-2}$	96		+11.3 -9.2	+5.0 -4.2	+1.0 -0.3	-0.6 +0.6	-2.1 +2.9	+1.7 -0.7	+0.1 -0.1	+2.4 -2.4	+1.0 -1.0
	0.07	$3.77 \cdot 10^{-1}$	215		+7.3 -6.3	+4.9 -4.9	+0.6 -0.4	-1.5 +1.1	-0.0 +0.6	+0.1 -0.1	+0.1 -0.1	+2.4 -2.4	+3.3 -3.3
	0.11	$1.89 \cdot 10^{-1}$	149		+8.9 -7.5	+5.1 -5.1	+0.6 -0.9	-1.8 +2.0	-0.3 -0.6	-0.3 +0.2	+0.1 -0.1	+2.4 -2.4	+3.3 -3.3
	0.17	$1.10 \cdot 10^{-1}$	126		+9.7 -8.1	+5.2 -4.9	+1.2 -0.4	-1.0 +1.0	-1.2 +1.6	+0.5 -0.4	+0.1 -0.1	+2.4 -2.4	+3.3 -3.3
	0.24	$7.26 \cdot 10^{-2}$	102		+10.9 -9.0	+4.2 -3.7	+1.1 -0.3	-0.8 +1.9	-0.5 +0.2	+0.9 -0.9	+0.1 -0.1	+2.4 -2.4	+1.0 -1.0
	0.34	$3.34 \cdot 10^{-2}$	69		+13.6 -10.6	+4.7 -4.2	+0.2 -1.0	-1.2 +0.8	-1.7 +2.6	+1.7 -0.9	+0.2 -0.2	+2.4 -2.4	+1.0 -1.0

Table B.5 (continued):

Q^2 (GeV ²)	x	$d^2\sigma/dxdQ^2$ (pb/GeV ²)	Nevt.	upper limit (pb/GeV ²)	stat. (%)	total sys. (%)	uncor. sys. (%)	δ_1 (%)	δ_2 (%)	δ_3 (%)	δ_4 (%)	δ_5 (%)	δ_6 (%)
2273	0.07	$2.41 \cdot 10^{-1}$	179		+8.1 -7.0	+5.1 -5.0	+0.9 -0.4	-1.4 +1.7	-1.0 +0.8	-0.0 -0.0	+0.2 -0.2	+2.4 -2.4	+3.3 -3.3
	0.12	$1.55 \cdot 10^{-1}$	150		+8.8 -7.5	+5.1 -5.1	+0.6 -1.0	-1.7 +2.0	-0.4 -0.2	-0.5 +0.4	+0.0 -0.0	+2.4 -2.4	+3.3 -3.3
	0.18	$8.25 \cdot 10^{-2}$	114		+10.3 -8.5	+5.1 -4.9	+0.2 -0.6	-0.6 +1.3	-1.4 +1.5	+0.2 -0.3	+0.1 -0.1	+2.4 -2.4	+3.3 -3.3
	0.26	$3.77 \cdot 10^{-2}$	68		+13.7 -10.7	+4.3 -3.7	+1.0 -0.2	-0.7 +1.8	+0.7 +0.4	+1.0 -1.1	+0.1 -0.1	+2.4 -2.4	+1.0 -1.0
	0.37	$1.71 \cdot 10^{-2}$	40		+18.5 -13.4	+5.1 -4.9	+0.8 -0.3	-1.4 +2.3	-2.8 +2.2	+1.9 -1.4	+0.3 -0.3	+2.4 -2.4	+1.0 -1.0
2644	0.09	$1.48 \cdot 10^{-1}$	135		+9.4 -7.9	+5.2 -5.1	+0.5 -0.5	-1.3 +1.8	-1.5 +1.4	-0.3 +0.3	+0.1 -0.1	+2.4 -2.4	+3.3 -3.3
	0.14	$7.74 \cdot 10^{-2}$	107		+10.6 -8.8	+4.9 -5.1	+0.5 -0.6	-2.1 +1.6	-0.1 +0.1	+0.1 -0.0	+0.1 -0.1	+2.4 -2.4	+3.3 -3.3
	0.21	$4.65 \cdot 10^{-2}$	77		+12.8 -10.1	+4.3 -4.0	+1.5 -0.6	-2.0 +0.8	-0.4 +1.9	+0.2 -0.2	+0.1 -0.1	+2.4 -2.4	+1.0 -1.0
	0.29	$2.58 \cdot 10^{-2}$	57		+15.1 -11.5	+3.7 -4.6	+0.0 -1.8	-1.6 +0.1	-1.1 +0.7	+1.2 -1.4	+0.0 -0.0	+2.4 -2.4	+1.0 -1.0
	0.40	$1.11 \cdot 10^{-2}$	33		+20.5 -14.6	+5.1 -5.6	+0.6 -0.5	-0.0 +0.0	-3.3 +2.4	+1.2 -1.3	+0.4 -0.4	+2.4 -2.4	+2.7 -2.7
3073	0.06	$1.24 \cdot 10^{-1}$	83		+12.2 -9.8	+5.1 -5.3	+0.3 -0.6	-2.4 +1.9	+0.8 -0.0	+0.4 -0.3	+0.1 -0.1	+2.4 -2.4	+3.3 -3.3
	0.10	$8.34 \cdot 10^{-2}$	87		+11.9 -9.6	+5.2 -4.8	+1.2 -0.8	-0.9 +1.7	-0.4 +0.8	-0.4 +0.2	+0.1 -0.1	+2.4 -2.4	+3.3 -3.3
	0.15	$5.79 \cdot 10^{-2}$	99		+11.1 -9.0	+4.9 -4.7	+0.5 -0.3	-0.7 +1.3	-0.5 -0.4	-0.2 +0.1	+0.1 -0.1	+2.4 -2.4	+3.3 -3.3
	0.23	$2.52 \cdot 10^{-2}$	53		+15.7 -12.0	+3.9 -3.8	+0.8 -0.2	-0.6 +1.1	-1.4 +0.9	+0.6 -0.4	+0.1 -0.1	+2.4 -2.4	+1.0 -1.0
	0.32	$1.79 \cdot 10^{-2}$	49		+16.4 -12.3	+4.7 -4.4	+0.2 -0.9	-2.2 +1.7	-1.0 +2.6	+0.7 -0.7	+0.1 -0.1	+2.4 -2.4	+1.0 -1.0
3568	0.43	$5.58 \cdot 10^{-3}$	21		+26.9 -17.4	+5.5 -5.4	+0.2 -0.6	-1.0 +1.2	-2.9 +2.9	+1.2 -1.3	+0.5 -0.5	+2.4 -2.4	+2.7 -2.7
	0.07	$6.73 \cdot 10^{-2}$	59		+14.8 -11.5	+5.2 -5.3	+1.4 -0.9	-2.2 +1.7	+0.6 -0.7	+0.3 -0.3	+0.1 -0.1	+2.4 -2.4	+3.3 -3.3
	0.11	$4.68 \cdot 10^{-2}$	64		+14.1 -11.0	+4.9 -5.4	+0.3 -1.2	-2.3 +1.5	-0.8 +0.6	-0.1 +0.2	+0.0 -0.0	+2.4 -2.4	+3.3 -3.3
	0.17	$3.15 \cdot 10^{-2}$	62		+14.4 -11.2	+4.8 -5.3	+0.7 -0.2	-2.4 +1.2	+0.1 -0.7	-0.2 +0.1	+0.1 -0.1	+2.4 -2.4	+3.3 -3.3
	0.25	$2.06 \cdot 10^{-2}$	56		+15.2 -11.6	+4.1 -4.4	+0.3 -0.6	-1.6 +1.0	-2.1 +1.9	+0.5 -0.2	+0.1 -0.1	+2.4 -2.4	+1.0 -1.0
4145	0.35	$8.84 \cdot 10^{-3}$	33		+20.5 -14.6	+4.3 -3.7	+1.5 -0.4	-0.7 -0.0	-0.9 +1.9	+0.6 -0.7	+0.2 -0.2	+2.4 -2.4	+1.0 -1.0
	0.47	$4.14 \cdot 10^{-3}$	19		+28.6 -18.0	+6.1 -5.4	+0.7 -0.4	-0.5 +1.3	-3.1 +3.6	+1.8 -0.6	+0.6 -0.6	+2.4 -2.4	+2.7 -2.7
	0.08	$5.56 \cdot 10^{-2}$	58		+15.0 -11.4	+6.3 -5.3	+1.8 -1.0	-2.3 +3.4	+1.6 -0.6	+0.5 -0.5	+0.1 -0.1	+2.4 -2.4	+3.3 -3.3

Table B.5 (continued):

Q^2 (GeV ²)	x	$d^2\sigma/dxdQ^2$ (pb/GeV ²)	Nevt.	upper limit (pb/GeV ²)	stat. (%)	total sys. (%)	uncor. sys. (%)	δ_1 (%)	δ_2 (%)	δ_3 (%)	δ_4 (%)	δ_5 (%)	δ_6 (%)	
4806	0.13	$3.04 \cdot 10^{-2}$	53		+15.7 -12.0	+5.4 -4.9	+0.8 -0.4	-1.2 +2.5	-0.7 +0.4	-0.3 +0.5	+0.0 -0.0	+2.4 -2.4	+3.3 -3.3	
	0.19	$1.74 \cdot 10^{-2}$	47		+16.8 -12.5	+4.8 -4.9	+0.3 -0.6	-1.3 +0.8	-0.5 +1.0	+0.1 +0.1	+0.2 -0.2	+2.4 -2.4	+3.3 -3.3	
	0.28	$1.05 \cdot 10^{-2}$	36		+19.7 -14.0	+5.4 -4.1	+3.0 -0.7	-1.3 +2.1	-1.6 +1.9	+0.1 -0.6	+0.1 -0.1	+2.4 -2.4	+1.0 -1.0	
	0.39	$5.24 \cdot 10^{-3}$	23		+25.4 -16.9	+4.0 -4.4	+0.6 -1.3	-1.3 +0.0	-1.8 +1.7	+0.8 -0.9	+0.3 -0.3	+2.4 -2.4	+1.0 -1.0	
	0.51	$1.21 \cdot 10^{-3}$	7		+53.7 -25.2	+6.1 -6.8	+1.2 -0.9	-2.4 +2.2	-4.5 +3.2	+1.4 -0.6	+0.5 -0.5	+2.4 -2.4	+2.7 -2.7	
	0.11	$2.12 \cdot 10^{-2}$	33		+20.5 -14.6	+4.9 -5.3	+0.3 -2.0	-1.6 +1.1	+0.4 +0.7	+0.1 -0.4	+0.1 -0.1	+2.4 -2.4	+3.3 -3.3	
	0.16	$2.12 \cdot 10^{-2}$	47		+16.8 -12.5	+5.0 -5.3	+0.7 -2.2	-1.1 +1.3	-0.7 +1.2	-0.4 +0.6	+0.1 -0.1	+2.4 -2.4	+3.3 -3.3	
	0.23	$8.94 \cdot 10^{-3}$	30		+21.7 -15.2	+3.8 -3.9	+0.2 -0.2	-1.5 +1.6	-1.0 -0.2	+0.3 +0.1	+0.1 -0.1	+2.4 -2.4	+1.0 -1.0	
	0.33	$5.20 \cdot 10^{-3}$	23		+25.4 -16.9	+4.6 -4.1	+1.3 -0.3	+0.8 +1.2	-2.2 +2.3	+0.1 -0.6	+0.1 -0.1	+2.4 -2.4	+1.0 -1.0	
	0.44	$1.88 \cdot 10^{-3}$	10		+42.7 -22.6	+5.2 -6.0	+0.5 -1.3	-1.2 +0.8	-3.6 +2.8	+0.6 -1.3	+0.4 -0.4	+2.4 -2.4	+2.7 -2.7	
5561	0.56	$6.34 \cdot 10^{-4}$	4		+78.5 -28.9	+7.6 -5.5	+2.0 -1.0	+1.1 +1.9	-3.2 +5.0	+0.2 +2.3	+0.4 -0.4	+2.4 -2.4	+2.7 -2.7	
	0.12	$1.44 \cdot 10^{-2}$	30		+21.7 -15.2	+5.0 -5.5	+0.5 -2.4	-1.3 +1.9	-0.8 -0.4	+0.3 +0.0	+0.0 -0.0	+2.4 -2.4	+3.3 -3.3	
	0.18	$8.24 \cdot 10^{-3}$	24		+24.9 -16.5	+5.7 -5.1	+0.7 -0.5	-1.8 +2.8	-0.6 +1.6	-0.7 +0.6	+0.2 -0.2	+2.4 -2.4	+3.3 -3.3	
	0.26	$5.46 \cdot 10^{-3}$	25		+24.2 -16.2	+4.6 -4.4	+0.7 -0.6	-2.3 +2.8	-1.3 +1.1	+0.3 -0.1	+0.1 -0.1	+2.4 -2.4	+1.0 -1.0	
	0.37	$2.41 \cdot 10^{-3}$	13		+36.0 -20.8	+3.8 -4.1	+0.3 -0.4	-0.5 +0.2	-2.1 +1.6	+0.1 -0.4	+0.2 -0.2	+2.4 -2.4	+1.0 -1.0	
	0.49	$7.28 \cdot 10^{-4}$	5		+67.3 -27.5	+7.0 -6.0	+1.0 -0.5	-1.9 +3.6	-3.7 +3.9	+1.2 +0.2	+0.5 -0.5	+2.4 -2.4	+2.7 -2.7	
	0.61	0	0	$< 1.52 \cdot 10^{-4}$										
	6966	0.14	$6.39 \cdot 10^{-3}$		39		+18.7 -13.6	+5.7 -5.3	+2.1 -1.1	-2.4 +2.6	+0.3 -0.2	+0.2 -0.1	+0.0 -0.0	+2.4 -2.4
0.21		$6.94 \cdot 10^{-3}$	53			+15.7 -12.0	+4.1 -4.0	+0.7 -0.3	-1.6 +1.7	-1.1 +1.3	-0.5 +0.5	+0.2 -0.2	+2.4 -2.4	+1.0 -1.0
0.30		$1.94 \cdot 10^{-3}$	24			+24.9 -16.5	+4.0 -4.1	+0.5 -0.1	-1.1 +1.2	-1.9 +1.5	-0.1 +0.0	+0.1 -0.1	+2.4 -2.4	+1.0 -1.0
0.41		$1.10 \cdot 10^{-3}$	16			+31.8 -19.2	+5.1 -5.0	+0.5 -0.3	-1.0 +1.4	-2.2 +2.3	+0.4 -0.4	+0.2 -0.2	+2.4 -2.4	+2.7 -2.7
0.53		$3.39 \cdot 10^{-4}$	6			+59.7 -26.4	+6.7 -6.1	+0.7 -0.7	-1.1 +1.0	-4.1 +4.9	+0.8 -0.2	+0.5 -0.5	+2.4 -2.4	+2.7 -2.7
0.66		$4.49 \cdot 10^{-5}$	1			+218.6 -29.8	+9.8 -7.8	+1.0 -0.9	-0.9 +0.8	-6.4 +8.6	-2.7 +3.1	+0.7 -0.7	+2.4 -2.4	+0.1 -0.1

Table B.5 (continued):

Q^2 (GeV ²)	x	$d^2\sigma/dxdQ^2$ (pb/GeV ²)	Nevt.	upper limit (pb/GeV ²)	stat. (%)	total sys. (%)	uncor. sys. (%)	δ_1 (%)	δ_2 (%)	δ_3 (%)	δ_4 (%)	δ_5 (%)	δ_6 (%)	
9059	0.13	$3.71 \cdot 10^{-3}$	11		+40.2 -22.0	+8.3 -9.4	+0.3 -5.5	-3.5 +4.1	+5.4 -4.8	+0.5 -0.9	+0.5 -0.5	+2.4 -2.4	+3.3 -3.3	
	0.19	$3.48 \cdot 10^{-3}$	28		+22.7 -15.5	+5.9 -5.7	+1.8 -0.6	-3.2 +3.2	-0.4 +0.4	+0.1 +0.3	+0.2 -0.2	+2.4 -2.4	+3.3 -3.3	
	0.27	$1.73 \cdot 10^{-3}$	22		+26.2 -17.2	+4.1 -4.5	+0.7 -0.3	-2.8 +1.8	-0.7 +1.0	-0.4 +0.1	+0.2 -0.2	+2.4 -2.4	+1.0 -1.0	
	0.38	$8.34 \cdot 10^{-4}$	16		+31.8 -19.2	+5.0 -4.9	+0.5 -0.3	-1.3 +1.2	-3.2 +3.3	+0.1 +0.2	+0.2 -0.2	+2.4 -2.4	+1.0 -1.0	
	0.51	$1.47 \cdot 10^{-4}$	3		+96.3 -30.4	+6.2 -5.5	+0.7 -0.1	-0.9 +1.7	-3.2 +4.0	+0.5 -0.7	+0.4 -0.4	+2.4 -2.4	+2.7 -2.7	
	0.64	$8.16 \cdot 10^{-5}$	2		+129.5 -32.0	+6.5 -7.0	+1.2 -0.5	-1.8 +2.2	-5.8 +5.1	-0.4 +0.1	+0.0 -0.0	+2.4 -2.4	+0.1 -0.1	
	0.78	0	0	$< 2.25 \cdot 10^{-5}$										
	0.93	0	0	$< 4.38 \cdot 10^{-6}$										
15072	0.61	$3.58 \cdot 10^{-5}$	4		+78.5 -29.0	+6.3 -7.8	+2.3 -0.9	-2.0 +1.5	-6.7 +4.5	-0.1 +0.3	+0.3 -0.3	+2.4 -2.4	+0.1 -0.1	
	0.75	$4.98 \cdot 10^{-6}$	1		+218.6 -29.8	+25.9 -6.8	+2.7 -0.7	-1.0 +2.0	-5.7 +25.4	-0.4 +0.2	+1.2 -1.2	+2.4 -2.4	+0.1 -0.1	
	0.91	0	0	$< 7.42 \cdot 10^{-7}$										

Q^2 (GeV ²)	x_{edge}	$\int_{x_{edge}}^1 d^2\sigma/dxdQ^2$ (pb/GeV ²)	Nevt.	upper limit (pb/GeV ²)	stat. (%)	total sys. (%)	uncor. sys. (%)	δ_1 (%)	δ_2 (%)	δ_3 (%)	δ_4 (%)	δ_5 (%)	δ_6 (%)
648	0.22	$1.33 \cdot 10^{-1}$	106		+10.7 -8.8	+9.8 -4.4	+2.4 -2.3	+9.0 -2.4	+0.2 +0.0	-0.6 +1.4	+0.1 -0.1	+1.6 -1.6	+0.1 -0.1
761	0.24	$6.73 \cdot 10^{-2}$	212		+7.3 -6.4	+3.8 -5.2	+2.0 -3.0	+1.7 -3.2	+0.1 +0.0	-0.1 +0.4	+0.0 -0.0	+1.6 -1.6	+0.1 -0.1
891	0.26	$4.41 \cdot 10^{-2}$	288		+6.2 -5.5	+3.3 -3.3	+1.0 -1.0	-1.4 +1.6	+0.0 +0.0	-0.9 +0.3	+0.1 -0.1	+1.6 -1.6	+0.1 -0.1
1045	0.29	$2.50 \cdot 10^{-2}$	224		+7.1 -6.3	+4.1 -3.3	+1.2 -0.7	-1.6 +2.7	+0.1 +0.0	-0.4 +0.3	+0.1 -0.1	+1.6 -1.6	+0.1 -0.1
1224	0.31	$1.48 \cdot 10^{-2}$	157		+8.6 -7.3	+3.7 -4.2	+1.7 -1.0	-3.0 +1.5	+0.1 +0.0	-0.5 +1.1	+0.1 -0.1	+1.6 -1.6	+0.1 -0.1
1431	0.34	$9.52 \cdot 10^{-3}$	120		+10.0 -8.3	+4.0 -3.7	+0.3 -0.4	-2.3 +2.7	+0.0 -0.0	-0.8 +0.9	+0.1 -0.1	+1.6 -1.6	+0.1 -0.1
1672	0.36	$3.90 \cdot 10^{-3}$	59		+14.8 -11.5	+4.6 -4.5	+0.2 -0.7	-3.4 +3.3	+0.0 +0.0	-0.7 +1.4	+0.2 -0.2	+1.6 -1.6	+0.1 -0.1
1951	0.39	$2.64 \cdot 10^{-3}$	46		+17.0 -12.7	+4.9 -4.7	+0.9 -1.0	-3.5 +3.8	+0.0 +0.0	-1.0 +1.2	+0.2 -0.2	+1.6 -1.6	+0.1 -0.1
2273	0.43	$1.52 \cdot 10^{-3}$	29		+22.3 -15.4	+4.8 -4.3	+0.6 -0.7	-3.0 +3.7	+0.0 +0.0	-1.2 +1.0	+0.1 -0.1	+1.6 -1.6	+0.1 -0.1

Table B.6: *The integral cross section table for 99-00 e^+p NC scattering. The first two columns of the table contain the Q^2 and x_{edge} values for the bin, the third contains the measured cross section $\int_{x_{edge}}^1 d^2\sigma/dxdQ^2$ corrected to the electroweak Born level, the fourth contains the number of events reconstructed in the bin, the fifth contains the upper limit in case of zero observed events, the sixth contains the statistical uncertainty and the seventh contains the total systematic uncertainty. The right part of the table lists the total uncorrelated systematic uncertainty followed by the bin-to-bin correlated systematic uncertainties δ_1 – δ_6 defined in the text. For the latter, the upper (lower) numbers refer to the variation of the cross section, whereas the signs of the numbers reflect the direction of change in the cross sections. Note that the normalization uncertainty, δ_7 is not listed.*

Table B.6 (continued):

Q^2 (GeV ²)	x_{edge}	$\int_{x_{edge}}^1 d^2\sigma/dxdQ^2$ (pb/GeV ²)	Nevt.	upper limit (pb/GeV ²)	stat. (%)	total sys. (%)	uncor. sys. (%)	δ_1 (%)	δ_2 (%)	δ_3 (%)	δ_4 (%)	δ_5 (%)	δ_6 (%)
2644	0.46	$9.16 \cdot 10^{-4}$	22		+26.2 -17.2	+4.2 -4.8	+1.4 -1.4	-3.6 +2.4	+0.0 +0.0	-0.9 +1.5	+0.2 -0.2	+1.6 -1.6	+0.1 -0.1
3073	0.50	$4.79 \cdot 10^{-4}$	13		+36.0 -20.8	+6.5 -7.2	+0.7 -0.3	-6.6 +5.8	+0.0 +0.0	-0.6 +0.9	+0.1 -0.1	+1.6 -1.6	+0.1 -0.1
3568	0.54	$2.27 \cdot 10^{-4}$	7		+53.7 -25.2	+4.8 -7.0	+1.1 -2.0	-5.8 +3.6	+0.0 +0.0	-2.0 +1.1	+0.1 -0.1	+1.6 -1.6	+0.1 -0.1
4145	0.58	$7.57 \cdot 10^{-5}$	3		+96.3 -30.4	+6.6 -6.4	+1.3 -2.2	-4.8 +5.4	+0.0 +0.0	-2.4 +2.3	+0.0 -0.0	+1.6 -1.6	+0.1 -0.1
4806	0.63	$7.05 \cdot 10^{-5}$	3		+96.3 -30.4	+15.4 -15.2	+5.4 -2.1	-7.1 +6.5	+0.0 +0.0	-3.6 +1.6	+0.2 -0.2	+1.6 -1.6	+12.5 -12.5
5561	0.68	$6.09 \cdot 10^{-5}$	3		+96.3 -30.4	+14.3 -14.0	+1.2 -3.4	-4.4 +5.3	+0.0 -0.1	-1.6 +3.5	+0.3 -0.3	+1.6 -1.6	+12.5 -12.5
6966	0.79	0	0	$< 4.07 \cdot 10^{-6}$									

References

- [1] M. Gell-Mann, Phys. Lett. **8**, 214 (1964).
- [2] R.P. Feynman, Phys. Rev. Lett. **23**, 1415 (1969).
- [3] R. Hofstadter, *Electron scattering & Nuclear and Nucleon Scattering*.
W. A. Benjamin, New York, 1963.
- [4] E.D. Bloom et al., Phys. Rev. Lett. **23**, 930 (1969);
M. Breidenbach et al., Phys. Rev. Lett. **23**, 935 (1969).
- [5] A. Salam, *Elementary Particle Physics*. (1968). Reprinted in Gauge Theory of
Weak and Electromagnetic Interactions, C.H. Lai, ed.(Singapore: World Scientific,
1981).
- [6] R.P. Feynman, Phys. Rev. **76**, 749 (1949);
R.P. Feynman, Phys. Rev. **76**, 769 (1949).
- [7] P.W. Higgs, Phys. Lett. **12**, 132 (1964);
P.W. Higgs, Phys. Rev. Lett. **13**, 508 (1964);
P.W. Higgs, Phys. Rev. **145**, 1156 (1966).
- [8] P.W. Anderson, Phys. Rev. **130**, 439 (1963).
- [9] F. Englert and R. Brout, Phys. Rev. Lett. **13**, 321 (1964).
- [10] S.L. Glashow, Nucl. Phys. **22**, 579 (1961).
- [11] J.I. Friedman and H.W. Kendall, Annual Review of Nuclear Science **22**, 203 (1972).
- [12] J.D. Bjorken, Phys. Rev. **179**, 1547 (1969).

- [13] C.G. Callan and D.J. Gross, Phys. Rev. Lett. **22**, 156 (1969).
- [14] G. Altarelli and G. Parisi, Nucl. Phys. **B 126**, 298 (1977);
V.N. Gribov and L.N. Lipatov, Sov. J. Nucl. Phys. **15**, 438 (1972);
L.N. Lipatov, Sov. J. Nucl. Phys. **20**, 94 (1975);
Yu.L. Dokshitzer, Sov. Phys. JETP **46**, 641 (1977).
- [15] BCDMS Coll., A.C. Benvenuti et al., Phys. Lett. **B 223**, 485 (1989).
- [16] L.W. Whitlow et al., Phys. Lett. **B 282**, 475 (1992).
- [17] M.Osipenko et al., Phys. Rev. **D 67**, 092001 (2003).
- [18] ZEUS Coll., S. Chekanov et al., Phys. Rev. **D 70**, 052001 (2003).
- [19] ZEUS Coll., S. Chekanov et al., Eur. Phys. J. **C 28**, 175 (2003).
- [20] ZEUS Coll., S. Chekanov et al., Phys. Lett. **B 539**, 197 (2002).
- [21] ZEUS Coll., S. Chekanov et al., Eur. Phys. J. **C 21**, 443 (2001).
- [22] ZEUS Coll., J. Breitweg et al., Phys. Lett. **B 487**, 53 (2000).
- [23] H1 Coll., C. Adloff et al., Eur. Phys. J. **C 30**, 1 (2003).
- [24] ZEUS Coll., J. Breitweg et al., Phys. Lett. **B 407**, 432 (1997).
- [25] ZEUS Coll., M. Derrick et al., Z. Phys. **C 72**, 399 (1996).
- [26] J. Pumplin et al., JHEP **0207**, 012 (2002).
- [27] A.D. Martin et al., EPJ **C 23**, 73 (2002).
- [28] ZEUS Coll., S. Chekanov et al., Eur. Phys. J. **C 42**, 1 (2005).
- [29] ZEUS Coll., U. Holm (ed.), *The ZEUS Detector*. Status Report (unpublished),
DESY (1993), available on <http://www-zeus.desy.de/bluebook/bluebook.html>.
- [30] A. Bamberger et al., Nucl. Inst. Meth. **A 401**, 63 (1997).
- [31] A. Dwurazny et al., Nucl. Inst. Meth. **A 277**, 176 (1989).
- [32] M. Derrick et al., Nucl. Inst. Meth. **A 309**, 77 (1991);
A. Andresen et al., Nucl. Inst. Meth. **A 309**, 101 (1991);

- A. Caldwell et al., Nucl. Inst. Meth. **A 321**, 356 (1992);
 A. Bernstein et al., Nucl. Inst. Meth. **A 336**, 23 (1993).
- [33] N. Harnew et al., Nucl. Inst. Meth. **A 279**, 290 (1989);
 B. Foster et al., Nucl. Phys. Proc. Suppl. **B 32**, 181 (1993);
 B. Foster et al., Nucl. Inst. Meth. **A 338**, 254 (1994).
- [34] A. Bamberger et al., Nucl. Inst. Meth. **A 382**, 419 (1996).
- [35] H. Bethe and W. Heitler, Proc. Roy. Soc. Lond. **A146**, 83 (1934).
- [36] J. Andruszków et al., Acta Phys. Pol. **B 32**, 2025 (2001).
- [37] G.A. Schuler and H. Spiesberger, *Proc. Workshop on Physics at HERA*,
 W. Buchmüller and G. Ingelman (eds.), Vol. 3, p. 1419. Hamburg, Germany, DESY
 (1991);
 H. Spiesberger, *HERACLES and DJANGO: Event Generation for ep Interactions at
 HERA Including Radiative Processes*, 1998, available on
<http://www.desy.de/~hspiesb/djangoh.html>.
- [38] A. Kwiatkowski, H. Spiesberger and H.-J. Möhring, Comp. Phys. Comm.
69, 155 (1992). Also in *Proc. Workshop Physics at HERA*, 1991, DESY, Hamburg.
- [39] G. Ingelman, A. Edin and J. Rathsman, Comp. Phys. Comm. **101**, 108 (1997).
- [40] T. Sjöstrand, Comp. Phys. Comm. **82**, 74 (1994).
- [41] CTEQ Coll., H.L. Lai et al., Eur. Phys. J. **C 12**, 375 (2000).
- [42] L. Lönnblad, Comp. Phys. Comm. **71**, 15 (1992).
- [43] R. Brun et al., GEANT3, Technical Report CERN-DD/EE/84-1, CERN, 1987.
- [44] S. Bentvelsen, J. Engelen and P. Kooijman, *Proc. Workshop on Physics at HERA*,
 W. Buchmüller and G. Ingelman (eds.), Vol. 1, p. 23. Hamburg, Germany, DESY
 (1992);
 K.C. Höger, *Proc. Workshop on Physics at HERA*, W. Buchmüller and
 G. Ingelman (eds.), Vol. 1, p. 43. Hamburg, Germany, DESY (1992).

- [45] A. López-Durán Viani and S. Schlenstedt, *Electron Finder Efficiencies and Impurities. A Comparison Between SINISTRA95, EM and EMNET* (unpublished). ZEUS-99-077, internal ZEUS note, 1999.
- [46] A. Caldwell, W. Liu, B. Straub, *BCAL electron study: I* (unpublished). Zeus-98-002, internal ZEUS-note, 1998;
A. Caldwell, W. Liu, B. Straub, *BCAL electron study: II* (unpublished). Zeus-98-058, internal ZEUS-note, 1998.
- [47] ZEUS Coll., J. Breitweg et al., Eur. Phys. J. **C 11**, 427 (1999).
- [48] S. Catani et al., Nucl. Phys. **B406**, 187 (1993).
- [49] S.D. Ellis and D.E. Soper, Phys. Rev. **D 48**, 3160 (1993).
- [50] J.E. Huth et al., *Research Directions for the Decade. Proceedings of Summer Study on High Energy Physics, 1990*, E.L. Berger (ed.), p. 134. World Scientific (1992). Also in preprint FERMILAB-CONF-90-249-E.
- [51] G.F. Hartner, *VCTRAK(3.07/04): Offline Output Information* (unpublished). ZEUS-97-064, internal ZEUS-note, 1997.
- [52] G. F. Hartner, *VCTRAK Briefing: Program and Math* (unpublished). Zeus-98-058, internal ZEUS-note, 1998.
- [53] X. Liu. Ph.D. Thesis, Columbia University, 2003.
- [54] F. Jacquet and A. Blondel, *Proceedings of the Study for an ep Facility for Europe*, U. Amaldi (ed.), p. 391. Hamburg, Germany (1979). Also in preprint DESY 79/48.
- [55] Particle Data Group, D.E. Groom et al., Eur. Phys. J. **C 15**, 1 (2000).
- [56] A. Arbuzov et al., Comp. Phys. Comm. **94**, 128 (1996).
- [57] C. Buettner, *Relative energy calibration with halo muons in the first inner ring of FCAL and RCAL* (unpublished). 2005.
- [58] J. Pumplin, et al., JHEP **0207**, 012 (2002).
- [59] ZEUS Coll., S. Chekanov et al., Phys. Rev. **D 67**, 12007 (2003).

[60] ZEUS Coll., S. Chekanov et al., Eur. Phys. J. **C42**, 1 (2005).

[61] C. Gwenlan, private communication, 2006.